Vilnius University
Center for Physical Sciences and Technology

Kipras Redeckas

ELECTRONIC KINETICS AND STRUCTURAL DYNAMICS OF PHOTOCHROMIC AND PHOTOSYNTHETIC PIGMENTS

Doctoral thesis
Physical sciences, Physics (02P)

Vilnius, 2016

Thesis was prepared at Vilnius University in 2012–2016, Vilnius, Lithuania.

SCIENTIFIC SUPERVISOR:

Prof. dr. Mikas Vengris (Vilnius University, Physical sciences, Physics — 02P).

Vilniaus universitetas
Fizinių ir technologijos mokslų centras

Kipras Redeckas

ELEKTRONINIAI VIRSMAI IR STRUKTŪRINĖ DINAMIKA FOTOCHROMINIUOSE BEI FOTOSINTETINIUOSE PIGMENTUOSE

Daktaro disertacija
Fiziniai mokslai, fizika (02P)

Vilnius, 2016

Disertacija rengta 2012–2016 metais Vilniaus universitete.

MOKSLINIS VADOVAS:

Prof. dr. Mikas Vengris (Vilniaus universitetas, fiziniai mokslai, fizika — 02P).

"Ideas or the lack of them can cause disease."

Kurt Vonnegut, Breakfast of Champions

ACKNOWLEDGMENTS

The ultrafast spectroscopy group has always been a relatively small part of Vilnius University Laser Research Center. Therefore, without fear of leaving someone out, my gratitude goes to two people in particular, who have supported me throughout this four-year journey.

First and foremost, I would like to thank my supervisor prof. Mikas Vengris, who was merely *dr. Mikas Vengris* when we first met. It was Mikas who had reignited my curiosity and enthusiasm for molecular physics, after I was feeling burned out by my early discouraging endeavors with quantum chemistry. Mikas taught me the ropes of experimental physics and has, more than anyone else, shaped my scientific perspective and the way of working. Mikas' astounding expertise on all matters scientific was a great catalyst to learn more and to take on new challenges. In all likelihood, aspiration to be a scientist like Mikas was one of the main reasons why I had decided to take the plunge and dedicate these four years for scientific ventures in the first place. Thank you, Mikas, for all the experience, enthusiasm, and encouragement.

Secondly, I would like to express my gratitude to dr. Vladislava Voiciuk, who, similarly, bore less academic titles when we met. Not only has Vlada been a great and dependable co-worker, but also one of the most fun people to work with. I have always admired Vlada's witty, prudent, and maybe oftentimes sardonic outlook on scientific and wordly affairs, her eagerness to discuss a wide array of topics, and her heartfelt enthusiasm for matters that truly interested her. Vlada's presence in the group and her lively energy were some of the reasons why work has never really become dull. Thank you for being a great colleague and a friend.

CONTENTS

ACRONYMS

ΔΔOD	Double difference absorption
ΔOD	Difference absorption
BBO	β-barium borate (β-BaB_2O_4)
DP	Dump-probe
ESA	Excited state absorption
FCP	Fucoxanthin-chlorophyll-protein
FP	Flash photolysis
FRIKES	Femtosecond Raman-induced Kerr effect spectroscopy
FSRS	Femtosecond stimulated Raman scattering
FWHM	Full width at half maximum
FX	Fucoxanthin
GSB	Ground state bleaching
GSI	Ground state intermediate
GVD	Group velocity dispersion
GVM	Group velocity mismatch
IA	Induced absorption
IB	Indolo[2,1-*b*][1,3]benzoxazine
ICT	Intramolecular charge transfer (state)
IND	3H-indolium ($C_8H_8N^+$)
IR	Infrared radiation (0.75–1000 μm)
IRF	Instrument response function
KDP	Potassium dihydrogen phosphate (KH_2PO_4)
LWIR	Long-wavelength infrared radiation (8–15 μm)
MCT	Mercury cadmium telluride (HgCdTe)
MECN	Acetonitrile (CH_3CN)
MEOH	Methanol (CH_3OH)
MIDIR	Mid-wavelength infrared radiation (3–8 μm)
MIDUV	Mid-wavelength ultraviolet radiation (200–300 nm)

NIR	Near-infrared radiation (0.75–1.4 µm)
NOPA	Non-collinear optical parametric amplifier
NUV	Near-ultraviolet radiation (300–400 nm)
OD	Optical density
OPA	Optical parametric amplifier
PA	Photoproduct absorption
PCP	Peridinin-chlorophyll-protein
PDA	Photodiode array
PDAT	Pump-dump-probe (action trace)
PDP	Pump-dump-probe (kinetic trace)
PES	Potential energy surface
pNPH	4-nitrophenol ($C_6H_5NO_3$)
pNPHE	4-nitrophenolate ($C_6H_4NO_3^-$)
PP	Pump-probe
pPPP	Prepump-pump-probe
PrPAT	Pump-repump-probe (action trace)
PrPP	Pump-repump-probe (kinetic trace)
RINE	Raman induced by nonlinear emission
rPP	Repump-probe
SADS	Species-associated difference spectrum
SE	Stimulated emission
SpRS	Spontaneous Raman scattering
SRS	Stimulated Raman scattering
TA	Transient absorption
TBAH	Tetrabutylammonium hydroxide ($((C_4H_9)_4NOH$)
THF	Tetrahydrofuran ($(CH_2)_4O$)
Ti:Sa	Titanium-sapphire ($Ti^{3+}:Al_2O_3$)
TST	Transition state theory
UV	Ultraviolet radiation (120–400 nm)
VIS	Visible radiation (380–750 nm)
WLSc	White light supercontinuum

Part I

A FOREWORD

1

INTRODUCTION

SHEDDING LIGHT ON THE MOLECULAR WORLD

Nearly one hundred years ago Henry Eyring, and (independently) Meredith Gwynne Evans and Michael Polany established the roots of transition state theory (TST) [1, 2]. Within its scope, all chemical reactions are described as a continuous change in the relative positions and potential energies of the reactive atomic or molecular species. A chemical reaction takes place when the reactants gain enough energy to overcome a potential energy barrier (ΔE_a) and are thereby able form the so-called activated complex—essentially a saddle point of a potential energy surface (PES). Since these activated complexes can convert into products, the kinetic theory implies that the rates of this conversion are:

$$k = \frac{k_B T}{h} K^{\ddagger}, \tag{1.1}$$

where $K^{\ddagger} \sim \exp\left(-\Delta E_a / k_B T\right)$ is the concentration equilibrium constant [2]. In essence, TST discloses that fastest chemical reactions, such as the reactant molecules getting close enough to form an activated complex, at room temperature develop in the timescale of $h/k_B T \approx 160\,\text{fs}$. This figure, while being slightly exaggerated, is very close to the currently-comprehended characteristic molecular vibration lifetimes of ca. 10–100 fs. This estimate essentially predicts the highest temporal resolution necessary to directly observe the fastest nuclear motions, taking place in a sub-ångström spatial scale [3, 4].

Back when the TST was first postulated no one had even dreamed of measuring processes of such rapidness—the activated complex was more of a useful (yet very rigorous) concept, rather than an actual observable chemical state. All things considered, scientists of the day were limited to a sub-second temporal resolution and thereby could only examine extremely slow chemical processes [3, 4]. The humble roots of modern time-resolved spectroscopy can be traced back to the pioneering works of stopped-flow enzyme studies

by Britton Chance in the early 1940's, that pushed temporal resolution to the millisecond time scale [5, 6], and flash photolysis (FP) measurements of free radicals in solutions by Ronald G.W. Norrish and George Porter in the early 1950's, that broke the microsecond limit [7, 8]. The advent of laser technology [9], the advancements in ultrashort high-intensity laser pulse generation (first by Q-switching [10] and later by mode-locking [11]), and the introduction of tunable optical parametric devices [12], that expanded the spectral limits of laser radiation well beyond the VIS/NIR, have all put the theoretical boundaries, established by Eyring et al., to test. Moreover, all these innovations have lead to the development of a new area in chemical physics—femtochemistry [3, 4]. During the half-century since the invention of the most valuable spectroscopic tool—the laser—scientists were finally able to directly "peer" into such overwhelmingly fast processes, such as electron and proton transfer dynamics in the molecular excited states [13], formation and breakage of chemical bonds [14], photosynthesis [15, 16], vibronic relaxation [17], solvation dynamics [18], human vision [19, 20], etc. With the dawn of attosecond laser technology we have breached well beyond the electronic limit and are tentatively able to witness processes that have previously been thought to be instantaneous even from a quantum mechanical perspective [21].

Presently we have the tools and technology whose speed can challenge that of the molecular world, albeit the complex nature of many natural and artificial molecular systems still leaves a great deal of unanswered questions. Most of the time we are less limited by the resolution of time-resolved measurements, but are oftentimes faced with the dilemma of how to properly interpret the elaborate experimental data. All these unanswered questions call for new types of measurement methods that would allow us to look at the same problem from a different perspective. In the thesis at hand we will try to take a glimpse into the inner workings of two seemingly distinct molecular systems—naturally occurring photosynthetic carotenoids and artificial photochromic indolo[2,1-*b*][1,3]benzoxazines (IBs). While the latter systems are relatively new, photosynthetic pigments and complexes have been puzzling photochemists for over a century [22]. The main tasks and goals of this thesis, as a matter of fact, did not stem from a practical necessity, but arose from a scientific aspiration to comprehend the complex molecular mechanisms that govern their photophysics. To disentangle the intricate spectral dynamics of these two molecular systems we have adapted a number of experimental techniques—some more and some less commonplace—to gain a knowledge of the electronic and structural dynamics occurring in the ultrashort timescale. Throughout the course of this thesis we will see that a single perspective on

the photodynamics is often not enough to fully appreciate the intricate phenomena of the nano-scale world.

STRUCTURE OF THE THESIS

The thesis is composed of six parts, including an introduction, an afterword, and an appendix. Parts II to IV are formally separated into four distinct chapters. The parts are organized thematically according to the subject of research (or the methodology), whereas the chapters are more focused on a particular set of experiments and/or experimental techniques. A short synopsis is presented at the beginning of each part, summarizing the inceptive ideas, core concepts, and the potential reconsideration of some the preceding notions.

THE MAIN TASKS OF THE THESIS

- Assembly and characterization of a tunable femtosecond stimulated Raman scattering (FSRS) apparatus, automation of the experimental setup, and development of software tools for signal retrieval and processing.
- Investigation of the excited state dynamics of the marine carotenoid fucoxanthin (FX), exploration of the interstate couplings and the evolutionary pathways between its excited state "cohabitants", conception of a model of the FX photoevolution.
- Investigation of the electronic kinetics, structural dynamics, and photochromic capabilities of phenyl-substituted IB compounds, analysis of their standard and temporally-perturbed photoevolution, elucidation of the steady- and excited-state vibronic characteristics of the oxazine ring-opening.

PRACTICAL AND SCIENTIFIC NOVELTY

- A tunable FSRS apparatus based on spectrally-limiting 2^{nd} harmonic generation was assembled, tested, and practically implemented to uncover the time-resolved structural dynamics of several carotenoids (β-carotene, FX) and IB-type molecular compounds.
- A direct coupling between the FX S_1 and ICT excited states was observed for the first time and the interstate population transfer rates (i.e.,

the coupling "strength") were determined via multi-pulse spectroscopic methods.

- A comprehensive evolutionary model, incorporating the vibronic features of the FX excited states, was proposed to interpret the FX photoevolution.
- Primary photodynamic events in structurally-modified IB systems were uncovered for the first time and a branched evolutionary model was introduced to explain their non-trivial femto-to-nanosecond scale spectral dynamics.
- The capability of multi-pulse light-controllable transient absorption modulation (i.e., optical "switching") was experimentally tested—and demonstrated to be possible—on an IB compound.
- A number of different IB molecular conformations were for the first time investigated by steady-state and time-resolved Raman spectroscopy, thus shedding additional structure-sensitive insight to the [1,3]oxazine ring-opening dynamics.

STATEMENTS TO DEFEND

1. Excited state equilibrium exists between the FX S_1 and ICT states. This interstate equilibrium is established with the average reciprocal rates of $\tau_{S_1 \to ICT} = 2.4\,ps$ and $\tau_{ICT \to S_1} = 4.1\,ps$, and is thus restored on a sub-6-picosecond timescale after its deliberate disturbance.
2. The FX S_1 state is distinguished by $1250\,cm^{-1}$ (C–C) and $1735\,cm^{-1}$ (C=C), whereas the FX ICT is distinguished by $1215\,cm^{-1}$ (C–C) and $1555\,cm^{-1}$ (C=C) excited state vibrations, the latter of which acts as a possible coupling channel for the $S_1 \longleftrightarrow$ ICT equilibrium.
3. The sub-nanosecond photoevolution in phenyl-substituted IB systems, evoked by the absorption of an ultrashort UV pulse, proceeds from the Frank–Condon state via two parallel evolutionary routes, that correspond to a fast ($\tau < 1\,ps$) "unsuccessful" and a slow ($\tau \sim 15\,ps$) "effective" reaction coordinates of the photoproduct formation.
4. Transient absorption of the UV-excited phenyl-substituted IB systems may be modulated via a properly-timed introduction of an ultrashort VIS/NIR pulse, resonant to the absorption of the IB excited state/photoproduct species. A perturbation of the ordinary IB photoevolution with

ca. 80 GW/cm^2 intensity pulsed NIR radiation allows us to achieve up to 20 % short-term (ca. 20 ps) and/or up to 6 % long-term (> 6 ns, i.e., "permanent") modulation of the transient IB signal.

5. The chemically ring-opened and the UV excitation-generated forms of phenyl-substituted IBs are, from a spectroscopic perspective, dissimilar both electronically and vibrationally. This vibronic disparity between the two—previously deemed equivalent—molecular species implies that the [1,3]oxazine ring-opening competes with a more effective auxiliary UV excitation-induced photochemical pathway. Products of this photoreaction predominate in the phenyl-substituted IB transient absorption spectra and exhibit an enhanced vibronic activity in the phenyl-indolic (and not the nitrophenolic) IB moiety.

APPROBATION

The results of the thesis were presented in the following peer-reviewed scientific publications:

[A1] Kipras Redeckas, Stepas Toliautas, Rasa Steponavičiūtė, Algirdas Šačkus, Juozas Sulskus, and Mikas Vengris. "A femtosecond stimulated Raman spectroscopic study on the oxazine ring opening dynamics of structurally-modified indolobenzoxazines." In: *Chemical Physics Letters* 653 (2016), pp. 67–72. DOI: 10.1016/j.cplett.2016.04.030.

[A2] Kipras Redeckas, Vladislava Voiciuk, and Mikas Vengris. "Investigation of the S_1/ICT equilibrium in fucoxanthin by ultrafast pump-dump-probe and femtosecond stimulated Raman scattering spectroscopy." In: *Photosynthesis Research* 128.2 (2016), pp. 169–181. DOI: 10.1007/s11120-015-0215-9.

[A3] Kipras Redeckas, Vladislava Voiciuk, and Mikas Vengris. "A Tunable Femtosecond Stimulated Raman Scattering System Based on Spectrally Narrowed Second Harmonic Generation." In: *Lithuanian Journal of Physics* 56 (2016), pp. 21–34. DOI: 10.3952/physics.v56i1.3273.

[A4] Vladislava Voiciuk, Kipras Redeckas, Vytas Martynaitis, Rasa Steponavičiūtė, Algirdas Šačkus, and Mikas Vengris. "Redefining the established understanding of excitation dynamics of photochromic oxazines." In: *Physical Chemistry Chemical Physics* 17.27 (2015), pp. 17828–17837. DOI: 10.1039/C5CP02143J.

[A5] Kipras Redeckas, Vladislava Voiciuk, Rasa Steponavičiūtė, Vytas Martynaitis, Algirdas Šačkus, and Mikas Vengris. "Optically Controlled Molecular Switching of an Indolobenzoxazine-Type Photochromic Compound." In: *The Journal of Physical Chemistry A* 118.30 (2014), pp. 5642–5651. DOI: 10.1021/jp505723q.

[A6] Kipras Redeckas, Vladislava Voiciuk, Rasa Steponavičiūtė, Vytas Martynaitis, Algirdas Šačkus, and Mikas Vengris. "Ultrafast spectral dynamics of structurally modified photochromic indolo[2,1-*b*][1,3]benzoxazines." In: *Journal of Photochemistry and Photobiology A: Chemistry* 285 (2014), pp. 7–15. DOI: 10.1016/j.jphotochem.2014.04.010.

[A7] Vladislava Voiciuk, Kipras Redeckas, Vytas Martynaitis, Rasa Steponavičiūtė, Algirdas Šačkus, and Mikas Vengris. "Improving the photochromic properties of indolo[2,1-*b*][1,3]benzoxazines with phenylic substituents." In: *Journal of Photochemistry and Photobiology A: Chemistry* 278 (2014), pp. 60–68. DOI: 10.1016/j.jphotochem.2013.12.022.

The author has also contributed to other scientific publications, not covered within the scope of this thesis:

[A8] Angela Eckstein, Renata Karpicz, Ramūnas Augulis, Kipras Redeckas, Mikas Vengris, Imge Namal, Tobias Hertel, and Vidmantas Gulbinas. "Excitation quenching in polyfluorene polymers bound to (6,5) single-wall carbon nanotubes." In: *Chemical Physics* 467 (2016), pp. 1–5. DOI: 10.1016/j.chemphys.2015.12.006.

[A9] Paulius Grivickas, Stephen Sampayan, Kipras Redeckas, Mikas Vengris, and Vytautas Grivickas. "Probing of Carrier Recombination in n- and p-Type 6H-SiC Using Ultrafast Supercontinuum Pulses." In: *Materials Science Forum* 821-823 (2015), pp. 245–248. DOI: 10.4028/www.scientific.net/MSF.821-823.245.

[A10] Greta Ragaitė, Vytas Martynaitis, Vilija Kriščiūnienė, Neringa Kleizienė, Kipras Redeckas, Vladislava Voiciuk, Mikas Vengris, and Algirdas Šačkus. "Fast and stable light-driven molecular switch based on a 5*a*,13-methanoindolo[2,1-*b*][1,3]benzoxazepine ring system." In: *Dyes and Pigments* 113 (2015), pp. 546–553. DOI: 10.1016/j.dyepig.2014.09.006.

[A11] Greta Ragaitė, Vytas Martynaitis, Kipras Redeckas, Vladislava Voiciuk, Mikas Vengris, and Algirdas Šačkus. "Synthesis, crystal structures, and laser flash photolysis of 3-nitro-7*a*,15-methanonaphtho[1′, 2′:6,7][1,3]oxazepino[3,2-*a*]indole derivatives." In: *Arkivoc (Archive for Organic Chemistry)* 2014.5 (2014), pp. 271–290. DOI: 10.3998/ark.5550190.p008.727.

[A12] Vladislava Voiciuk, Kipras Redeckas, Nadezhda A. Derevyanko, Andrii V. Kulinich, Martynas Barkauskas, Mikas Vengris, Valdas Sirutkaitis, and Alexander A. Ishchenko. "Study of photophysical properties of a series of polymethine dyes by femtosecond laser photolysis." In: *Dyes and Pigments* 109 (2014), pp. 120–126. DOI: 10.1016/j.dyepig.2014.05.012.

[A13] Miglė Dagilienė, Vytas Martynaitis, Mikas Vengris, Kipras Redeckas, Vladislava Voiciuk, Wolfgang Holzer, and Algirdas Šačkus. "Synthesis of 1′,3,3′,4-tetrahydrospiro[chromene-2,2′-indoles] as a new class of ultrafast light-driven molecular switch." In: *Tetrahedron* 69.44 (2013), pp. 9309–9315. DOI: 10.1016/j.tet.2013.08.020.

The author has presented the results of the thesis at the following scientific conferences:

[C1] Kipras Redeckas and Mikas Vengris. *Investigation of the S_1/ICT Equilibrium in Fucoxanthin by Ultrafast Pump-Dump-Probe and Femtosecond Stimulated Raman Scattering Spectroscopy*. Nordic Femtochemistry XII. Landskrona, Sweden, May 25, 2016.

[C2] Kipras Redeckas, Vladislava Voiciuk, and Mikas Vengris. *Femtosekundinė priverstinės Ramano sklaidos sistema: teorija, aparatūra ir taikymai*. Lietuvos Nacionalinė Fizikos Konferencija 41. Vilnius, Lithuania, June 17, 2015.

[C3] Kipras Redeckas, Vladislava Voiciuk, and Mikas Vengris. *Femtosecond Stimulated Raman Scattering: Theory, Apparatus and Applications*. Northern Optics & Photonics 2015. Lappeenranta, Finland, June 2, 2015.

[C4] Kipras Redeckas, Vladislava Voiciuk, and Mikas Vengris. *Femtosecond Stimulated Raman Scattering: Theory, Apparatus and Applications*. LTΦ. Vilnius, Lithuania, Jan. 3, 2015.

[C5] Kipras Redeckas, Vladislava Voiciuk, Rasa Steponavičiūtė, Vytas Martynaitis, Algirdas Šačkus, and Mikas Vengris. *Optically Controlled Bidirectional Switching of an Indolobenzoxazine Type Photochromic Compound*. Nordic Femtochemistry XI. Vilnius, Lithuania, May 5, 2014.

[C6] Kipras Redeckas, Mikas Vengris, Greta Ragaitė, Vytas Martynaitis, and Algirdas Šačkus. *Fotoizomerizacijos dinamika ir jos optinis valdymas spiropirano tipo fotochrominiame junginyje*. Lietuvos Nacionalinė Fizikos Konferencija 40. Vilnius, Lithuania, June 10, 2013.

AUTHOR'S CONTRIBUTION

The author has set up the measurement schemes used throughout the course of this thesis (pubs. [A1–A7]) and carried out all the steady-state and ultrafast time-resolved spectroscopic experiments from pubs. [A1–A3, A5, A6], along with a portion of the nanosecond-resolution experiments from pubs. [A4, A7]. The author has performed the analysis of the acquired femtosecond-resolution data, as well as other numeric simulations presented in the thesis at hand. The author has also devised and assembled the FSRS experimental front-end and written the software back-end for the spectroscopic data post-processing and handling. The author has prepared the manuscripts for pubs. [A1–A3, A5, A6] an was heavily involved in data analysis and manuscript revision for pubs. [A4, A7].

CO-AUTHORS' CONTRIBUTION

- PROF. MIKAS VENGRIS[1] formulated the scientific tasks, helped to interpret the experimental results, proof-read the submitted manuscripts, and provided invaluable advices and insight concerning experimental laser physics, measurement automation, electronics, numeric methods, photosynthesis, and overall photophysics. In one way or another, Mikas was involved in all the studies outlined in the presented thesis.

- DR. VLADISLAVA VOICIUK[1] performed the majority of the nanosecond-resolution FP experiments from pubs. [A4, A7], provided helpful assistance in the laboratory (especially concerning the *–chemical* part of the photochemical experiments), helped to interpret the acquired data and publish the results.

1 Vilnius University, Faculty of Physics, Department of Quantum Electronics

- Dr. Rasa Steponavičiūtė,[2,3] prof. Vytas Martynaitis,[2] and prof. Algirdas Šačkus[2,3] synthesized the IB compounds and provided samples for spectroscopic analysis described in pubs. [A1, A4–A7].
- Dr. Stepas Toliautas[4] and prof. Juozas Šulskus[4] performed the quantum chemistry calculations for pub. [A1] that helped to designate the characteristic Raman frequencies of IBs.
- Prof. Gediminas Niaura[5] and prof. Valdas Šablinskas[6] supervised and helped to perform the steady-state spontaneous Raman scattering measurements on crystalline IB samples, described in pub. [A1].

2 Kaunas University of Technology, Faculty of Chemical Technology, Department of Organic Chemistry
3 Kaunas University of Technology, Faculty of Chemical Technology, Synthetic Chemistry Institute
4 Vilnius University, Faculty of Physics, Department of Theoretical Physics
5 Center for Physical Sciences and Technology, Department of Organic Chemistry
6 Vilnius University, Faculty of Physics, Department of General Physics and Spectroscopy

Part II

TOOLS OF THE TRADE

The following chapter gives a brief outlook on key concepts of time-resolved transient absorption spectroscopy. The reader is introduced to both basic two-pulse and the more advanced multipulse spectroscopic methods, the physical principles of their operation, the constitution and temporal behavior of the observable transient signals, spectroscopic data acquisition and handling techniques, etc. A great portion of the chapter is dedicated to "dissection" of the femtosecond stimulated Raman scattering spectroscopic setup, as its conception and development were some of the main objectives of this thesis.

2

SPECTROSCOPIC AND DATA ANALYSIS METHODS

2.1 TRANSIENT ABSORPTION SPECTROSCOPY IN A NUTSHELL

Transient absorption (TA) or pump-probe (PP) spectroscopy is one of the most widespread spectroscopic techniques to investigate the dynamic behavior of various biological and artificial photo-active systems [15]. In a typical PP measurement a sample is subjected to a pair of ultrashort laser pulses. An intense femtosecond pulse—the "pump"—initiates the light-driven reaction by inducing an electronic transition to an excited molecular (typically singlet) state. If the duration of the excitation pulse is short enough, the molecular systems experiences an instantaneous "departure" from its ground state thermodynamic equilibrium and is left to freely evolve in time. If the interaction with the pump pulse is not destructive, the perturbed molecular system eventually dissipates the excess excitation-gained energy via radiative and non-radiative decay or uses it to initiate an inter- or intra-molecular reaction. All of the intermediary steps that the photoexcited system undergoes throughout its photoevolution and all the electronic/vibrational transitions that accompany them leave a specific spectral "footprint" in the molecular absorption spectrum. Therefore, an auxiliary temporally variable pulse—the "probe"—can be used to monitor the spectral changes that occur within the evolving system. The probe pulse is nearly always chosen to be significantly less intense than the pump pulse, as its purpose is to inspect the on-going photoreaction without any undesirable interference. Considering the fixed time-bandwidth product of an ultrashort pulse, a femtosecond probe pulse provides both a good temporal resolution—as most electronic processes take place in the femto-to-nanosecond timescale—and a broad bandwidth, that is typically desired in order to collect as much spectral information about the evolving system as possible. When it comes to electronic PP spectroscopy, white light supercontinuum (WLSc) generated in bulk media is the most common choice for the probing radiation. Broadband femtosecond non-collinear optical parametric amplifiers (NOPAs) are typically employed only when a very high temporal resolution

is necessary [15, 20]. Since PP is a two-pulse experiment, there is no physical difference which of the two pulses is "stationary" and which is progressed in time. Proper relative timing of the pulses becomes only significant in multi-pulse experiments (see Section 2.2). From an experimental point of view it is practical to consider the pump beam to be fixed at $t = 0$ and the probe beam to be traversing from $t = -\infty$ (prior to the interaction with the sample) to $t = +\infty$ (after the interaction), as depicted in Figure 2.1(c).

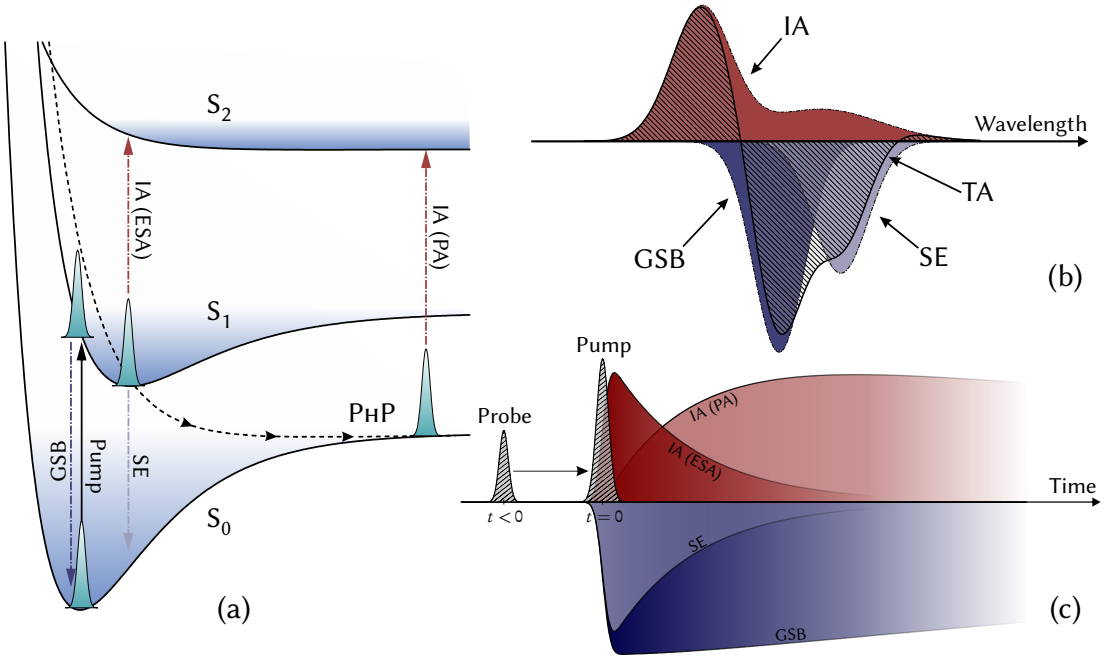

FIGURE 2.1: An illustration of PP dynamics of a model molecular system. The pump pulse promotes the system to the S_1 singlet excited state from which the molecule may decay to the ground state S_0 or undergo formation of a photoproduct (herein labeled PHP). Panel (a) depicts a simplified PES diagram of the photoreaction. Panel (b) illustrates the isolated constituents of the TA spectrum and their gross product (dashed). Panel (c) portrays the pulse sequence of a typical PP experiment and an idealized temporal behavior of GSB, SE, and IA (both the S_1 ESA and the PA) signals.

As the name implies, TA experiment must estimate the time-dependent light-induced absorption changes that occur in the investigated system. According to the Bouguer–Beer–Lambert law, the time-integrated (as we are employing "slow" detection techniques) spectral intensity of the probe pulse, passing through an absorptive sample, can be expressed as:

$$I_0(\lambda) = I(\lambda)10^{-\varepsilon(\lambda)cl} = I(\lambda)10^{-A_0(\lambda)}, \tag{2.1}$$

where $I(\lambda)$ is the initial spectral intensity of the probe pulse, $\varepsilon(\lambda)$ is the molar attenuation coefficient, c is the molar concentration of the absorbing species, l is the optical path length of medium, and $A_0(\lambda)$ is the total (steady-state) spectral absorbance of the sample. The latter term changes in the photoexcited system (and is likewise dependent on time), hence the intensity of the probe pulse at the temporal instance $t = t_i$ after the excitation can be expressed as:

$$I_1(t_i, \lambda) = I(\lambda) 10^{-A_1(t_i, \lambda)}. \tag{2.2}$$

If we iteratively measure and collect these two signals over a span of temporal delays $t = t_1, t_2, \ldots, t_n$ between the two pulses,[1] we obtain the full time-resolved TA spectrum that can be calculated (in dimensionless optical density (OD) units) as:

$$\Delta A(t, \lambda) = A_1(t, \lambda) - A_0(t, \lambda) = \log_{10} \frac{I_0(t, \lambda)}{I_1(t, \lambda)}. \tag{2.3}$$

Three types of spectral contributions are typically observed in a TA signal:

- Ground state bleaching (GSB). The pump pulse promotes a fraction of the sample molecules to a higher excited state, thus partially depleting the thermally equilibrated ground state population. The decrease of the primary absorbing species causes a partial decrease of the sample absorption within the light-matter interaction volume. This temporally-induced transparency—i.e., "bleaching"—surfaces as a negative transient signal (i.e., $I_1^{\mathrm{GSB}} > I_0$) that spans the frequency range of the original ground state absorption spectrum (see Figure 2.1(b)). The bleaching signal eventually diminishes as the system returns to the ground state equilibrium. As exhibited in Figure 2.1(c), the GSB contribution (ideally) lingers until the system is fully restored back to S_0.

- Stimulated emission (SE). If the spectral bandwidth of the femtosecond probe is broad enough to cover the band gap between the ground and the higher energy excited singlet states, then the electromagnetic field of the probe pulse may trigger a radiative decay—i.e., stimulated emission—to the S_0 vibrational continuum. The red-shifted photons generated in this process coherently add up to the probe field, thus increasing its net intensity (i.e., $I_1^{\mathrm{SE}} > I_0$). Therefore, SE is registered as "negative absorption" in the TA spectrum and its spectral outline principally

1 While I_0 is technically independent on inter-pulse delay time, the said term is nonetheless evaluated at each temporal instance t_i in a standard PP realization to compensate for the slow intensity drifts of the probe.

mimics that of the sample fluorescence (in actuality, it is modified by the spectrally-dependent $B_{m\to n} \propto \omega^3$ Einstein coefficient for SE [23]).

- Induced absorption (IA) is a positive contribution to the overall TA signal that signifies a temporary increase of electronic absorption at a particular spectral region (i.e., $I_1^{\mathrm{IA}} < I_0$). If the development of the molecular wavepacket is limited to a singlet or triplet PES, then the observed IA signal corresponds to the dipole-allowed transitions to the higher electronic states, i.e., $\mathrm{S}_n \to \mathrm{S}_{m>n}$ or $\mathrm{T}_n \to \mathrm{T}_{m>n}$. This type of signal is sometimes distinguished as excited state absorption (ESA). If the system evolves beyond the excited state PES—e.g., the molecule undergoes isomerization or ionization, or an energy and/or charge transfer occurs in the excited state, etc.—then the ESA signal, as demonstrated in Figure 2.1(c), gradually transforms into the absorptive contribution of the transient product—i.e., photoproduct absorption (PA).

TA spectrum is much more elaborate than, e.g., a fluorescence decay spectrum, since it provides information not only about the excited states of the system, but also about all the intermediate evolutionary transients and non-emissive states both on the ground and the excited state PES's. Nevertheless, a proper "dissection" of a PP signal is not trivial as it may seem. The exemplary kinetic signals in Figure 2.1(c) are somewhat exaggerated. In many actual molecular systems the GSB, SE, and IA signals can partially or fully overlap both temporally and spectrally (the latter case is emphasized in Figure 2.1(b)), thus, to some extent, complicating the interpretation of TA dynamics.

2.2 MULTI-PULSE SPECTROSCOPIC METHODS

2.2.1 *Incoherent Ultrafast Three-Pulse Spectroscopy*

When talking about multi-pulse spectroscopic methods, nonlinear spectroscopic techniques, such as three-pulse photon echo or coherent two-dimensional spectroscopy [24–26]. The multi-pulse techniques discussed in this section can be considered as "incoherent" from the density matrix formalism point of view [25], since they predominantly deal with the populations (and not the coherences) of the excited system. While technically these techniques are based on the $\chi^{(5)}$ optical nonlinearity [26], they generally do not require an elaborate theoretical description [24, 25] and can be viewed as an "extension" of a typical PP experiment. In an incoherent three-pulse experiment, in contrast to a standard PP realization, an additional pulse is used to disrupt

the on-going evolution of the photoexcited system. The auxiliary pulse, depending on its functionality, spectral characteristics, and relative timing, can be designated as a:

- Dump pulse: when the pulse is resonant to a SE transition, and is thereby able to deliberately depopulate the excited state species and revert the system back to the ground state PES;
- Repump pulse: when the carrier frequency corresponds to an IA resonance, and the pulse is thus able to elevate the system to a higher excited state (that may or may not be detectable in the standard photoevolution) or return it to an earlier evolutionary transient;
- Prepump pulse: when the pulse is resonant to an electronic ground-to-excited state transition, i.e., $S_0 \rightarrow S_n$, thus making it possible to "replenish" the excited state population.

If the optical path of pump beam is temporally fixed, two possible experiments can be carried out in a three-pulse configuration (see Figure 2.2). In a pump-dump-probe kinetic trace (PDP) or a pump-repump-probe kinetic trace (PRPP) experiment[2] the pump and the auxiliary pulses are temporally held at a fixed delay between them, so that from the perspective of a $t \rightarrow +\infty$ traversing probe pulse $t_{\mathrm{PU}} = 0$ and $t_{\mathrm{DU/RP}} > 0$ (see Figure 2.2(a)). This type of experiment provides the information on how a perturbation disturbs the standard photodynamic behavior of the investigated system. In a pump-dump-probe action trace (PDAT) or a pump-repump-probe action trace (PRPAT) experiment, on the other hand, temporal delay between the pump and probe pulses is held fixed ($t_{\mathrm{PU}} = 0$ and $t_{\mathrm{PR}} > 0$), and the auxiliary pulse is propagated from $t < 0$ towards $t = t_{\mathrm{PR}} > 0$ (see Figure 2.2(b)). In other words, this experiment allows us to monitor how the exact timing of perturbation influences the TA spectrum at a fixed evolutionary phase.

If the pulse sequence is properly timed, synchronized, and shuttered, four types of raw spectral data are collected in course of a three-pulse experiment. This data can be categorized as:

- Probe-only data $I_{00}(t, \lambda)$: when both pump and the auxiliary beams are blocked;
- Pumped data $I_{10}(t, \lambda)$: when the pump beam is unblocked and the dump/repump beam is blocked;

2 Prepump-pump-probe (PPPP) experiments were not performed in the course of this work, therefore they will not be discussed in greater detail, albeit the same naming/pulse-timing formalism would also apply [27].

- Dumped/repumped data $I_{01}(t,\lambda)$: when the pump beam is blocked and the dump/repump beam is unblocked;
- Pumped-dumped/pumped-repumped data $I_{11}(t,\lambda)$: when both pump and repump beams are unblocked.

The first two terms coincide with, correspondingly, I_0 and I_1 from Equations (2.1) to (2.3) and provide the conventional PP data. The PDP/PRPP term I_{11} provides information about the deviation from the typical PP dynamics ($\Delta A_{\mathrm{P}n\mathrm{P}} = \log_{10}(I_{00}/I_{11})$). The I_{01} term provides the complimentary dump-probe (DP)/repump-probe (RPP) data $\Delta A_{n\mathrm{P}} = \log_{10}(I_{00}/I_{10})$, i.e., a PP-like data where the dump/repump pulse takes the "role" of the pump. If the dump/repump pulse does not create neither single-, nor multi-photon electronic excitation, then the DP/RPP data contains no significant spectro-temporal information, apart from cross-phase modulation produced coherent artifacts at $t = t_{\mathrm{Du/RP}}$ [28–30], hence these spectra can be subtracted from the final PDP/PRPP signals ($A'_{\mathrm{P}n\mathrm{P}} = A_{\mathrm{P}n\mathrm{P}} - A_{n\mathrm{P}}$). Additional information about three-pulse TA experiments can be found in refs. [31–33].

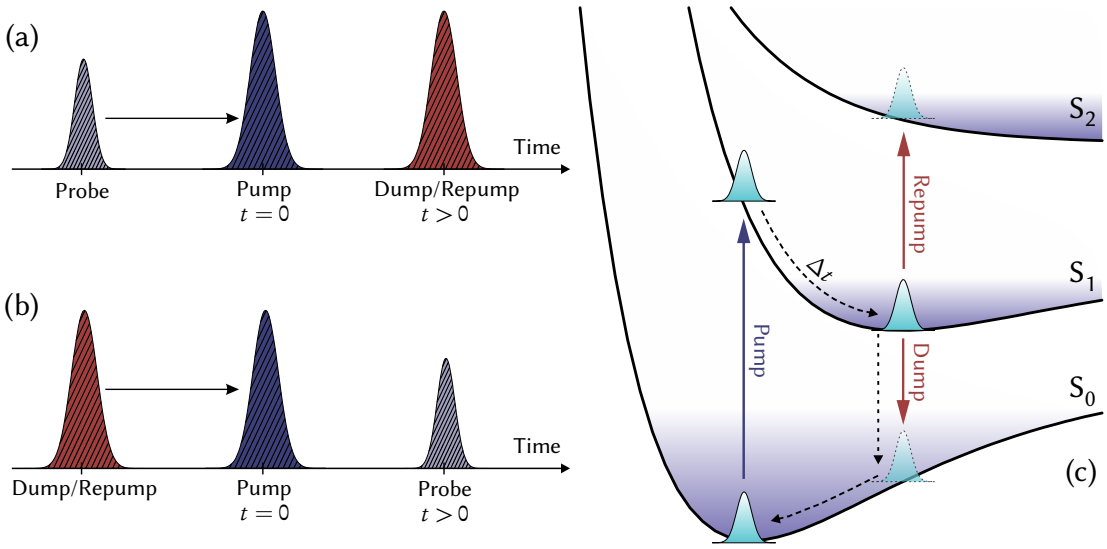

FIGURE 2.2: Pulse timing sequences of three-pulse TA measurements: (a) a kinetic trace-type experiment (simply referred as PDP/PRPP throughout the text) and (b) an action trace-type (PDAT/PRPAT) experiment; all presented in a reference system tied to the pump pulse ($t_{\mathrm{PU}} = 0$). Panel (c) depicts a scenario, where the auxiliary pulse disrupts the standard photoevolution (dashed lines) at $t = t_{\mathrm{Du/RP}} > 0$ by relocating the excited state population to either a higher excited state (PRPP), or by returning it to a thermally unequilibrated site on the S_0 PES (PDP).

2.2.2 *Femtosecond Stimulated Raman Scattering*

Time-resolved vibrational spectroscopy is a powerful experimental tool for identifying and characterizing the molecular motions taking place as a result of electronic excitation. High-resolution spectral information on the vibrational coordinates of the photoreaction can give additional insight on the photodynamics, which is normally "lost" on conventional (electronic) UV–NIR TA experiments. Contemporary commercial or home-built femtosecond laser systems, equipped with broadband tunable UV-to-LWIR parametric devices, facilitate the technical design aspects of high spectro-temporal resolution UV/VIS pump–MIDIR/LWIR probe spectroscopic experiments. While these techniques have been the staple of one-dimensional vibrational PP spectroscopy for a long time [34, 35], they often suffer from such drawbacks as limited bandwidth of the probing radiation, low parametric conversion efficiency and stability of the long-wavelength ($\geq 10\,\mu m$) radiation, and high cost and low resolution of the typically employed mercury cadmium telluride (MCT) sensors and IR-designated optics. To circumvent the latter problem, MIDIR-to-NIR frequency upconversion techniques have been recently suggested as an alternative [36, 37]. However, other experimental inconveniences, such as the requirement of gas-purged chambers for the IR probe, the necessity of high sample concentrations (due to low extinction coefficients of vibrational transitions), and the difficulty of measuring samples in solutions (especially aqueous), hinder the time-resolved IR measurements.

Femtosecond stimulated Raman scattering (FSRS) spectroscopy [38–42] is a relatively recent, yet moderately widespread time-resolved spectroscopic method. Since its inception in the early 2000's [39, 40, 43], FSRS techniques have been utilized to investigate various photobiological pigments [44–48], compounds that undergo photo-isomerization [49–51], metalorganic molecules [52, 53], donor-acceptor systems [54–57], etc. During its development numerous spin-off FSRS techniques, such as impulsive FSRS [58], femtosecond Raman-induced Kerr effect spectroscopy (FRIKES) [59], surface-enhanced FSRS [60], two-dimensional FSRS in the impulsive limit [61, 62], chirped-pulse FSRS [63], and even such outlandish approaches as FSRS with quantum-entangled light [64] or FSRS in the X-ray regime [65], have been both theoretically suggested and experimentally implemented. At its core, FSRS, as depicted in Figure 2.3, is a multi-pulse technique that can be summarized as follows. An ultrashort actinic pulse acts on a molecular system in its ground state $|g,0\rangle\langle g,0|$ (the first symbol denotes electronic, and the second—vibrational quantum number) and initiates the photoreaction by preparing a wavepacket in the excited state $|e,n\rangle\langle e,n|$. A pair of temporally delayed pulses probes the suc-

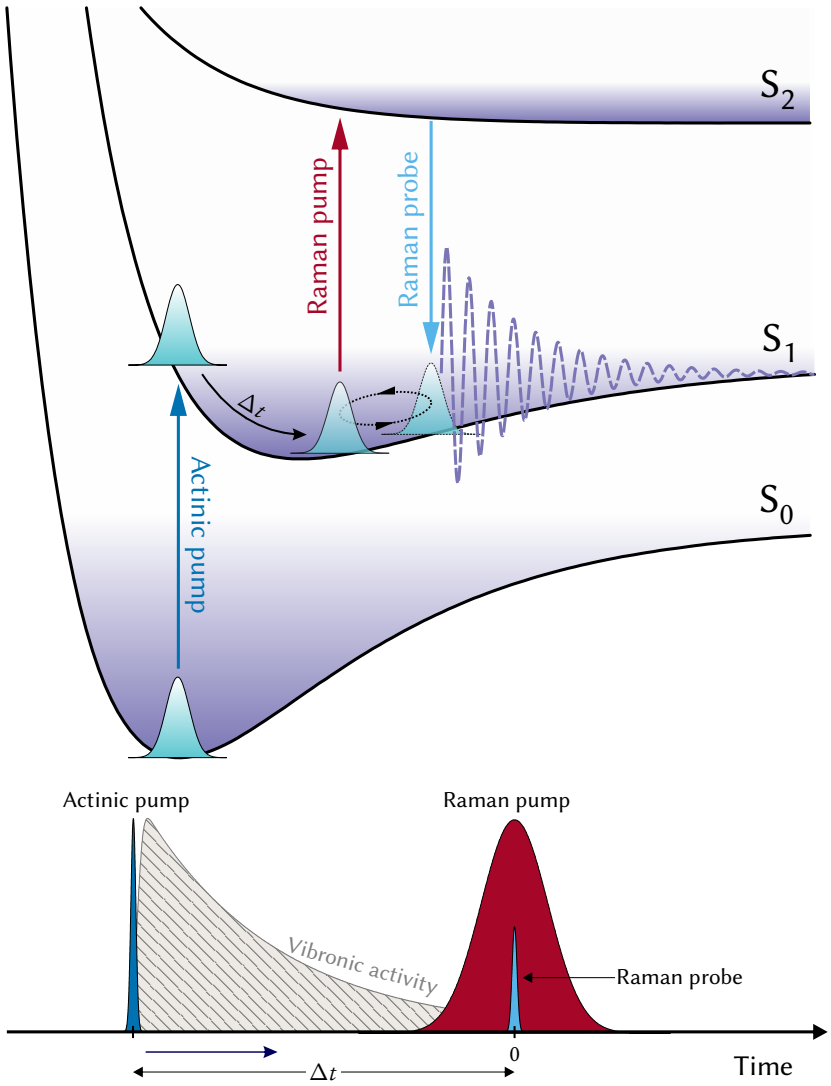

FIGURE 2.3: A simplified scheme of the FSRS process within a hypothetical three-level vibronic system. A femtosecond actinic pulse excites a molecular system, while a pair of synchronized narrowband Raman pump (resonant to the $S_1 \rightarrow S_2$ transition) and broadband Raman probe pulses produce a vibrational coherence in the evolving excited state, resulting in the emission of Stokes (and anti-Stokes) photons on top of the probe field [38]. Note that the experiment is performed in a "reversed" time frame, i.e., the Raman pump and Raman probe pulses are stationary at $t = 0$, while the actinic pump pulse is propagated from $t = -\infty$ to $t \gtrsim 0$.

cessive photoevolution. An intense narrowband (picosecond) pulse triggers Raman scattering within the evolving system. The scattering process is predominantly incoherent prior to the arrival of a broadband (ultrashort) probe pulse. A temporal overlap of these two pulses brings about a coherence in the

excited (or the eventual photoproduct) state $|e,n\rangle\langle e,m\neq n|$, resulting in the amplification of the Stokes and anti-Stokes frequencies within the probe field (i.e., stimulated Raman emission). Since a high degree of coherence is achieved only during the short temporal overlap of the Raman pump and probe pulses, FSRS spectroscopy offers both good spectral ($\Delta\nu \leq 5\,\mathrm{cm}^{-1}$, limited by the bandwidth of the Raman pump pulse and capabilities of the imaging optics) and temporal ($\Delta\tau \leq 50\,\mathrm{fs}$, limited by the duration of the actinic and probe pulses) resolution, without violating the Heisenberg uncertainty principle[3] [38, 66, 67]. Furthermore, many of the drawbacks of conventional MIDIR/LWIR TA spectroscopy mentioned above are circumvented in FSRS, because the vibrational experiment is reallocated to the VIS–NIR domain, where both the lasers and the detectors perform significantly better.

2.3 A UNIVERSAL PP/PDP/FSRS SETUP

As it was established in the sections above, PDP, PRPP, and FSRS are all three-pulse experiments that can technically be performed on a single spectroscopic setup. A versatile PDP/PRPP/FSRS configuration requires the capability to fine-tune the wavelength and temporal arrangement of the interacting pulses. In the FSRS case, it also becomes crucial to properly regulate the spectral narrowness of the Raman pump pulses (i.e., the spectral resolution of the measurement). For this task we have resorted to a number of nonlinear and Fourier optics techniques that are, along with various alternative approaches, discussed in greater detail in Section 2.3.3.

The principal measurement system on which the core three-pulse setup is based on was presented earlier in ref. [68]. In this chapter we will focus mainly on the FSRS side of the optical setup since the above-described experimental realizations are essentially interchangeable, yet the FSRS component requires a somewhat more intricate experimental "tweaking", and the FSRS results require much more post-processing, in contrast to the typical PP/PDP/PRPP data. Essentially, the FSRS setup can be "reduced down" to a PDP/PRPP configuration by discarding some of its optical branches and by readjusting the timing of the pulse sequence. In this section we showcase the technical design aspects and working principles of the FSRS branch of the three-pulse spectroscopic system. Additionally, in Section 3.2 we will demonstrate a practical application of the presented setup by measuring the time resolved FSRS spec-

3 Another way of looking at it is that the two pulses are mutually independent do not constitute a Fourier transform pair [66].

tra of β-carotene by exploiting either the $S_2 \rightarrow S_n$ or the $S_1 \rightarrow S_n$ electronic resonances, and discuss the possible future prospects of the system.

2.3.1 *Actinic Pump Generation*

A simplified diagram of the experimental setup is presented in Figure 2.4. The FSRS system is based on a commercial titanium-sapphire (Ti:Sa) Kerr lens mode-locked oscillator/chirped pulse regenerative amplifier system Libra (Coherent) that provides a 1 kHz train of 3.5 mJ, 50 fs, $\lambda_0 = 800$ nm, $\Delta\lambda_{\mathrm{FWHM}} = 25$ nm pulses.[4] Roughly 1/5 of the laser output (ca. 750 µJ) is used to pump a travelling-wave optical parametric amplifier (OPA) Topas-800 (Light Conversion), achieving a ca. 30 % conversion efficiency at 1300 nm (signal) and 2080 nm (idler) with $\leq 1\,\%$ σ/μ (i.e., standard deviation divided by the mean) pulse-to-pulse energy stability (due to gain narrowing and the inner dispersion of the OPA, the actinic pulse is prolonged up to ca. 70 fs, albeit the residual chirp is left uncompensated in the FSRS experiments). Frequency doubled, quadrupled or upconverted output of this OPA (typically in the UV or violet-to-green portion of the VIS spectrum) is used as the actinic pump radiation in the FSRS experiments.[5] An optical chopper (Stanford Research Systems SR540) controlled by a home-built phase-locking circuit periodically blocks the actinic pump beam and a synchronized photodiode monitors its blocked/opened state and the shot-to-shot energy stability (pulses with the pump energies more than 3σ away from the mean value, are omitted from the measurement). Temporal delay of the actinic pulse is realized by a 30 cm travel single-pass optical delay line (Aerotech ALS10030), achieving ca. 2 ns of probe time window.

2.3.2 *Raman Probe Generation*

WLSc, generated by tightly focusing a small fraction (ca. 1 %) of the fundamental Libra output into a 3 mm thick sapphire ($\Delta\lambda_{\mathrm{WLSc}} = 450$–$1100$ nm) or calcium fluoride ($\Delta\lambda_{\mathrm{WLSc}} = 300$–$1100$ nm) crystal, is used as the broadband Raman probe. The WLSc is spectrally filtered from the excessive 800 nm radiation using either a custom made dielectric notch filter ($\lambda_0 = 815$ nm, $\Delta\lambda_{\mathrm{band}} = 200$ nm, $T_{>85\,\%} = 300$–730 nm) or a long-pass colored glass filter

4 The particular Libra system contains a dual stretcher/compressor configuration that allows generation of either 50 or 100 fs (nearly) bandwidth-limited pulses. The subsidiary 100 fs configuration was employed in some of the experiments outlined in this thesis.

5 An identical 3rd OPA (not depicted in Figure 2.4) is used to generate the dump/repump radiation in PDP/PrPP experiments.

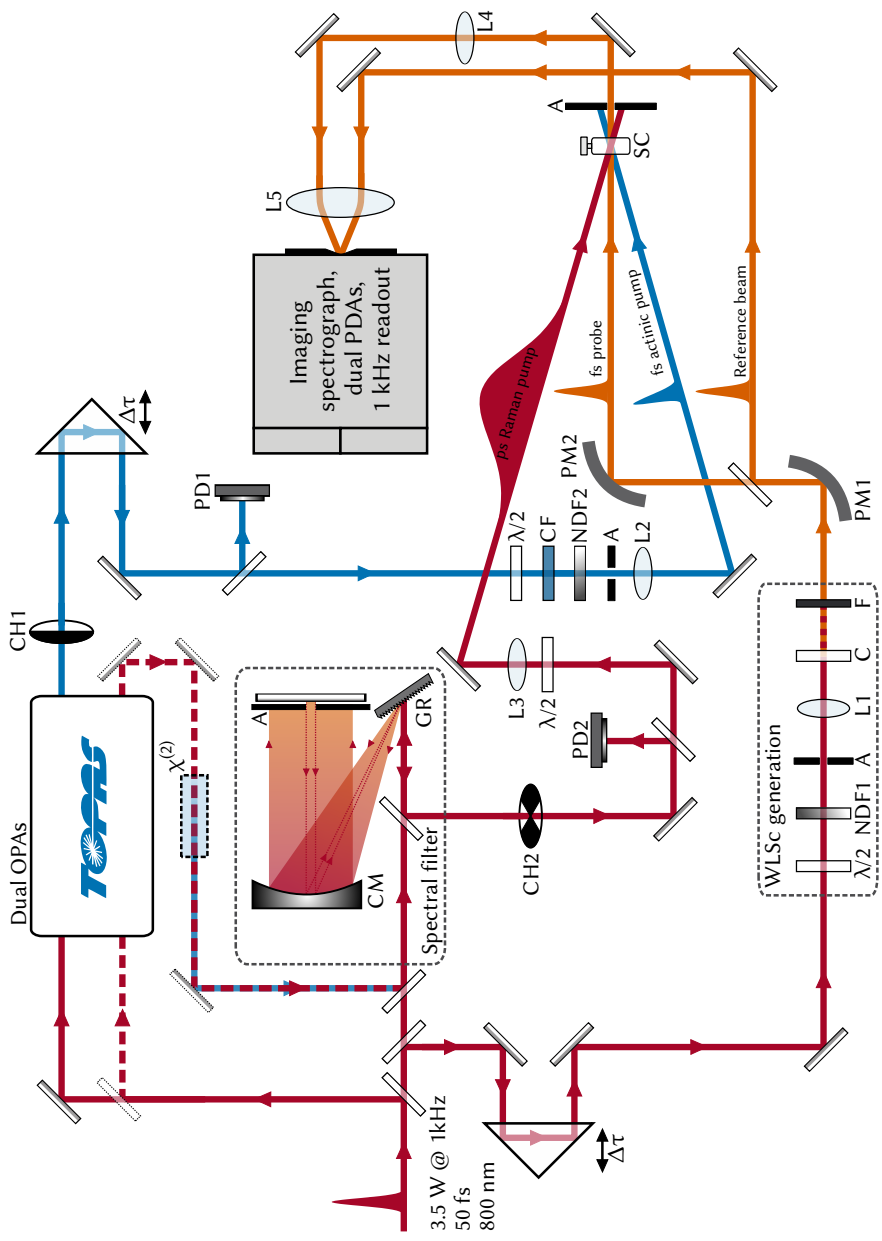

FIGURE 2.4: Simplified layout of the FSRS apparatus. Abbreviations: A: aperture, C: WLSc generation crystal (Al_2O_3 or CaF_2), CF: color filter, CM: concave mirror, CH*n*: optical choppers, F: WLSc pump blocking (notch or colored glass) filter, GR: diffraction grating, L*n*: lenses, NDF*n*: neutral OD filters, PD*n*: photodiodes, PM*n*: parabolic off-axis mirrors, SC: sample compartment, $\lambda/2$: half-wave plates, $\chi^{(2)}$: nonlinear 2nd harmonic generation crystal (KDP).

(SHOTT GLASS RG830, $T_{>85\,\%} = 830$–2700 nm). Since the Raman pump optical branch is fixed (see Figure 2.4), proper temporal arrangement of Raman pump and Raman probe pulses (see Figure 2.3) is achieved by precisely delaying the probe pulse using a double-pass 60 cm delay line AEROTECH ALS10060 to realize the highest Raman gain signal (illustrated in greater detail in Section 2.3.3). The positive chirp of WLSC (ca. 600 fs between 450 and 1000 nm, albeit significantly lower in the actual $\Delta\lambda \approx 50$ nm probe window) is left uncompressed in order to avoid any energy losses of the weak (ca. 20 nJ) probe pulses and the chirp correction is implemented purely numerically (refer to Section 2.4). These two shortcomings can be generally overcome, if a broadband tunable NOPA is used as the Raman probe instead of WLSC [69, 70].

After passing the sample (1 mm HELLMA quartz cuvette) the probe beam is re-collimated and focused into the 100 µm-wide entrance slit of an imaging spectrograph (ORIEL MS127I, focal length 127 mm) and read-out with a 256 pixel photodiode array (PDA) (HAMAMATSU S8380-256Q, pixel size 50 µm). Depending on the necessity to achieve either enhanced spectral resolution (up to 3.5 cm^{-1}) or a broader Stokes shift region (up to 2000 cm^{-1}) a 1200 mm^{-1} or a 600 mm^{-1} diffraction grating (THORLABS GR50-1205, GR25-1210, or GR25-610) is, appropriately, used to disperse the Raman probe spectrum. The pixel-to-wavenumber calibration is typically performed by measuring the ground state (i.e., "unpumped") stimulated Raman scattering (SRS) spectrum of a vibrationally "rich" solvent (e.g., toluene or *n*-hexane) and by least square fitting the spectrally-resolved signals to best match the independently acquired, properly calibrated Raman data.

The achievable pulse-to-pulse probe energy stability is typically acceptable for any standard FSRS experiments in the VIS-to-NIR region (ca. $\leq 0.7\,\%\ \sigma/\mu$ throughout the entire spectral window). The low-energy extent of WLSC in the NIR (i.e., 820–850 nm, which amounts to the lower-wavenumber region of 300–750 cm^{-1} with a 800 nm Raman pump) is, however, notably less stable (ca. $\geq 3\,\%\ \sigma/\mu$) due to the more prominent self-phase modulation and the steep continuum-to-seed-pulse transition near the WLSC pump central wavelength. Therefore, in the NIR detection measurements the probe, as depicted in Figure 2.4, is divided into sample and reference beams and a synchronized dual PDA detection system is typically employed, allowing to achieve probe stability as high as ca. $0.1\,\%\ \sigma/\mu$. In practice, Stokes shift frequencies, ranging from ca. 100 cm^{-1} up to ca. 3200 cm^{-1}, can be measured using this FSRS setup, although the uncompensated temporal chirp of the WLSC can hinder the amplitude or spectral resolution at the highest and the lowest frequencies due to coherence loss between the Raman pump and probe pulses. The lower wavenumber bound is typically irresolvable due to Rayleigh wing scattering

of the Raman pump pulse, whereas the upper limit is restricted by either the probe light instabilities in the close proximity of the WLSc pump central wavelength (800 ± 20 nm) in the VIS/NIR boundary or the limited spectral sensitivity of silicon-based PDAs in the further NIR (up to ca. 1 µm).

All three interacting beams are polarized parallel to one another to realize the best Raman gain and signal-to-noise ratio of the FSRS signals (as suggested in ref. [71]). *p*-polarization is typically preferred for detection purposes, albeit "magic angle" (54.7°) configuration is also possible. The actinic and Raman pump beams are focused with plano-convex UV-grade fused silica lenses ($f = 200$–300 mm), whereas parabolic collimating/focusing optics are used in the Raman probe branch to avoid any unnecessary pulse stretching/chirping. The Raman pump and probe beams are focused to have the smallest possible beam waist at the sample plane ($\varnothing_{RP} \simeq 80$ µm, $\varnothing_{PR} \simeq 70$ µm at full width at half maximum (FWHM)), whereas the actinic pump beam is normally kept larger ($\varnothing_{AP} \simeq 120$ µm at FWHM). Data acquisition is performed with National Instruments PCI-6120 data acquisition board and the measurement is fully automated in National Instruments LabVIEW. A conventional FSRS experiment, consisting of approximately 150 temporal delay points, is typically performed in under 3 hours. In order to avoid sample over-exposure during the duration of the experiment, the sample cell is translated transversely to the beam propagation direction in a Lissajous pattern, using a set of two perpendicularly assembled translation stages (Standa 8MT173).

2.3.3 *Raman Pump Generation*

Several different approaches can be undertaken in order to obtain the narrowband Raman pump pulses from a femtosecond laser source. The simplest (not to mention the cheapest) way of generating picosecond pulses is spectral filtering of the fundamental Ti:Sa radiation by a Fourier $4f$ filter [40, 72] or a Fabry–Pérot etalon [73, 74]. Alternatively, a portion of the locally-narrowband temporally-chirped output of the regenerative amplifier can be employed, though not without raising some calibration inconveniences [75, 76]. Considering the ca. 400 cm^{-1} bandwidth of the Libra system, spectral filtering can be effectively implemented in the NIR region of ca. 775–825 nm (or, alternatively, at the UV/VIS boundary of ca. 395–405 nm by exploiting 2nd harmonic generation). The obvious drawbacks of this approach are the immense energy losses (e.g., in order to obtain a Raman pump pulse with a bandwidth of 5 cm^{-1}, more than ca. 98 % of the initial pulse energy is lost both due to filtration and the diffraction/reflection losses) and the limited tun-

ability of the picosecond radiation. The highest energy efficiency is, beyond doubt, achieved by utilizing a commercial [56, 77] or a home-built [69, 70, 78] picosecond OPA pumped by the 2nd harmonic bandwidth compressed Ti:Sa radiation. This approach not only minimizes the energy losses, arising from the femto-to-picosecond conversion, but also offers a broad tunability of the Raman pump pulses in the entire VIS and NIR regions, which is usually desired for attaining resonant or pre-resonant conditions with the investigated molecular system. The penalty, however, is greatly increased complexity and the overall cost of the Raman pump system.

Tunability of the Raman pump is typically desired in FSRS experiments, considering that FSRS is a $\chi^{(5)}$ process and a resonant enhancement of the vibrational modes greatly increases the resolvable signal amplitude and raises it well above the electronic background [51, 69, 70]. When designing our picosecond Raman pump source, we have opted for a compromise between the two above discussed approaches, enabled by high pulse energy of the current off-the-shelf Ti:Sa systems. The largest portion (ca. 1.2 mJ) of the fundamental laser radiation is used to pump an additional high-power (HP) travelling-wave OPA Topas-800, achieving ca. 50 % energy conversion efficiency at 1300/2080 nm (signal/idler waves can be typically tuned in the 1150–2500 nm region [79]). The HP-OPA output beams are then passed through a lengthy potassium dihydrogen phosphate (KDP) nonlinear crystal (type I: $\theta = 41°$, $\phi = 45°$, $20 \times 20 \times 65$ mm, or type II: $\theta = 58°$, $\phi = 0°$, $20 \times 20 \times 45$ mm), where they are either frequency-doubled, quadrupled, or sum-frequency mixed with the OPA-pump radiation, thus effectively (up to ca. 45 % at 650 nm) frequency-shifting them into the blue VIS-to-NIR (ca. 400–800 nm) part of the spectrum. Standalone 800 nm Ti:Sa pump or its 2nd harmonic can obviously also be utilized in this configuration, as indicated in Figure 2.4.

The extensive length of the birefringent crystal ensures high nonlinear conversion efficiency and, because of the group velocity mismatch (GVM) between the interacting beams and strict phase-matching conditions for only a certain set of wavevectors ($\Delta kz \gg 0$), the upconverted pulses become temporally stretched and spectrally-narrowed [80]. Due to temporal walk-off between pulses and the constant depletion of the fundamental beam energy along the span of the lengthy nonlinear medium, the frequency-doubled pulses obtain a nearly exponential temporal profile [80, 81]. The said effect can be easily exemplified by simulating the pulse propagation in a nonlinear medium. For all intents and purposes, we can limit ourselves to the 1st order approximation of dispersion theory, i.e., use the slowly varying pulse envelope approximation and a two-term Taylor series expansion of the propagation constant:

$k(\omega) \approx k(\omega_0) + \frac{\omega-\omega_0}{u}$, where $u = \left.\frac{d\omega}{dk}\right|_{\omega_0}$ is the group velocity of the pulse [82, 83]. Assuming there is no phase-mismatch (i.e., $\Delta k = 0$), the nonlinear coupled wave equations for pulsed 2nd harmonic generation can be expressed as:

$$\frac{\partial A_1}{\partial z} = -\nu\frac{\partial A_1}{\partial t} - \sigma A_1^* A_3, \tag{2.4}$$

$$\frac{\partial A_3}{\partial z} = \sigma A_1^2. \tag{2.5}$$

These equations are presented in a retarded time frame of reference, traveling with the 2nd harmonic wave ($t = t' - z/u_3$). A_1 and A_3 are the complex envelopes of, accordingly, 1st and 2nd harmonic pulses, ν is the GVM between them ($\nu = u_1^{-1} - u_3^{-1}$), and σ is the nonlinear coupling coefficient ($\sigma \propto \chi^{(2)} \propto d_{\text{eff}}(\omega, 2\omega)$). The coupled wave equations 2.4 and 2.5 of the nonlinear interaction can be rewritten in a dimensionless form by defining the complex field amplitudes as:

$$A_i(t,z) = a_0 B_i(t,z), \tag{2.6}$$

where $[a_0] = \mathrm{V}\cdot\mathrm{m}^{-1}$, and $B_i(t,z)$ are the dimensionless complex functions that describe the shapes of the pulse envelopes. Note that, since a_0 is identical for both pulses, A_3, according to Equation 2.6, is defined "proportionate" to A_1. We can then introduce new units:

$$T = \frac{t}{\tau_0}, \tag{2.7}$$

$$L_\nu = \frac{\tau_0}{\nu}, \tag{2.8}$$

$$L_N = \frac{1}{a_0\sigma}, \tag{2.9}$$

$$Z = \frac{z}{L_n}, \tag{2.10}$$

where T is the dimensionless time, τ_0 is the duration of the 1st harmonic pulse, L_ν is the GVM length, L_n is the nonlinearity length, and Z is the dimensionless nonlinear pulse propagation length. Using all the above-defined notations, Equations (2.4) and (2.5) can be reduced to:

$$\frac{\partial B_1}{\partial Z} = -\frac{L_N}{L_\nu}\frac{\partial B_1}{\partial T} - B_1^* B_3, \tag{2.11}$$

$$\frac{\partial B_3}{\partial Z} = B_1^2. \tag{2.12}$$

We can solve this set of differential equations using the initial conditions $B_1(T, Z = 0) = f(T)$ and $B_3(T, Z = 0) = 0$. Numerical solution of these equations, obtained under several different L_N/L_v values, are presented in Figure 2.5. We can see that if the coupling between the pulses is strong (or the nonlinearity is weak), the 2nd harmonic generation is very effective, albeit the resulting spectrum of the upconverted radiation remains rather broad (Figure 2.5(a)). As the L_N/L_v ratio grows (Figures 2.5(b) and 2.5(c)), the temporal separation between the two pulses increases and the temporally stretched 2nd harmonic pulse attains a narrow spectral profile.

An experimentally-resolved temporal profile of a 2nd harmonic spectrally-narrowed pulse, generated from a $\lambda_0 = 1250\,\text{nm}$, $\tau_0 \approx 50\,\text{fs}$ signal wave input, is presented in Figure 2.6(a). We can see that the pulse becomes ca. 5× prolonged in time and, as the theoretical calculations imply, it obtains a temporally asymmetrical (roughly exponential) envelope. In Figure 2.6(d) we can see that spectrum of the said pulse is not symmetric around ω_0, contrasting the numerical results of Figure 2.5. This kind of deviation from theory can be expected, since the above-discussed model only accounts for GVM and fundamental wave depletion. In reality, we are dealing with sub-100-femtosecond pulses, thereby higher order approximations of the dispersion theory should be incorporated to Equations (2.4) and (2.5) to acknowledge both group velocity dispersion (GVD) ($\sim \partial^2 A_i/\partial t^2$) and nonlinear amplitude distortion ($\sim \partial^3 A_i/\partial t^3$) effects [82, 83]. Also KDP absorption becomes significant in the NIR [85] which can lead to considerable deformations of the spectral pulse envelope. Nonetheless, even a simple 1st order expansion gives a sufficient estimate of the underlying nonlinear processes. For referential purposes, a numerical simulation of the coupled wave equations, that incorporates higher order dispersive terms, is presented in Figure A.1.

A more "usual" temporal shape (i.e., Gaussian, sech^2, or sinc^2) and a narrower spectrum—since the $30\,\text{cm}^{-1}$ resolution, suggested by Figure 2.6(c), is typically insufficient for most vibrational measurements—can be achieved either via negatively pre-chirping the initial pulse prior its passing through the nonlinear medium [81] or by successive spectral filtering of the 2nd harmonic output [80]. Since the energy losses of both of these methods can be expected to be roughly the same, we have opted for the latter approach because it automatically ensures a virtually bandwidth-limited temporal shape of the Raman pump pulse. Spectral filtering of the 2nd harmonic of the HP-OPA output is performed by a Fourier $4f$ filter, consisting of a $1200\,\text{mm}^{-1}$ grating (blazed at either 500 or 800 nm), a concave $f = 500\,\text{mm}$ silver mirror, and a plane back-reflecting silver mirror located in the Fourier plane (dashed rectangular box in Figure 2.4). An adjustable optical slit (Standa 10AOS10-1), positioned

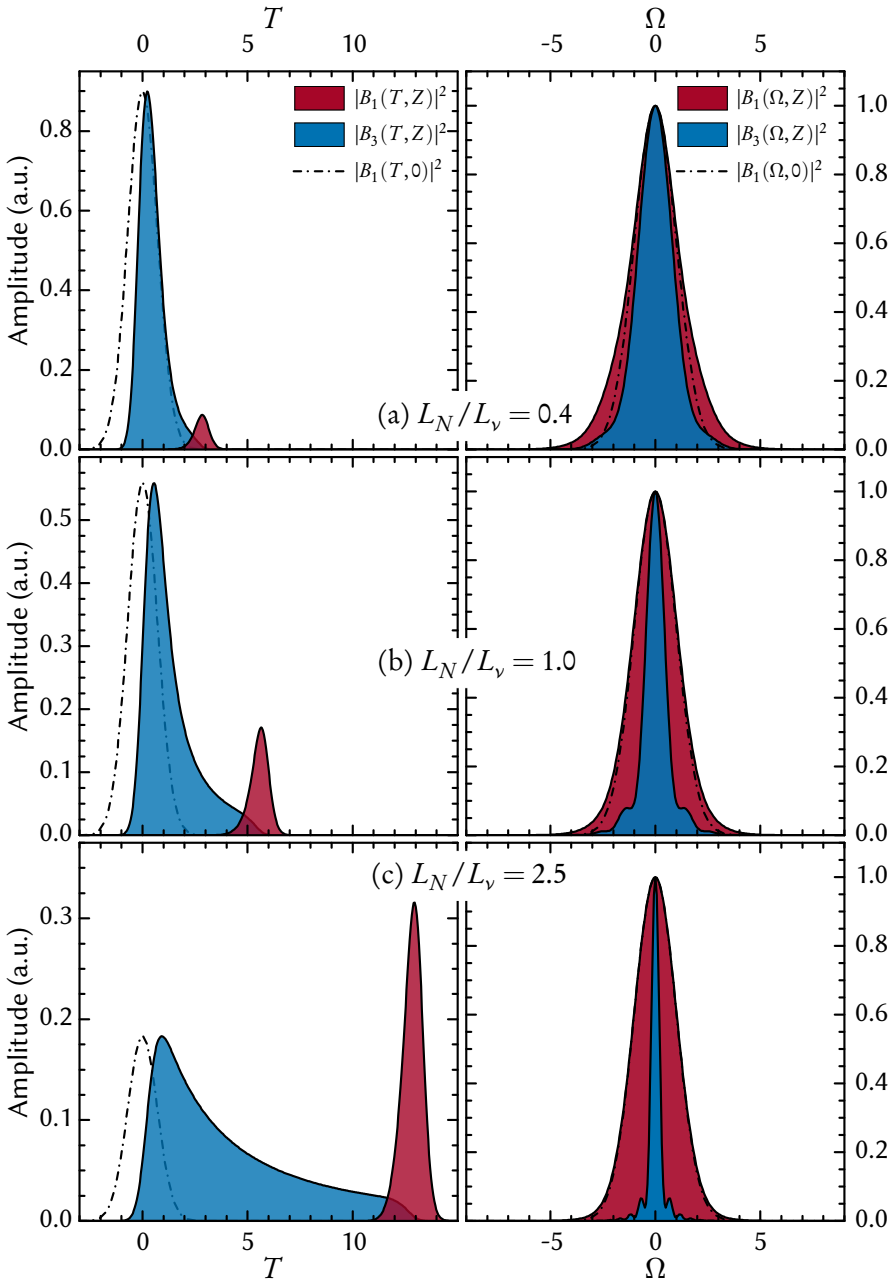

FIGURE 2.5: Numeric simulation of 2nd harmonic generation in lengthy nonlinear medium under GVM (Equations (2.11) and (2.12)). The left-hand side panels illustrate temporal, while the according right-hand side panels illustrate spectral intensities of the 1st (red) and 2nd (blue) harmonic pulses. The simulation was performed under three different L_N/L_ν values. The initial condition for the simulation were $B_1(T, Z = 0) = \exp(-T^2)$ and $B_3(T, Z = 0) = 0$. In all the examples pulses were propagated over a span of $Z = 5$ in $\delta Z = 0.005$ steps, using the split-step Fourier method [84]. Scaled replicas of the 1st harmonic pulse and its spectrum at $Z = 0$ are presented in all panels as a reference (dashed-dotted curves). The spectra are normalized in the right-hand side panels for better viewing.

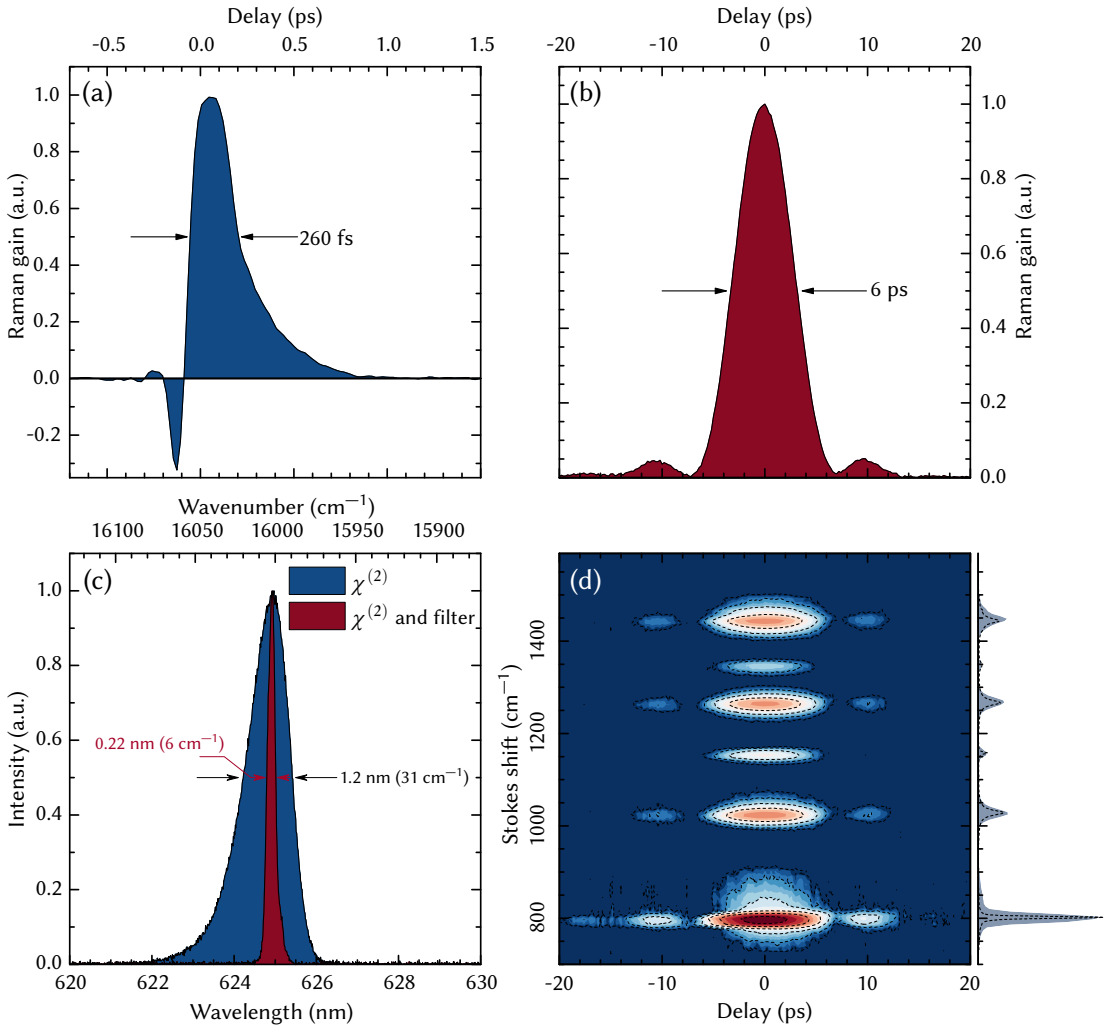

FIGURE 2.6: Temporal Raman gain profiles of the 802 cm^{-1} C–C A_{1g} stretching vibration of cyclohexane, obtained by using 2nd harmonic temporally stretched ($\chi^{(2)}$ in Figure 2.4) $\lambda_{RP} = 625$ nm Raman pump pulses (a) without and (b) with the implementation of spectral filtering (dashed rectangular box in Figure 2.4). Panel (c) depicts spectral profiles of the said pulses. Panel (d) depicts the entire spectro-temporal cross-correlation signal in cyclohexane between the spectrally filtered Raman pump (b) and the ultrashort Raman probe pulses. A time-based integral of the cross-correlation map—depicted alongside a corresponding spectrum measured with a dedicated Raman spectrometer (black dashed curve)—is presented on the right-hand side of panel (d). Since $\tau_{PR} \ll \tau_{RP}$, these intensity cross-correlation relations roughly estimate the envelope of the Raman pump pulses (note the exponential "tail" of the Raman pulses in panel (a) and the sinc^2-like sidebands in panel (b)).

adjacent to the Fourier plane mirror, simultaneously controls the central wavelength, bandwidth, and the energy of the picosecond pulses. Pulses as narrow as 1.5 cm^{-1} (ca. 10 ps) can be easily achieved in this configuration. While ultimately FSRS gain depends on the investigated sample, from our experience, Raman pump energies ranging from 300 nJ up to 5 µJ were typically required to achieve a good signal-to-background ratio in standard FSRS experiments (an exemplary Raman pump pulse is presented in Figure 2.6(b)). An entire spectro-temporal cross-correlation map, as the one presented in Figure 2.6(d), is typically measured before or after the experiment in order to gain both the spectral calibration data and the Raman pump pulse duration.

A better spectral resolution can always be achieved by an increased spectral narrowing of the Raman pump pulses, albeit this leads to the linear reduction of the FSRS signal [40], thus disclosing that a compromise between signal strength and spectral resolution should be sought under the given experimental conditions. Spectrally-limiting 2nd harmonic generation and Fourier filtering processes do not greatly impair the stability of the HP-OPA output, therefore the ultimate pulse-to-pulse stability of the Raman pump radiation can be achieved as high as 2 % σ/μ. It should be also mentioned that, despite the low cost and wide commercial availability of large crystals, KDP is impaired by its limited transparency (0.2–1.6 µm) and low nonlinearity ($d_{\mathrm{eff}} \propto 0.39\,\mathrm{pm\,V^{-1}}$) [85], thus suggesting other feasible candidates for Raman pump generation, such as β-barium borate (BBO) [86]. Optical chopping and pulse stability monitoring of the Raman pump are analogous to the actinic pump branch (see Section 2.3.1), differing only that the optical chopping of the picosecond pulses is performed at a twice lower rate.

2.4 FSRS DATA MANIPULATION AND HANDLING

With a set of two phase-locked optical choppers, operating at 1/2 and 1/4 of the repetition rate of the laser system (or, alternatively, 1/4 and 1/8, if a larger amount of probe light is necessary to be accumulated on the detector), four discrete sets of background-corrected sample ($I(t,\nu) = I_{\mathrm{Raw}}(t,\nu) - I_{\mathrm{Bckg}}(t,\nu)$) and reference ($R(t,\nu) = R_{\mathrm{Raw}}(t,\nu) - R_{\mathrm{Bckg}}(t,\nu)$) data are collected per trigger event. Under these conditions, the entire time- and wavenumber-resolved FSRS gain spectrum (in dimensionless mOD units) can be expressed as:

$$\Phi^{(0)}(t,\nu) = 1000 \cdot \log_{10}\left(\left(\frac{I_{11}(t,\nu)}{R_{11}(t,\nu)} \cdot \frac{I_{00}(t,\nu)}{R_{00}(t,\nu)}\right) \Big/ \left(\frac{I_{01}(t,\nu)}{R_{01}(t,\nu)} \cdot \frac{I_{10}(t,\nu)}{R_{10}(t,\nu)}\right)\right), \tag{2.13}$$

and the ground state FSRS gain as:

$$\Gamma^{(0)}(t,\nu) = 1000 \cdot \log_{10}\left(\left(\frac{I_{01}(t,\nu)}{R_{01}(t,\nu)}\right)\Big/\left(\frac{I_{00}(t,\nu)}{R_{00}(t,\nu)}\right)\right), \tag{2.14}$$

where the subscript indices indicate the open/blocked state of the actinic pump (1st index) and the Raman pump (2nd index) beams. As a whole, the ground state FSRS spectrum does not depend on the actinic pump delay t. This implies that FSRS measurements can be performed without modulating the Raman pump beam [40, 44, 87] (i.e., only registering the temporal changes of the Raman gain spectrum with and without the actinic pump). However, modulating both beams has its merits: it simultaneously provides the conventional PP data:

$$\Pi(t,\nu) = 1000 \cdot \log_{10}\left(\left(\frac{I_{10}(t,\nu)}{R_{10}(t,\nu)}\right)\Big/\left(\frac{I_{00}(t,\nu)}{R_{00}(t,\nu)}\right)\right), \tag{2.15}$$

and allows monitoring fluctuations and the slow drift of the ground state Raman gain during the measurement.

Both of the aforementioned signals $\Phi^{(0)}$ and $\Gamma^{(0)}$ contain a smooth continuous baseline, that appears either from SE, various higher- or lower-order nonlinear ($\chi^{(3)}$, $\chi^{(5)}$, etc.) non-FSRS interactions between the pulses [66], pump-dump depletion (sometimes referred as Raman induced by nonlinear emission (RINE) [48]), or pump-repump-induced absorption effects on the transient species. It is possible to diminish the baseline contribution by using Raman pump wavelength modulation [57, 78, 88, 89], however, most of these methods, nonetheless, require heavy FSRS signal post-processing in order to "flatten-out" the final transient spectrum. Similarly to several previously described approaches [44, 46, 55, 90], we have opted to reconstruct the time-resolved baseline- and solvent Raman line-free FSRS signal by using a data handling algorithm, which is depicted in Figure 2.7 and can be summarized as follows:

1. Temporal chirp of the probe pulse is estimated by the rise of the PP signal $\Pi(t,\nu)$ in the interval $-1\,\text{ps} \leq t_i \leq 1\,\text{ps}$, the dispersion is approximated by a polynomial curve ($N_{\text{Poly}} \geq 4$) and the kinetic signals are appropriately shifted and interpolated along a fixed temporal axis (see Figure 2.7(a)). The half-rise point of the difference absorption (ΔOD) signal is typically designated as the "actual" zero moment, albeit in some cases, e.g., when the appearance of TA is not entirely IRF-limited, a more precise evaluation is required.

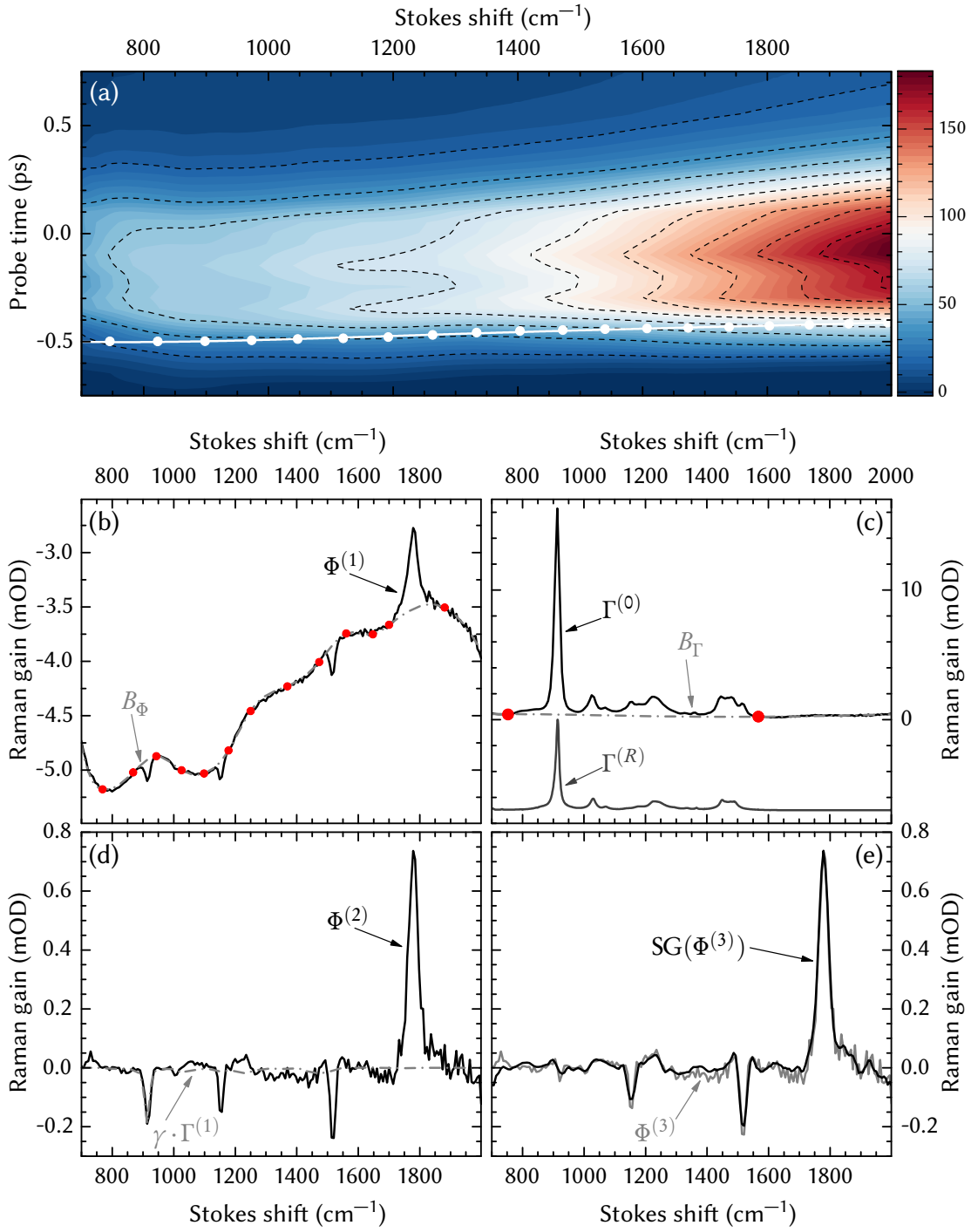

FIGURE 2.7: FSRS signal recovery procedure for β-carotene in THF ($\lambda_{AP} = 490\,nm$, $E_{AP} = 150\,nJ$, $\tau_{AP} = 70\,fs$; $\lambda_{RP} = 790\,nm$, $E_{RP} = 3\,\mu J$, $\tau_{RP} = 6\,ps$; $t_{P_R} = 2.5\,ps$): (a) Raman probe dispersion correction according to the PP signal (Equation 2.15); (b) separation of signal and background components for the "pure" FSRS signal (Equation 2.17); (c) separation of signal and background components for the solvent/ground state FSRS signal (Equation 2.18); (d) removal of the solvent/ground state FSRS contribution (Equation 2.19); (e) noise suppression via Savitzky–Golay filtering. Refer to main text for more details.

2. The pre-actinic pump (i.e., $t \leq -1$ ps) FSRS spectrum is averaged over temporal delay points and subtracted from the FSRS dataset:

$$\Phi^{(1)}(t,\nu) = \Phi^{(0)}(t,\nu) - \sum_{t_i \leq -1} \frac{\Phi^{(0)}(t_i,\nu)}{N_{t_i \leq -1}}. \tag{2.16}$$

This removes (or at least lessens) the solvent Raman line artifacts remaining in the FSRS signal.

3. A set of baseline-defining points (i.e., a constant number $N \geq 10$ of spectral points that exhibit insignificant Raman gain and only outline the baseline signal) is chosen manually for both FSRS and ground state FSRS signals (red dots in Figure 2.7(b)) and the baseline is approximated by a cubic spline curve, passing through these zero-intersection points. Alternatively, a peak-isolation method can be employed, in which a set of N points (where N is a multiple of 2) is used to define the peak or peak cluster locations (with the i^{th} point signifying the "beginning" and the $(i+1)^{\text{th}}$ point signifying the "end" of a particular peak region). All of the remaining (i.e., "non-peak") points are then assumed to represent only the baseline and are approximated by a high order (≥ 5) polynomial curve (e.g., in Figure 2.7(c) this method is applied to isolate the $\Gamma^{(0)}$ vibrational signatures in-between 750–1550 cm^{-1}). The baselines $B_\Phi(\nu)$ and $B_\Gamma(\nu)$ (dashed-dotted gray curves in Figures 2.7(b) and 2.7(c)) are then calculated according the chosen method for each temporal point, resulting in two baseline matrices $B_\Phi(t,\nu)$ and $B_\Gamma(t,\nu)$. These are then subtracted from the FSRS and ground state FSRS spectra:

$$\Phi^{(2)}(t,\nu) = \Phi^{(1)}(t,\nu) - B_\Phi(t,\nu), \tag{2.17}$$

$$\Gamma^{(1)}(t,\nu) = \Gamma^{(0)}(t,\nu) - B_\Gamma(t,\nu). \tag{2.18}$$

It should be noted that if any significant spectral shifts occur throughout the spectral evolution (e.g., as in the theoretical illustration of ref. [91]), a careful reassessment of the zero-intersection points at different temporal windows is necessary in order not to distort the resulting FSRS dynamics.

4. At each delay point a scaled ground state FSRS signal is subtracted from the excited state FSRS signal in order to diminish any residual solvent vibrational lines in the final FSRS spectrum:

$$\Phi^{(3)}(t_i,\nu) = \Phi^{(2)}(t_i,\nu) - \gamma_i \cdot \Gamma^{(1)}(t_i,\nu), \tag{2.19}$$

where γ_i is the scaling factor, based on the amplitude of the largest residual solvent Raman peak in each individual $\Phi^{(2)}(t_i,\nu)$ (e.g., in Figure 2.7(d) γ_i is determined by the amplitude of the 913.1 cm^{-1} Raman line of tetrahydrofuran (THF) [92]). It should be emphasized that $\Gamma^{(1)}$ ought be meticulously checked for ground state FSRS signals of the investigated sample prior the subtraction, e.g., ground state FSRS contribution of β-carotene under off-resonant (i.e., $\nu_{RP} \ll \nu_{S_0 \rightarrow S_{n>1}}$) conditions is minimal (i.e., the pure THF FSRS signal is more than 15× more intense than that of β-carotene in Figure 2.7(c)), thus scaled subtraction of $\Gamma^{(1)}(t,\nu)$ in Equation 2.19 can be performed without greatly distorting the original data. Otherwise, if the contributions of sample and solvent FSRS signals are comparable, an independently measured pure solvent FSRS reference ($\Gamma^{(R)}(\nu)$ in Figure 2.7(c)) should, preferably, be used as a replacement for $\Gamma^{(1)}(t_i,\nu)$ in Equation 2.19. The remaining negative Raman lines of the sample (i.e., ground state Raman line bleaching) can be removed in a similar fashion, with the aim of amassing only the Raman gain (and not the Raman loss) spectrum [46, 47, 93], though we have chosen to leave the Raman bleaching contribution intact in our FSRS spectra.

5. A Savitzky–Golay filter, typically composed of a 4^{th} order polynomial within a 6 point window, is applied to each $\Phi^{(3)}(t_i,\nu)$ in the dataset to reduce the pixel-to-pixel noise, if necessary (Figure 2.7(e)).

The FSRS data management is performed using homemade software, written in C++ with Qt 5.4 framework [94] and the QCustomPlot [95] library for graph visualization. Source code and pre-compiled Windows binaries of the data management program can be found in ref. [96].

2.5 GLOBAL ANALYSIS OF TIME-RESOLVED DATA

A typical PP of FSRS experiment generates a two-dimensional set of temporally- and spectrally-resolved data. For illustrative purposes this data can be visualized as a tree-dimensional surface, with the TA or Raman gain amplitude representing its "height", or a topographic map, projecting the said surface on a two-dimensional plane. While this kind of portrayal always provides a nice visual outlook for the data (not to mention that it always looks good in print), it is usually preferred to analyze the spectroscopic data by "dissecting" it into discrete spectrally-resolved kinetic traces or temporally-resolved TA (or Raman gain) spectra. In the former case, each individual kinetic trace can be

fit to a sum of exponential decay curves convoluted with the temporal instrument response function (IRF) of the measurement system. Alternatively, the time-resolved spectra can be fit to a linear combination of spectrally displaced Gaussian of Lorentzian peaks. The biggest drawback of this approach is the lack of generalized information on the time-resolved data, because the entire spectro-temporal dataset is not interpreted as an integral unit. By analyzing only the discrete cuts of the whole time-resolved spectrum we either ignore a significant amount of underlying information or end up with a large number of seemingly uncorrelated variables.

One of the best ways to characterize and parametrize the time-resolved spectroscopic data is global analysis [97–99]. Global analysis, as the name implies, is a numerical fitting procedure in which the entire temporally- and spectrally-resolved dataset is approximated as a whole. The time-resolved spectrum, from the global analysis standpoint, is assumed to be the result of a number of discrete interacting spectral components, everyone of which is, ideally, prototypical of a real physical state. Each of these components is fully described by a time-varying concentration $c_i(t)$ (i.e., the relative population of a certain component at a given temporal moment) and a component-specific species-associated difference spectrum (SADS) $\sigma_i(\lambda)$. One or more of these components is presumed to be populated during the interaction of the system with the excitation pulse. As the system evolves in time, the excitation-generated population is reallocated among these components in a certain fashion—sequentially, parallelly, cyclically, etc. In other words, the population of each component changes over time according to predetermined connectivity scheme, i.e., the global analysis fitting model. Therefore, the free variables of a global fitting procedure are the inter-species population transfer rates and the SADS of the components.

To gain a better understanding on global analysis, we shall examine several simple evolutionary schemes. One of the most common is the sequential evolution model. In this connectivity scheme the initial component is populated by the excitation pulse and the excited state population is progressively transferred from one component to its closest "neighbor", i.e., $c_1(t) \rightarrow c_2(t) \rightarrow \ldots \rightarrow c_n(t) \rightarrow \ldots$. This evolutionary model can be described by the following set of differential equations:

$$\frac{dc_1}{dt} = I(t) - \frac{c_1(t)}{\tau_1}, \qquad \text{when } i = 1, \tag{2.20}$$

$$\frac{dc_i}{dt} = \frac{c_{i-1}(t)}{\tau_{i-1}} - \frac{c_i(t)}{\tau_i}, \qquad \text{when } i > 1. \tag{2.21}$$

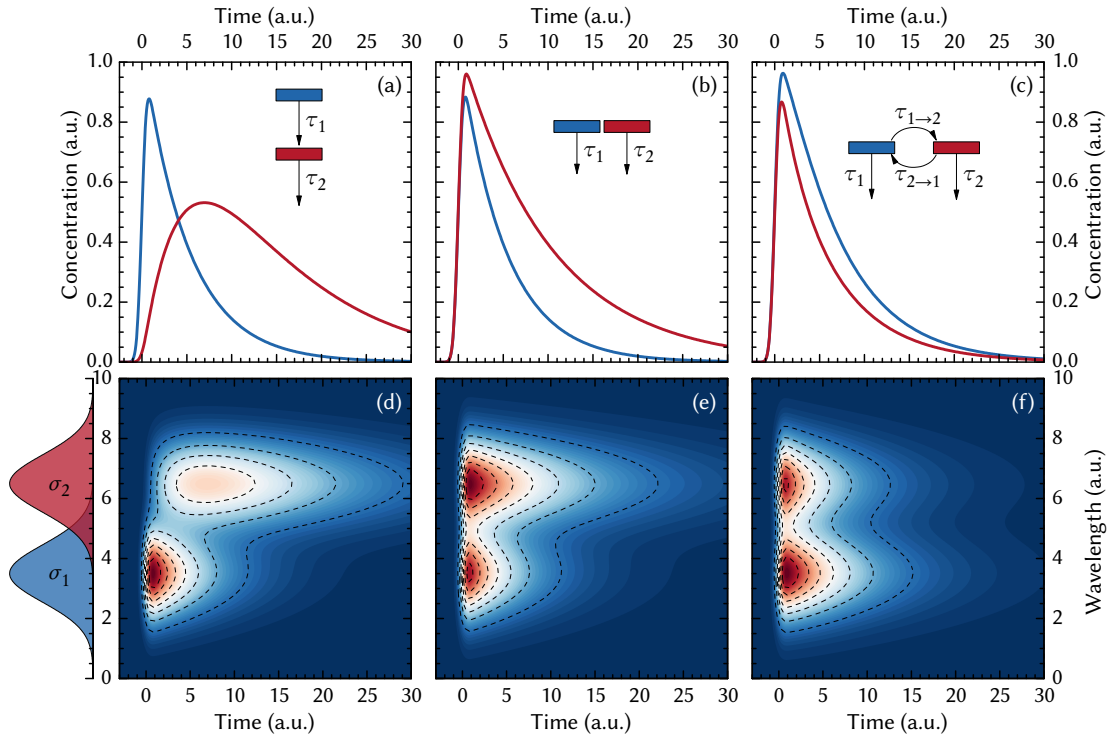

FIGURE 2.8: An example of several global analysis models, illustrating sequential (left), parallel (middle), and coupled-parallel (right) evolution. The upper panels (a)–(c) depict the development of time-dependent concentrations $c_i(t)$ (Equations (2.20) to (2.23)), while the insets in the said graphs provide a visual representation of the component connectivity. The bottom panels (d)–(f) portray simulated TA spectra (Equation 2.25), acquired using the appropriate time-dependent concentrations $c_i(t)$ and a pair of Gaussian-shaped SADS $\sigma_i(\lambda)$, presented in the bottom outer graph. The intrinsic lifetimes of the components were designated to $\tau_1 = 5$ and $\tau_2 = 10$ in all the examples, while the population interchange rates in panels (c) and (f) were set to $\tau_{1\to2} = 8$ and $\tau_{2\to1} = 4$. The population generation function $I(t)$ is described by a Gaussian with a FWHM of 1.

Here $I(t)$ is the (typically) Gaussian-shaped IRF, that describes the excitation pulse, and τ_i are the characteristic lifetimes (i.e., the reciprocal transfer rates) of the successively linked components. Sequential evolutionary model is illustrated in Figures 2.8(a) and 2.8(d). As causality would imply, the emergence of the 2$^{\text{nd}}$ spectral component (red) in the presented example is "delayed" in respect to the 1$^{\text{st}}$ one (blue).

Analogously, we can construct a parallel spectral evolution model. In this case the excitation pulse populates not one but several spectral species, every one of which decays to the ground state and does not interact with any of the

other components. Parallel spectral evolution of $i = 1, 2, \ldots, n$ non-interacting species can be generally described as:

$$\frac{dc_i}{dt} = \alpha_i I(t) - \frac{c_i(t)}{\tau_i}. \tag{2.22}$$

Here α_i is the fraction of the excited state population "imposed" on each of the components by the excitation pulse.[6] Parallel spectral evolution of two discrete components is depicted in Figures 2.8(b) and 2.8(e). In the presented example both species simultaneously surface at $t = 0$ and in the course of the spectral evolution disperse with their characteristic lifetimes τ_i. Since $\tau_2 > \tau_1$, the 2nd component continues to linger in the long haul.

In many actual photoactive systems the interstate interaction may not necessarily be irreversible, as exemplified by Equations (2.20) and (2.21). If a thermodynamic equilibrium exists between some of the components, then the excited state population is constantly shifted forward and backwards between the coupled species until the system ultimately relaxes to the molecular ground state. If we take the parallel spectral evolution model, described by Equation (2.22), as a starting point and incorporate the conjugate interstate population transfer rates $\tau_{j\to i}$ and $\tau_{i\to j}$ to the evolutionary scheme, then the mutually coupled component model can be written as:

$$\frac{dc_i}{dt} = \alpha_i I(t) - \frac{c_i(t)}{\tau_i} + \sum_{j\neq i}^{n}\left(\frac{c_j(t)}{\tau_{j\to i}} - \frac{c_i(t)}{\tau_{i\to j}}\right). \tag{2.23}$$

This model is illustrated in Figures 2.8(c) and 2.8(f). In the presented example $\tau_{2\to 1} < \tau_{1\to 2}$ and, thereby, the 1st component acts as a "drain" for the population flow. We can see that despite the fact, that the intrinsic lifetimes of the states are identical to those of Figures 2.8(b) and 2.8(e), the existence of an interstate coupling effectively "short-circuits" the longer lived 2nd component and slightly prolongs the lifetime of the 1st one.

All things considered, any conceivable evolutionary model can be described as a certain combination of Equations (2.20) to (2.23). Essentially, any n component global analysis connectivity scheme can be expressed as the following set of differential equations:

$$\frac{dc_i^{\mathrm{PP}}}{dt} = \delta_{i,P}\alpha_i^{\mathrm{PP}} I_P(t) \pm \sum_{j=1}^{n}\frac{c_j(t)}{\tau_{i\to j}}, \tag{2.24}$$

6 Generally, $\sum_{i=1}^{n}\alpha_i = 1$, albeit renormalization only changes amplitudes of the $\sigma_i(\lambda)$'s.

where $\delta_{i,P}$'s indicate the components that are explicitly populated by the pump pulse (hence "P" in the subscript), $\tau_{i\to j}$ represents the reciprocal population transfer rates ($i \to j$ denotes the temporal evolution from the i^{th} to the j^{th} component, $i \to i$ denotes the decay of the i^{th} component to the ground state, sign of τ (herein presented before the summation sign) denotes the "direction" of the population flow, i.e., $\text{sgn}(\tau_{i\to j}) = -\text{sgn}(\tau_{j\to i})$ and $\text{sgn}(\tau_{i\to i}) < 0$).[7] Under a given connectivity scheme, the population transfer rates can be refined, and the wavelength-dependent SADS of each of the n model states can be estimated by least-square fitting the experimentally-resolved PP (or FSRS) dataset to the spectro-temporal product:

$$S_{\text{PP}}(t,\lambda) = \sum_{i=1}^{n} c_i^{\text{PP}}(t)\sigma_i(\lambda). \tag{2.25}$$

PDP experimental data (or PrPP data for that matter) can also be similarly fit using global analysis techniques [99–101]. In a PDP experiment, in addition to the conventional PP data, we acquire a spectro-temporal dataset that contains the information about the post-perturbation development. The two datasets should ideally coincide prior to the arrival of the dump pulse and diverge afterwards. The PDP data can, therefore, be described by an additional set of differential equations:

$$\frac{dc_i^{\text{PDP}}}{dt} = \frac{dc_i^{\text{PP}}}{dt} \pm \delta_{i,D} I_D(t-t_D) \times \sum_{j=1}^{n} \phi_{j\to i} c_j(t). \tag{2.26}$$

Here $\frac{dc_i^{\text{PP}}}{dt}$ is the same as in Equation 2.24, $\delta_{i,D}$ indicates the specific perturbation-affected states that are either depopulated ($-$) or repopulated ($+$) during the interaction with the dump pulse (hence "D" in the subscript), $I_D(t-t_D)$ is the IRF for the dump pulse incoming at $t = t_D$, and $\phi_{j\to i}$ represents the relative amount of population transferred (or received) from component j to component i in the perturbative process. The PP and PDP spectra can then be them simultaneously fit to, accordingly, Equation 2.25 and:

$$S_{\text{PDP}}(t,\lambda) = \sum_{i=1}^{n} c_i^{\text{PDP}}(t)\sigma_i(\lambda), \tag{2.27}$$

to get a unified set of $\tau_{i\to j}$'s and $\sigma_i(\lambda)$'s that best describe both the unperturbed and perturbed time-resolved spectroscopic data.

7 The label in the superscript is given to separate the PP- and PDP-specific equations.

Part III

THE LIFE AND TIMES OF CAROTENOIDS

The following chapter can be separated into two major parts. At first, in Section 3.2 we demonstrate a practical application FSRS setup presented in the preceding part by measuring the time-resolved FSRS spectra of β-carotene. The choice for the preliminary specimen does not come off as an unpredictable one, since β-carotene (and various other carotenoids for that matter) have been some of the most successful targets for FSRS analysis in the past. This brief, yet informative, study allows us to showcase the features, capabilities, and limitations of the said FSRS system, and to predict its possible future applications. Furthermore, in Section 3.3 we utilize both PDP and FSRS multi-pulse techniques to unravel the somewhat more intricate excited state vibronic dynamics of the aquatic carotenoid fucoxanthin.

3

ULTRAFAST VIBRONIC DYNAMICS OF CAROTENOIDS

3.1 A BRIEF INTRODUCTION TO CAROTENOIDS

Carotenoids are some of the most widespread and important pigments in nature that are responsible for both light-harvesting and photo-protective functions of the photosynthetic apparatus [102–105]. The molecular backbone of carotenoids is composed of an extensive conjugated π-electron system (see Figure 3.1(a)) that effectively defines their spectroscopic properties. The high degree of symmetry of the π-electron chain ascribes carotenoids to the C_{2h} symmetry point group, thus directly prohibiting one-photon electronic transitions between ground state and the lowest lying singlet electronic state of the polyene molecule (i.e., $S_0(1^1A_g^-) \nrightarrow S_1(2^1A_g^-)$). As a result, the carotenoid steady-state absorption surfaces in the blue-green part of the VIS spectrum (see Figure 3.1(b)), stemming from the optically-allowed electronic $\pi \rightarrow \pi^*$ transitions to a short-lived higher excited singlet state S_2 (i.e., $S_0(1^1A_g^-) \rightarrow S_2(1^1B_u^+)$). These symmetry-allowed transitions are associated with a large change of dipole moment and the molar extinction coefficients in the VIS may exceed $150\,000\,M^{-1}\,cm^{-1}$ at the $S_0 \rightarrow S_2$ resonance peak (ca. 460–500 nm) [105]. Moreover, the broad carotenoid steady-state absorption spectrum typically exhibits clearly resolved vibronic substructures (the so-called vibronic "fingers") spaced at ca. $1400\,cm^{-1}$. In less than a hundred femtoseconds the excitation-created S_2 decays via internal conversion to the longer lived S_1, with a small portion of the S_2 population typically experiencing radiative decay back to S_0 [104]. The carotenoid $S_1 \rightarrow S_{n>1}$ ESA typically surfaces red-shifted from the ground state absorption maximum by ca. $4000\,cm^{-1}$ (see Figure 3.1(b)) and has a strong molar absorption coefficient that is comparable to that of the $S_0 \rightarrow S_2$ transitions. Due to the aforementioned symmetry restrictions, S_1 is not fluorescent and is depopulated purely via non-radiative internal conversion to S_0. Thereby, the S_1 lifetime depends on the energy gap between S_1 and S_0 and is, consequently, inversely proportional to the π-electron conjugation

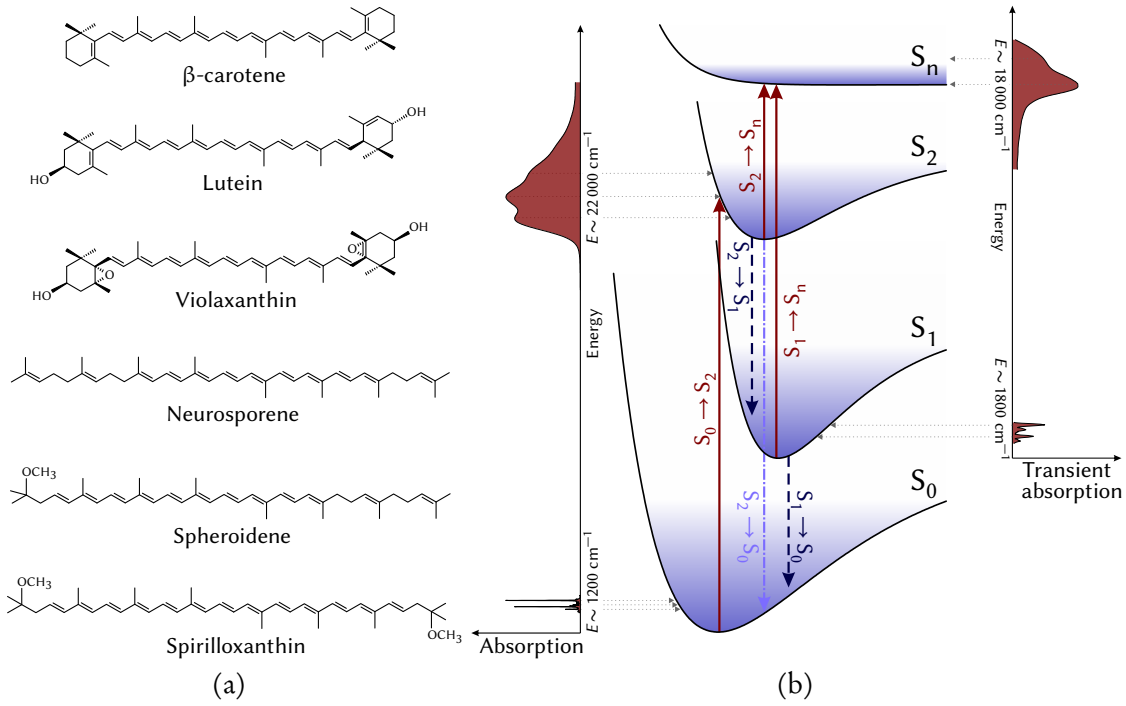

FIGURE 3.1: Panel (a): chemical formulae of several frequently naturally occurring carotenoids. The three upper carotenoids (β-carotene, lutein, and violaxanthin) are found in higher plants, whereas the three lower carotenoids (neurosporene, spheroidene, and spirilloxanthin) appear in various photosynthetic bacteria [105]. Panel (b): a simplified PES diagram of typical carotenoid photodynamics. The red solid upwards arrows indicate the optically-allowed singlet electronic transitions, the blue dashed downwards arrows indicate non-radiative internal conversion, the cyan dashed-dotted downwards arrow indicates the relatively weak $S_2 \rightarrow S_0$ SE. The vibronic absorption spectra of the S_0 and the S_1 states are presented on, respectively, the left-hand and right-hand sides of the PES diagram.

length of the polyene backbone, i.e., $\tau_{S_1 \rightarrow S_0} \sim \exp(\Delta E_{S_1 - S_0}) \sim 1/N_\pi$ [106]. The typical carotenoid S_1 lifetimes may range from ca. 1.4 ps for spirilloxanthin (see Figure 3.1(a)) to ca. 407 ps for the synthetic seven double C=C bond tetrahydrospheroidene [106].

3.2 THE FSRS SPECTRA OF β-CAROTENE

Carotenoids, in general, exhibit very intense Raman scattering signals both in the ground state and the excited state, thus making them perfect targets for FSRS analysis. β-carotene needs little introduction, owing to its excessive

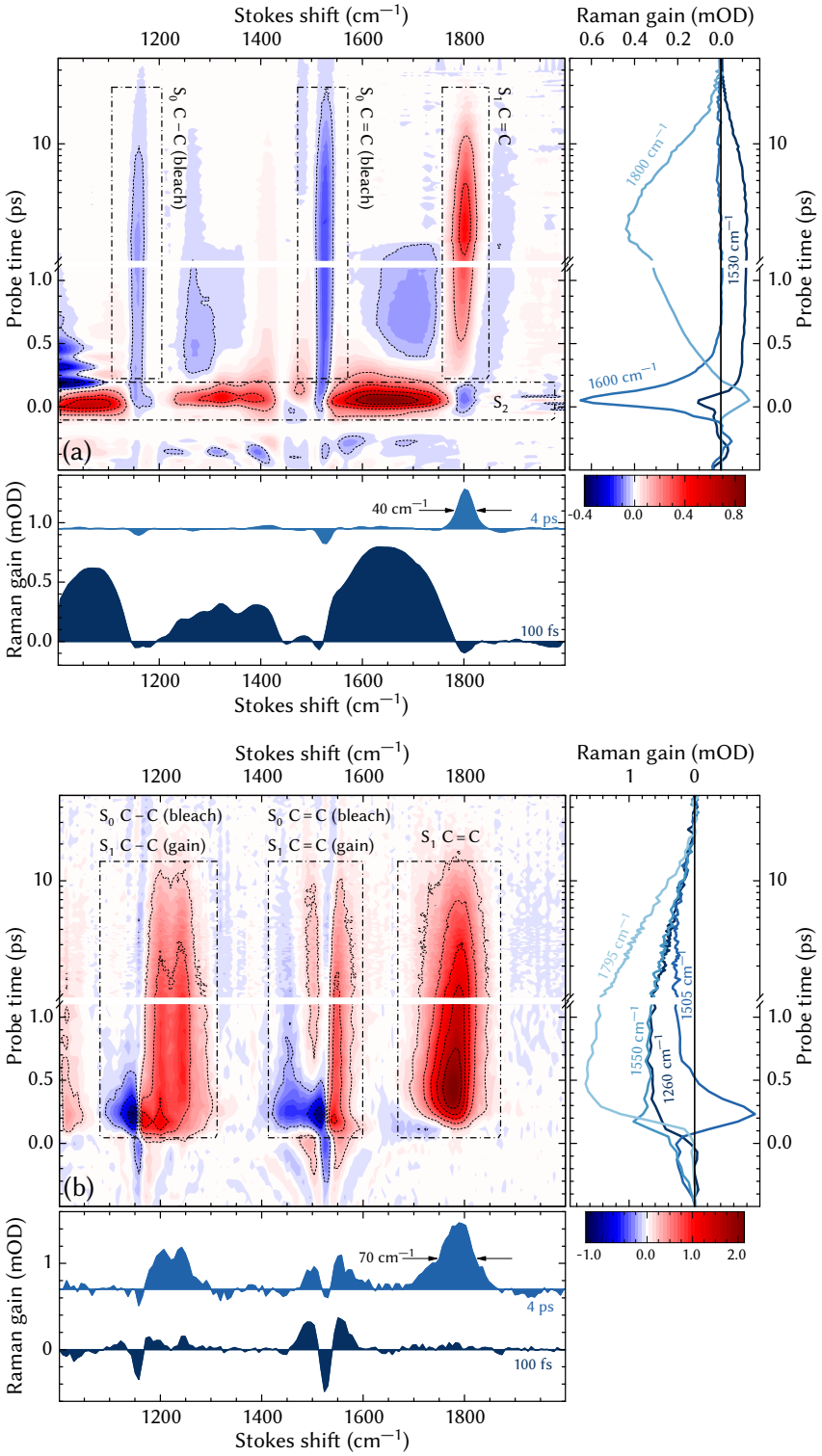

FIGURE 3.2: FSRS dynamics of β-carotene in *n*-hexane, obtained by using (a) 790 nm, and (b) 550 nm Raman pumps. The central panels depict the full time- and wavenumber-resolved FSRS spectrum, whereas the right-hand side and bottom graphs accentuate several selected spectral and temporal cuts of the FSRS datamap. Certain regions of interest are highlighted and annotated in the main FSRS graphs.

natural abundance in plants and fruit and its importance to the nutrition of humans and other animals [107]. β-carotene (see Figure 3.1(a)) has already been subjected to multiple FSRS studies [43, 47, 88, 108]. The well documented nature of β-carotene FSRS (and IR [109, 110]) dynamics make it a great archetypal candidate for evaluating the performance of the FSRS setup presented in Section 2.3. The $S_2 \rightarrow S_n$ ESA of β-carotene peaks in the NIR in-between 900 and 1100 nm [111], whereas the $S_1 \rightarrow S_n$ ESA reaches its maximum at ca. 450 nm [32] (see Figure 3.1(b)). With this knowledge in mind, FSRS techniques utilizing different Raman pump wavelengths can be applied to spectrally resolve the vibrational constitution of the β-carotene $1^1B_u^+$ and $2^1A_g^-$ states and to temporally monitor the transition between them.

For the FSRS experiments β-carotene (Sigma-Aldrich 22040) was dissolved in *n*-hexane (Rotisolv, HPLC grade) and diluted to OD of 1 at 490 nm in a 1 mm optical pathway. $S_0 \rightarrow S_2$ actinic excitation was performed by using $\lambda_{AP} = 490\,\text{nm}$, $E_{AP} = 150\,\text{nJ}$, $\tau_{AP} = 70\,\text{fs}$ ultrashort pulses, while the Raman pump pulses were set to either $\lambda_{RP} = 550\,\text{nm}$, $E_{RP} = 500\,\text{nJ}$, $\tau_{RP} = 3\,\text{ps}$; or $\lambda_{RP} = 615\,\text{nm}$, $E_{RP} = 2\,\mu\text{J}$, $\tau_{RP} = 6.5\,\text{ps}$.

The $S_2 \rightarrow S_n$ absorption peaks at around ca. 950 nm in *n*-hexane [111], albeit application of such a Raman pump (or even a proximate one) is near impossible due to spectral sensitivity limitations of the silicon-based CCD arrays: the Stokes-shifted wavelengths will be at or beyond the edge of the upper sensitivity limit (ca. 1100 nm). In order to have the FSRS signals within the detectable wavelength range, we have utilized a 790 nm Raman pump. These Raman pump pulses are primarily resonant with the $S_2 \rightarrow S_n$ transitions [111], albeit the low-intensity long-wave tail of the $S_1 \rightarrow S_n$ absorption extends beyond the VIS spectrum [32], hence making the 790 nm Raman pump partly resonant with both the $S_2 \rightarrow S_n$ and $S_1 \rightarrow S_n$ electronic transitions. The formation of the S_2 state can be best observed in Figure 3.2(a), where the sub-500-femtosecond photoevolution reveals an emergence of a distinct three-band structure, peaking at ca. 1070, 1350, and 1640 cm^{-1}. These peak clusters (that have been decomposed into seven discrete Gaussian peaks in a study by Kukura et al. [47]) have been previously identified as the S_2 vibrational spectrum. The S_2 vibrational features vanish from the FSRS spectrum within the first few hundred femtoseconds (once again, mirroring the results in ref. [47]), just as S_1 is gradually formed via internal conversion. Since S_1 is only weakly resonant with the 790 nm Raman pump, only the most intense S_1 vibrational band—the high-frequency C=C stretching at ca. 1800 cm^{-1}—appears in the sub-100-picosecond FSRS spectrum of NIR-pumped β-carotene [47, 109, 110]. As evident in Figure 3.2(a), the particular mode demonstrates a peak-shift (to higher frequencies) and spectral narrowing during the first few picoseconds

that can be ascribed to initial formation of a hot S_1 intermediate and its eventual vibrational cooling [43]. Other indications of a molecular system, not yet fully restored to a thermal equilibrium, show up as the negative bleaching of the two ground state resonances, i.e., the negative peaks at 1159 cm^{-1} (depletion of the S_0 C–C stretching mode [112]) and 1526 cm^{-1} (depletion of the S_0 C=C stretching mode [112]).

The 550 nm Raman pump, in contrast, falls directly under the $S_1 \rightarrow S_n$ absorption maximum, hence all of the positive (i.e., FSRS gain) features in Figure 3.2(b) can be ascribed exclusively to the S_1 manifold. It is obvious that the broadband multi-peak structure is not present in Figure 3.2(b) during the initial steps of the post-excitation vibrational evolution, and is instead replaced by the gradual formation of the S_1-indicative vibrational peaks. The intense C=C vibrations at ca. 1800 cm^{-1} similarly dominate within the S_1 vibrational photodynamics, and likewise demonstrate the peak-shift and band-narrowing spectral dynamics, associated with vibrational cooling on the S_1 PES. In contrast to the 790 nm experiments, the FSRS spectra in Figure 3.2(b) feature two additional spectral bands that prevail throughout the entire S_1 lifetime: the ca. 1240 cm^{-1} S_1 C–C stretching mode and the lower-frequency S_1 C=C vibrations at ca. 1550 cm^{-1} [46]. The latter band lies close to the hot S_0 peak at 1510 cm^{-1} [46] that slowly develops in a sub-20-picosecond temporal interval (see Figure 3.2(b)). Both S_1 spectral peaks arise near their corresponding (yet bleached) ground state positions, thus giving the FSRS time-gated spectra a distinctive cleft-like profile (which can be patched-up by the addition of a scaled ground state Raman spectrum [47]). The vibrational peaks in Figure 3.2(b) are notably broader (up to 75 % at FWHM) than their equivalents in Figure 3.2(a) (the previously reported values of the S_1 C=C bandwidth were ca. 50 cm^{-1}) [43]. Recognizing that the spectral detection resolution is essentially identical in both the experiments ($\bar{\nu}_{VIS} = 6.5\,cm^{-1}$ with a 1200 mm^{-1} grating in the VIS, and $\bar{\nu}_{NIR} = 7\,cm^{-1}$ with a 600 mm^{-1} grating in the NIR), the spectral broadening in the 540 nm Raman pump measurements is most likely instigated by either (a) Raman line bandwidth dependence on the resonant enhancement conditions; (b) a relatively larger bandwidth of the VIS Raman pump ($\tau_{RP}^{VIS}/\tau_{RP}^{NIR} \approx 2.2$); or (c) the possible influence of "parasitic" band-widening $\chi^{(5)}$ signals, such as hot luminescence [66, 113, 114].

Disregarding the intrinsic differences between the two FSRS spectra in Figure 3.2, it is obvious that they both paint an equally informative photo-evolutionary picture: most significant development steps, i.e., population and depopulation of the S_2 state, its sub-picosecond decay into the hot S_1 manifold, the latter state's vibrational cooling, and eventual decay to the main ground state, can be inferred from either one of the FSRS datasets. In conclu-

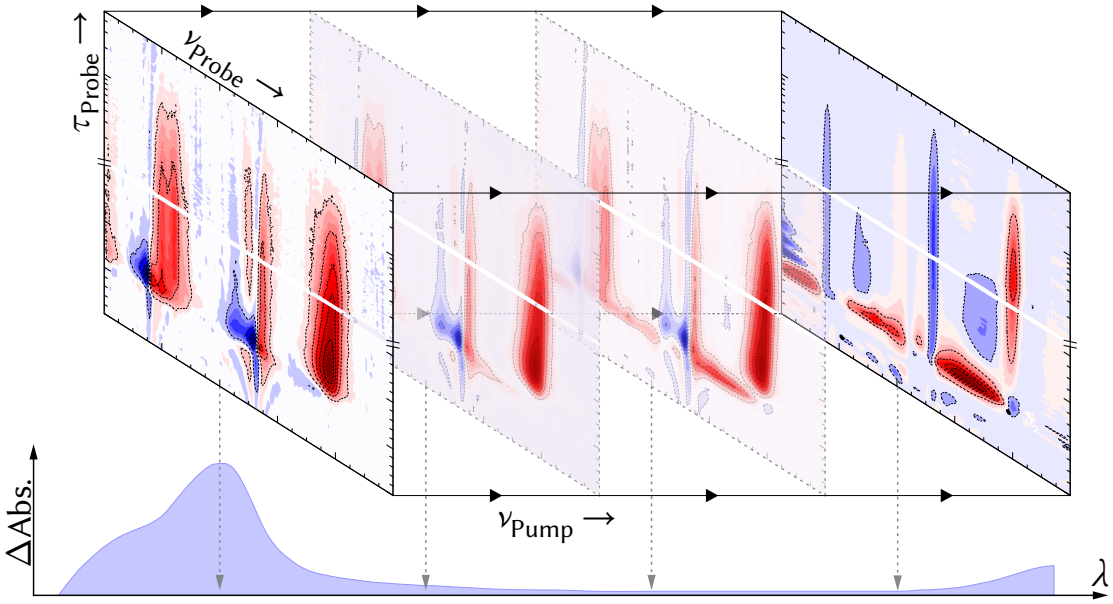

FIGURE 3.3: Proposed scheme of a 2D FSRS experiment: the Raman pump is scanned through the IA profile, measuring a series of FSRS spectra, thus providing time- and detection/excitation wavenumber-resolved FSRS data.

sion, we can see that, contrary to typical PP experiments, FSRS offers a lot constructive information on the vibrational structure of the excited state spectrum. The easy tunability of the presented FSRS setup allows us to suggest its application in future 2D FSRS measurements. As depicted in Figure 3.3, continuously scanning the Raman pump over a wide spectral range (essentially, covering the bulk of the electronic IA spectrum) would provide us with two-dimensional FSRS data $S(\nu_{PU}, \nu_{PR}, t_{PR})$. This kind of FSRS mapping would, expectedly, shed additional insight on the constitution of the electronic states, their mutual interaction, and the possible coupling between them. Raman spectra emerging at different Raman pump wavelengths could be used as a basis in disentangling and attributing overlapping bands observed in PP spectra. In this way, the excellent time resolution and accurate dynamic information of electronic PP spectroscopy (note that PP data come as a "byproduct" of this implementation of FSRS setup) would be complemented by the structural sensitivity and selectivity of Raman signals. We predict that these type of experiments could be easily carried out on such photosynthetic systems as peridinin-chlorophyll-protein (PCP) [115] and fucoxanthin-chlorophyll-protein (FCP) [116] light-harvesting complexes (to uncover the interplay between the internal charge transfer bearing carbonyl-carotenoids and the chlorophylls), or to gain more understanding on the dark states of carotenoids [117–119].

3.3 INVESTIGATION OF THE S_1/ICT EQUILIBRIUM IN FUCOXANTHIN BY ULTRAFAST PUMP-DUMP-PROBE AND FEMTOSECOND STIMULATED RAMAN SCATTERING SPECTROSCOPY

3.3.1 *An Introduction to Fucoxanthin*

Fucoxanthin (FX) is one of the most abundant xanthophyll carotenoids in the world due to its natural occurrence in such biomass "giants" as brown algae, seaweed and marine diatoms [120, 121]. The FX backbone, as pictured in Figure 3.4, consists of eight conjugated double bonds,[1] terminated by two non-symmetrical ring groups at different ends of the molecule. As is the case with the majority of carotenoids, the polyene skeleton of the molecule imposes C_{2h} symmetry, that, as a rule, prohibits one-photon transitions between the ground state $S_0(1A_g^-)$ and the low-lying singlet state $S_1(2A_g^-)$ [104]. This constrains the carotenoid's electronic absorption properties exclusively to the optically allowed transitions $S_0(1A_g^-) \rightarrow S_2(1B_u^+)$ that surface in the blue/green part of the VIS spectrum ($\lambda_{max} = 449\,nm$ in methanol (MeOH), as depicted in Figure 3.4; the underlying vibronic "fingers" become more pronounced in a non-polar environment [122]). A carbonyl group (—C(=O)—CH_3), conjugated to one of the terminal rings, significantly alters the FX excited state dynamics. The presence of carbonyl group incites charge transfer within the FX excited state manifold [122], which in a polar environment give rise to a clearly distinguishable intramolecular charge transfer (ICT) state [123–125], coexisting alongside the S_1 [122, 126]. The ICT typically emerges redshifted from the S_1 (by ca. $3000\,cm^{-1}$, as seen in Figure 3.4 and refs. [122, 126–128]) and, contrarily to S_1, displays moderate SE in the NIR [127]. From the optical absorption standpoint, ICT is an optically "dark" state, since direct one-photon transitions $S_0 \rightarrow$ ICT are not observed in the FX steady-state spectrum. This implies that charge transfer and molecular stabilization processes, which bring about the ICT, occur mainly via relaxation from the S_2 state [122].

The S_1 and the ICT are two distinct species that are generally believed to coexist in an excited state equilibrium [127, 130]. The existence of such equilibrium is, in fact, one of the main reasons why the excited state lifetime of FX is relatively short (ca. 15–20 ps) for a carotenoid of such short length. While many femtosecond time-resolved TA studies have been carried out on FX [122, 126–128], none of them explicitly show the S_1/ICT coupling or predict the kinetic coupling rates. Multi-pulse TA methods have been successfully applied in the past to uncover the S_1/ICT coupling in peridinin—another ICT pos-

1 Seven C=C bonds with conjugation extension to the carbonyl group.

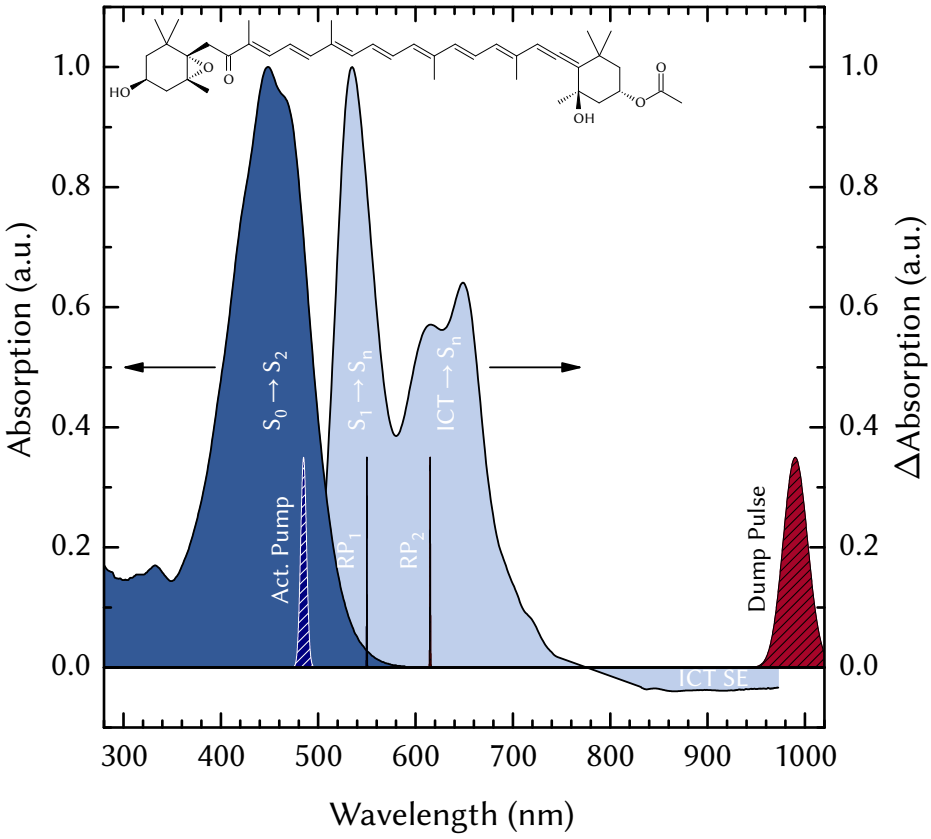

FIGURE 3.4: Steady-state absorption (left-hand side, blue) and excited state (right-hand side, cyan) TA spectra of FX in MEOH (the latter spectrum was obtained with $\lambda_{AP} = 485$ nm excitation at the optical delay of 4 ps). Negative signal at > 775 nm corresponds to SE of the ICT state. Molecular structure of FX is presented in the inset. Gaussian curves on the abscissa indicate spectral positions (and the approximate bandwidths) of the actinic pump, dump, and Raman pump (RP_1, RP_2) pulses. Assignment of the electronic transitions is adapted from ref. [129].

sessing carotenoid [131, 132]. Herein we present an experimental multi-pulse study of the FX photodynamics. PDP methods are utilized to perturb the FX excited state evolution by inducing a deliberate SE of the ICT state and to explore the dynamics of the temporary destabilized molecular system. In addition, FSRS techniques are applied to elucidate the vibrational constitution and time-resolved vibrational behavior of both of the excited state species. The clear distinction between the two "cohabitants" of the excited state manifold, as depicted in Figure 3.4, allows selective FSRS measurements of either one of the co-occurring electronic states. Global analysis methods from Section 2.5 are employed to parametrize the experimental data and to numerically resolve spectra, lifetimes, and coupling rates of the interconnected transient species.

3.3.2 *Materials and Methods*

3.3.2.1 *Overview of the Three-Pulse Experiments*

The theoretical basis and the experimental configuration of PDP/PDAT experiments are presented in, respectively, Sections 2.2.1 and 2.3. In the PDP experiments the FX sample was excited with $\lambda_{AP} = 485\,nm$, $E_{AP} = 150\,nJ$ ($\tau_{AP} = 70\,fs$) ultrashort laser pulses. The dump pulses were adjusted to spectrally and temporally correspond to the ICT SE (see Figure 3.4) and were set to $\lambda_{DU} = 990\,nm$, $E_{DU} = 400\,nJ$ ($\tau_{DU} = 70\,fs$) at the temporal delay of $t_{DU} = 1.8\,ps$. In the PDAT experiments the probe pulse was positioned at $t_{PR} = 15\,ps$, the actinic excitation conditions were the same as in the PDP measurements, while a slightly higher excitation energy ($E_{DU} = 600\,nJ$) was used for the ICT dumping. The three-pulse experiments were performed back-to-back in two separate spectral windows (VIS 440–750 nm, and NIR 830–970 nm) and the data of each experimental instance (either PDP or PDAT) were merged into a single spectro-temporal dataset. GVD of the probe pulse for the PDP data was estimated from the rising segments of the kinetic curves at each wavelength (similar to the approach described in Section 2.4). The wavelength dependence of the mid-rise point within these segments was approximated by a polynomial function of the 5th degree and the polynomial parameters were further refined in the global fitting procedure.

The FSRS theory and methodology are discussed in greater detail in Sections 2.2.2 and 2.3. In general, we have adapted the concepts described in refs. [54, 133] to perform FSRS measurements on the above-described three-pulse PDP/FSRS setup [68, 134, 135]. The FSRS data handling techniques were adapted from refs. [44, 136] (see Figure A.2 and Section 2.4 for additional details). Actinic excitation in the FSRS experiments was performed using $\lambda_{AP} = 485\,nm$, $E_{AP} = 250\,nJ$, $\tau_{AP} = 70\,fs$ ultrashort pulses, whereas the Raman pump pulses were adjusted to either $\lambda_{RP} = 550\,nm$, $E_{RP} = 500\,nJ$, $\tau_{RP} = 3\,ps$ (to achieve the $S_1 \rightarrow S_n$ resonance), or $\lambda_{RP} = 615\,nm$, $E_{RP} = 1500\,nJ$, $\tau_{RP} = 6.5\,ps$ (to achieve the ICT $\rightarrow S_n$ resonance). Spectral resolution of the FSRS experiments was ca. $5\,cm^{-1}$.

3.3.2.2 *Sample Preparation*

FX was purchased from SIGMA-ALDRICH (F6932, > 95 % purity) and the crystal powder samples were dissolved in MEOH (CHROMASOLV, HPLC Grade) producing solutions of OD = 1 at 485 nm in a 1 mm optical pathway quartz cuvette (HELLMA). The cuvette was translated transversely to the beam direction in a Lissajous pattern via two perpendicularly assembled translational

stages (STANDA 8MT173) in order to avoid sample over-exposure during the experiments.

3.3.3 *Experimental Results*

3.3.3.1 *Fucoxanthin Pump-Probe Dynamics*

Selected temporal cuts of the FX PP spectrum are presented in Figure 3.5(a). The FX TA dynamics have been discussed in greater detail previously in refs. [122, 126–128], therefore we will simply summarize the most important aspects of the dynamic processes taking place after the $S_0 \rightarrow S_2$ excitation. The 485 nm one-photon excitation prepares the FX molecular system in the optically-allowed singlet state S_2, whose appearance is mostly expressed by the intense short-lived IA in the NIR during the very early stages of the photoevolution (0 fs spectrum in Figure 3.5(a)). In several hundred femtoseconds following its formation, S_2 decays via internal conversion to the S_1/ICT manifold (see how IA at 0 fs in Figure 3.5(a) transforms into SE at 350 fs in Figures 3.5(a) and 3.5(b); for a more direct comparison refer to Figure A.3). The FX excited state dynamics, and especially the relative yield of S_1 and ICT IA in the TA spectra, greatly depends on the excitation wavelength (presumably, due to the involvement of several FX isomers in the solution [127]). A 485 nm excitation creates an ample amount of both the S_1 and the ICT population (or, according to the current interpretation in ref. [127], it effectively excites the supposed "red" FX isomeric species that exhibit strong S_1/ICT coupling). IA in the 500–580 nm region (along with the intense ESA peak at 535 nm) is typically associated with the S_1 state, whereas the red wing IA shoulder at 600–750 nm and the SE in the NIR (> 780 nm) are normally attributed to the ICT state. The mutually coupled S_1/ICT species relax to the ground state with an average reciprocal rate of ca. 20 ps [127], albeit the well-averaged low-noise data from our PP measurements indicates that a certain residual IA lingers at the later stages of the photoevolution (see Figure 3.5(c)).

3.3.3.2 *Fucoxanthin Pump-Dump-Probe Dynamics*

The dump-induced effects to the regular FX photodynamics can be best apprehended by examining the kinetic behavior in specific parts of its TA spectrum. As the differences between the pre-dump and post-dump spectra in Figure 3.6 indicate, the 990 nm dump pulse incoming at 1.8 ps instigates SE of the radiative ICT state and causes a net decrease of the TA signal over the larger part of the entire spectral window. The dump-induced depopulation of ICT is best

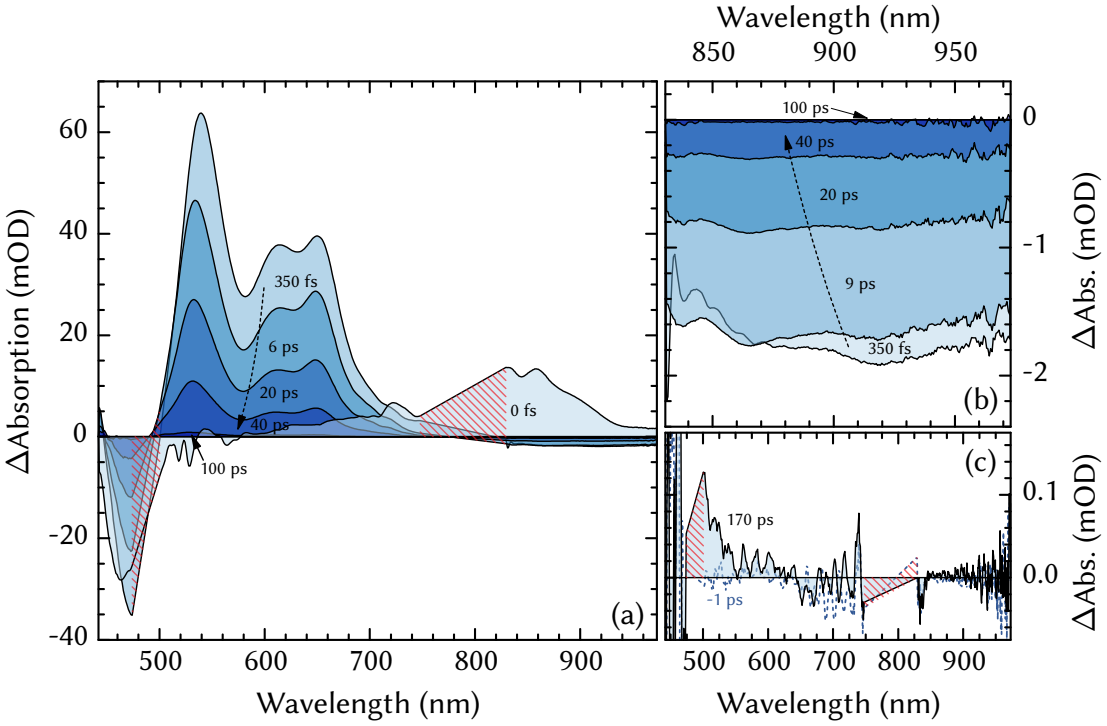

FIGURE 3.5: Dispersion-corrected time-resolved PP spectra of FX at different probe delay instances. The overall FX spectro-temporal development is depicted in panel (a); photoevolution of the NIR-based ICT SE signal is highlighted in panel (b) (note the omission of the 0 fs spectrum); the pre-pump (−1 ps) and the late (170 ps) time-gated spectra are accentuated in panel (c). Red dashed areas at 475–500 nm and 750–830 nm in panels (a) and (c) represent the spectral regions omitted due to scattering of, respectively, the pump (485 nm) and the WLSc seed (800 nm) pulses (the time-gated spectra in-between the spectral windows are connected by straight lines for better viewing).

highlighted by the instantaneous decline of the spectral amplitude in the short wave GSB segment (ca. 11 %, 470 nm traces in Figure 3.7(a)), the long-wave IA region (ca. 25 %, 625 nm traces in Figure 3.7(e)), and SE fragment in the NIR (ca. 40 %, see the 945 nm traces in Figure 3.7(f)).[2] Since only the ICT is predominantly active in the NIR region [127], we can assume that latter fraction of its population is diminished under the given experimental conditions.

Disregarding the general decrease in amplitude, TA in the blue-most boundary (< 480 nm in Figure 3.6 and 470 nm traces in Figure 3.7(a)) does not ex-

2 Percentages here and further in the chapter denote the maximal difference between the PP and PDP signals, achieved within the ca. 140 fs cross-correlation period between the dump and probe pulses.

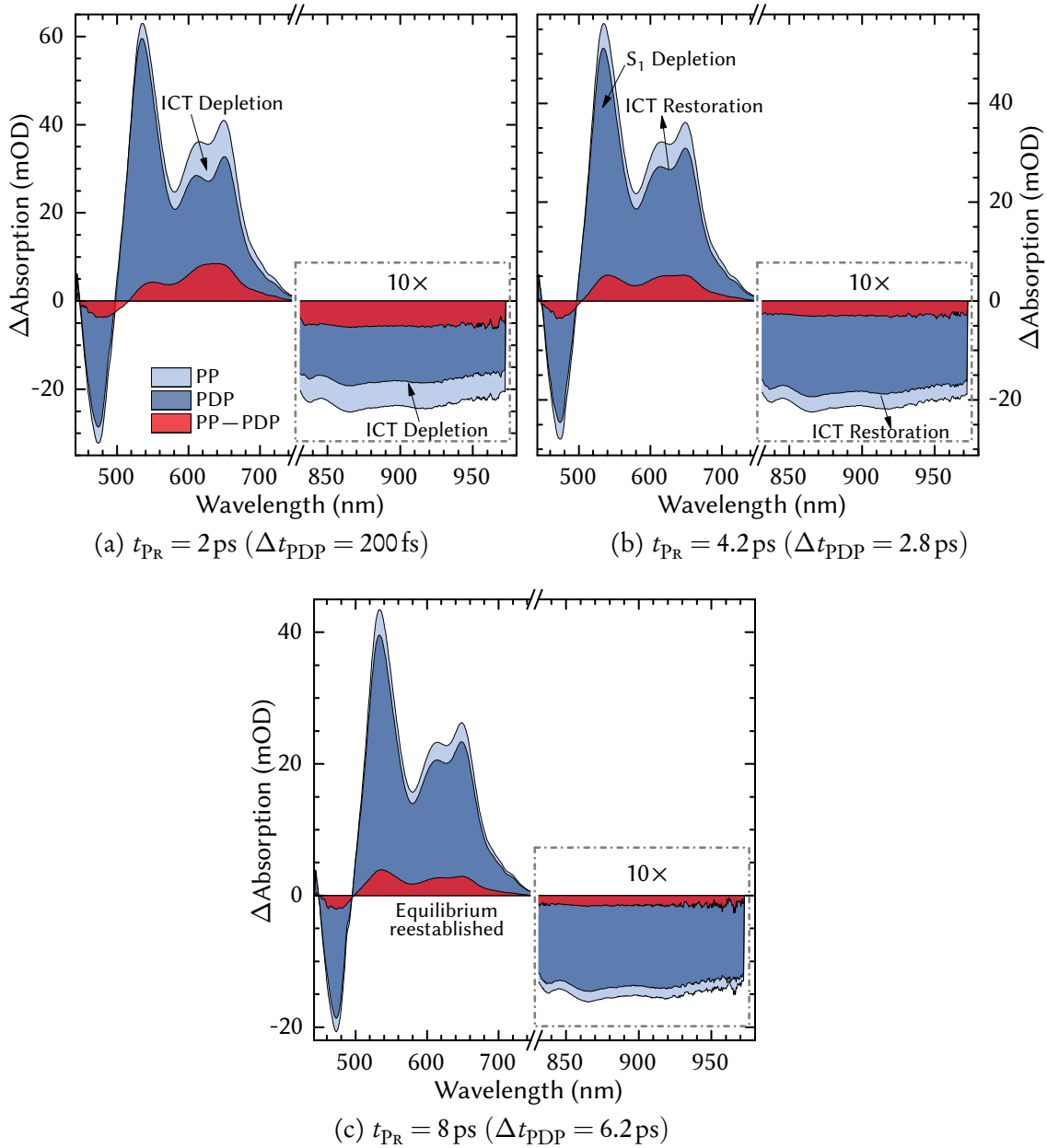

(a) $t_{P_R} = 2\,\text{ps}$ ($\Delta t_{PDP} = 200\,\text{fs}$) (b) $t_{P_R} = 4.2\,\text{ps}$ ($\Delta t_{PDP} = 2.8\,\text{ps}$)

(c) $t_{P_R} = 8\,\text{ps}$ ($\Delta t_{PDP} = 6.2\,\text{ps}$)

FIGURE 3.6: Time-resolved PP (cyan), PDP (blue), and their difference (red) spectra at three different probe delay instances (numbers in the parentheses indicate the amount of time elapsed after the introduction of the dump pulse). The SE signals on the lower right-hand side of the panels are scaled ten times for better viewing. The entire time- and wavelength-resolved development of the ΔΔOD signal is presented in Figure A.4.

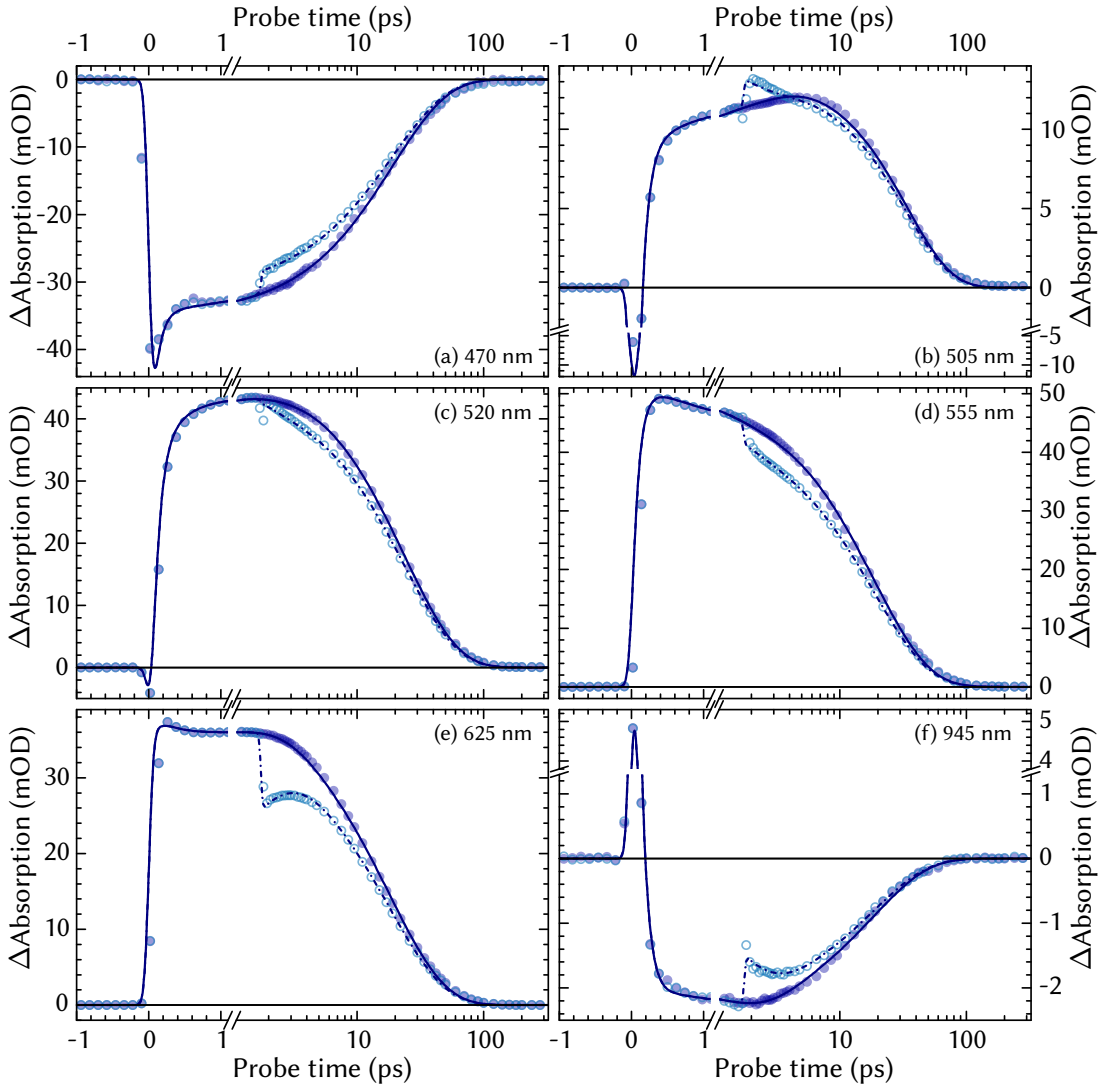

FIGURE 3.7: Spectrally-resolved PP (full symbols) and PDP (hollow symbols) kinetic traces at different probe wavelengths (every second experimentally-resolved point is omitted from the graphs for better viewing). Continuous solid and dashed-dotted curves represent, respectively, the results of global analysis fitting on the PP and the PDP data according to model given in Figure 3.10(b). Note that the PP and the PDP signals coincide prior to arrival of the dump pulse at 1.8 ps. Breaks are included in the ordinate axes of panels (b) (from —4.5 to —2.5 mOD) and (f) (from 1.5 to 3.5 mOD) for a better viewing.

hibit any atypical behavior following the induced stimulation of the ICT state. The post-dump GSB signals demonstrate a steady bleach recovery of the now depopulated molecular species, thus implying that the intermediate states that come into play after the perturbation of the ICT are not prominently active in the high-frequency boundary of the experimental window.

TA in the long-wave spectral region (> 600 nm in Figure 3.6), on the other hand, exhibits a significant signal recovery in the course of ca. 5 ps succeeding the arrival of the dump pulse. The transient signal regrowth is exhibited both by the IA in the long-wave VIS (625 nm traces in Figure 3.7(e)) and the SE in the NIR (945 nm traces in Figure 3.7(f)), thereby disclosing that the characteristic low-frequency "residing" intermediates are effectively repopulated within the sub-5-picosecond temporal window.

The post-dump behavior is partly different in the spectral proximity of the main IA peak (Figure 3.7(c)). Herein we do not observe a clear-cut IRF-limited loss of the signal amplitude after the arrival of the dump pulse. The PDP transient signals in the spectral vicinity of ca. 520–540 nm steadily decrease (see how the double difference absorption ($\Delta\Delta$OD) signal grows from Figure 3.6(a) to Figure 3.6(b), also refer to Figure A.4) after the temporal separation of the dump and the probe pulses, until attaining a stable, PP-like decay in the course of several picoseconds. It is evident from both the post-dump kinetic traces in Figure 3.7 and the time-gated PP and PDP transient spectra in Figure 3.6 that the loss of IA at ca. 520–540 nm counterbalances the gain of both the IA and SE in the long-wave limit of the TA spectrum and persists until the excited state equilibrium is restored (Figures 3.6(c) and A.4).

The ultrafast induced emission of ICT also provokes a peculiar spectral behavior in the blue/green part of the spectrum. As the 505 nm kinetic traces in Figure 3.7(b) indicate, the dump-triggered depopulation of ICT causes an instantaneous increase of the IA signal. Moreover, amplitudes of the post-dump transient signals even surpass the eventual IA maxima that are ultimately reached at ca. 10 ps in the ordinary PP photoevolution (solid curves and full symbols in Figure 3.7(b)). Additionally, relaxation towards the main molecular ground state in this particular spectral window becomes more rapid after the induced depopulation of ICT (see how the PP and PDP kinetic curves intersect at ca. 4 ps in Figure 3.7(b)).[3] These observations suggest that the dump pulse evokes a state, whose spectral signatures in the PP data are obscured by the intense 535 nm ESA peak. This notion, as hinted in the PP overview, becomes particularly clear upon closer examination of the high signal-to-noise ΔOD data in Figure 3.5. The late IA signals at 500–520 nm are not entirely

3 It should also be noted that the time needed for PDP decay to eventually "catch up" with PP decay is 2–3 times longer than the one observed in the abovementioned regions.

zero (see Figure 3.5(c); a pre-pump spectrum is provided to indicate that the particular TA signals do not stem from scattering artifacts). These PP and PDP data confirm the presence of state that arises on the ground state PES in the later stages of the FX photoevolution (which can be anticipated, seeing as the NIR SE signal—and a greater portion of the VIS-based ESA, for that matter—is absent in Figure 3.5(c)).

3.3.3.3 *Fucoxanthin Pump-Dump Action Trace Dynamics*

Results of the FX PDAT measurements are presented in Figure 3.8 (note that herein we only demonstrate the ΔΔOD data, as the PP signals in the particular measurement remain constant throughout the entire dump delay time). Three major development steps can be deduced from the graphs in Figure 3.8. Firstly, we can see that the transient ΔΔOD signals do not appear immediately after the S_2 excitation at $t = 0$ ps. Essentially, all the PDATs in Figure 3.8(b) experience a slow ascent of the ΔΔOD signal that is temporally comparable to the IRF of the measurement (ca. 130 fs). After the sub-picosecond rise the kinetic signals "saturate" throughout the entire measurement

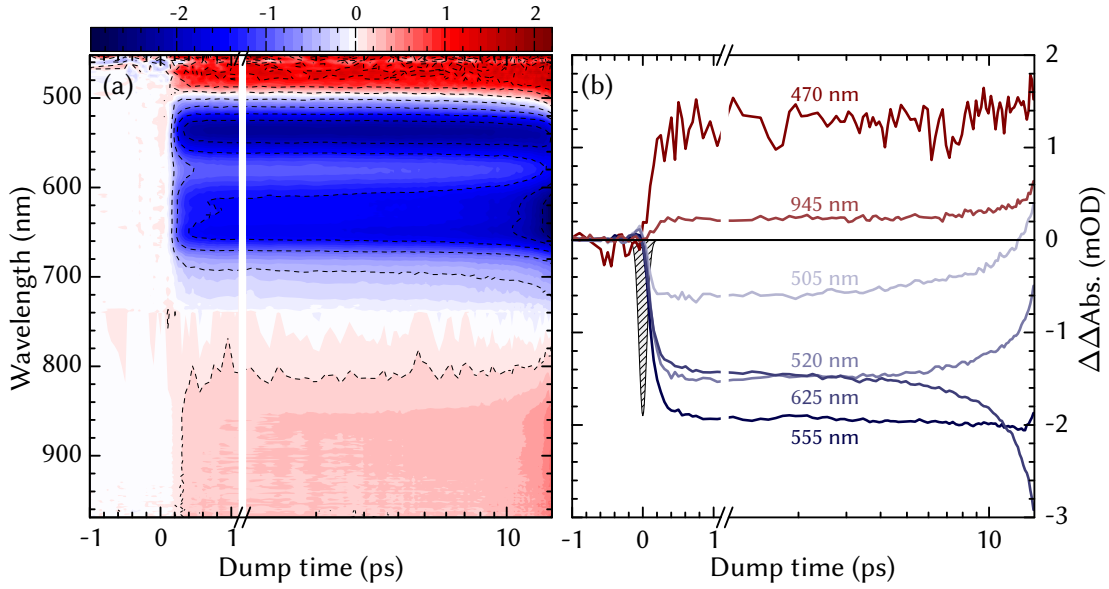

FIGURE 3.8: Experimentally-resolved FX PDAT ΔΔOD data measured at $t_{PR} = 15$ ps after the $S_0 \rightarrow S_2$ excitation. Panel (a) depict the entire spectrally- and temporally-resolved PDAT datamap, while panel (b) depicts several selected spectral cuts of the said dataset (note that the PDATs are at the same wavelengths as the kinetic PP/PDP traces in Figure 3.7). The (inverted) Gaussian curve at $t_{DU} = 0$ ps in panel (b) illustrates the approximate IRF of the measurement (refer to the main text for more details).

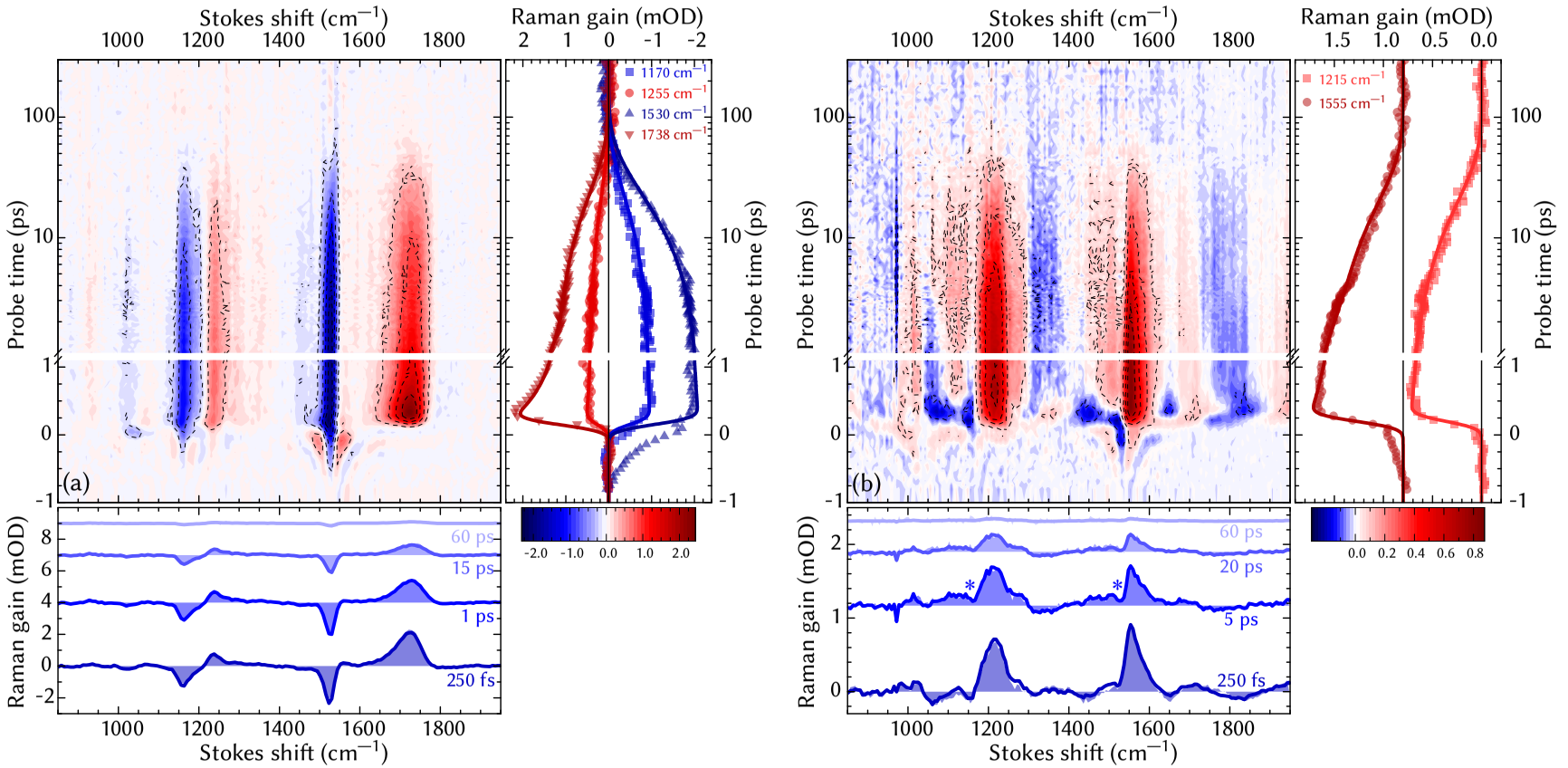

FIGURE 3.9: FSRS spectra of FX, obtained by exploiting either the (a) $S_1 \rightarrow S_n$ (λ_{RP} =550 nm) or the (b) ICT $\rightarrow S_n$ (λ_{RP} = 615nm) excited state Raman resonances. The entire experimentally-resolved and background-corrected FSRS signals are presented in the central graphs, whereas the right-hand side and bottom graphs depict, accordingly, spectral and temporal cuts of the spectro-temporal dataset (note that the temporal cuts (as well as spectral cuts in panel (b)) are offset from the zero line for better viewing). Experimentally-resolved points are presented in discrete symbols and area-filled curves, while the continuous lines in all of the graphs represent results of a two component global fit of the experimental data.

window, i.e., very little spectral development occurs for the remaining 4–5 ps. This indicated that from the "remote" reference time frame of $t_{PR} = 15$ ps an equilibrium has already been established. Following the monotonous signal behavior at $t_{DU} = 1$–5 ps, we eventually begin to see an overall intensification of spectral dynamics. Spectral development at $t_{DU} = 5$–10 ps essentially mirrors that of Figure 3.7. In the PDAT case, however, the ΔΔOD traces are flipped in time, as the temporal difference between the dump and the probe pulses decreases with increasing dump delay time (see Figure 2.2). In Figure 3.8(b) we can see with more clarity that the dump pulse has a kinetically equivalent, yet differently directed, effect on the 520 nm and 625 nm PDATs. The 470 nm and 555 nm PDATs show very little dependence on the dump delay. In contrast, the PDAT at 505 nm shows a clear change of the ΔΔOD signal sign from negative to positive at $t_{DU} \approx 12.8$ ps (i.e., ca. 2.2 ps before the probe).

3.3.3.4 *Fucoxanthin FSRS Dynamics*

The full time- and wavenumber-resolved maps of the FX FSRS photodynamics, along with selected spectral and temporal cuts, are presented in Figure 3.9. At first glance, the FSRS dynamics of FX share a lot of similarities to those of β-carotene (refs. [43, 46, 47] and Section 3.2) as well as some other carotenoids [136, 137]. Since the 550 nm Raman pump lies close to the FX ground state Raman resonance $S_0 \rightarrow S_2$ (see Figure 3.4), the time-resolved FSRS spectra in Figure 3.9(a) exhibit a substantial amount of GSB, as evident by the negative signals at 1170 cm^{-1} (depletion of the C–C stretching mode [138, 139]) and 1530 cm^{-1} (depletion of the C=C stretching mode [138, 139]) that appear directly after the actinic excitation and persist throughout the entire photoevolution. Minute traces of the ca. 1005 cm^{-1} carbon-methyl stretching mode [138, 139] bleach are also discernible in the contour datamap, albeit they are mostly obscured by the low frequency shoulder of the near lying intense 1030 cm^{-1} MeOH C–O stretching band yielding this observation unreliable [92]. The most prominent positive FSRS signals emerge at ca. 1250 and 1735 cm^{-1}. Throughout the entire photodynamics the 1250 cm^{-1} peak exhibits a dispersive shape due to its close proximity to the 1170 cm^{-1} S_0 C–C bleaching band. Similarly to β-carotene [43, 46, 47], this energy upshifted (ca. 75 cm^{-1}) peak can be attributed to the S_1 C–C vibrations. The intense 1735 cm^{-1} Raman band can be, in a similar fashion, designated as the S_1 C=C stretching vibrations [43, 46, 47].

The 615 nm Raman pump experiments, on the other hand, show different results. Firstly, the FSRS gain is weaker, notwithstanding an effectively similar

excited state yield (see Figure 3.4) and a more intense (ca. 3×) Raman pump. Moreover, the vibrational GSB signals are less prominent in the FSRS spectra and surface only as spectrally-burned dips in the vicinity of the main spectral maxima (indicated by asterisks in Figure 3.9(b)). In the ICT → S_n resonance experiments the main FSRS gain bands peak at ca. 1215 and 1555 cm^{-1}. Acknowledging the $S_1 \rightarrow S_n$ Raman resonance experiments, the 1215 cm^{-1} band can be attributed to the C–C vibrations within the ICT state (the lesser influence of the bleaching signal at 1170 cm^{-1} allows as to trace the position of this peak more precisely). It should be emphasized that the absence of any distinguishable FSRS gain signal at ca. 1735 cm^{-1} in Figure 3.9(b) (which generally is the most intense FSRS mode of the carotenoid S_1 state [43, 47, 88, 136, 137, 140]) suggests that the C–C vibrations herein belong exclusively to the ICT (and not the S_1) state. The 1555 cm^{-1} band lies near the ground state C=C vibrational mode and, most likely, represents the C=C vibrations of the ICT state. The equienergetic vibrations on the S_1 surface are either significantly weaker or are entirely absent (a small positive signal at energies slightly above the C=C bleach can, perhaps, be acknowledged in the early time-gated FSRS spectra in Figure 3.9(a), but it is too low to make any meaningful conclusions). This ascription is also corroborated by a recent time-resolved IR study on peridinin [140], where a similar C=C vibration was observed in an ICT-favoring environment (although our experiments did not detect any higher frequency—ca. 1600 cm^{-1} [140]—ICT-indicative modes in FX).

3.3.4 *Discussion*

The PDP/PDAT experiments clearly indicate that:

1. The excitation-created S_2 decays with a sub-200-femtosecond reciprocal rate to create the primary FX excited state species ICT and S_1. The population of S_2 is split parallelly between S_1 and ICT, i.e., the two states are not conceived in a step-wise manner, as suggested by the temporally even signal rise throughout the entire PDAT spectrum in Figure 3.8);

2. The low-frequency-residing ICT and the high-frequency-residing S_1 species interact in the FX excited state manifold and are strongly coupled to one another;

3. Equilibrium between the two interacting states is reestablished very rapidly (i.e., in the course of several picoseconds) via "funneling" of the excited state population from the high-lying S_1 to the low-lying ICT state [125, 127, 129].

4. Relaxation to the global ground state S_0 is indirect and involves an appearance of a transient on the molecular ground state potential surface.

Based on the presented PP and the PDP/PDAT data, the current knowledge of the FX ultrafast dynamics [122, 126–128], and the photophysics of a related carotenoid peridinin, also containing a carbonyl group [131, 132], we can assemble a comprehensive picture of the FX photodynamics.

The branched evolutionary scheme, summarizing our interpretation of the FX photodynamics, is presented in Figure 3.10(b). The SADS of the intermediate states, along with their appropriate time-dependent concentrations and the reciprocal state-to-state population transfer rates, are given in, respectively, Figures 3.10(a) and 3.10(c) and Table 3.1. The results of the global analysis approximation are shown as solid curves in Figure 3.7. The evolutionary model can be summarized as follows. The 485 nm femtosecond pulse promotes FX to the short lived (ca. 80 fs) state S_2. The SADS of S_2 features a broad IA plateau in the NIR (peaking at ca. 865 nm) and some predictable S_2 SE at 560 nm (that can be traced by the minute negative ΔOD signals such as the small dip at $t \approx 0$ ps in Figure 3.6(c)). Since S_2 is a short-lived state and the $S_2 \rightarrow S_0$ fluorescent decay yield is generally small [141, 142], the ground relaxation pathway $S_2 \rightarrow S_0$ can be omitted from the photoevolutionary scheme for simplicity's sake. S_2 is swiftly depopulated via a branched relaxation channel to a pair of vibrationally hot states S_1^* and ICT* with the reciprocal rates of $\tau_{S_2 \rightarrow S_1^*} = 120$ fs and $\tau_{S_2 \rightarrow ICT^*} = 410$ fs (or, specifically, the population is split $\sim 75/25$ between S_1^*/ICT*).

Vibrationally unrelaxed intermediate species are often observed in carotenoid femtosecond photodynamics [143, 144]. Inclusion of vibrationally hot precursors of both the ICT and S_1 states was found to be obligatory to appropriately approximate the sub-picosecond FX PP/PDP data. This inclusion is reasonably justified by the marginal spectral differences between the initial vibrationally hot and the consecutive vibrationally relaxed states and the fast dynamic components observed in the FSRS spectra. The S_1^*/S_1 and ICT*/ICT SADS in Figure 3.10(a) clearly illustrate tendencies associable with vibrational cooling in the excited state manifold, such as blue-shifting of IA and red-shifting of the SE spectral maxima, band narrowing, formation of sharper vibrational features within the IA bands, and an overall attainment of a more well-defined spectral shape. Vibrational relaxation of the hot intermediates S_1^* and ICT* succeeds with the reciprocal rates of, accordingly, 0.51 ps and 1.25 ps (latter of which agrees well with the previous predictions in ref. [126]) and leads to the formation of the final excited state products ICT and S_1.

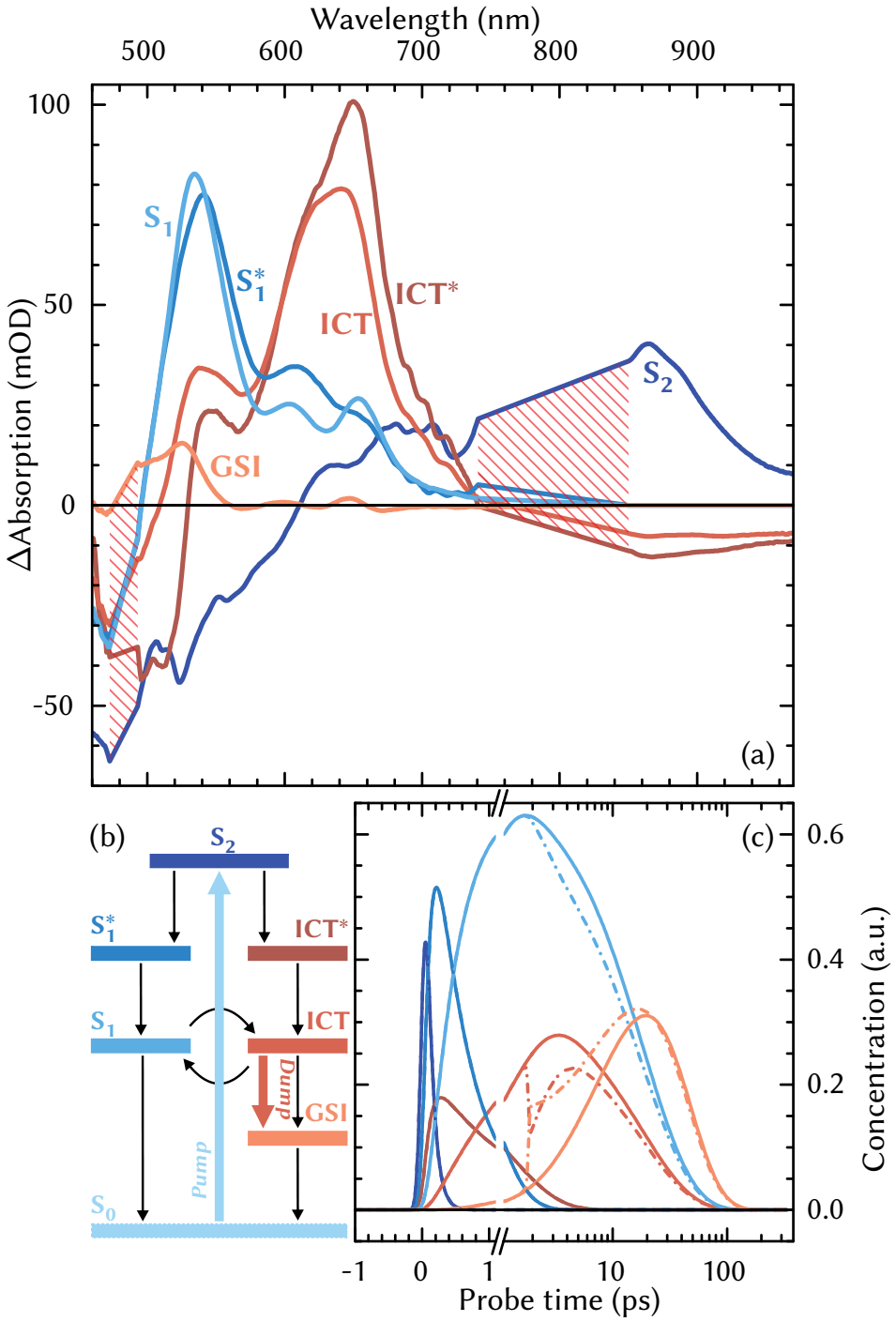

FIGURE 3.10: SADS of the FX PP/PDP photoevolution (panel (a)) obtained from global analysis fitting according to the connectivity scheme in panel (b). Panel (c) depicts the temporal dependence of the transient state population, i.e., $c_i^{\mathrm{PP}}(t)$ and $c_i^{\mathrm{PDP}}(t)$ from Equations (2.24) to (2.27) (solid curves: PP data, dashed-dotted curves: PDP data). The population transfer rates are given in Table 3.1. Dashed areas in panel (a) represent the omitted spectral regions (SADS in-between the spectral windows are connected by straight lines for better viewing).

Evolutionary Stage	Transition	Reciprocal rate (ps)
Depopulation of the photoexcited S_2	$S_2 \rightarrow S_1^*$	0.12
	$S_2 \rightarrow ICT^*$	0.40
Vibrational relaxation within the S_1/ICT manifold	$S_1^* \rightarrow S_1$	0.51
	$ICT^* \rightarrow ICT$	1.25
Interstate coupling	$S_1 \rightarrow ICT$	2.4
	$ICT \rightarrow S_1$	4.1
Relaxation to the molecular ground state	$S_1 \rightarrow S_0$	75
	$ICT \rightarrow GSI$	6.8
	$GSI \rightarrow S_0$	20

Table 3.1: Population transfer rates between the intermediary states (i.e., state lifetimes) obtained from the global analysis fitting of the PP/PDP data according to the connectivity scheme in Figure 3.10(b). A 40 % ICT dumping efficiency was assumed in the fitting procedure (see Figure 3.10(c)).

The SADS of S_1 primarily peaks at 535 nm. In addition, it possesses a less intense, red-wards extending spectral shoulder that bears a pair of spectral bands at ca. 600 nm and 650 nm. While subjection of these two low-frequency bands to the S_1 state was hinted by the previous FX time-resolved measurements [126], global analysis of the mutual PP/PDP data confirms that S_1 is partly responsible for the IA in the red part of the TA spectrum. The ICT state predominantly peaks at 625 nm. The main spectral band of the ICT SADS has a seemingly inhomogeneous outline that is likely comprised of several near-lying peaks. Moreover, the SADS of the ICT spreads to the higher-frequency region and reveals a lower amplitude spectral band surfacing at ca. 540 nm. It should be emphasized that spectral shapes of the S_1 and ICT SADS in Figure 3.10(a) are notably different from the ones obtained previously, where S_1/ICT interaction was not taken into account [126]. The S_1/ICT reciprocation in Figure 3.10(a)—namely, the appearance of S_1 features in the red wing ($>$ 580 nm) and ICT features in the blue wing ($<$ 580 nm) of the TA spectrum—can only be qualitatively resolved from the PDP (and not solely PP [126, 128]) measurements. As it has been addressed previously, spectral traits that primarily define the ICT surface in the long-wave limit of the TA spectrum (considering that in this spectral margin we observe a

direct dump-induced loss and a sub-5-picosecond recovery of the TA signal), whereas the S_1-defining features are concentrated at ca. 520–540 nm (seeing that in the particular spectral window we observe a population influx from S_1 to ICT that persists until an equilibrium between the states is reestablished). The range where the two states interconnect—i.e., ca. 540–580 nm, as distinguished by the SADS in Figure 3.10(a)—contains a reasonable contribution from both excited state species, thus elucidating why the 555 nm PDP traces in Figure 3.7(d) do not show an obvious gain or loss tendency (as opposed to ones exemplified in the neighboring regions). Due to this spectral co-occurrence the 555 nm traces are more reminiscent of those of the GSB signals seen in Figure 3.7(a).

It should also be addressed that the experimental PDP data indicate that the dump pulse interacts purely with the ICT state. It has been previously demonstrated that FX $S_1 \rightarrow S_2$ ESA lies in the NIR and spans over the spectral breadth of the utilized $\lambda_0 = 990$ nm dump pulse [130]. Nonetheless, repopulation of S_2 is negligible—SE to the ground state by and large appears to be the "preferred" evolutionary pathway of the perturbed molecular system. This notion is best corroborated by the fact that dumping does not promote the reappearance the S_2 spectro-temporal features in the PDP photoevolution. Most specifically, we observe neither a resurgence of the intense IA in the red/NIR part of the spectral window (Figure 3.6), nor an appearance of a spectral transient with the characteristic S_2 lifetime of ca. 90 fs (Figure 3.7). Moreover, a dump pulse-induced repopulation of S_2 would implicitly cause a repopulation of S_1, since $S_2 \rightarrow S_1^* \rightarrow S_1$ is one of the two chief S_2 relaxation pathways. Such sub-picosecond photodynamics are not observed in the PDP data. On the contrary, the S_1 ESA constantly decreases after the dumping (Figure 3.7(c)), thus indicating that S_1 is not "replenished", and yet is rather forced to repopulate the depleted ICT.

The S_1/ICT population equilibration rates can also be obtained only from the complete set of PP/PDP data. Global analysis calculations estimate the reciprocal transfer rates to be $\tau_{S_1 \rightarrow ICT} = 2.4$ ps and $\tau_{ICT \rightarrow S_1} = 4.1$ ps, thus inferring that the excited state population transfer is directed towards the ICT. This, in turn, indicates that presence of the interstate equilibrium "short-circuits" the regular S_1 relaxation channel $S_1 \rightarrow S_0$, forcing the S_1 to be mainly depopulated via dissipation to the strongly-coupled ICT. Since "leakage" of S_1 is relatively fast ($\Delta\tau = (\tau_{ICT \rightarrow S_1}^{-1} - \tau_{S_1 \rightarrow ICT}^{-1})^{-1} \approx 5.8$ ps), the lifetime of S_1 must be sufficiently long for it to be discernible throughout the greater part of the photoevolution, as perceived in Figure 3.5(a) (i.e., much longer than previously assessed < 20 ps [122, 126–128]). The natural lifetime of S_1 was estimated to be 75 ps. This is a relatively close proximate (albeit not an

exact match) to the 62 ps lifetime of the FX S_1 in nonpolar environments, evaluated both experimentally [122, 130] and estimated numerically via the energy gap law [129]. We believe that the discrepancy between the relaxation rates in the polar/nonpolar environments might stem from the slight intrinsic S_1 lifetime dependence on the solvent (and, in turn, the polarity of the environment), and also other factors, such as the environment-dependent S_1/S_0 displacement, coupling between the initial and final electronic states, and other possible deviations from the energy gap law, as indicated in ref. [122]. In general the branched photoevolution model is largely insensitive to variations of the S_1 lifetime parameter, and provides an equally good approximation of the experimental PP/PDP data, as long as it is kept sufficiently long (typically ≥ 70 ps). This is mostly instigated by the fact that S_1 acts as a "reservoir", and the excited state population is "funneled" via the ICT due to the interstate coupling. It should also be noted that an interstate equilibrium might also be present between the vibrational hot S_1^* and ICT* (which is indirectly implied by the constance of the PDATs in Figure 3.8). However, in our experiments dumping was performed at 1.8 ps, when the majority of the excited state population has already achieved vibrational equilibrium (see the concentrations in Figure 3.10(c)), and the interaction between the two short lived precursors cannot be judged adequately.

The ICT state is of highly polar nature and, as a result, can be stabilized by the polar environment of the solvent [123]. Due to this aspect, the ICT state in FX does not relax directly to S_0 (or its close vicinity), but does so via an intermediate state on the ground state potential surface—the so-called ground state intermediate (GSI), as illustrated in Figure 3.10(a); analogous effect was also observed in peridinin [131, 132]. The SADS of the FX GSI surfaces at 500–525 nm and bears negligible absorption in the remaining part of the TA spectrum. Appearance of this low spectral intensity state during the terminal stages of the photoevolution explains the somewhat slower development (see Figure A.4) and the residual positive signals (see Figures 3.5(c) and 3.8(b)) in the green/blue part of the TA spectrum. Interestingly, the FX GSI is significantly more stable than its counterpart in peridinin [131, 132]. Thermal re-equilibration rate of the FX GSI was estimated to be ca. 20 ps, which is almost an order of magnitude slower than the one distinguished in peridinin. These results imply that ICT is effectively stabilized both in the excited and ground state manifolds of FX.

To conclude the global analysis results of the PP/PDP/PDAT data, validity of the global model is also corroborated by the unvarying amplitude of the SADS in the GSB region. This aspect signifies a consistency between the SADS and their temporal concentrations. In other terms, the constant spec-

tral amplitude in the GSB region verifies the previous observations that no significant spectral development (apart from excited state population depletion) takes place in the bluest part of the spectral window.

Whilst PDP experiment provides direct insight into the kinetic behavior of photoexcited FX, FSRS results allow us to glean some information on the physical nature of these kinetic processes. Firstly, FSRS spectra obtained using different Raman pump wavelengths indicate that S_1 and ICT are two distinct vibronic species in the FX excited state manifold (which is an interesting outcome and a good illustrative example of the FSRS vibrational selectivity, considering that S_1 and ICT were previously identified having similar transient IR absorption features in the PCP complex [145]). The FSRS spectrum of S_1, with its characteristic high frequency 1735 cm^{-1} C=C peak and sharp vibrational GSB lines is reminiscent of the typical carotenoid S_1 vibrational spectra [43, 46, 47, 110]. The ICT FSRS spectrum, on the other hand, holds more resemblance to the FX S_0 Raman spectrum (refs. [138, 139]; also traceable by the GSB lines in Figure 3.9). The major difference between the S_0 and ICT vibrational spectra are the ca. 45 cm^{-1} and ca. 25 cm^{-1} energy upshifts (that can be interpreted as slight bond length protractions) exhibited by, respectively, the C–C and the C=C Raman bands.

As depicted in Figure 3.9, both the S_1 and the ICT share a common low-frequency C–C vibrational mode at ca. 1250 cm^{-1}. Despite its co-occurrence in both vibronic states, this vibrational mode is an unlikely coupling channel for the interstate equilibrium because of the potential energy offset between the S_1 and the ICT [122, 127]. Two-photon excitation experiments estimate the $S_0 \rightarrow S_1$ and $S_0 \rightarrow$ ICT gaps in FX to be 2.06 eV and 1.86 eV, respectively [122]. This, in turn, implies that the energetic difference between the two interacting states is ca. 1613 cm^{-1}. This rough estimate (since the transitional band shapes are not precisely known) is comparatively close to the 1555 cm^{-1} vibrational frequency, observed in the ICT FSRS spectrum in Figure 3.9(b) (especially considering that the particular vibrational band is wide and encompasses the said frequency). Therefore we suggest that the 1555 cm^{-1} C–C vibrational mode acts as a coupling channel for the S_1/ICT equilibrium. Generally speaking, we predict that the interstate coupling commences via internal conversion from the S_1 potential minimum to the C=C vibrational mode on ICT PES, ultimately ending in vibrational relaxation within the ICT vibronic manifold ($S_1(\nu_0) \rightarrow$ ICT(C=C) $\rightarrow$ ICT(ν_0), see Figure 3.11). The backwards coupling $S_1 \leftarrow$ ICT is also possible in this scheme. As the rates in Table 3.1 indicate, it is expectedly less efficient because it has to commence via the low-populated (and possibly worse coupled) vibrational modes on the ICT PES.

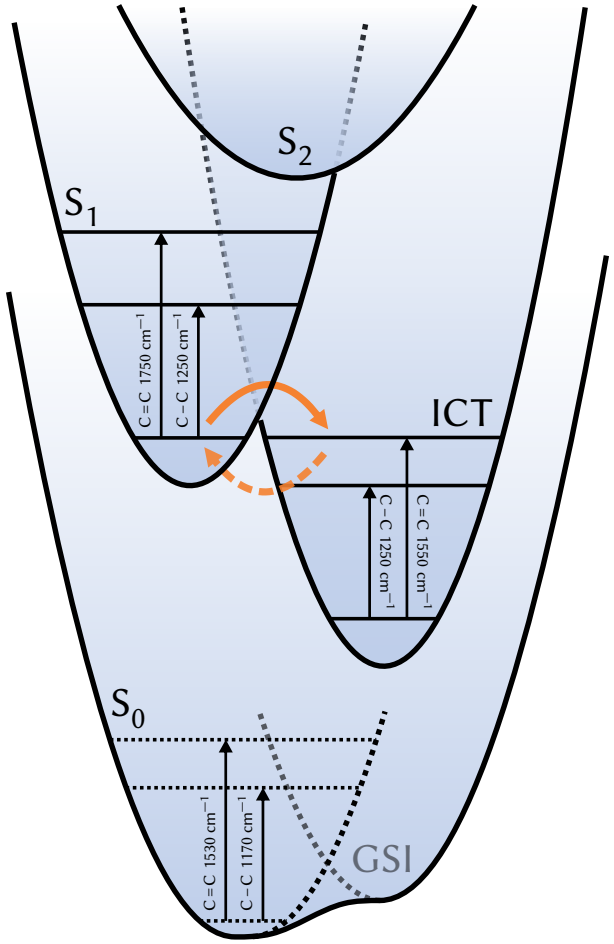

FIGURE 3.11: A simplified PES diagram, summarizing the FX PDP/PDAT and FSRS experiments. Solid arrow represents the strong (forward) $S_1 \rightarrow$ ICT coupling, whereas the dashed arrow represents the weaker (backwards) $S_1 \leftarrow$ ICT coupling (see Table 3.1 for details).

The time-resolved FX FSRS spectra (Figure 3.9) cannot be qualitatively fit to the interstate equilibrium model presented in Figure 3.10, because FSRS data is essentially one dimensional and, same as the standalone PP data, does not contain any explicit (kinetic) coupling information.[4] Moreover, the FSRS spectra, as demonstrated in Figure 3.9, are very species-specific, i.e., particular vibrational modes become active only upon proper resonant enhancement. Most significantly, the S_2 Raman lines are not observed in either of the FSRS spectra in Figure 3.9, since the $S_2 \rightarrow S_n$ resonance of FX lies in the NIR (see Figure 3.5). Analysis of the S_2 vibrational features in FX would require a NIR Raman pump (as was implemented on β-carotene in ref. [47] and Section 3.2),

4 Or rather, the fit would turn out good enough, just the SADS would be meaningless because of overparametrization.

which would, presumably, cause SE of the ICT state (essentially, producing a picosecond PDP) rather than FSRS gain from the S_2. In the best case scenario, we can expect to observe indirect FSRS signals, e.g., RINE in the same way as in bacteriorhodopsin [48].

Bearing the above-mentioned limitations in mind, we can fit the FSRS data to a simple sequential photoevolutionary model, solely to gain some quantitative information on the FX vibrational photodynamics. The entire S_1 FSRS dataset from Figure 3.9(a) was globally fit to a sequential two state model[5] with the lifetimes of 500 fs and 23 ps. The ICT $\rightarrow$ S_n resonance FSRS spectra from Figure 3.9(b) were fit to an analogous model with the lifetimes of 1 ps and 16 ps (results of both global fits are presented by continuous curves in Figure 3.9). The most remarkable outcome of the FSRS global fitting is the fact that the early (short) FSRS lifetimes coincide almost ideally with the dissipation rates of the hot intermediate states S_1^* and ICT* from Table 3.1. In view of the PP/PDP results, these early lifetimes of the FSRS dynamics can be designated to the collective process of S_2 decay (since S_2 features are absent in Figure 3.9) and the subsequent formation/relaxation of the vibrationally hot states (the vibrational cooling processes generally appear as the peak displacement/narrowing during the first few picoseconds in the FSRS datamaps—more apparent in Figure 3.9(a)). The longer (later) lifetimes from the FSRS global fits correspond to the depopulation of the equilibrated S_1/ICT manifold and the return to the ground state PES (the GSI is unlikely to appear in either of the FSRS spectra due to its low spectral intensity (see Figure 3.10(a)) and off-resonant Raman pumping (see Figure 3.4)). Setting aside the fact that existence of interstate coupling prevents an objective evaluation of S_1 and ICT lifetimes solely from the FSRS data, the resolved 23 ps and 16 ps coincide well with the already published results in refs. [122, 126, 128], that report the lifetime of the FX S_1 to be ca. 33 % longer than that of the ICT in a polar environment (i.e., when the $S_1 \leftrightarrow$ ICT coupling is not taken into account).

3.3.5 *Concluding Remarks*

We have applied multi-pulse time-resolved spectroscopic methods to investigate the excited state dynamics of marine carotenoid FX. PDP measurements indicate that an equilibrium exists between the two FX excited state species S_1 and ICT. This equilibrium is established with the average reciprocal rates of $\tau_{S_1 \rightarrow ICT} = 2.4$ ps and $\tau_{ICT \rightarrow S_1} = 4.1$ ps, and is thus restored on a sub-6-picosec-

5 Equations (2.20), (2.21) and (2.25).

ond timescale after an ultrafast SE is imposed upon the ICT. Furthermore, the PDP experiments indicate that ICT decays to a stabilized intermediate form on the molecular ground state PES (the so-called GSI), that is thermally re-equilibrated to S_0 with a reciprocal rate of ca. 20 ps. FSRS experiments show that S_1 and ICT are two vibrationally different species. The FX S_1 possesses a vibrational structure comparable to S_1 of many other carotenoids [43, 46, 47, 136], whereas the ICT bears a vibrational semblance to the FX S_0 [138, 139]. The ICT FSRS spectrum exhibits characteristic C=C vibrations at 1555 cm^{-1} that, based on the current understanding of the FX excited state structure [122], may act as a coupling channel for the $S_1 \longleftrightarrow$ ICT equilibrium.

Part IV

IN SEARCH OF THE INDOLOBENZOXAZINE PHOTOCHROMISM

The following part, most likely, deserves the biggest disclaimer. As it is not uncommon in most natural sciences, experimental results and theories are not treated as axioms and interpretations of physical processes change as new discoveries are made. For the author's discontent, a perceptive change on the indolobenzoxazine dynamics has transpired during the short preparation time of this thesis. Without trying to obscure all of our early assumptions, we have decided present both points of view. Chapter 4 is devoted to initial optical spectroscopic measurements of indolobenzoxazines, were the particular molecules where (unequivocally) assumed to be photochromic. All the interpretations of experimental data provided in this chapter are, therefore, based on this supposition. Chapter 5 presents a different take on the indolobenzoxazine photodynamics that was inspired by later experimental studies. This chapter outlines the electronic and vibrational experiments that intuitively back up this new knowledge and provide a fresh new take on their photodynamics.

4

ULTRAFAST ELECTRONIC KINETICS AND THEIR CONTROL IN INDOLOBENZOXAZINE SYSTEMS: THE RING-OPENING PRESUMPTION

4.1 THE PRINCIPLES AND CONCEPTS OF PHOTOCHROMISM

Chromism is a chemical process in which a physical perturbation evokes a color transformation of a molecular compound. Depending on the nature of the perturbation causing the color change we can discern electrochromic, thermochromic, piezochromic, solvatochromic, and many other *—chromic* processes [146]. Photochromism, as the name implies, is a reversible light-induced photochemical process, whereby a molecular compound can toggle between two (typically isomeric) chemical forms, defined by their distinctive absorption spectra [147–149]. Photochromism was first discovered and annotated in the mid-19th century [150], albeit a resurgence of interest in photochromic materials sparked only in the 1960's, prompted by numerous technical advances in organic synthesis and physical analysis methods. The introduction of photochemically stable spiropyrans and chromenes in the 1980's can be regarded as major breakthrough and a catalyst for further development in photochromic research [146]. The metastable nature of various photochromic materials, their fast response times, and numerous unique photosensitive abilities have gained a lot of interest in the fields of contemporary optoelectronics and photonics during the past couple of decades. Various types of photochrome-based molecular devices, ranging from molecular memory and logic elements [151–157] to optically controllable molecular switches, sensors, and limiters [153, 158–162], have been both envisioned theoretically and developed practically.

Most photochromic materials exhibit positive photochromism, i.e., they are transparent to VIS radiation and absorb mainly in the UV. The induced color change in a positively photochromic material prompts a transient appearance of absorption in the VIS–NIR. Negative photochromism—a light-induced absorption intensification in a shorter-wave domain—is also possible, albeit less common [146]. The change of color likewise causes changes of other

physical characteristics of the molecule, such as refractive index, dielectric permittivity, oxidation and reduction potentials, etc. [153].

Photochromism, on a structural level, may stem from a multitude of inter- and intra-molecular processes. Some of the more common photochromic mechanisms are depicted in Figure 4.1. These reaction can be classified as electrocyclic ring-opening or ring-closing reactions in spiropyrans, spirooxazines, and chromenes (Figures 4.1(a) to 4.1(c)), conformational *trans* → *cis* or *cis* → *trans* isomerization in stilbene- or azobenzene-type compounds (Figure 4.1(d)), inter-molecular proton or electron transfer in viologens or anils (Figure 4.1(e)), molecular dissociation processes in hydrazines or triarylmethanes (Figure 4.1(f)), etc. More information about the photophysics of photochromic processes can be found in refs. [146–149].

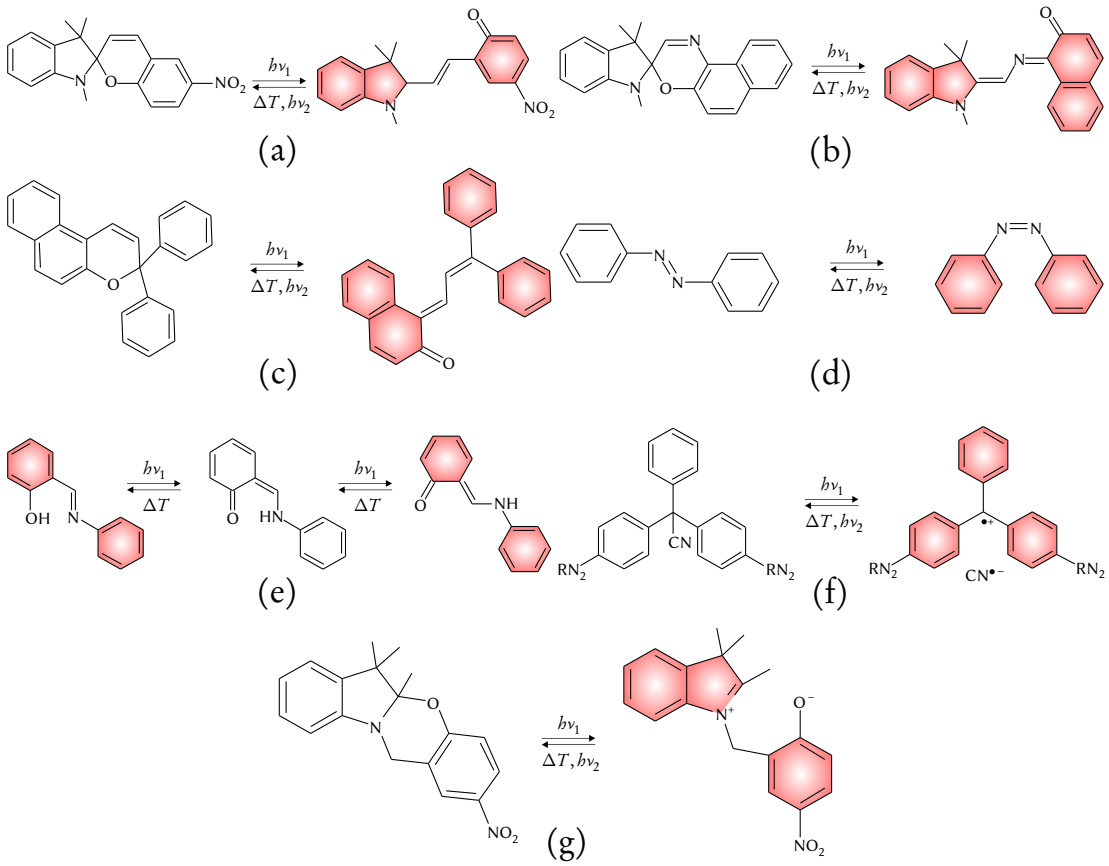

FIGURE 4.1: Photochromic reactions of (a) spiropyran, (b) spirooxazine, (c) chromene, (d) azobenzene, (e) anil, and (f) triarylmethane molecular compounds [146, 149]. Panel (g) depicts the alleged photochromic transformation of an (unsubstituted) indolo[2,1-*b*][1,3]benzoxazine [163–165]. $h\nu_1$ denotes the forward and $h\nu_2$ denotes the backward photochromic transformation ($h\nu_1 > h\nu_2$); ΔT denotes the intrinsic thermal "de-coloration".

4.2 THE PRIMARY ELECTRONIC KINETICS OF STRUCTURALLY-MODIFIED INDOLOBENZOXAZINES: FROM ABSORPTION OF A PHOTON TILL FORMATION OF THE PHOTOPRODUCT

4.2.1 *An Introduction to the Indolobenzoxazine Family: The Base Compound and Its Phenylic Derivatives*

A novel addition to the diverse family of photochromic compounds are the synthetic indolo[2,1-*b*][1,3]benzoxazines (IBs) (see Figure 4.1(g)) [164–169]. Being structurally similar to the well-explored and documented spiropyrans and spirooxazines (Figures 4.1(a) and 4.1(b)) [147–149, 170–175], IBs offer relatively good photochemical stability, as well as comparatively high molecular switching speeds. As illustrated in Figure 4.1(g), absorption of a UV photon in an IB molecular system initiates a C–O bond cleavage and a subsequent formation of two distinct chromophoric groups [164, 168]. A 3H-indolium (IND) cation, containing a conjugated electron system due to the formation of a π-bond between the indole nitrogen and the chiral carbon atom, and a 4-nitrophenolate (PNPHE) anion, typically exhibiting a pronounced absorption band in the short-wave VIS region (ca. 430 nm [168]), are formed within this photoreaction (Figure 4.1(g)). Eventually, the zwitterionic colored form reverts back to the closed [1,3]oxazine ring conformation via thermal relaxation in a span of a few tens of nanoseconds [164, 168, 176].

Time-resolved spectroscopic methods within the sub-microsecond temporal range have already been used in the past to analyze the photochromic behavior of the unsubstituted ("base") IB compound (Figure 4.1(g)) [164, 168, 176] and its various derivatives [165, 166]. For instance, a recent time-resolved FP study—concerning the late (i.e., nano-to-microsecond) dynamics of several structurally-altered IBs—has shed some new and intriguing insight on how phenylic substituents modify the photochromic behavior of the parent IB molecule [177]. While the widely-implemented sub-microsecond FP methods reveal some of the most practically important aspects of the IB photodynamics (namely, quantum yield, spectral constitution, and thermal back-switching rates of the terminal light-induced forms), they are not particularly informative with regard to the mechanisms behind the underlying molecular transformations. The primary photodynamic steps of the nanoseconds-spanning IB photoevolution, such as development of the photoinduced IB excited state, [1,3]oxazine ring-opening, and stabilization of the ring-opened chromophoric form in the solvent environment, occur on the femto-to-picosecond time scale, thus necessitating ultrafast spectroscopic techniques to adequately comprehend them. Very few studies concerning the femto-to-nanosecond spectral

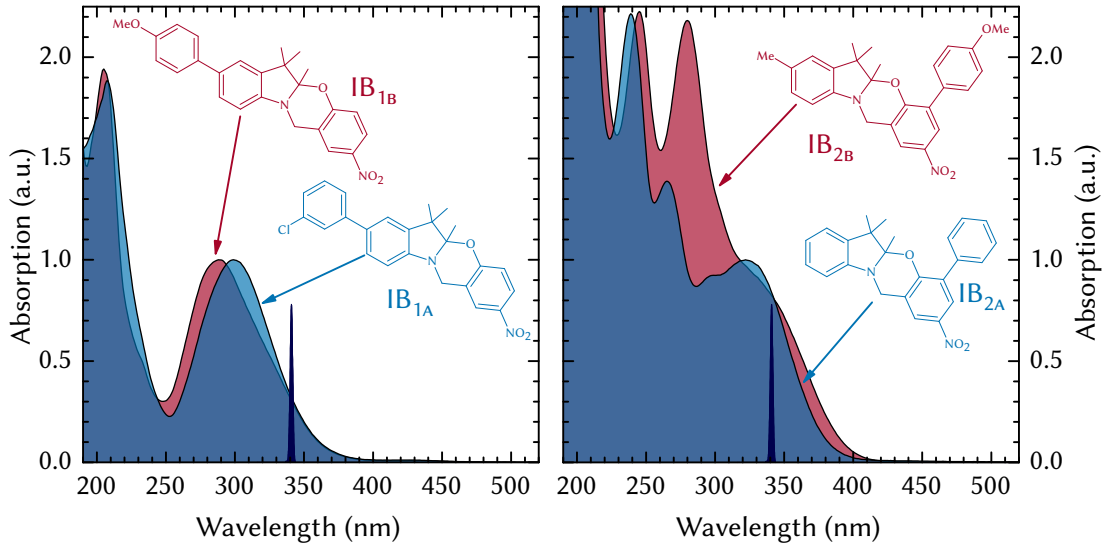

(a) GROUP I (b) GROUP II

FIGURE 4.2: Structural formulae of the investigated photochromic compounds and their steady-state absorption spectra in MECN. Each compound is composed of a parent IB molecule [164–169] with an additional 4-methoxyphenyl (IB_{1A}, IB_{2B}), 3-chlorophenyl (IB_{1B}), or phenyl (IB_{2A}) substituent attached to either indole or nitrophenol moiety. Spectrum of the excitation pulse of the main PP experiments ($\lambda_{PU} = 340$ nm, see Section 4.2.2.2 for details) is also shown in the graphs.

dynamics of IBs have been published so far and the detailed knowledge about the ultrafast pathways resulting in the IB photochromic transformations is still lacking. To address these issues, four compounds from the above-mentioned FP study in ref. [177] were selected for a more comprehensive femtosecond time-resolved examination. Based on an established classification [177] the compounds presented in this chapter are arranged into two groups according to the attachment site of the phenylic substituents. GROUP I compounds are modified at the *para* position relative to the nitrogen of the indole ring, while the representatives of GROUP II—in the *ortho* position relative to the oxygen atom of the 4-nitrophenol (PNPH) moiety. Structural formulae of the analyzed compounds are given in Figure 4.2 together with their steady-state absorption spectra. On the basis of global analysis of time-resolved PP data, in this chapter we propose a branched model of the IB excited state dynamics. To the best our knowledge, this is the first attempt to explain the complicated femtosecond dynamics of photochromic [1,3]oxazines, with a detailed mathematical analysis of the experimental data employed to define a nontrivial relaxation scheme.

4.2.2 *Materials and Methods*

4.2.2.1 *Sample Preparation*

Synthesis of the investigated compounds is reported in ref. [177]. For spectroscopic measurements polycrystalline IB samples were dissolved in acetonitrile (MeCN) (Sigma Aldrich LiChrosolv, gradient grade) and diluted to an OD of 1 at the necessary excitation wavelength in a 1 mm quartz cell (Starna Scientific).

4.2.2.2 *Femtosecond Resolution Pump-Probe Measurements*

For the particular set of TA experiments the Libra Ti:Sa system was operated in the 100 fs regime, generating 3.45 W of optical power at 1 kHz. The Topas-800 OPA was tuned to generate ca. 15 µJ energy ultrashort pulses centered at 340 nm (4^{th} harmonic of the signal wave). Excitation pulse energy for the experiments was set to, respectively, 600 nJ for Group I compounds and 800 nJ for Group II compounds (focal spot size of the pump beam at the sample plane was ca. 300 µm). This particular configuration was used for the main PP experiments, whereas the wavelength was adjusted from 305 nm to 345 nm for the excitation wavelength dependency measurements. WLSc generated in a mechanically translating 3 mm thick CaF_2 plate was used as the probe (focal spot size at the sample plane—ca. 80 µm). Polarizations of pump and probe beams were set at the "magic" angle (54.7°) in order to avoid rotational diffusion influence on TA signals. The PP experiments were performed back-to-back in two overlapping spectral windows (330–640 nm/430–740 nm) and the results of consecutive experiments were, after proper scaling, merged into a single continuous dataset. GVD of the probe pulse was estimated from the rising segments of the kinetic curves at each wavelength. The wavelength dependence of the mid-rise point within these segments was approximated by a polynomial function of the 4^{th} or 5^{th} degree and the polynomial parameters were further refined in the global fitting procedure. All the presented TA data are corrected for probe pulse GVD. The estimated IRF of the experiments was about 180 fs.

4.2.3 *Experimental Results*

4.2.3.1 *Time-Resolved Spectroscopic Study of Group I*

Steady-state UV-to-VIS absorption spectra of Group I compounds are generally similar and feature two distinct bands: a broad long-wave absorption band,

positioned at either 290 nm (IB_{1A}) or 300 nm (IB_{1B}), and an intense MidUV absorption band peaking at ca. 205 nm (see Figure 4.2(a)). The 340 nm excitation is resonant with the far red-wing of the red-most absorption band and, thereby, is likely to promote the molecule to its lowest excited state.

The femtosecond TA dynamics observed in the photochromic compounds of Group I is presented in Figure 4.3. Both compounds exhibit similar dynamic features in their corresponding time-gated spectra. Immediately after the UV excitation, a wide IA plateau is formed, covering almost the entire NUV-to-NIR spectral range and enclosing three distinguishable spectral maxima: a narrow and intense short-wave band, a smoother mid-wave crest and a wide, relatively intense spectral band in the long-wave spectral domain (see the 400 fs and 300 fs ΔOD spectra in Figures 4.3(c) and 4.3(f)). For compound IB_{1A} the first two bands are positioned at 380 nm and 510 nm, whereas the red-most band peaks at around 615 nm. The high frequency peak of IB_{1B} is slightly red-shifted in comparison to IB_{1A} and lies at around 415 nm, while its central spectral crest retains its position at ca. 510 nm, and the broad long-wave maximum peaks beyond 730 nm. This particular compound also exhibits a minute trace of GSB in the blue-most edge of the spectral window (the rapid swing of the ΔOD signal during the first few hundred femtoseconds—the dark blue dips in Figures 4.4(a) and 4.4(d)—is caused by either the coherent interaction between the pump and probe pulses [28–30] or pump-induced SRS by the solvent [92]). Within the first few picoseconds after the excitation, the initial signal decays swiftly and a global minimum of IA signal is reached at ca. 3 ps (see the 2–3 ps ΔOD spectra in Figures 4.3(c) and 4.3(f)). During this phase, the major spectral peaks retain their relative initial positions. Subsequently, as the delay between pump and probe pulses exceeds 3 ps, prominent changes occur in the TA spectra. During the following 10 ps, a significant growth of the spectral amplitude, accompanied by a slight blue-shift of all bands, is observed throughout almost the entire spectral range. This spectral relocation is more pronounced for compound IB_{1A}, where the initial blue-most spectral peak shifts towards 375 nm, the red-most peak moves towards 610–620 nm, and their IA spectra become significantly more structured. A corresponding early blue-shift for IB_{1B} is seen more clearly for the 415 nm spectral peak, which starts increasing within the first 10 ps, followed by a minor blue shift towards 410 nm. A strong increase of IA is observed in both the short- and the long-wave sides of the spectrum (the GSB signal of IB_{1B} is gradually transformed into UV-based IA, growing concomitantly with the blue-most band), whereas the decay of the signal continues (or, at least, the rise is much less pronounced) in the central part (ca. 450–550 nm) of the spectral window. The central spectral crest from the primary TA spectrum continues to decay and

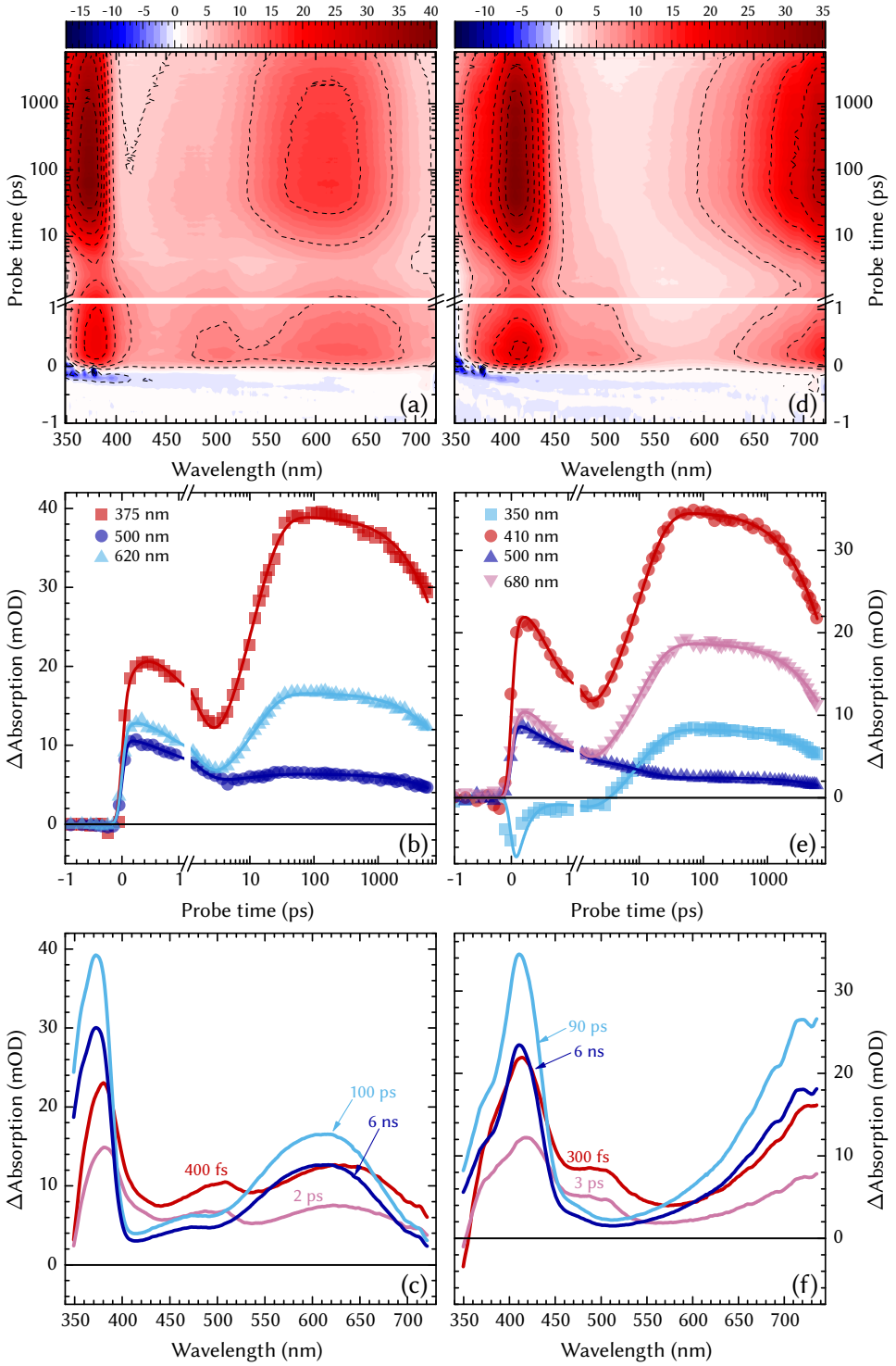

FIGURE 4.3: PP dynamics of GROUP I photochromic compounds IB_{1A} ((a) to (c)) and IB_{1B} ((d) to (f)). Panels (a) and (d): overview of the entire TA dataset; panels (b) and (e): kinetic traces at selected wavelengths—experimental points are depicted by solid symbols (every 2nd point is omitted for clarity) and continuous curves represent the results of global analysis fitting; panels (c) and (f): ΔOD spectra at selected delay times.

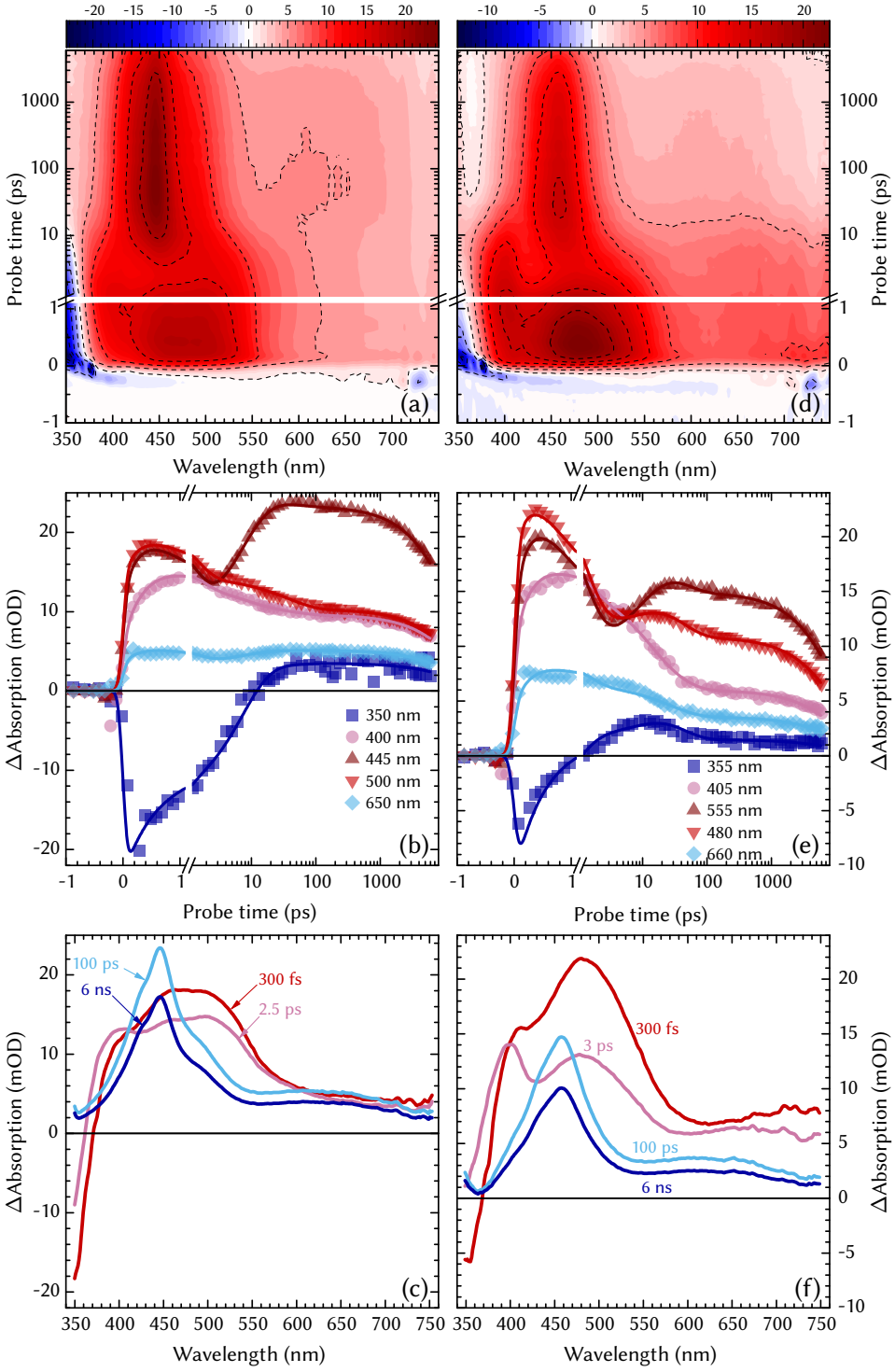

FIGURE 4.4: PP dynamics of GROUP II photochromic compounds IB_{2A} ((a) to (c)) and IB_{2B} ((d) to (f)). Panels (a) and (d): overview of the entire TA dataset; panels (b) and (e): kinetic traces at selected wavelengths—experimental points are depicted by solid symbols (every 2nd point is omitted for clarity) and continuous curves represent the results of global analysis fitting; panels (c) and (f): ΔOD spectra at selected delay times.

becomes almost indistinguishable within the following 10 ps (500 nm trace in Figure 4.3(b)). Spectral development is less discernible in the long-wave spectral edge of IB_{1B} (mostly due to the more prominent self-phase modulation and the lack of dynamic range near the prevalent WLSc pump central wavelength), however, sub-microsecond TA measurements show that the NIR band eventually peaks at ca. 750 nm [177]. The emergent IA spectra of both compounds feature two distinct spectral bands that continue to grow in amplitude for the remaining 100 ps, until reaching their ultimate maxima. The formation of this spectral form marks the transition to a longer-lived species, whose spectral evolution extends to the nanosecond temporal domain [177].

4.2.3.2 *Time-Resolved Spectroscopic Study of Group II*

Ground state absorption spectra of Group II compounds (see Figure 4.2(b)) are composed of several closely overlapping bands, covering almost the entire the MidUV-to-NUV spectral range.[1] The red-most absorption bands of these compounds are slightly red-shifted in comparison to the Group I constituents (330 nm for IB_{2A} and 330 nm for IB_{2B}), therefore the 340 nm excitation falls closer to the characteristic short-wave maxima.

As seen in Figure 4.4, a broad IA structure predominantly concentrated in the blue part of the VIS spectrum is formed immediately after the excitation of compounds IB_{2A} and IB_{2B} (see the 300 fs ΔOD spectra in Figures 4.4(c) and 4.4(f)). This transient signal spans the 350–600 nm spectral range and, despite the lack of the fine structure observed in Group I molecules, it can be generally viewed as a combination of two broad overlapping bands, centered at around ca. 400 nm and 500 nm for compound IB_{2A}, and at ca. 400 nm and 470 nm for compound IB_{2B}. Clear-cut GSB signals are evident at early delay times in the NUV boundary (ca. 345–365 nm) of the spectral window (350–355 nm transient signals in Figures 4.4(b) and 4.4(e)). A decay of the initial TA signal persists for the first few picoseconds after the excitation and prevails in the larger portion of the spectral window. In contrast to Group I compounds, where initial dynamics was dominated by a spectrally uniform decay (see Figures 4.3(c) and 4.3(f)), more prominent spectral changes are observed within this early period for the Group II constituents. Only a moderate decay dominates in the red part of the spectrum (see the 600–650 nm traces in Figures 4.4(b) and 4.4(e)), whereas in the blue spectral edge (ca. 400 nm) the IA signal grows steadily (see the 400–405 nm traces in Figures 4.4(b) and 4.4(e)). A turning point in the early spectral evolution is reached within ca. 4 ps after

1 Also note how the steady-state absorption spectra are much more susceptible to modification of the pNph moiety.

the UV excitation. The resulting spectrum still resembles the initial IA profile, albeit the band structure is sharper and better defined (2–3 ps ΔOD spectra in Figures 4.4(c) and 4.4(f)). Further spectral rearrangement continues for about 50 ps and throughout this phase the short-wave ($\lambda_{P_R} < 400$ nm) and long-wave ($\lambda_{P_R} > 500$ nm) spectral parts decay rapidly, leading to the formation of a more homogeneous spectral shape. Negative GSB signals, similarly to IB_{1B}, vanish within 10 ps, successively evolving into IA of the final photoproduct. Roughly 100 ps after the excitation, the final TA spectra (see the 100 ps ΔOD spectra in Figures 4.4(c) and 4.4(f)) are formed, featuring a single spectral band, peaking at either 445 nm (IB_{2A}) or 460 nm (IB_{2B}), and a much weaker, virtually featureless long-wave IA plateau that extends up to 750 nm. From this point on, the entire spectrum decays in a uniform fashion and the molecular ground state is fully restored in several tens of nanoseconds [177].

4.2.3.3 *The Role of the Excitation Wavelength*

The dependence of observed dynamics on the excitation wavelength was investigated in selected compounds from each photochromic group (IB_{1A} and IB_{2A}). PP measurements, analogous to ones presented in the previous section, were performed using several different excitation wavelengths, namely: $\lambda_{P_U} = 305$, 315, 325, and 345 nm. The results of these experiments are summarized in Figure 4.5. Kinetic traces at the IA maxima, normalized to the amplitude of the final photoproduct, are shown in the main graphs. The early and the late TA spectra (500 fs and 6 ns delays, respectively), normalized to the absolute largest spectral amplitudes, are given in the insets on the right.

From the kinetic curves in Figure 4.5 it is obvious that variation of the excitation wavelength results in redistribution between the relative amplitudes of the initial excited form and the final photoproduct. Apparently, the ratio between the TA signals of the early and the late spectral forms increases with shortening of the excitation wavelength. In respect to the final photoproduct,[2] excitation with a shorter wavelength increases the relative initial amplitude of the signals. This is especially noticeable for compound IB_{1A}—increase of the excitation energy by ca. 3800 cm^{-1} causes an almost twofold increase in the sub-picosecond signal, which, in this particular instance, exceeds even the amplitude of the final PA. A similar trend is observed for compound IB_{2B}, albeit the effect is less pronounced—amplitude of the initial spectral signal increases only by ca. 33 % upon an equal alteration of the excitation wavelength. It is

2 The PA signal was taken as a reference, since photodynamic development stabilizes after ca. 50 ps and remains spectrally invariable throughout the remaining course, i.e., ca. 7 ns, of the experiment

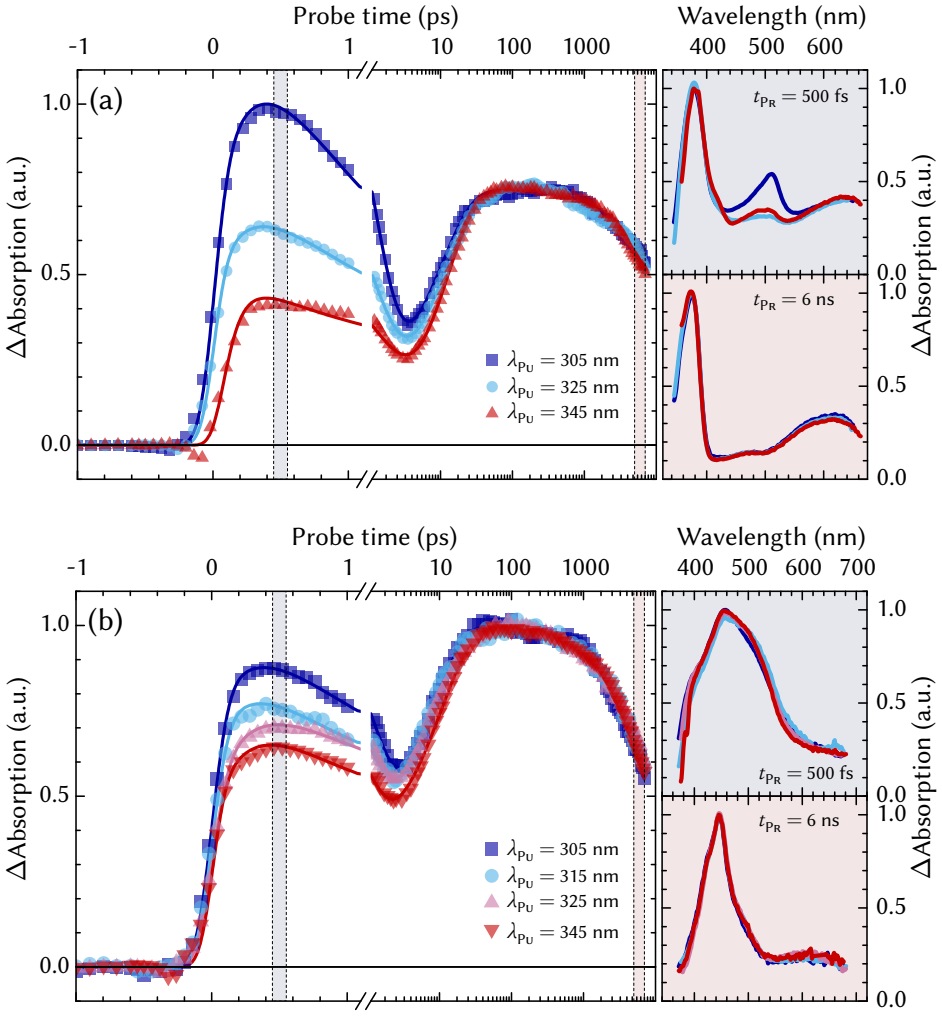

FIGURE 4.5: Time-resolved kinetic traces of compounds (a) IB_{1A} and (b) IB_{2A}, measured at 375 nm and 450 nm, respectively, as a function of the excitation wavelength. The traces are scaled to yield identical final magnitude of the signals at $t_{PR} \approx 1$ ns. Normalized ΔOD spectra at early (500 fs delay) and late (6 ns delay) probe times (see the main graphs for reference) at the matching pump wavelengths are shown in the insets on the right-hand side of the main graphs.

worth noting that the variation of the excitation wavelength has almost no effect on neither the initial, nor final transient spectra (see insets in Figure 4.5). Generally, only the intensity of the observed spectral bands and, to a lesser extent, the rate of the sub-picosecond relaxation are different (with an exception of the short-lived band around ca. 500 nm in IB_{1A}, which increases significantly in the case of $\lambda_{PU} = 305$ nm). Apparently, virtually equivalent long-lived photochromic species are formed irrespectively of the excitation photon energy;

furthermore, all photodynamic differences, caused by variation of initial excitation conditions, effectively disappear within the first 10 ps. Alternatively, from the perspective of primary excited forms, the observed excitation wavelength-related effects can be regarded as an increase/decrease of losses in the pathway of the photoproduct formation (i.e., the quantum yield of photoinduced final forms).

4.2.4 *Discussion*

4.2.4.1 *Revisiting the Non-Interacting Chromophore Model*

A non-interacting chromophore model is often used to describe the constitution of either the ground or excited state spectra of IBs [164, 165, 168, 176]. Previously, in a work concerning the femtosecond dynamics of the parent IB, the early photodynamics of the compound were ascribed to the formation of the IND chromophore in the excited state, due to a considerable resemblance between the intrinsic $S_1 \rightarrow S_n$ transitions of the IND cation and the early-emerging absorption bands of the base IB compound (namely, the 350 nm and 600 nm spectral maxima) [176]. Incidentally, similar spectral peaks are not characteristic to the early photodynamic stages of IB_{2A} (and to an extent to IB_{2B}, which features only a slightly modified IND cationic fragment in its supposed open molecular configuration). Likewise, the early photodynamic behavior of GROUP I compounds is dissimilar to that of the prototypical 5-phenyl-3H-indolic derivatives in their excited (or ground) state (see Figure A.5 and the brief discussion provided in Section A.3), i.e., the characteristic intense ca. 450 nm IA bands are absent in all their time-gated spectra. Considering the componential structure of the ground state absorption spectrum of the parent IB compound [168], an increase of the excitation effectiveness can be expected in the indole fragment upon the decrease of the excitation wavelength (specifically when $\lambda_{PU} \rightarrow 300$ nm [176]). Nevertheless, as it was shown in Section 4.2.3.3, all major aspects of the spectral dynamics are retained regardless of the excitation wavelength, aside from the relative change in amplitude of the initial spectra. The absence of the "pure" IND spectral component [176] in the early spectra and independence of the spectral shapes on the excitation wavelength suggest that attribution of the observed spectral features to specific constituent parts of the molecule [164, 165, 168, 176] is too simplistic and becomes invalid as the parent compound is structurally expanded. In other words, a complete spectral separation between the chromophoric constituents is not present in the excited molecular state (and, most likely, in the ground state as well). Moreover, in previous nanosecond-resolution stud-

ies the spectral shape of the ring-open form also exhibited an characteristic absorbance plateau in the 480–600 nm spectral range, where the constituent chromophores have zero ground state absorbance [163, 166, 177].

4.2.4.2 *Interpretation of the Early Photodynamic Stages*

Despite the intricate photodynamic behavior of the studied compounds, several common traits can be recognized in the time-resolved data of Figures 4.3 to 4.5. First and foremost, a distinctive resemblance between the very early and very late stages of the spectral evolution is exhibited by all the compounds investigated in this study. Even though this trend is most obvious for GROUP I constituents, where the sub-picosecond and late nanosecond spectra virtually coincide, a strong resemblance between the ΔOD spectra of the initially excited molecular forms and the final photoproducts is observed in GROUP II compounds as well (especially considering the kinetic behavior in the spectral vicinity of ca. 450 nm). This resemblance between the earliest and final TA spectra and the evolution of the former to the latter via a "dark" transition state—the IA minimum at ca. 4 ps—brings about the characteristic "descent → ascent → descent" (asymmetric letter "$\mathcal{M}$"-shaped) kinetic traces. Such striking swings, evidently, cannot be understood in terms of a simple sequential evolutionary model [176], since two near-identical SADS would arise both in the very early and very late stages of the photoevolution, for which it is hard to envision a valid physical reason. In order to explain the peculiar spectral behavior, we have chosen to adapt a non-sequential evolutionary model, encompassing a branching within the primary IB excited state. Such branched evolution of photochromic reactions has been proposed previously for other photochromic compounds. For example, fulgide photochromic reaction (an electrocyclic ring-opening/closing sequence) is conceived via two pathways—along a fast (ca. 1 ps) and slow (ca. 10 ps) reaction coordinates—and kinetic traces, similar to ones observed in Figures 4.3 to 4.5, result from this spectral evolution [149, 178]. A multiple-route decay model was also used to interpret the course of photoproduct formation in the early photoevolutionary stages of some spiropyran-type compounds [179].

Schemes (a) and (b) in Figure 4.6 depict the general connectivity diagrams for the models used to fit the time-resolved data presented in Figures 4.3 and 4.4. The SADS of different compartments are presented in Figure 4.7 and their characteristic lifetimes are given in Table 4.1. A simple four- or five-component model provides an adequate description of the experimentally resolved data (the quality of the fits can be best judged from the kinetic curves in Figures 4.3 and 4.4). The physical basis of the proposed branched evolutionary

Reciprocal rates (ps)		Photochromic compounds			
		I		II	
		A	B	A	B
Excited state intermediates	$\tau_{1\to2}$	2.1	0.8	1.04	1.6
	$\tau_{2\to3(a)}$	13.1	11.9	11.1	20
	$\tau_{1\to1}$	3	6	4.1	10
	$\tau_{2\to2}$	83	65	20	20
Main photoproduct states	$\tau_{3a\to3b}$	—	—	56.2	46.4
	$\tau_{3a\to3a}$	—	—	120	90
	$\tau_{3(b)\to3(b)}$	18 200	12 700	15 900	12 100
Auxiliary photoproduct states	$\tau_{1\to0}$	1.9	0.9	2	2
	$\tau_{0\to0}$	0.6	0.4	0.6	0.4

Table 4.1: Population transfer rates between the different transient states presented in Figure 4.6 estimated from the global analysis fitting of the PP data.

model is summarized in Figure 4.6(c) and can be interpreted as follows. Femtosecond excitation promotes the ring-closed molecule to the Frank–Condon region of its excited singlet state. Part of the photogenerated population remains in the excited state manifold and experience either vibrational cooling, solvation, or non-adiabatic diffusion/drift along the singlet PES, thus leading the excited state population towards a local energy minimum. Intensification of the blue edge TA signals at ca. 400 nm of Group II compounds (see Figures 4.4(b) and 4.4(e)) may be regarded as a direct result of said relaxation processes in the excited state. Therefore, the spectrally comparable early components 1 and 2 and the transition between them represent the population stabilization and the primary conformational changes in the excited singlet state of the molecule, occurring prior to the main photochromic reaction.[3] The assumption that SADS 1 and 2 represent a common molecular state (namely, S_1) is corroborated by the fact that only these early species contribute to the GSB signal, which is subsequently outweighed by the competing positive contribution of IA of the ultimate photochromic form.

The intermediate state 2, consequently, serves as the primary channel for the formation of final ring-opened molecular photoproduct (3) via a radia-

3 Note that SADS decomposition reveals the IA maxima of these transients more clearly.

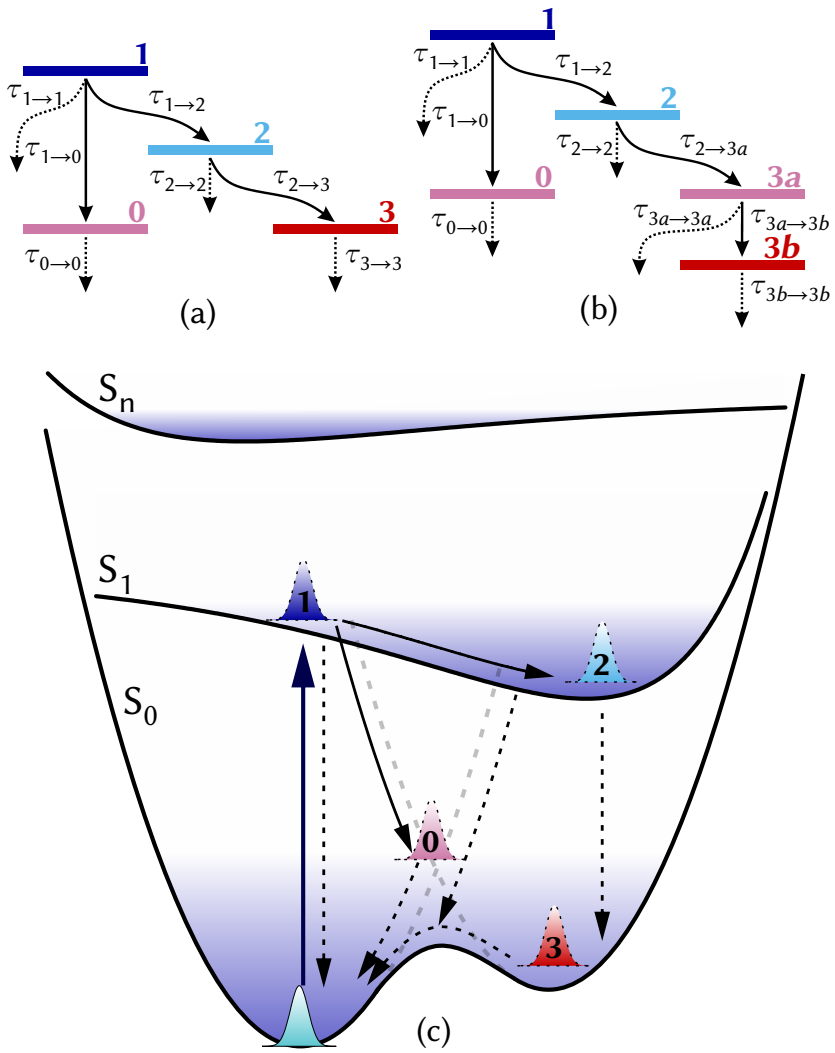

FIGURE 4.6: Connectivity schemes used in the global analysis procedure for (a) GROUP I and (b) GROUP II compounds. Solid arrows represent the transitions between different spectral states and the dotted arrows represent the decay to the molecular ground state. The colors of the compartments match those of the SADS provided in Figure 4.7 (compartments of the same color—namely, 0 and 3*a* in panel (b)—are characterized by identical (i.e., fixed) spectra in the global fitting procedure). Panel (c) shows a generalized PES reaction diagram based on the general connectivity scheme.

tionless relaxation $2 \to 3$. In addition, for GROUP II compounds a biexponential transition sequence $2 \to 3a \to 3b$ within the ring-opened ground state manifold was assumed to yield a better fit of the data. These biexponential dynamics can be explained by assuming a diffusion/drift-like decay along a non-uniformly sloped PES of the ring-opened ground state 3. Alternatively, they might arise from concomitant decay of several different isomeric forms

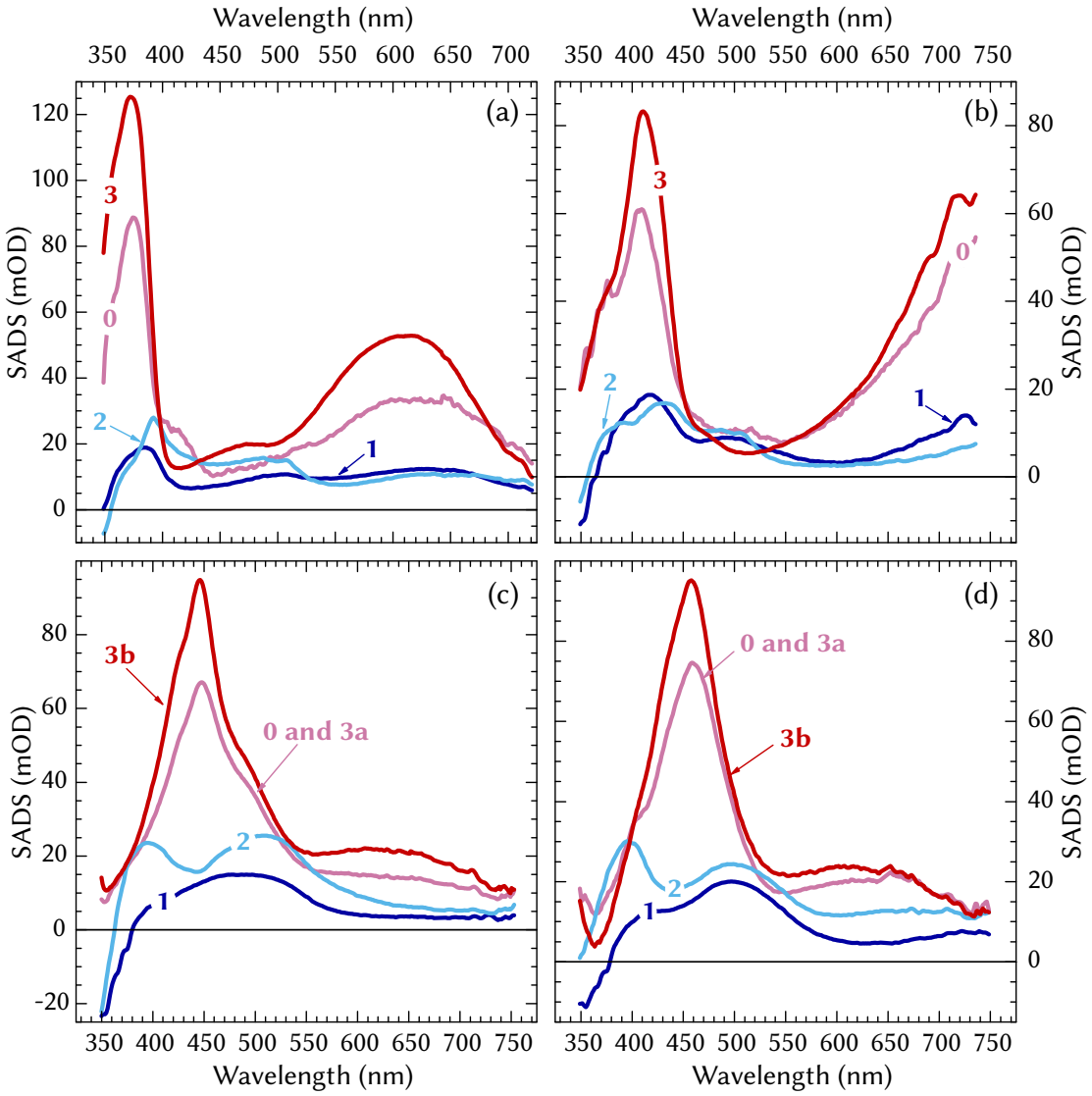

FIGURE 4.7: SADS of compounds (a) IB_{1A}, (b) IB_{1B}, (c) IB_{2A}, and (d) IB_{2B} obtained from global fitting of the experimental PP data (presented in Figures 4.3 and 4.4) using the models shown in Figure 4.6. The rates of population transfer between the components are given in Table 4.1. The temporal dependence of the state population concentrations is presented in the appendix of the thesis (see Figure A.6).

(e.g., with a different rotational angle of the phenylic group), as suggested in ref. [180]. In principle, some similarities can be drawn between the spectral structure (i.e., the broadband IA maxima at ca. 500 nm) and the characteristic lifetimes (ca. 1 ps and ca. 10 ps) of these early SADS and the excited state photodynamics of a single PNPH moiety [176]; however, they are probably co-

incidental, since a complete electronic isolation between the constituent chromophores, as it was mentioned before, is highly unlikely.

In general, intersystem crossing effects from S_1 cannot be wholly excluded: photoinduced opening of photochromic oxazine ring was suggested to occur in the triplet state PES due to experimentally observed triplet → triplet energy transfer in BODIPY-oxazine dyads [181]. Furthermore, a computational study in ref. [182] provided a mechanistic model of excitation dynamics, where ring-opened photoisomer is formed in the triplet state, followed by intersystem crossing to the singlet ground state of ring-opened species. Therefore, it is possible that certain stages of photodynamics of the investigated compounds involve triplet states, albeit the lifetimes are unusually short for typical triplet states. However, the proposed connectivity scheme and parameters obtained from global analysis are fully valid despite any uncertainties regarding the multiplicity of excited states.

The terminal step in the proposed relaxation model involves the decay of final species (3) to the ground state via thermal relaxation within a sub-microsecond time scale; the spectral shapes of the corresponding SADS along with their lifetimes agree well with the nanosecond-resolution data [177]. The initial Frank–Condon state in the suggested model is assumed to be heterogeneous and a portion of the excited molecules takes another relaxation path as an alternative to the photoproduct-favoring $1 \rightarrow 2$. Our model presumes that state 1 is an unstable point of the PES and it acts as a transition state (or possibly a conical intersection crossing seam) for a part of the excited state population. Molecules that do not undergo the excited state vibrational cooling process ($1 \rightarrow 2$) produce a short lived ($\tau < 1$ ps) transient product 0, whose spectrum is, intriguingly, strikingly similar to that of the final photochromic formation 3. It is important to emphasize that these SADS were constrained to have identical spectral shapes (i.e., $\sigma_0(\lambda) = \sigma_{3a}(\lambda)$) in the numeric modelling procedures of the Group II time-resolved data. This constraint virtually did not reduce the quality of the fit (whereas the parameter space was significantly narrowed); it can be roughly justified by the fact that both intermediate states are located on the same PES in the final model (see Figure 4.6). Despite its delusively small concentration (see Figure A.6),[4] this component is necessary for an accurate approximation of the sub-nanosecond kinetics, and, as mentioned before, similar spectro-temporal features emerge in the analysis even if a different (e.g., sequential) model is assumed.

In most cases, the transient photoproduct 0 is slightly red-shifted and less spectrally uniform in comparison to the final ring-opened species 3, hence it

4 Considering all the deactivation routes of component 1 from Table 4.1, the amount of population relocated to component 0 may actually be as high as 43 %.

can be regarded as a sort of hot state in the bond-cleaved (but not yet fully ring-opened) ground state manifold. A similar relaxation model was used to explain the deactivation of the excited state to a hot GSI via a conical intersection (i.e., a failure to isomerize) for a certain species of photochromic spirooxazines [183]. A parallel formation of the ring-opened molecular form via both $1 \rightarrow 2 \rightarrow 3$ and $1 \rightarrow 0 \rightarrow 3$ channels was not incorporated into the general connectivity scheme. If this pathway is included in the model, it turns out that the reaction rate via the photodynamic coordinate $0 \rightarrow 3$ (supposedly, a vibrational cooling of the bond-cleaved transient product to the final photochromic form) is not nearly as rapid as a pure deactivation to the main molecular ground state (i.e., $\tau_{0\rightarrow 0} \lesssim 10 \cdot \tau_{0\rightarrow 3}$) and can therefore be neglected. From the kinetic perspective of several related photochromic compounds, the main ("slow") path of the photoproduct formation via the thermally relaxed S_1 state is comparable to the ring-opening reaction in various ironfulgides [184], whereas the auxiliary ("fast") photoreaction route bears a resemblance to the ultrafast C–O disassociation and isomerization of certain spiropyran compounds [31, 185]. Evidently, the appearance of this short-lived transient state explains the resemblance between the early and late stages of the photoevolution. Provided the structural similarity between the initial and final open ring formations (only a minor orientational conversion takes place [164]), the appearance of an electronically comparable conformer in the early spectral development is highly probable.

A satisfactory description of the sub-nanosecond data can be obtained without the inclusion of decay to ground state pathways $1 \rightarrow 1$, $2 \rightarrow 2$, and $3a \rightarrow 3a$, however, this results in quantum yields values, which are significantly higher than those determined experimentally [177]. A large margin of error can be expected when comparing the experimental and numeric results, as (a) the experimental estimation of quantum yield is performed under different experimental conditions (nanosecond-domain FP with $\lambda_{PU} = 355\,\text{nm}$ and $\tau_{PU} = 5\,\text{ns}$ [177]); and (b) molar extinction of ring-opened photoproduct is never measured directly, and similar chemical compounds [165, 166] or chemically initiated molecular forms [177] are used as a reference instead. Considering the possible inconsistencies, the population decay rates from states 1, 2, and $3a$ were chosen to give "safe" quantum yield estimates ($< 30\,\%$ for GROUP I and $< 20\,\%$ for GROUP II), combined with the best least-square approximation of the experimentally resolved data (quantum yield was regarded as the residual concentration at 5 ns, see Figure A.6). Excitation losses within the excited state via either a direct leakage ($1 \rightarrow 1$, $2 \rightarrow 2$) or the formation of the transient photoproduct 0 can be used to explain the dependence of the IA signal on the excitation wavelength in the early photodynamic phases

(Figure 4.5). Three-pulse PPPP experiments [186] have shown that reaction rates and quantum yields of photochromic processes may be influenced by the population of vibrational states. Therefore, excess energy, provided to the IB system by a higher photon energy pulse, may be transferred into the population of higher vibrational modes, coupled to either to the direct decay or the "lossy" photoproduct formation ($1 \rightarrow 0$) channels. Since these population losses occur before the formation of the final photochromic form, no significant differences, apart from a relative increase/decrease of the initial and final spectral amplitudes, are observed in the long run and both the early femtosecond and the late nanosecond spectra remain intact.

The validity of this branched model has to be confirmed further. Particularly intriguing question that remains to be addressed is the structural basis for the branching in the excited molecular state. From the ultrafast electronic spectroscopy data presented here, it seems that early on the photoreaction pathway the investigated molecules seem to make a "decision" of either proceeding to ring-open, VIS-absorbing form, or dissipating the excitation energy on a non-productive portion of ground state PES. The structural factors determining the outcome of this "decision" could potentially be revealed by time-resolved vibrational spectroscopy, perhaps, aided by molecular dynamics simulations. On the other hand, the precise nature of ground- and excited-state PES's and "decision" point could further be explored using multi-pulse TA spectroscopies [32, 132, 187]. Finally, the presence of red-VIS-to-NIR IA bands in the compounds belonging to GROUP I remains to be explained. For this, quantum chemical investigations, similar to the ones made earlier on the parent IB compound [188], could be instrumental.

4.2.5 *Conclusions*

We have investigated the ultrafast dynamics of four novel phenyl-substituted IB photochromic compounds with PP spectroscopy. For the first time, the excited state dynamics of photochromic oxazines was described by a branched relaxation model, which was used for global analysis of the experimental transient data. In the suggested model, the final ring-opened forms are created in ca. 100 ps via radiationless transitions from the singlet molecular excited state S_1, and a full thermal ring closure occurs with a rate of tens of nanoseconds on a sub-microsecond timescale. Intricate spectral development in the early photodynamic stages is explained by the appearance of a short-lived photoproduct—presumably, a bond-cleaved or destabilized molecular form on the ground state PES—directly from the initial excited state of the molecule.

4.3 OPTICALLY CONTROLLED MOLECULAR SWITCHING OF AN INDOLO-BENZOXAZINE-TYPE PHOTOCHROMIC COMPOUND

4.3.1 *Introduction*

Photochromism, as briefly introduced earlier, is a reversible photochemical reaction that results in a temporary structural change (isomerization, electrocyclic ring-opening or ring-closing, dissociation, etc.) of a molecular compound along with a distinctive transformation of its absorption spectrum [146, 149, 189]. Unique photochemical properties of various photochromic compounds are of great interest for practical uses in such fields such as data storage [155, 156], optical switching [151, 158], or molecular based digital processing [160, 190]. One of the more interesting aspects of photochromism is its bidirectionality. Typically, a forward photochromic reaction, leading to the formation of a metastable form ("switching on"), is initiated by the absorption of a photon, whereas the backward reaction ("switching off") proceeds via thermal relaxation to the main molecular ground state. Forward photochromic reaction may be extremely fast (the reciprocal rates of photoproduct formation may go as low as several picoseconds [149, 185]), whereas the back-switching dynamics tend to occur over significantly longer timescales. In some cases, reverse switching can be induced by the absorption of photon of a different frequency (typically resonant with the absorption band of the metastable photoproduct form) [146]. Such intentional back-switching is especially desirable for practical optical switching and data processing applications, since a reduced reaction time (or at least a controllable modulation of the photochromic process) would allow a larger data bandwidth. Although several femtosecond time-resolved studies have been published on bidirectional switching of photochromic molecules [31, 185, 186, 191], the detailed understanding of precise mechanisms of such reactions is still lacking.

In the experimental work presented in refs. [177, 192] (and, likewise, in Section 4.2 of the thesis at hand), we have examined the photodynamic behavior of several members of the fast-switching IB [164, 165, 168, 193, 194] photochromic family, whose photochromism is based on the light-induced opening and intrinsic thermal closing of the oxazine ring (see the inset in Figure 4.8). Perhaps some of the more intriguing spectroscopic properties were found in 8-phenylindolo[2,1-*b*][1,3]oxazines, i.e., IBs with a phenylic extension in the *para* position, relative to the nitrogen of the indole ring (see refs. [177, 192] and Section 4.2.1). A "representative" of this group—previously classified as IB_{1B} [192] (see Figure 4.8)—was selected for an extended ultrafast bidirectional

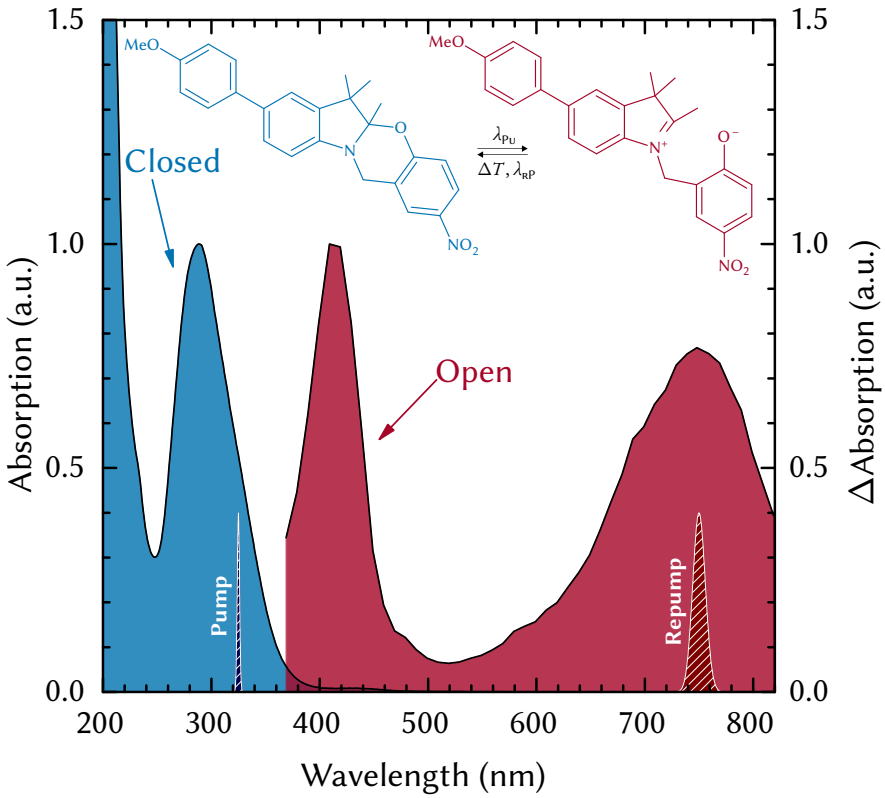

FIGURE 4.8: Steady-state absorption spectrum of compound IB_{1B} (portrayed in light blue) along with TA spectrum of its optically generated form (portrayed in light red; spectrum is taken from the nanosecond-resolution FP experiments, described in detail in ref. [177]). The UV- and NIR-situated dashed dark blue and dark red Gaussian curves represent, respectively, the pump and repump pulse spectra.

switching study. The particular compound was chosen for some of its outstanding photophysical properties:

(a) relatively high quantum yield (ca. 30 % [177]), that allows us to predict that the back-switching reaction may also be induced effectively;

(b) a satisfactory photochemical stability (i.e., nearly 5× more switching cycles in comparison to the parent IB molecule [177]), that ensures lower sample degradation when exposed to multiple laser beams;

(c) a huge distinction between the closed and the open conformation spectra (ca. 22 400 cm^{-1} bathochromic shift of the red-most spectral maximum, see Figure 4.8), that reduces the probability of multi-photon effects, when reexciting the photoproduct, and grants control of the pho-

tocycle with highly distinct radiation (i.e., "switching on" with NUV and "switching off" with NIR).

In this section we present the results of time-resolved multi-pulse experiments that demonstrate both light-induced ring-opening and closing dynamics of IB_{1B} and shed more insight on the photochromic behavior of IBs in general. Global analysis techniques are employed to parameterize the experimental results and to elucidate the transient states observed both in the forward and backward photochromic reactions. To our knowledge, these are the first experiments of this kind to be performed on compounds of the IB family.

4.3.2 *Materials and Methods*

4.3.2.1 *Sample Preparation*

Polycrystalline sample of IB_{1B} (see ref. [177] for chemical synthesis details) was dissolved in MeCN (Sigma Aldrich LiChrosolv; gradient grade) and diluted to an OD of 1 at the excitation wavelength (325 nm) in a 1 mm optical path quartz cell (Starna Scientific). In order to diminish sample degradation during the experiments and to avoid a local overexposure to the laser radiation, cell was translated transversely to the beam propagation direction with a two-axis motorized linear stage (Standa 8MT173).

4.3.2.2 *Experimental Setup*

The basis of multi-pulse experiments (notably, the Ti:Sa system parameters and the PP side of the setup) is described in greater detail in Section 4.2.2.2. An additional Topas-800 OPA was pumped by ca. 550 mW of the fundamental Libra output to generate the reexcitation radiation. The IB sample was excited ("pumped") with 325 nm NUV radiation adjusted at 1 µJ (red edge of the main UV–VIS absorption band). Reexcitation (i.e., "repumping") was performed with NIR radiation of 750 nm and 8.5 µJ (approximately at the center of the red-most IA band of the optically activated isomer, see Figure 4.8 for details). The estimated durations of the NUV and NIR pulses were, respectively, 150 fs and 100 fs. The diameter of both beams at the sample plane was ca. 300 µm (i.e., $I_{PU} = 6.5\,GW/cm^2$ and $I_{RP} = 83\,GW/cm^2$). Polarizations of the pump and repump beams were aligned parallel to one another and at a 57.4° ("magic") angle in accordance to the probe beam. The experimental data was acquired over several (6–8) multiple scans, i.e., the entire TA spectrum was repeatedly measured back-to-back and the multiple sets of wavelength- and time-resolved data were averaged over the number of performed scans. The

PRPP/PRPAT experiments were carried out in two overlapping spectral windows (325–635 nm/505–810 nm) and the data from consecutive experiments were merged into a single continuous dataset. The scan-to-scan kinetic traces were virtually identical and the pre- and post-experiment steady-state absorption spectra also did not show any significant changes. Additional information about the optical layout and the data acquisition of the measurements system can be found in Section 2.3 and ref. [192].

4.3.3 *Experimental Results*

4.3.3.1 *IB Pump-Repump-Probe Dynamics*

Sub-nanosecond TA dynamics were discussed in greater detail in Section 4.2 of the thesis and/or ref. [192]. As it was established from the PP experiments, the formation of the final photochromic forms of phenyl-substituted IBs is a result of complicated photodynamics, involving several evolutionary intermediates. The PP kinetic traces exhibit characteristic "rise → fall → rise → fall" behavior (see the data shown in solid symbols and curves in Figure 4.9) which was previously attributed to the fast-decaying and slowly-decaying photoproducts on different portions of ground state PES [192]. After these dynamic steps are complete, the formation of the final photoproduct spectrum occurs within a temporal span of ca. 100 ps and all further spectral development is associated only with thermal relaxation to the main molecular ground state. To ensure that only the terminal state (and not an earlier intermediate) is affected in the repumping process, the temporal delay between pump and repump pulses was set at 1 ns, and the probing was performed from 10 ps before till 6 ns after the actinic UV excitation.

Results of the PRPP experiments are presented in Figures 4.9 and 4.10. As the kinetic traces in Figure 4.9 indicate, the PP and PRPP signals coincide prior to the arrival of the repump pulse. The NIR reexcitation at 1 ns causes an immediate bleaching of both main photoproduct bands, resulting in a ca. 20 % decrease of the TA signal in their spectral vicinity (see the open symbols and the dashed curves in Figure 4.9). The bleaching effect is more notable for the short-wave photoproduct band (see Figures 4.10(a) and 4.10(c)), since the ΔΔOD signals in the vicinity of the 750 nm band were largely contaminated by the scattering of the repump pulse. The negative ΔΔOD signal peaks at 407 nm, which is slightly blue-shifted (ca. 200 cm^{-1}) from the maximum of the original IA band. Contrary to the main PA bands, in the mid-band region (430–550 nm), a positive ΔΔOD signal is observed. Immediately after the reexcitation, this IA plateau is largely featureless and does not exhibit a distinct

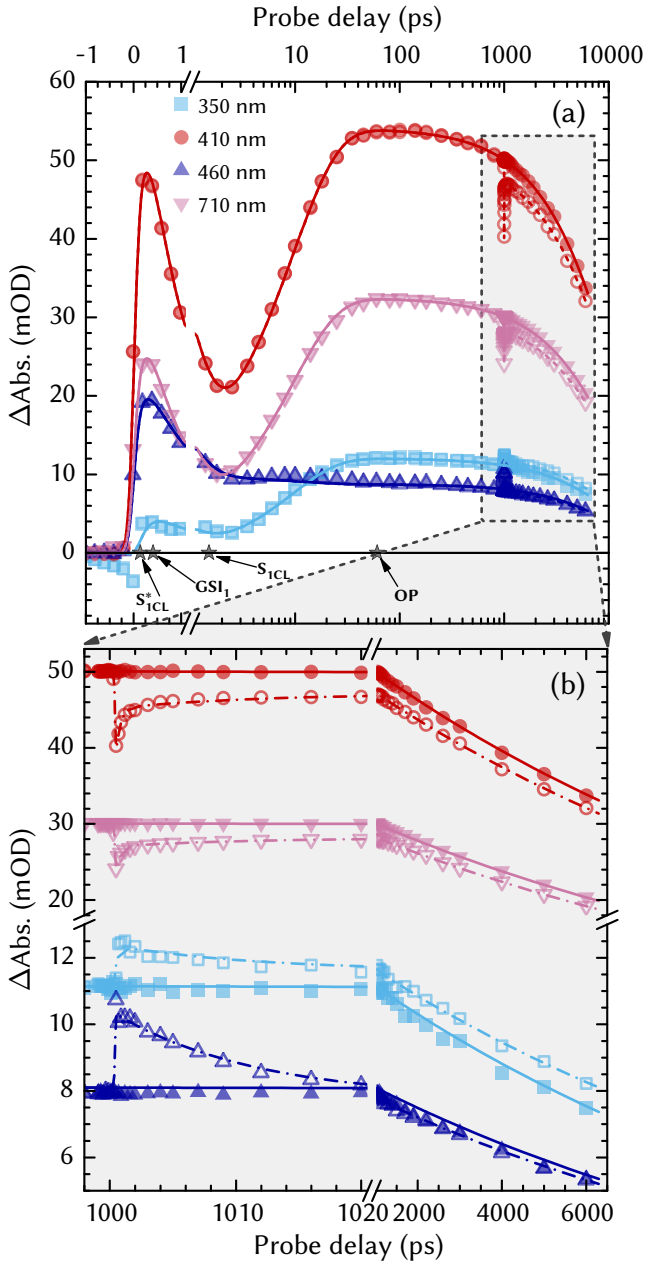

FIGURE 4.9: Dispersion corrected time-resolved PP (solid symbols) and PRPP (hollow symbols) kinetic traces of IB_{1B}. The full sub-10-nanosecond PP and PRPP spectral dynamics at selected wavelengths are presented in panel (a), while the post-repump ($t_{RP} = 1$ ns) evolution is highlighted in panel (b). Solid and dashed curves, respectively, represent the global fits of the PP and PRPP experimental data. For simplicity purposes, only the global fit according to MODEL I (see Section 4.3.4 for more details) is presented in this figure. Femtosecond-resolution time-gated spectra of the PP photodevelopment can be found in Figure A.7. Symbols on the abscissa of panel (a) indicate temporal instances at which the transient states of the PP photoevolution reach their population maximum (see Section 4.3.4 and Figure 4.13(b) for more information).

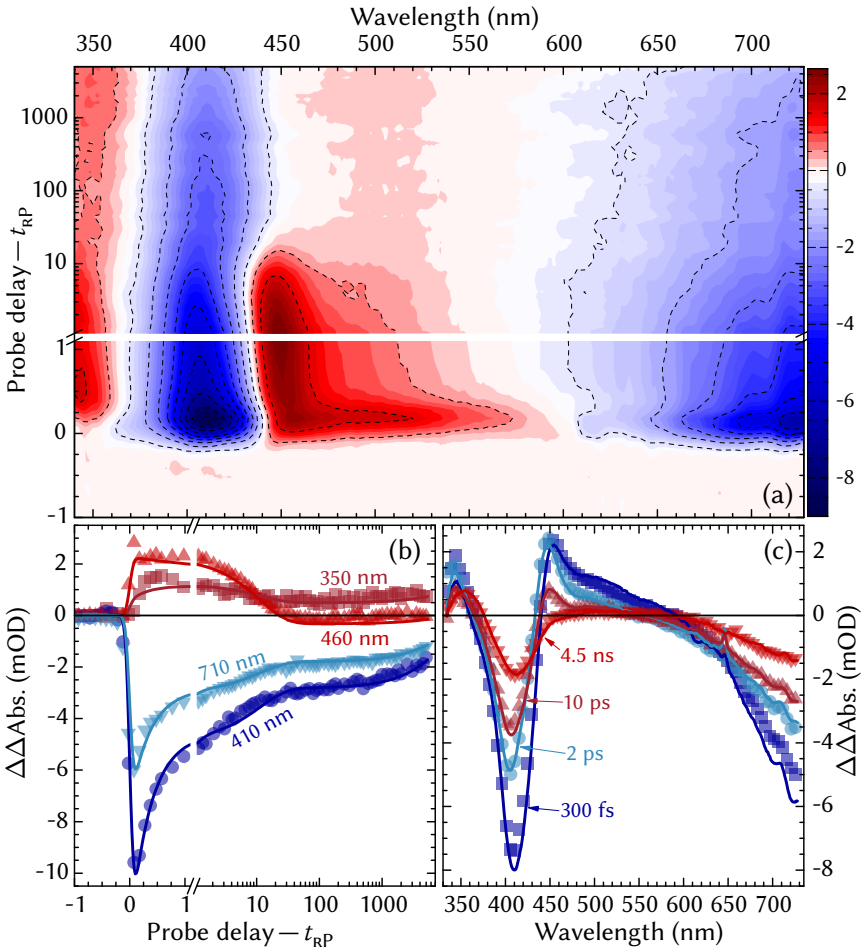

FIGURE 4.10: Time- and wavelength-resolved PRPP ΔΔOD ($\Delta\Delta A = \Delta A_{\mathrm{PRPP}} - \Delta A_{\mathrm{PP}}$ from Figure 4.9) spectrum of IB_{1B} (panel (a)), along with its spectral and temporal cuts (panels (b) and (c), respectively). Measured data is depicted in solid symbols. Continuous lines correspond to differential global analysis fits from Figure 4.9 (i.e., $\Delta\Delta A^{\mathrm{Fit}} = \Delta A^{\mathrm{Fit}}_{\mathrm{PRPP}} - \Delta A^{\mathrm{Fit}}_{\mathrm{PP}}$). For simplicity purposes, only global fit according to MODEL I is presented in the figure. Spectral data beyond 730 nm in panels (a) and (c) is omitted due to intense scattering of the repump pulse. Note that the probe timescale is offset to start at $t_{\mathrm{RP}} = 1$ ns in the panels.

band structure (see the 300 fs spectra in Figure 4.10(c)). During the first few picoseconds after the reexcitation, the repump-induced signals measured around the photoproduct peaks experience a significant (ca. 50 %) loss of their initial amplitudes. Concomitant to this recovery, the red wing (> 460 nm) of the positive mid-band ΔΔOD spectrum decays rapidly (compare the 300 fs and 10 ps curves in Figure 4.10(c)), leading to the emergence of a single prominent ΔΔOD band located near the short-wave zero-crossing point. This band, orig-

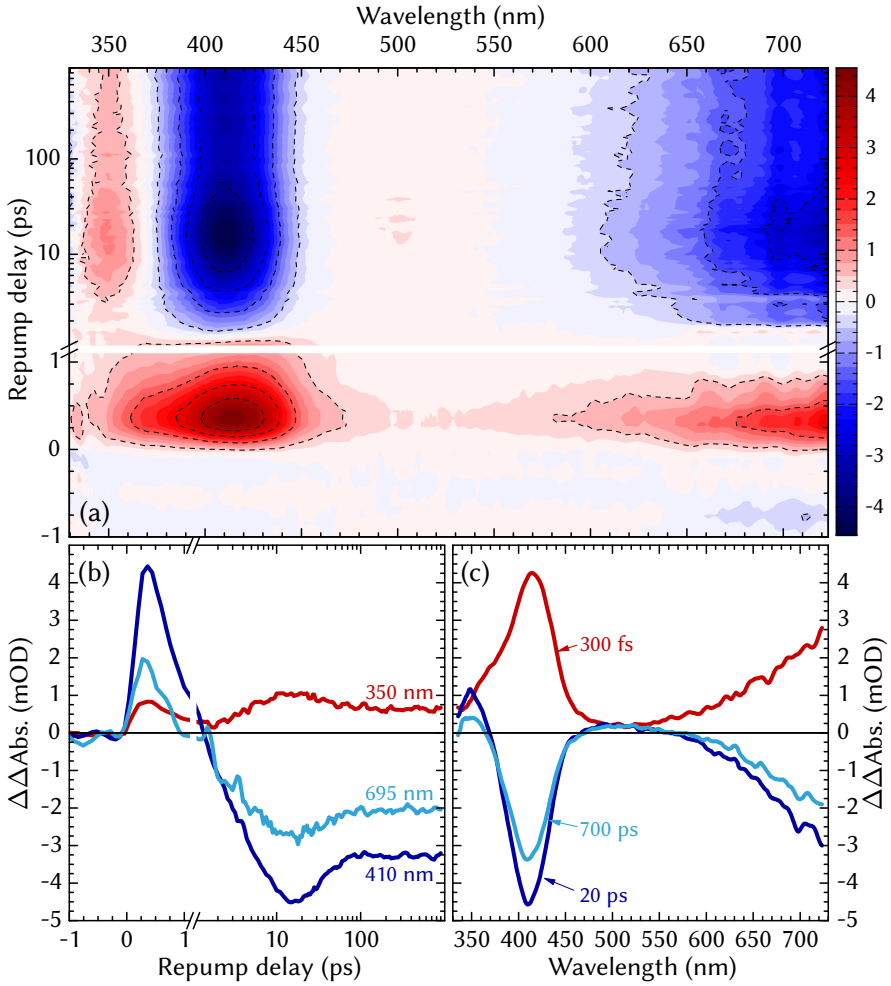

FIGURE 4.11: Results of the PRPAT measurements, performed at $t_{PR} = 1$ ns. Panel (a) depicts the entire ΔΔOD ($\Delta\Delta A = \Delta A_{PRPP} - \Delta A_{PP}$) transient spectrum, whereas panels (b) and (c) indicate, respectively, spectral and temporal cuts of the said spectrum. Spectral data beyond 730 nm in panels (a) and (c) is omitted due to intense scattering of the repump pulse.

inally peaking at ca. 455 nm, experiences a slight growth and a blue-shift of ca. 395 cm^{-1} within the succeeding 3–4 ps. The kinetic development subsequently slows down at ca. 5 ps after the repump (see Figure 4.10(b)) and no significant spectral changes, aside from a steady decay of the kinetic signals, are observed within the ΔΔOD spectrum for the following 100 ps. The positive ΔΔOD band entirely vanishes in this timescale, gradually being replaced by the negative signal mimicking the PA (see the 4.5 ns curves in Figure 4.10(c)). The post-repump spectral development ceases at later probe delays (> 50 ps) with almost 6 % of the initial IA lost in comparison to PP data without repump. Additional PRPP experiments were performed with $\lambda_{RP} = 400$ nm radiation,

resonant to the short-wave band of the optically excited form. The obtained results (see Figure A.8 in the appendix of the thesis) were virtually identical to NIR reexcitation ones, thus underlining the fact that both spectral bands belong to the same molecular state.

4.3.3.2 *IB Pump-Repump Action Trace Dynamics*

Results of the PrPAT measurements are presented in Figure 4.11. Probing was performed at 1 ns after the UV excitation (assuming, as earlier, that the photoproduct is fully formed at this time) and the NIR reexcitation pulse was scanned from 10 ps before till 900 ps after the 325 nm excitation pulse. Three major development stages can be observed in the PrPAT kinetic curves in Figure 4.11(b).[5] Firstly, a very early repumping (< 1 ps after the UV excitation) causes a net increase (ca. 6 %) of the entire TA signal, as indicated by the rise of a positive ΔΔOD signal. The repump-induced increase in PA rapidly disappears as the repump pulse overtakes the pump pulse and almost no gross effect is observed if the repumping is performed at ca. 1.3 ps after the UV excitation. Subsequently, the PrPAT signals at the main TA bands of the photoproduct become negative and continually grow for ca. 15 ps. After reaching their maximum at the repump time of ca. 20 ps, the ΔΔOD bleaching signals stabilize on a time scale of 100 ps and remain principally independent on the repump timing between 100 and 900 ps. Either positive or negative, the ΔΔOD signals peak at 410 nm throughout the entire temporal extent of the measurement, and do not show any peak-shift dynamics, in contrast to the PrPP data in Figure 4.10. The final ΔΔOD signals from the PrPAT measurements (700 ps curves in Figure 4.11(c)) agree well with the late time-resolved spectra of the PrPP measurements (4.5 ns curves in Figure 4.10(c)), likewise exhibiting a ca. 6 % decrease of the transient photoproduct signal.

4.3.4 *Discussion*

4.3.4.1 *Key Development Stages of the PP Photodynamics*

From a single glance at Figure 4.9, it is obvious that the intricate photoevolution of IB_{1B} spans a wide femto-to-nanosecond timescale and exhibits several distinct interstate transitions between both short- and long-lived spectral species. In order to establish a unified model that encapsulates both the post-UV-pump and post-NIR-repump dynamics, we must first recognize all of the

5 Standalone PP and PrPP kinetic traces, analogous to ones in Figure 4.9, are not presented, since the PP signals remain constant throughout the PrPAT measurement.

important spectral transients that come into play during the various photoevolutionary stages. The highlights of the PP photodevelopment can be summarized as follows:

1. Succeeding the IRF-limited rise, the PP TA signals, by and large, experience a rapid decay that lasts for several picoseconds. The sub-3-picosecond spectral progression is spectrally uneven, exhibiting a rapid amplitude drop in the spectral vicinity of the blue- and red-positioned photoproduct maxima (410 nm and 710 nm kinetic traces in Figure 4.9), a slightly slower signal decay in the mid-band region of ca. 500 nm (460 nm traces in Figure 4.9), and a competition between ESA and GSB that takes place in the shortwave boundary at $\lambda_{PR} < 360$ nm (350 nm traces in Figure 4.9) [192]. This spectrally (and temporally) uneven development suggest a complex interplay of several transient species during this period.

2. The subsequent evolution of the TA signal at $2\,\text{ps} < t_{PR} < 100\,\text{ps}$ is largely spectrally uniform, demonstrating a disappearance of the bleach signals, a constant growth of IA in the spectral surroundings of the 410 nm and 750 nm spectral maxima, and a concomitant decay of TA signals in the mid-band regions.

3. The two characteristic spectral bands fully evolve at $t_{PR} \approx 100\,\text{ps}$. A uniform decay of the entire TA signal predominates the final stages of spectral evolution, until the photochromic system is fully reverted back to the molecular ground state in a sub-microsecond timescale [177].

As the mentioned observations indicate, at least four transient states define the post-UV-excitation photodynamics: two short-lived transients arise in the sub-picosecond development, one at sub-50-picosecond development, and one at the final evolutionary stages. The PP photoevolution, depicted in Figure 4.9, can be construed via the previously suggested branched model of the IB photochromic reaction [192]:

1. Absorption of a UV photon promotes the ring-closed photochromic system from the molecular ground state to the Frank–Condon region of its singlet excited state (S^*_{1CL} in Figures 4.12 and 4.13). Vibrational cooling along with primary conformational changes in the excited state manifold take place within ca. 1 ps after the excitation, as indicated by the $S^*_{1CL} \rightarrow S_{1CL}$ transition in Figure 4.12. SADS of both of these excited state transients exhibit traces of GSB in the short-wave edge of the experimental window followed by a multiple band structure, peaking

at 420 nm and ca. 510 nm. The vibrationally hot S^*_{1CL} is more (but not exclusively, see the temporal component population evolution in Figure 4.13(b)) prominent during initial stages of the photodevelopment (< 1 ps), whereas state S_{1CL} prevails during the ensuing sub-50-picosecond photoevolution. We assume that interstate transfer $S^*_{1CL} \rightarrow S_{1CL}$ is rapid and lossless, whereas state S_{1CL} has a slower ground state leakage pathway $S_{1CL} \rightarrow$ GS (see Table 4.2), incorporated to the global fit in order to account for the reported values of the quantum efficiency of the ring-opening reaction [177].

2. Photoevolution of the S_{1CL} state leads to the formation of the ring-opened photoproduct OP ($S_{1CL} \rightarrow$ OP in Figures 4.12 and 4.13), that fully reverts back to the ring-closed conformation in a sub-microsecond timescale [177]. A fraction of the S^*_{1CL} population is assumed to decay to a short-lived (< 1 ps) ground state intermediate GSI_1 ($S^*_{1CL} \rightarrow GSI_1$ in Figures 4.12 and 4.13), which, most notably, instigates an emergence of a photoproduct-like spectrum in the early stages of the photoevolution (principally, the early (t_{PR} < 2 ps) peaking of ΔOD signals at the photoproduct maxima in Figure 4.9).[6] Separation of this intermediate from the main photoevolutionary pathway $S^*_{1CL} \rightarrow S_{1CL} \rightarrow$ OP is motivated by the dissimilarity of its spectral shape (Figures 4.13(a) and A.9) and, notably, its spectral amplitude (Figure 4.13(a)) from the remaining excited state SADS.[7]

4.3.4.2 *Key Development Stages of the PP and PRPP Photodynamics*

At least three distinct development phases can be discerned in the post-reexcitation photodynamics of IB_{1B} (Figures 4.10 and 4.11):

1. The actinic NIR repump at 1 ns primarily bleaches the greater part of photoproduct spectrum and triggers an increase of repump-induced absorption in both the short-wave and the mid-photoproduct-band regions. The first stage of the post-repump photodevelopment is best signified by the IRF-limited formation and rapid decay of the nearly featureless ΔΔOD IA plateau within the first picosecond after the reexcitation.

2. The sub-20-picosecond post-repump evolutionary stage brings about a substantial bleach recovery of the two main photoproduct bands and

6 Note the lack of GSB and the S_{1CL} maximum at ca. 500 nm in SADS of this state.

7 This separation is especially substantial for some other members of the IB family, whose early and late photodynamics is more spectrally diverse, see ref. [192].

Model I ("Leaky hot ground state model"):						
Post-UV-pump dynamics:						
Transition:	$S^*_{1CL} \rightarrow S_{1CL}$	$S^*_{1CL} \rightarrow GSI_1$	$S_{1CL} \rightarrow OP$	$OP \rightarrow GS$	$S_{1CL} \rightarrow GS$	$GSI_1 \rightarrow GS$
Reciprocal rate (ps):	0.95	0.70	11.7	12 800	50	0.37
Post-NIR-repump dynamics: (Repump efficiency: 58.0 % to state S_{1OP}, 3.2 % to state I_0)						
Transition:	$S_{1OP} \rightarrow GSI_2$	$GSI_2 \rightarrow OP$	$GSI_2 \rightarrow GS$	$I_0 \rightarrow GS$		
Reciprocal rate (ps):	0.35	11.9	194.5	∞		
Model II ("Return to the transition state model"):						
Post-UV-pump dynamics: identical to Model I.						
Post-NIR-repump dynamics: (Repump efficiency: 58.1 % to state S_{1OP}, 3.2 % to state I_0)						
Transition:	$S_{1OP} \rightarrow GSI_2$	$S_{1OP} \rightarrow S_{1CL}$	$GSI_2 \rightarrow OP$	$I_0 \rightarrow GS$		
Reciprocal rate (ps):	0.5	1.34	10.8	∞		

Table 4.2: Population transfer rates between the intermediary states obtained from the global analysis based on the suggested models (Figure 4.12). Note that the rates of the post-UV-pump dynamics are identical in both instances.

a concomitant rise of a new species, distinguishable by a characteristic IA maximum in the blue edge of the ΔΔOD spectrum (see the 2–10 ps ΔΔOD spectra in Figure 4.10(c)). Spectral dynamics during this stage are dominated by such features as narrowing of the principal ca. 450 nm ΔΔOD band, along with a continuous blueward shift of its spectral maximum.

3. A residual ΔΔOD signal, indicating a permanent deactivation of the photoproduct, persists within the later, post-20-picosecond photoevolution. It is evident from both the PrPP and PrPAT data that the terminal ΔΔOD spectra (4.5 ns in Figure 4.10 and 900 ps in Figure 4.11) are not entirely negative throughout the entire spectral range of the experimental window. A positive ΔΔOD peak surfaces in the blue-most spectral edge at ca. 350 nm and a positive ΔΔOD plateau can be observed in the mid-wave region, spreading throughout 450–540 nm (also see the 350 nm kinetic traces in Figures 4.10(b) and 4.11(b)).

Within the framework of the above-described PP photoevolution model, the post-repump spectral evolution presented in Figures 4.9 and 4.10 can be interpreted as follows. The NIR repump pulse at 1 ns promotes a significant

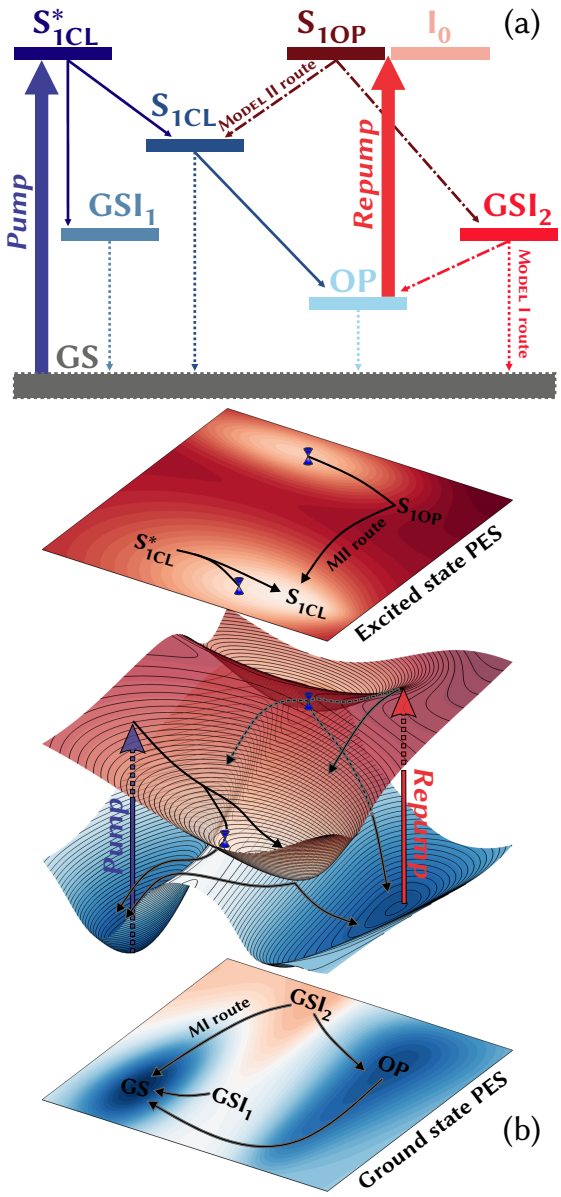

FIGURE 4.12: Generalized connectivity scheme (a) and a simplified 2D PES diagram (b) of the models used in global analysis of the IB_{1B} PP/PRPP data. States S^*_{1CL}, S_{1CL}, OP, and GSI_1 correspond to the main UV excitation photocycle. States S_{1OP}, GSI_2, and I_0 emerge only after the reexcitation of the terminal photoproduct OP. Population transfer routes that are exclusive to a certain model only are indicated by labels in both panels. Different colors of the transient states in panel (a) represent different SADS from the global fit. The rates of interstate population transfer are given in Table 4.2, whereas the SADS and the temporal evolution of the state population are given in Figure 4.13. For illustrative purposes, state-to-state population transfer along the UV-excitation reaction coordinate is depicted in solid arrows, decay to the ground state is depicted in dotted arrows and the post-repump population dynamics along the repump reaction coordinate are represented in dashed-dotted arrows in panel (a).

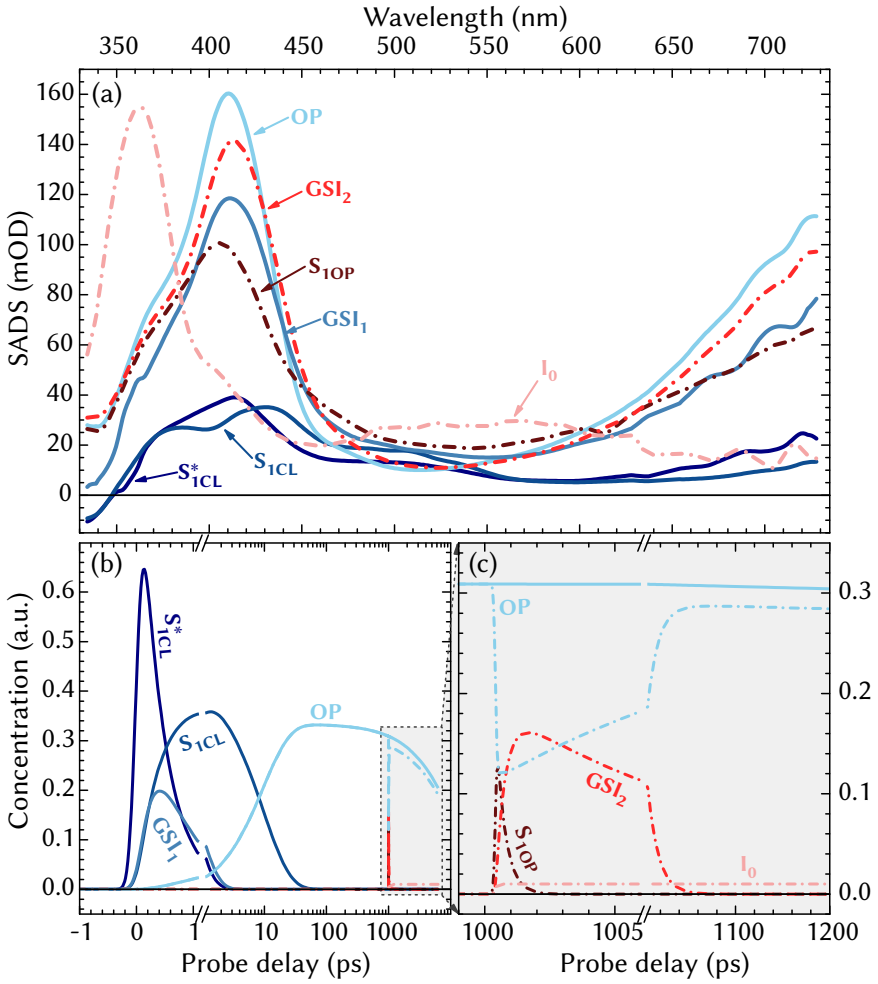

FIGURE 4.13: Panel (a): SADS of IB_{1B} obtained from global fitting of the PP/PRPP data (Figure 4.9) using the MODEL I shown in Figure 4.12. SADS of MODEL II are not depicted since they are virtually identical in their spectral shape and only differ in their relative amplitudes of states S_{1OP}, GSI_2 and I_0. Panel (b) depicts the temporal dependence of the transient state population ($c_i^{PP}(t)$ and $c_i^{PDP}(t)$ from Equations (2.24) to (2.27)). The evolution of the post-repump states is highlighted in panel (c). Component numbering and coloring are kept the same as in Figure 4.12(a). The rates of population transfer between the components are given in Table 4.2.

portion (ca. 60 %, see Table 4.2 for details) of the ring-opened population OP to a short-lived state. Judging by its sub-picosecond lifetime (and to an extent by the intrinsic absorption in the mid-band region) this state is mostly reminiscent of S^*_{1CL} from the post-UV photoevolution, which, at first glance, would suggest that reexcitation reverts the system back to its original excited state. Global analysis simulations disprove this assumption: designation of

OP $\rightarrow S^*_{1CL}$ as the main repump-induced pathway gives a poor approximation of the early post-repump data (not shown), inferring that the first post-repump transient species does not participate in the main UV excitation photocycle $S^*_{1CL} \rightarrow S_{1CL} \rightarrow$ OP. Therefore, we presume that this distinctive state can only be accessed by repumping the photoproduct (i.e., OP $\rightarrow S_{1OP}$) and assert it to the S_1 excited state of the ring-open form. A closer inspection between the SADS of S^*_{1CL} and S_{1OP} (see Figure A.9(a)) reveals that similarities of their lifetimes are merely coincidental, since both of these spectral transients peak at notably different spectral positions (ca. 1200 cm^{-1} separation between the main spectral maxima), have contrasting spectral bandwidths and shapes, and the bleaching component at $\lambda_{PR} < 350$ nm is completely absent from the SADS of the reexcitation-produced S_{1OP}.

As the spectral development during the following ca. 20 ps indicates, a new spectral transient emanates from depopulation of S_{1OP}. Judging by the rate of the ΔΔOD signal decay of in Figure 4.10, it is, yet again, tempting to designate it to the previously established S_{1CL}. This would imply that greater part of the S_{1OP} population overcomes a potential barrier separating the excited state manifolds of the ring-opened and ring-closed forms. Global analysis, however, contradicts this notion. Designation of $S_{1OP} \rightarrow S_{1CL}$ as the major post-repump pathway in the global fit provides an inadequate description of both the PP and the PRPP data (not shown) and disproves that a spectrally identical state plays a chief role in both the post-pump and post-repump photodevelopment (see Figures A.9 and A.10 for more information). In order not to overcomplicate the model, we simply assume that population of S_{1OP} is transferred yet to another repump-exclusive transient species. Interestingly enough, the numerically resolved SADS of this intermediary state (GSI_2 in Figures 4.12 and 4.13) indicates a slightly red-shifted (ca. 250 cm^{-1}) and spectrally broader replica of the open form spectrum OP.[8] This implies that the excited state S_{1OP} does not experience an intrastate cooling, contrastingly to $S^*_{1CL} \rightarrow S_{1CL}$ in the standard post-UV-pump evolutionary route, but rather is swiftly transferred to the hot ground state manifold of the open form via a conical intersection (similarly to observations in ref. [183]). The principal part of the 1–50 ps the post-reexcitation ΔΔOD spectra from Figure 4.10 can be, thus, virtually understood as a superposition of two main components: bleach of the ring-opened form (a negative contribution of the photoproduct spectrum) and IA (a positive contribution) of the repump-evoked GSI. The characteristic sub-40-picosecond ΔΔOD peak in Figure 4.10(c), in consequence, arises in the wavelength region, corresponding to the largest difference between the closely related spec-

8 Note that resurfacing of S_{1CL} would prompt a significantly more red-shifted ΔΔOD signal than one seen in Figure 4.10.

tra GSI_2 and OP, i.e., at the red wing of the original 410 nm spectral band, where the former component bares an extensive long-wave absorption slope (normalized SADS of the ground state transients are compared directly in Figure A.9). A similar redward shift from the main photoproduct spectrum can also be expected for the long-wave band of GSI_2, since we can clearly see an intersection of the two SADS at ca. 620 nm, analogous to the blue edge intersection at 385 nm of the short-wave bands (see Figure A.9). This allows us to predict a similar rise of a positive ΔΔOD signal at the long-wave slope of the second band (ca. 780–820 nm), albeit the quality of data in this region is poorer. Vibrational and/or structural relaxation of the vibrationally-hot GSI_2 causes a minor continuous hypsochromic shift of the ΔΔOD spectrum, seen in Figures 4.10(a) and 4.10(c), and an eventual decay to the metastable ground state in a matter of several tens of picoseconds ($GSI_2 \rightarrow$ OP, see Table 4.2 for details). The notion that cooling down dynamics of a hot ground state take place within this timescale is also corroborated by the behavior of the bleaching signals in Figures 4.10(a) and 4.10(c)—concomitant to the temporal decay of GSI_2, the bleached short-wave band broadens and red-shifts to its supposed spectral position at ca. 410 nm.

It is worth noting that, despite the first-glance similarity of the SADS of GSI_1, GSI_2, and OP (see Figures 4.13 and A.9), their representative states are intrinsically different (which can be easily determined from their diverse lifetimes, varying from sub-1-picosecond of GSI_1 to ca. 12 ns of OP) and are all obligatory to fully describe the time-resolved data. Inclusion of the final-photoproduct-resembling intermediate GSI_1, as discussed earlier, is necessary for a correct broadband characterization of the sub-picosecond PP photodynamics. The same concept applies for the intermediate GSI_2. Even with the implication that both GSI_1 and GSI_2 belong to the ground state manifold of the ring-opened form, the intrinsic temporal and spectral differences between them indicate that they either belong to different points of the ground state PES (as depicted in Figure 4.12(b)), or that the ground state PES is to a certain extent "deformed" due to the filling of the vibrational states (since the post-repump population experiences the OP manifold in which the low frequency modes are, to a degree, occupied). The short lifetime of the early post-UV-excitation surfacing state GSI_1—which was previously identified an "unstable" configuration within the bond-cleaved (albeit not fully ring-opened) configuration manifold [192]—suggests that this state lies closer to a saddle point on the PES and leads to a fast deactivation of the evolving system to the molecular ground state. State GSI_2, on the other hand, has a much longer lifetime ($\tau_{GSI_2}/\tau_{GSI_1} \approx 30$, see Table 4.2) and, as a result, more likely represents a local

maximum on the open ring-opened manifold, mainly through which state OP is repopulated (see Figure 4.12(b)).

It is possible to add a constraint to the fitting procedure, requiring some or all of the spectra attributed to GSI_1, GSI_2, and OP to be identical (they are highly similar after all). However, if such requirements are added, the resulting estimates of the PP and PRPP spectra begin to greatly deviate from the experimental values in the most "sensitive" regions, where the SADS of the interacting states differ the most, i.e., at $\lambda < 380$ nm or 450–600 nm in our experimental window (see Figure A.9(c)). An example of the fit where GSI_1 and GSI_2 were required to have identical spectra is, for illustrative purposes, presented in Figure A.10. Therefore, we have to conclude that seven—four for PP and three for PRPP—is the smallest amount of independent spectral components needed to adequately describe the pre- and post-repump spectral dynamics of the IB_{1B} photochromic system, without over-parameterizing the kinetic model.

4.3.4.3 *Ionization of the Ring-Opened Photoproduct*

If ring-closing was the sole repump-induced photoreaction, the late ΔΔOD spectra (t_{P_R} or $t_{RP} > 100$ ps in Figures 4.10 and 4.11) then would be exclusively composed of photoproduct bleach. The late ΔΔOD spectra in Figures 4.10 and 4.11, on the other hand, indicate residual repump-induced absorption both in the NUV ($\lambda_{P_R} < 400$ nm) and the mid-VIS (450–550 nm) spectral regions that undoubtedly emanates from a separate spectral species. In order to account for these phenomena, we have added an additional repump-induced pathway OP → I_0 with a yield of ca. 3 % that leads to the formation of a separate, indefinitely long-lived species ($\tau_{I_0 \rightarrow GS} = \infty$, since these post-reexcitation effects decay outside the temporal window of the experiment).[9] The resulting species I_0 differs significantly from the remaining SADS, exhibiting a sharp absorption peak at 360 nm and a semi-continuous IA plateau, which extends beyond the NIR boundary of our spectral window (see Figure 4.13(a)). While solvated electrons in MECN exhibit a similar featureless absorption plateau in the 400–700 nm spectral region [195, 196], they, for the most part, can be ruled out as a possible source of this ΔΔOD signal, since the lifetime of the excess electron population in MECN is only ca. 80 ps [195, 196]. More likely these long lasting absorption effects stem from the ionization of the photoproduct and a concomitant formation of a solvated electron/radical pair. The high energy NIR pulse creates a long lived UV-active solvated electron/radical

9 The "real" lifetime of these species is below 1 ms, since no accumulation effects were observed during the experiments.

species (similar effects have previously been observed in other three pulse experiments [33, 187, 197, 198]). Interestingly enough, the PRPAT measurements show that the metastable ring-opened form is more susceptible to repump-induced ionization. The PRPAT spectra in Figure 4.11(c) indicate, the early (positive) ΔΔOD signals are exact spectral replicas of the final photoproduct (for comparison, normalized early PRPAT spectra and SADS of component OP are presented in Figure A.11), whereas the late repump spectra show definite indications of the predicted radical form, implying that the ring-opened form has a lower ionization potential.

4.3.4.4 *Repump-Induced Molecular Back-Switching Dynamics*

While the suggested appearance of an excited transient S_{1OP}, a vibrationally hot GSI_2, and the ionic form I_0 explains the spectral constitution of the post-reexcitation transient spectra, the switching back dynamics remain, to a certain extent, ambiguous. In order to address both the light-induced forward and backward switching processes, we propose two possible evolutionary schemes (see Figure 4.12 and Table 4.2) that complement the previously suggested branched evolution model:

I. The first model explains the back-switching mechanism via a direct involvement of the hot ground states. This model suggests that after the reexcitation, population of S_{1OP} is coupled back directly to the hot ground state manifold without any significant population losses ($S_{1OP} \rightarrow GSI_2$). Within the ground state PES the molecules experience either a several tens of picoseconds lasting vibrational cooling to the ground state potential minimum $GSI_2 \rightarrow OP$, or a ring-closing reaction to the main molecular ground state. This ring-closing reaction is incorporated in the said model as direct hot ground state leakage $GSI_2 \rightarrow GS$, somewhat similarly to the merocyanine-to-spiropyran re-isomerization reaction described in ref. [185]. In other words, molecules with excess vibrational energy are presumed to have a higher probability to overcome the (now reduced) potential barrier separating the ring-opened and ring-closed potential minima. With the kinetic rates being $\tau_{GSI_2 \rightarrow OP} = 12\,ps$ and $\tau_{GSI_2 \rightarrow GS} = 195\,ps$ (see Table 4.2), ca. 6 % of the reexcited state population is returned back to the main molecular ground state before GSI_2 is ultimately depopulated.

II. The second model also incorporates the appearance of hot ground state transient GSI_2 in the ring-opened form, however, it suggests a different repump-induced ring-closure pathway. In this model, the evolution

on the hot ground state manifold of the photoproduct is assumed to be unidirectional, i.e., GSI_2 is not "leaky" and all of the hot ground state population is transferred back to the potential minimum of the ring-opened form. Instead, a linkage—presumably a potential energy barrier that can be overcome with excess vibrational energy, as depicted in Figure 4.12(b)—between the excited state manifolds of both the ring-opened and ring-closed forms (i.e., states S_{1OP} and S_{1CL}) is assumed to be present, thus allowing a portion ($< 30\,\%$) of the reexcited population to revert back to the original excited state S_{1CL} ($S_{1OP} \rightarrow S_{1CL}$ in Figure 4.12). These species repeatedly undergo the lossy route of the "standard" UV excitation ($S_{1CL} \rightarrow$ OP) and the ring-closing results as a consequence of direct transient state leakage ($S_{1CL} \rightarrow$ GS, see Table 4.2 for the appropriate transfer rates).

Despite the implied photophysical differences, both models are not fundamentally different from a kinetic perspective. It is obvious from Table 4.2 that in either case the vast majority (100 % in MODEL I and ca. 73 % in MODEL II) of the reexcited state population ends up in the hot ground state manifold. The only uncertainty, from a purely numerical standpoint, is whether the back-switching proceeds directly via the post-repump (GSI_2) or the "original" (S_{1CL}) states. The PRPP experiments cannot unambiguously answer this question since:

(a) the molecular state S_{1CL} is not fluorescent (a resurfacing SE would be observed in the PRPP signals if a radiative decay route was present);

(b) due to relatively low back-switching yield, it is hard to resolve the "original" states, with their signals being less than 3 mOD (i.e., $< 30\,\%$ of the entire PRPP difference signal according to MODEL II).

With the current knowledge available both models give a valid description of both the PP and PRPP dynamics with the minimal amount of SADS and, due to the intricacy of the PRPP signals, it is hard to choose a clear preference of one over the other.

4.3.4.5 *Interpretation of the PRPAT Dynamics*

PRPAT signals in Figure 4.11 indicate that an early reexcitation causes a net increase of the entire IA signal of the ring-opened form. This effect is closely linked to the short-lived states S^*_{1CL} and GSI_1, since the largest net growth of ca. 6 % is achieved within their lifetime (at ca. $t_{RP} \approx 400\,\text{fs}$). This allows us to predict that either:

(a) reexcitation prior to depopulation of state S^*_{1CL} promotes the molecular system to a higher excited state ($S_{n>1}$, for the sake of simplicity not pictured in Figure 4.12(b)), thus causing an indirect formation of the ring-opened species OP (e.g., $S^*_{1CL} \rightarrow S_{n>1} \rightarrow S_{1OP} \rightarrow GSI_2 \rightarrow OP$);

(b) a portion of the molecules "lost" due to formation of GSI_1 are returned back to the excited state manifold ($GSI_1 \rightarrow S^*_{1CL}$), hence allowing them to undergo the photocycle.

In other words, via some repump-induced "shortcut" certain lossy pathways, like $S_{1CL} \rightarrow GS$ or $S^*_{1CL} \rightarrow GSI_1 \rightarrow GS$, are ultimately overcome. Decay of the excited state leads towards the gradual development of the terminal photoproduct (see Figure 4.13(b)), whose appearance in the PRPAT signals is mirrored by the intensification of the negative ΔΔOD at $t_{RP} > 1$ ps. Growth of this signal at $t_{RP} = 1$–20 ps and its stabilization at $t_{RP} = 20$–100 ps roughly coincide with the buildup of the ring-opened isomer (see Figure 4.9). This result is to be expected (similar effects were reported before in ref. [31]), given that, as t_{RP} nears t_{PR} in the PRPAT experiment, progressively more ring-opened molecules are affected by the repumping pulse and are thereby able to undergo the formerly discussed reexcitation-induced molecular back-switching process. Due to the intricate arrangement of both the excited and ground state PES's it is difficult to predict a precise early reexcitation photoevolutionary pathway. Additional PRPP measurements at several different early reexcitation instances prior to formation of the photoproduct (e.g., $t_{RP} = 0.5$–10 ps) could clarify any of the above-proposed sub-picosecond repump pathways, albeit this would raise the difficulty of not knowing which exact state is monitored in this kind of measurement (see the state population dependence in Figure 4.13(b)).

4.3.5 *Conclusions*

We have investigated the light-induced oxazine ring-opening and ring-closing reactions of a structurally substituted IB-type photochromic compound. Our measurements indicate that its photocycle can be controlled by a properly timed UV/NIR pulse sequence. A NIR reexcitation pulse, succeeding directly after ($0 < t_{RP} < 1$ ps) the primary UV actinic excitation pulse, causes a 6 % net increase of the photoproduct population, whereas a late reexcitation ($t_{RP} > 100$ ps) triggers a ring-closing reaction with a similar efficiency. PRPP experiments indicate that more than half of the photoproduct population can be reexcited to a short lived state—most likely S_1 of the ring-opened form—that eventually decays to hot ground state manifold of the ring-opened form. A portion (ca. 3 %) of the photoproduct population is ionized, leading to the

formation of a long lived (> 6 ns) electron/radical species. Two models, based on global analysis of the time-resolved data, are suggested to interpret the post-repump photodevelopment. The first model implies that the hot ground state manifold of the ring-opened form is "leaky" and molecules with excess vibrational energy can be coupled back to the main ground state of the ring-closed form. The second model predicts that a fraction of the reexcited state population is reverted back to an early transition state, thereby repeating the initial lossy photoevolution pathway.

5

REDEFINITION OF THE INDOLOBENZOXAZINE PHOTOCHROMISM

5.1 SHADOW OF A DOUBT: THE TRIPLET PATHWAY HYPOTHESIS

Ever since the introduction of the IB photochromic family [163–166, 168, 193, 194] two concepts of their photodynamics were, more or less, acknowledged indisputably. The first of them is the notion that the ΔOD spectra of photoexcited IBs can be assigned to the ground state of the ring-opened IB isomer. IBs were normally assumed to be positively photochromic and their photochromism was purportedly associated with UV excitation-induced C–O bond breakage and the sub-nanosecond formation of IND and pNPH chromophores, the latter of which exhibits absorption in the blue part of the VIS spectrum [164–166, 168]. The discrepancies of the ΔOD spectra from the indicative pNPHE-like anionic band at 430 nm were typically attributed to either influence of the imposed substitutions to the molecular backbone[1] or the intrinsic differences between the electronic nature of the chemically- and optically-generated species. In essence, the general spectral resemblance was deemed to be close enough and was not questioned any further. Nevertheless, a more thorough comparison of the steady-state and the ΔOD spectra indicates that such attribution is somewhat dubious. In fact, even in the case of the simplest unmodified photochromic oxazine IB_o (see Figure 4.1(g)), the maximum of its TA spectrum (ca. 440 nm) does not perfectly coincide with the absorption maximum of the chemically-induced species (ca. 430 nm); furthermore, there is a broad IA plateau extending redwards from the main IA band, which is absent in the steady-state absorption spectra of chemically-opened compound [163, 166]. Therefore, the very assignment of TA bands of photochromic oxazines to ring-opened forms can be generally put to question.

The other *de facto* concept, that eventually had to be revisited, is that of the IB excited state multiplicity. The vast majority of pioneering works on IB

1 Since structural alterations to the basic IB chemical structure can heavily alter the TA spectra, see refs. [166, 177, 192].

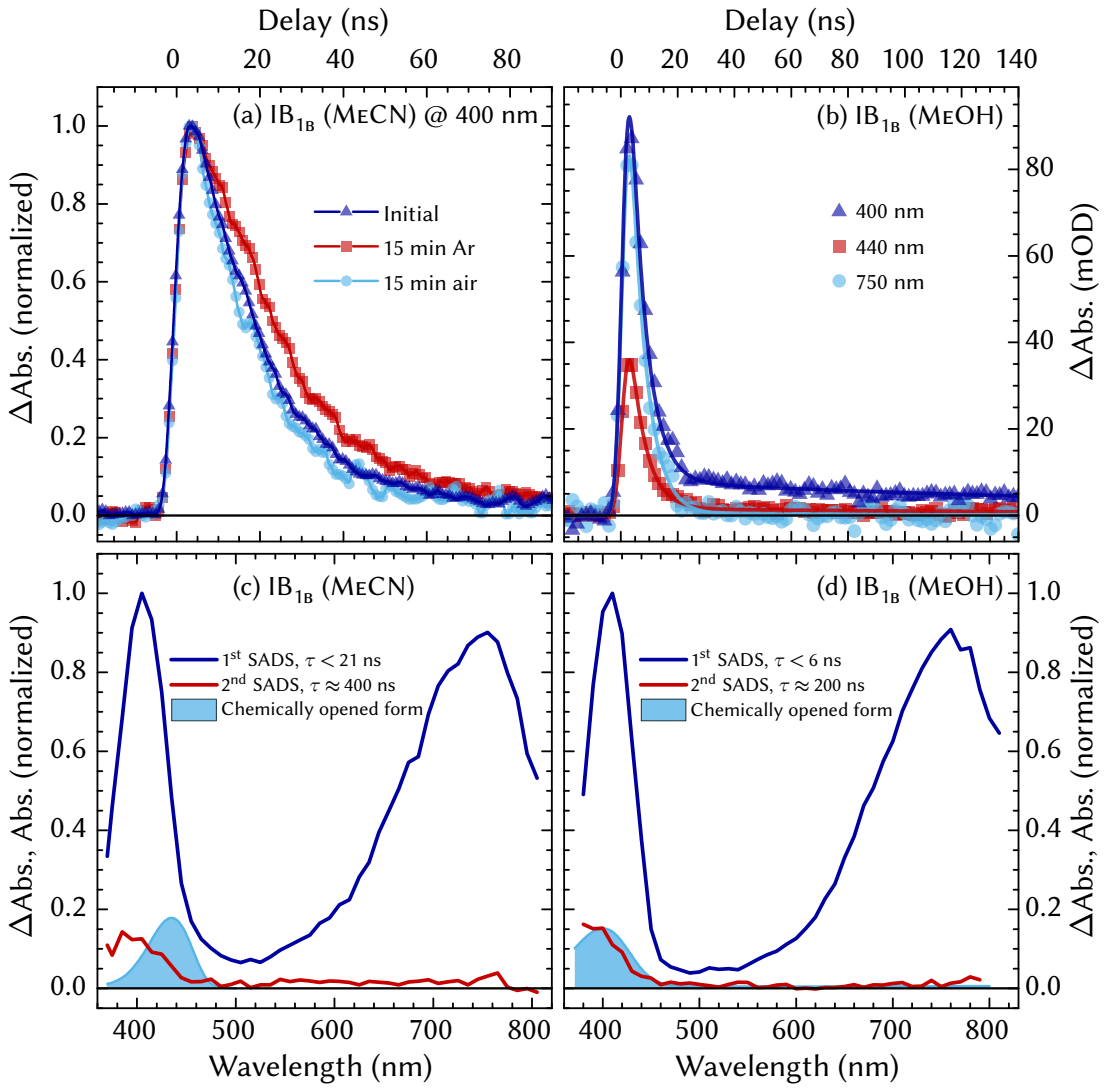

FIGURE 5.1: Panel (a): kinetic traces of IB_{1B} in MeCN, measured at 400 nm before (blue) and after (red) purging the solution with argon for 15 min. Orange traces correspond to recovered original traces obtained after argon purged solutions were flushed with ambient air. Panel (b): FP results of IB_{1B} in MeOH solution. Panels (c) and (d): global analysis of the nanosecond-resolution FP data of IB_{1B} in, respectively, MeCN and MeOH. Cyan plots depict the steady-state absorption spectra of chemically ring-opened forms in MeCN. Refer to ref. [199, 200] for additional information on the experimental methodology and conditions.

photodynamics [163–165, 168] have claimed that triplet states does not participate in the IB photoevolution. As a matter of fact, the triplet states were generally dismissed in Section 4.2.4.2 due to the relatively short recovery times to S_0. In fact, establishment of the (presumably) ring-opened IB isomer ex-

clusively via a singlet pathway, was one of the key "appeal" factors of the photochromic [1,3]oxazines, since absence of a triplet state effectively reduces the possibility of interaction with molecular oxygen (and, hence, formation of the destructive $^1\Delta_g$) [163]. Nonetheless, the photoinduced photochromic opening of oxazine ring was suggested to occur via the triplet state PES due to experimentally observed triplet → triplet energy transfer in BODIPY-oxazine dyads in a study by Raymo [182]. A computational study provided a mechanistic model of the IB excitation dynamics, in which ring-opened photoisomer is formed in the triplet state, followed by intersystem crossing to the singlet ground state of the ring-opened species [182].

Both of these assumption were put to test in an experimental FP study by Voiciuk et al. [199]. Results of the said study are outlined in Figure 5.1 and can be summarized as follows:

1. The triplet character of IBs was tested by removing dissolved oxygen from the sample solution. TA at 400 nm was monitored before and after the oxygen removal by purging the MeCN solution with argon for 15 min. The results shown in Figure 5.1(a) reveal a slight prolongation of the relaxation time after oxygen removal. The initial decay rate, as estimated by monoexponential fitting of the kinetic traces, is equal to 21 ns. For compound IB_{1B} a 4 ns increase was observed after oxygen purging. The observed change in lifetime is very small, albeit discernible and reproducible. To rule out the possibility of this observation being due to some modification of the sample during the argon purging procedure (i.e., contamination), after the measurement on the de-oxygenated sample, the solution was purged with air to restore the equilibrium oxygen concentration. The control measurement on re-oxygenated sample revealed the recovery of the original kinetic traces (cyan curves in Figure 5.1). According to the Stern–Volmer relationship, for lifetimes as short as 21 ns, a complete removal of the quencher would result in 10–20 % increase of the lifetime [199]. This means that the quantitative effect of oxygen removal, observed in these experiments, is perfectly consistent with the calculations, assuming the triplet character of the excited state.

2. A more effective solvation and stabilization of the zwitterionic ring-opened IB forms could be expected in protic solvents. To test the solvent influence on the excited state dynamics of IB_{1B}, FP measurements were performed in MeOH solutions. The presence of two transient species is clearly discernible in the kinetic traces in Figure 5.1(b). The initial signal decays very rapidly at all wavelengths, with lifetimes shorter

than the sub-5-nanosecond IRF. Subsequently, in the second stage of the spectral evolution kinetic traces in the 380–460 nm region, instead of decaying to zero, reveal an emergent contribution of a long-lived component with an absorption band, centered at 400 nm (in the kinetic traces of IB_{1B} in Figure 5.1(b) the long-lived component manifests as an offset, which comprises about 10 % of the initial signal amplitude). The experiments in alcohol solutions revealed spectral signatures similar to those observed in MeCN with an important addition of a long-lived (ca. 200 ns) species (see Figures 5.1(c) and 5.1(d)), exhibiting excellent spectral resemblance to chemically opened forms. The similarity of the initial transient spectra to those recorded in MeCN allows tentative attribution of these spectra to the triplet states. The long-lived spectral features (see Figure 5.1(d)) were (fairly confidently) assigned to the ring-opened isomers. The general connectivity scheme, used in global analysis of the experimental data in alcohols (see ref. [199]), was tested on data obtained in MeCN to re-examine tiny small long-lived components observed (but largely ignored) in previous nanosecond-resolution studies. However, global analysis of the FP data has revealed that the spectra of the long-lived species bear little resemblance to that of the chemically opened forms (see Figure 5.1(c)), and the origin of the long-lived spectral features observed in MeCN still remains to be determined.

These observations called for additional structure-sensitive methods to elucidate on the nature of the IB post-UV-excitation photodynamics.

5.2 A FEMTOSECOND STIMULATED RAMAN SPECTROSCOPIC STUDY ON THE OXAZINE RING-OPENING DYNAMICS OF STRUCTURALLY-MODIFIED INDOLOBENZOXAZINES

5.2.1 *Introduction*

Even though numerous sub-microsecond [164–168] and sub-nanosecond [134, 176, 192] time-resolved studies have been carried out on IB compounds, the mechanism of their photodynamics remains unclear. As briefly presented in the section above, spectral discrepancies between the chemically ring-opened and the optical excitation-induced forms [168, 177], prominent influence of the molecular substitutions [166, 177, 192], and the dependence of ground state recovery times on molecular oxygen level [182, 199] have led to suggestions that an intersystem crossing process effectively competes with the oxazine ring-opening. A certain level of ambiguity stems from the fact that all time-

resolved studies on IBs, performed until now, were based on the electronic absorption spectra [134, 162, 164–168, 176, 177, 182, 192, 199, 201] that inherently provide very little explicit information on the structural changes of the molecule, thus suggesting that structure-sensitive spectro-temporal methods are necessary to provide a more comprehensive understanding of the intricate IB photodynamics. Moreover, the current knowledge of the vibrational behavior of these molecular species is rather scarce. In this chapter we aim to address these issues by presenting a joint theoretical/experimental study elucidating the vibrational statics and dynamics of the IBs. We employ FSRS spectroscopic techniques [38–40, 202] to analyze the ground- and the photoexcited-state vibronic development of several selected members of the IB family. These experiments shed additional insight to the general photophysics of IBs and, to our knowledge, this is the first vibrational study–both steady-state and time-resolved–on compounds of this kind.

5.2.2 *Materials and Methods*

For the study, we have selected several previously investigated (refs. [134, 177, 192, 199] and the bulk of Chapter 4) IB compounds with phenylic substituents in the *para* position, relative to the nitrogen of the indole ring: IB_{1B} (4-methoxyphenyl substitution, orange structural formula in Figure 5.2(a)) and IB_{1A} (3-chlorophenyl substitution, blue structural formula in Figure 5.2(a)). These compounds were chosen mainly for their relatively high quantum yield [177], compared to numerous other IBs [162, 164, 165, 167, 168], and excellent photodynamic stability [177]. The unsubstituted ("base") compound IB_o [164, 165, 168, 176] was, for comparative purposes, studied only via steady-state (i.e., SRS) techniques, since its lower quantum yield [164, 165, 168] and fatigue resistance [177] proved to be inadequate for time-resolved FSRS measurements (which necessitated higher excitation intensities to produce a feasible amount of the excited state population). The ground state absorption of the phenyl-substituted IBs peaks at ca. 290–300 nm, while the TA of their photo-induced forms is distinctive for its double-band structure, peaking in the UV/VIS (415 nm for IB_{1B} and 375 nm for IB_{1A}) and the VIS/NIR (750 nm for IB_{1B} and 600 nm for IB_{1A}) boundaries. These spectra are in striking contrast to the ones of the chemically-induced ring-opened forms—produced via addition of tetrabutylammonium hydroxide (TBAH) to the sample solutions [164, 165, 168, 177, 199]—that exhibit only a single spectral maximum in the VIS/NIR region, peaking for both compounds at ca. 430 nm [177, 192, 199] (see the red spectrum in Figure 5.2(a)).

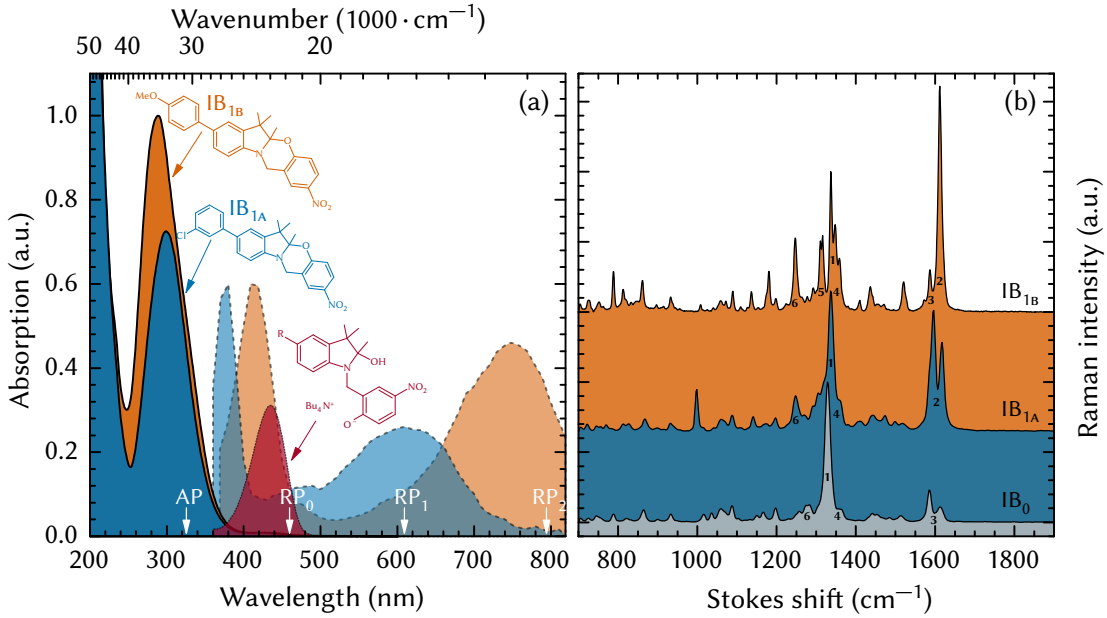

FIGURE 5.2: Panel (a): steady-state (solid lines, opaque plot area) and excited-state [177, 192] (dashed lines, transparent plot area) absorption spectra of the phenyl-substituted IB-type compounds IB_{1B} (orange) and IB_{1A} (blue) dissolved in MeCN (the dotted line/semi-transparent red plot represents the NUV–VIS part of the chemically-opened form steady-state absorption spectrum [177]). The molecular structures of the compounds are presented adjacent to the proper spectra; arrows on the bottom abscissa indicate spectral positions of the actinic and the Raman pump pulses. Panel (b): steady-state SpRS spectra of compounds IB_{1B}, IB_{1A}, and the unsubstituted indolo[2,1-*b*][1,3]benzoxazine IB_o [165, 168, 176]. The spectra are offset vertically and normalized in respect to the ca. 1330 cm^{-1} $-NO_2$ band for better viewing. Numbers indicate the positions of several significant spectral peaks (see Table 5.1).

FSRS experiments were performed using a home-built spectroscopic setup introduced in ref. [203] and Section 2.3. Two different types of Raman measurements were simultaneously performed on the IB solutions:

(a) Steady-state SRS (without the actinic pulse, see Equation 2.14) on the chemically ring-opened IB forms (i.e., investigation of the characteristic ground state Raman frequencies of the blue-absorbing ring-opened molecules);

(b) Time-resolved FSRS on the photoexcited IB species (i.e., investigation of the time-dependent vibrational changes, occurring after the UV photon absorption).

Crystalline IB samples were dissolved in MeCN (Lichrosolv, gradient grade) and diluted to an appropriate concentration for the either of the experiments. In the time-resolved FSRS experiments both of the IB samples, concentrated to 1 OD at 325 nm in a 1 mm optical pathway, were excited with $\lambda_{AP} = 325\,nm$, $E_{AP} = 1\,\mu J$, $\tau_{AP} = 70\,fs$ actinic pulses, while the Raman pumps were set to either $\lambda_{RP} = 795\,nm$,[2] $E_{RP} = 5\,\mu J$, $\tau_{RP} = 3.5\,ps$ for IB_{1B}, or $\lambda_{RP} = 610\,nm$,[3] $E_{RP} = 4\,\mu J$, $\tau_{RP} = 4\,ps$ for IB_{1A}. In the steady-state SRS experiments the concentrations were slightly increased in order to produce a sufficient amount of ring-opened species via introduction of a small amount (ca. 10 µL) of highly-concentrated TBAH (1.0 M in MeOH, Alfa Aeser) to the IB solutions. Samples of 1 OD at 450 nm were used in the steady-state SRS measurements. The ground-to-excited state SRS resonance was achieved with $\lambda_{RP} = 460\,nm$,[4] $E_{RP} = 2\,\mu J$, $\tau_{RP} = 2\,ps$ spectrally-narrowed pulses.

Tunability of narrowband Raman pump in our FSRS setup is generally limited to ca. 390–400 nm on the short-wave side (i.e., 2nd harmonic of the fundamental Ti:Sa radiation, see Section 2.3.3), which disallows resonant enhancement of the UV-absorbing IB solutions (see Figure 5.2(a)).[5] Spontaneous Raman scattering (SpRS) spectra of crystalline IB samples were measured as an alternative. SpRS spectra of samples IB_{1B} and IB_{1D}[6] were recorded using an Echelle-type spectrometer RamanFlex 400 (PerkinElmer, Inc.), equipped with a thermoelectrically cooled (up to −50 °C) CCD camera and a fiber optic cable for excitation and collection of the Raman spectra in a 180° scattering geometry. The excitation of the IB samples was performed with a $\lambda = 785\,nm$, $P = 30\,mW$ diode laser radiation, focused to a 200 µm diameter spot. The resolution of the experiments was ca. $1\,cm^{-1}$. SpRS spectra of samples IB_{o}, IB_{1A}, and IB_{1C}[6] were recorded using a FT-Raman spectrometer Multiram (Bruker Optik GmbH). The excitation was performed with a $\lambda = 1064\,nm$, $P = 300\,mW$ Nd:YAG laser, and the spectra were recorded with liquid nitrogen cooled germanium diode detector. The resolution of the experiments was ca. $4\,cm^{-1}$. All of the above-described SpRS measurements were performed on crystalline IB samples at room temperature.

A computational study was conjointly performed to characterize the fundamental vibrational modes of the investigated IBs. Molecular structures of the IB compounds in ground electronic state were optimized using density-

2 Spectrally-filtered fundamental Ti:Sa radiation.

3 Bandwidth-limited 2nd harmonic of the HP-OPA signal wave.

4 Bandwidth-limited 4th harmonic of the HP-OPA idler wave.

5 Additional restraints arise due to limitations of the employed diffraction optics that restrict the resolution to ca. $20\,cm^{-1}$ in the NUV region.

6 See Figure A.12 for the supplementary SpRS/FSRS measurements on IB_{1C} and IB_{1D}.

functional theory [204] with B3LYP functional [205] and cc-pVTZ basis set [206]. Vibrational frequency analysis including anharmonic corrections [207] and calculation of Raman scattering activities were carried out for the optimized structures. Calculations were performed using GAUSSIAN09 package [208], using computational resources at the High Performance Computing Center HPC SAULĖTEKIS (Vilnius University, Faculty of Physics) [209]. Obtained scattering activities were subsequently converted to simulated Raman intensities by calculating scattering cross-section [210] (λ_0 and T values were taken from corresponding experiments).

5.2.3 *Results and Discussion*

The ground state SpRS spectra of the phenyl-substituted IBs (see Figure 5.2(b)) feature a multitude of vibrational bands, most prominent of which surface at ca. 1330 cm^{-1} and 1600 cm^{-1}. The intense vibrations at 1330 cm^{-1} are observed for all compounds of the IB variety and can be ascribed to the symmetric $-NO_2$ stretching in the pNPH moiety [212, 213]. While the 1600 cm^{-1} region also envelops the relatively weaker antisymmetric $-NO_2$ vibrations [212] (as exhibited by the unsubstituted IB_o in Figure 5.3), the substantially intensified vibrations of IB_{1B} and IB_{1A} that arise in the particular spectral vicinity are of a different origin. The intense ca. 1600 cm^{-1} vibrations in the substituted IBs stem from the phenylic extensions of the molecule and can be ascribed to the biphenyl-like symmetric inter-aromatic ring stretching in

No.	Intensity	IB_o	IB_{1B}	IB_{1A}	Description
1.	Very strong	1334	1331	1332	$-NO_2$ deformation
2.	Very strong	—	1604	1588, 1609	Biphenyl ring stretching along axis
3.	Strong	1585, 1615†	1582†	1583†	Phenyl ring and $-NO_2$ stretching
4.	Strong	1315–1360	1315–1360	1315–1360	CH_2 out-of-plane deformations
5.	Strong	—	1282, 1306	1282	Biphenyl ring CH rocking/twisting
6.	Strong	1233†	1237	1237	Various CH bends

TABLE 5.1: Calculated properties (frequencies (in cm^{-1}) and relative intensities) of steady-state Raman scattering of IB compounds. The scattering intensities can be assessed from Figure 5.2(b). The values marked with daggers (†) denote peaks of a given character that are less pronounced in the corresponding compounds (as evident in Figure 5.2(b)). A full list of characteristic vibrational frequencies is presented in the supporting material of ref. [211].

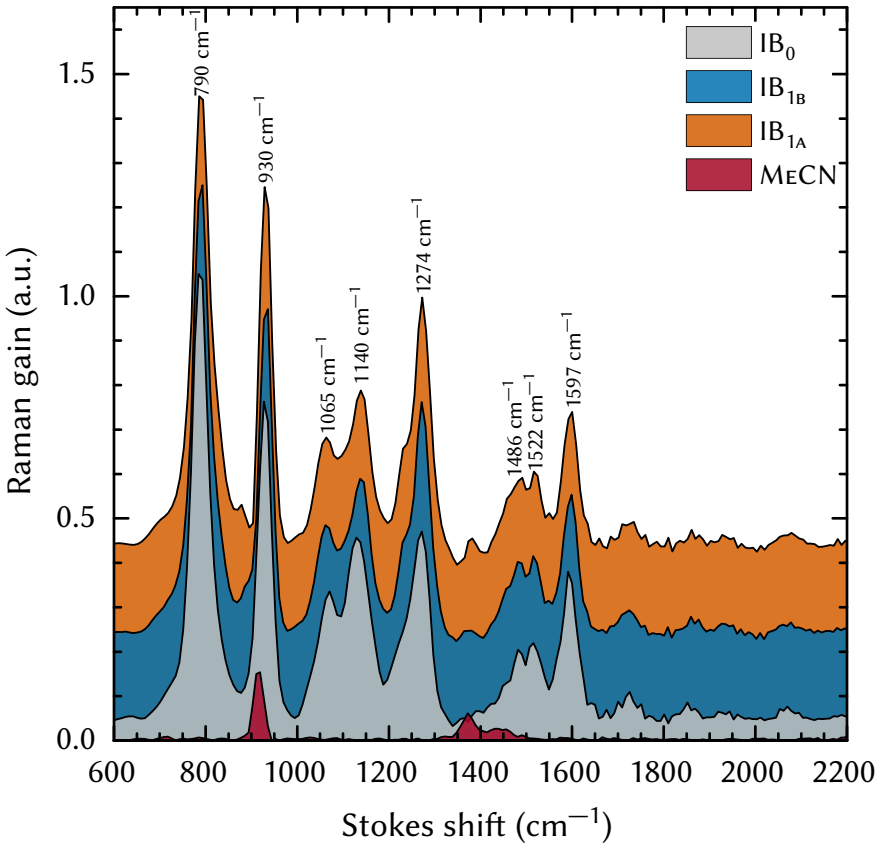

FIGURE 5.3: Baseline- and solvent line-corrected ground state SRS spectra of the chemically ring-opened forms (via addition of TBAH to the sample solutions) of IB_{1B}, IB_{1A} and the unsubstituted IB compound IB_0. The resulting anionic pNPHE-like forms exhibit strong absorption at ca. 430 nm (red spectrum in Figure 5.2(a)) that allows us to exploit the 460 nm resonant enhancement conditions (RP_0 in Figure 5.2(a)). The SRS spectra are normalized and offset vertically for better viewing. Red spectrum depicts the properly scaled (according to the 2250 cm^{-1} C≡N line) FSRS spectrum of MeCN (spectral data beyond 2200 cm^{-1} is not depicted, as it bears no significant vibrational contribution from the IB compounds).

the phenyl-indole moiety [214–216] (see also Figure A.12). The phenylic substituents also give rise to reasonably intense aromatic ring rocking/twisting vibrations appearing in the close proximity of the $-NO_2$ peak at ca. 1280–1300 cm^{-1}. Ascription of the key vibrational modes of the investigated compounds is outlined in Table 5.1, whereas a full list of nearly 40 characteristic Raman bands can be found in the supporting material of ref. [211].

In Figure 5.3 we can see that in spite of the alterations to the molecular backbone (or the eventual differences emanating in the electronic excited state evolution [134, 176, 177, 192]), the chemically-induced open-ring conforma-

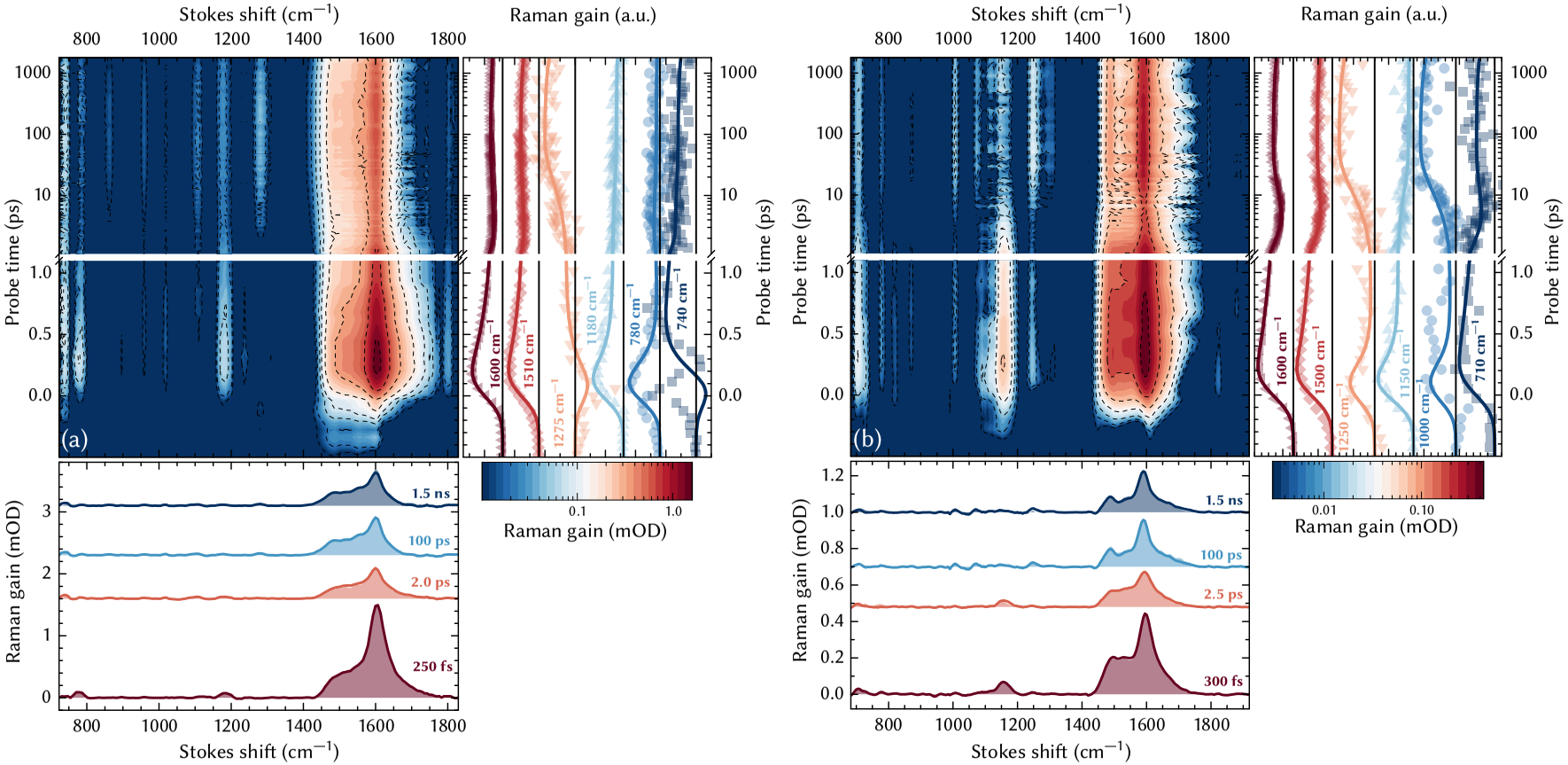

FIGURE 5.4: FSRS spectra of compounds (a) IB_{1B} ($\lambda_{RP} = 610\,nm$), and (b) IB_{1A} ($\lambda_{RP} = 795\,nm$). The entire experimentally-resolved and background-corrected FSRS signals are presented in the central graphs, whereas the right-hand side and bottom graphs depict, accordingly, spectral and temporal cuts of the FSRS dataset. Note that the time-gated FSRS spectra (bottom) are offset vertically from the zero line, and the kinetic curves (right-hand side) are offset vertically and normalized for better viewing. Experimentally-resolved points are presented in discrete symbols and area-filled curves, while the continuous lines in all of the graphs represent results of a four component global fit of the experimental data (see Table A.1 for more details).

tions of all the investigated compounds exhibit virtually identical SRS spectra. This equivalence allows us to assume that the SRS features in Figure 5.3 belong mainly to the pNPHE moiety, considering that the blue-absorbing ionic chromophore is predominantly resonant with the 460 nm Raman pump (for explicitness, properly scaled SRS lines of the solvent are presented in Figure 5.3; the indole segment of the bond-cleaved molecule is an unlikely candidate to be stimulated by the utilized Raman pump, as it absorbs principally in the UV [176, 217, 218]). The majority of higher frequency ($> 1000\,cm^{-1}$) vibrational bands, that accompany the chemical ring-opening, generally correlate with the ones, observed upon the deprotonation of pNPH [219, 220]. While there are some discrepancies between the absolute positions and the relative amplitudes, in view of the main pNPHE spectral peaks [219, 220], the general outline of the Raman spectrum is, by and large, similar. Most notably, formation of pNPHE prompts a decline of the intense ca. $1330\,cm^{-1}$ $-NO_2$ vibrations that redshift [219] and, likely, change their vibrational character [220] following the reaction. Moreover, the SRS signals at ca. $1400–1600\,cm^{-1}$ are common to all of the IB compounds, including the unsubstituted IB_o. This suggests that in the ring-opened forms they stem from the pNPHE-like $C–O^-$, C–C, and C–H [219] vibrations (since the intense phenyl-indole vibrations, that occupy the same spectral region in Figure 5.2(b), cannot surface in the SRS spectrum of the unsubstituted IB_o). Perhaps one of the most distinguishing vibrational features of the chemically-opened form SRS spectra are the two intense Raman bands, emerging at 790 and $930\,cm^{-1}$. Interestingly, none of the particular bands can be associated exclusively with formation of the pNPHE moiety. While pNPHE does in fact exhibit a characteristic intense lower-frequency Raman peak [219, 220]—i.e., joint $-NO_2$ and C–C vibrations at $858\,cm^{-1}$ [219]—the SRS peaks in Figure 5.3 are interspersed from the "expected" spectral location by $\pm 70\,cm^{-1}$ (which is somewhat too large to be interpreted as Fermi resonance splitting of the band). While it is unclear whether these two bands appear due to either the probable upshift of the said mode, accompanied by an intensification of the ring-breathing in the indole fragment at ca. $760\,cm^{-1}$ [221], or the possible intra-chromophore vibrations, developing intrinsically from the C–O bond dissociation, it is nonetheless evident that the emergence of these intense Raman modes is one of the key "identifiers" of the ring-opening reaction of an IB molecule.

In contrast to the multitude of well-defined spectral peaks of the chemically-induced open-ring forms, the time- and wavenumber-resolved FSRS datamaps in Figure 5.4 indicate the presence of a single dominant vibrational band that prevails through both the early and the late stages of the IB photoevolution. It should be noted that due to the relatively low Raman yield of

the IB samples, as well as the significant deviation of both 610 and 795 nm Raman pumps from the ground state electronic resonances ($> 15\,000\,cm^{-1}$, see Figure 5.2), bleaching contributions do not surface in either of the time-gated FSRS spectra. This observation, along with the fact that the pre-actinic pump interaction FSRS signals are zero, allows us to designate all the Raman gain signals in Figure 5.4 entirely to the excited and/or photoproduct states [192] of the investigated IBs. The distinguishing broad Raman peak emerges at $1606\,cm^{-1}$ for IB_{1B} and at $1595\,cm^{-1}$ for IB_{1A}, and is adjoined by a cluster of near-lying lower-frequency vibrational bands at ca. $1400–1500\,cm^{-1}$. At least two clear-cut Raman maxima on the red wing of the main peak—at 1490 and $1540\,cm^{-1}$—can be discerned for IB_{1A}, whereas the corresponding maxima of IB_{1B} are slightly more dispersed spectrally, indicating a potential contribution of hot luminescence [66, 202] instigated by the repopulation of higher excited states of the compound [134]. Femtosecond time-resolved studies have previously shown that IB-type compounds exhibit a sub-picosecond decay and consequent sub-nanosecond growth of the TA signal (refs. [176, 192] and Section 4.2). As observed in Figure 5.4, the temporal behavior of the IB_{1B} and IB_{1A} FSRS bands in the spectral vicinity of ca. $1600\,cm^{-1}$ (and, to an extent, at the lower-frequency shoulder at ca. $1500\,cm^{-1}$) clearly mimics the familiar "rise → fall → rise → fall" dynamics of the transient electronic absorption signals [134, 176, 192] and on that account, can be well described by the same kinetic model (see Table A.1 for additional information). Moreover, spectral evolution during the sub-50-picosecond period distinctly shows the peak-shift to lower frequencies (by ca. $7\,cm^{-1}$) and band-narrowing phases. These FSRS dynamics, similarly to those observed in other molecules (e.g., in various carotenoids [46, 88, 136]), can be attributed to the vibrational relaxation, which, in our case, accompanies the formation of the photoproduct (also suggested in ref. [192]). The ratios between the initial (ca. 300 fs) and the final (ca. 100 ps) spectral amplitudes at $1600\,cm^{-1}$ slightly differ from those of the "pure" electronic signals [134, 192]—also a discrepancy between the intermediate state lifetimes (see Table A.1) and the ones from ref. [192] can be acknowledged—which can be explained by the fact that the Raman pumps can likewise irreversibly relocate the excited state/photoproduct population (i.e., "dump" or "repump" it), thereby, partially altering the "standard" photoevolution [134] (also observed in other multi-pulse experiments [89, 198]). Some of the more notable vibrational modes, accompanying the excited-state-to-photoproduct transition, are observed in the spectral region of ca. $750–1200\,cm^{-1}$. The vibrational frequencies at ca. 780 and $1180\,cm^{-1}$ (IB_{1B}), and ca. 1000 and $1250\,cm^{-1}$ (IB_{1A}) can be associated with the initial Frank–Condon and the singlet excited states, as suggested in ref. [192], seem-

ing as they rapidly decay within the first picosecond of the photoevolution. Likewise, the most prominent vibrational modes of the final forms can be identified at ca. 1275 cm^{-1} (IB_{1B}) 1000 and 1250 cm^{-1} (IB_{1A}), acknowledging their growth in amplitude (and the escalation above their initial amplitudes) for the first 100 ps, which coincides with the formation of the final evolutionary forms [192]. On the whole, the majority of these Raman signals, as indicated by the bottom graphs of Figure 5.4, are almost an order of magnitude less intense than the main 1600 cm^{-1} maxima (note the logarithmic amplitude coloring in the main graphs of Figure 5.4). It should also be mentioned that no clear-cut spectro-temporal activity is observed in the spectral vicinity of the main $-NO_2$ band at ca. 1330 cm^{-1}. The post-excitation behavior (i.e., bleach recovery and peak-shift) of the nitro functional group was shown to accompany the ring-opening dynamics of the related photochromic nitro-spiropyrans [31, 222], and, bearing in mind the steady-state vibrational changes of pNPH [219, 220], a similar effect can also be expected upon the ring-opening of IBs. Nonetheless, the data in this particular spectral region is less "reliable", as it lies in the close proximity of the comparatively strong 1375 cm^{-1} C–H deformation frequency of MeCN and is more susceptible to the solvent line subtraction artifacts [40, 43].

Comparing all the presented data, one can notice an inherent dissimilarity between the chemically- and optically-generated IB forms. While the contrast between the steady-state and transient electronic absorption of the chemically- and photo-generated species has been addressed previously (see refs. [177, 192, 199] and Figure 5.2(a)), the SRS/FSRS data in Figures 5.3 and 5.4 indicate that the particular molecular forms also bear very little vibrational semblance. This implies that although the general vibronic features of the chemically-induced forms can be ascribed to pNPHE [219, 220], the same assumption cannot be explicitly made about the ones produced via a UV photon absorption. Essentially, none of the characteristic low-to-mid-frequency (i.e., $\nu <$ 1400 cm^{-1} in our experimental window) components correlate between the SRS and FSRS spectra of the two—expectedly equivalent—molecular forms. Principally, all time-resolved FSRS spectra in Figure 5.4 peak in the close proximity of the characteristic higher-frequency ground state SpRS maxima (Figure 5.2(b)). Moreover, this tendency is exhibited not only by compounds IB_{1B} and IB_{1A}, but also by many other *para*-substituted IBs, including the ones investigated in ref. [177] (see Figure A.12). Acknowledging the key contribution of phenyl-indole inter-ring vibrations to the ground state SpRS spectra (Figure 5.2(b)), it is safe to assume that the signals at ca. 1600 cm^{-1}, emerging in the post-excitation FSRS dynamics, also originate from vibrations of the same molecular moiety. Since these biphenyl-like vibrations are not bleached

after the optical excitation (as the FSRS signal in Figure 5.4 is always positive) the temporal development of the 1600 cm^{-1} region can be interpreted as an intensification of molecular vibrations (stemming from the possible electronic excitation re-localization) within the phenyl-indolic moiety. The signals that could be potentially linked to oxazine ring opening (i.e., the sub-100-picosecond growth at ca. 1250 cm^{-1} in Figure 5.4) are much weaker than the ones assumedly associated with the phenyl-bearing fragments. These observations agree well with the earlier predictions that the UV excitation does not, in fact, cause a C–O bond breakage or (a spectrally-resolvable) pNPHE formation in photoexcited IB systems (especially in MECN environment [199], as indicated in Figure 5.1).

It has been suggested that intersystem crossing competes with ring-opening in both the substituted and unsubstituted IBs [199]. While the presented FSRS data supports the notion that ring-opening is not a likely outcome from UV excitation, the overwhelming biphenyl-like nature of the ground- and excited-state FSRS dynamics of the phenyl-substituted IBs allows us to propose yet another possible photoevolutionary route. The transient electronic absorption spectra in Figure 5.2(a) bear a striking semblance to the radical forms of biphenyl and its various derivatives [215, 216, 223–225] (obtained both via optical excitation [215, 216] and pulse radiolysis [223, 224] experiments). Most specifically, both electronic species display a presence of two characteristic spectral bands—a sharp NUV/VIS peak and a broad NIR maximum. Moreover, the transient Raman spectra [216, 226, 227] of the said radicals also share a great deal of likeness to the ones depicted in Figure 5.4 (i.e., an increased Raman activity at $\nu > 1500\,cm^{-1}$). Acknowledging the earlier observations, concerning the dependence of the sub-nanosecond dynamics on the UV excitation wavelength [192] and the susceptibility of the sub-microsecond relaxation rate to molecular oxygen [182, 199], it is possible to predict that the photoexcited phenyl-substituted IB systems develop a biphenyl radical-like (ionic) state—or, possibly, a charge-separated form, in which the electron traverses from one of the chromophoric segment to the other—that predominates throughout the entire photoevolution. The radical formation, most likely, develops not from the excited singlet state, familiar to most IBs [134, 192]. The unsubstituted IB_o has also been found to decay faster in the presence of oxygen [199], which suggests that the photopathway of the substituted systems is, presumably, singlet → triplet → radical. The proposed radical nature, all things considered, would elucidate why the basic photophysical properties of the phenyl-substituted IBs—the noticeably higher yield [177, 192], the excitation saturation dynamics [177], the atypical multi-peak TA spectra [177, 192], and the strong contrast to pNPHE [219, 220]—are dras-

tically different from numerous close counterparts of the IB family [162, 164–168, 176, 177, 182, 192, 199, 201]. Nonetheless, one should recognize that this photoevolutionary ascription is established on the spectral similarity of the transient species, which, as discussed earlier, may not always be a credible source of judgment [199].

5.2.4 *Conclusions*

We have performed an experimental FSRS study on the chemically-induced and the optically-generated molecular forms of phenyl-substituted IBs. The vibrational (as well as the electronic [134, 177, 192, 199]) spectra of the "factual" ring-opened molecules show an inherent similarity to pNPHE [164, 165, 168, 219, 220], whereas the UV excitation generated species exhibit a single dominant vibrational peak at ca. 1600 cm^{-1}. The latter results suggest an increased vibrational activity within the phenyl-indolic (and not the nitrophenolic) moiety, thus indicating that the substituents heavily alter the vibronic photodynamics of IB systems. The FSRS data support the earlier assumptions [182, 199] that the ring-opening competes with an auxiliary electronic process. Moreover, the peculiar FSRS activity within the indolic fragment of the molecule allow us estimate that the UV-generated excited state species might actually be not of a triplet (as suggested in refs. [182, 199]), but of a ionic radical-like [216, 226, 227] character.

Part V

AN AFTERWORD

6

MAIN RESULTS AND CONCLUSIONS

- We have demonstrated an economic home-built FSRS apparatus, capable of time-resolved vibrational measurements with a spectral resolution of $\Delta\nu \leq 6\,\mathrm{cm}^{-1}$, temporal resolution of $\Delta\tau \leq 70\,\mathrm{fs}$, and a resolvable spectral bandwidth of up to ca. $3000\,\mathrm{cm}^{-1}$. Tunability of the narrowband (up to ca. $1.5\,\mathrm{cm}^{-1}$) Raman pump pulses are produced by generating and spectrally filtering the second harmonic of a high-power OPA output, and can be implemented in the 400–800 nm region. Time-resolved vibrational dynamics of β-carotene S_2 ($1^1B_u^+$) and S_1 ($2^1A_g^-$) states are presented as a functional example of the FSRS setup, highlighting its qualities. The setup simultaneously measures PP and FSRS signals and allows combining excellent dynamic resolution and signal-to-noise of the former with the structural sensitivity of the latter.

- Multi-pulse time-resolved spectroscopic methods were applied to investigate the excited state dynamics of the marine carotenoid FX. PDP measurements indicate that an equilibrium exists between the two FX excited state species S_1 and ICT. This equilibrium is restored on a sub-6-picosecond timescale, after the ICT is deliberately depopulated via NIR SE. The joint PP/PDP experiments indicate that ICT decays—both naturally and via forced SE—to a GSI form on the molecular ground state PES. This GSI is thermally re-equilibrated to S_0 with a reciprocal rate of ca. 20 ps. FSRS experiments show that S_1 and ICT are two vibronically distinct states. The FX S_1 possesses a vibrational structure comparable to S_1 of many other carotenoids, whereas the ICT bears a vibrational semblance to the FX S_0. The ICT FSRS spectrum exhibits characteristic C=C vibrations at $1555\,\mathrm{cm}^{-1}$, that, based on the current understanding of the FX excited state structure, may act as a coupling channel for the $S_1 \leftrightarrow$ ICT equilibrium.

- Ultrafast dynamics of four novel IB compounds were, for the first time, investigated with the means of PP spectroscopy. The excited state dy-

namics of the IBs was described by a branched evolutionary model, which was used for global analysis of the experimental transient data. In the suggested model, the final forms are created in ca. 100 ps via radiationless transitions from the molecular excited state S_1, and a full thermal restoration to S_0 occurs with a rate of tens of nanoseconds on a sub-microsecond timescale. Intricate spectral development in the early photodynamic stages is explained by the appearance of a short-lived photoproduct directly from the initial excited state of the molecule. Initially the "fast" and "slow" forming intermediates were associated with the ring-opened (or a bond-cleaved) molecular form. Judging on later findings it is safe to assume that the kinetic model still holds, albeit the late transient species should be "relocated" to either triplet or radical PES.

- Multi-pulse PRPP/PRPAT measurements on a phenyl-substituted IB compound indicate that its photocycle can be controlled by a properly timed UV/NIR pulse sequence. A NIR reexcitation pulse, succeeding directly after ($0 < t_{RP} < 1$ ps) the primary UV excitation pulse, causes a 6 % net increase of the photoproduct population, whereas a late reexcitation ($t_{RP} > 100$ ps) triggers a back-switching reaction (i.e., permanent loss of PA) with a similar efficiency. PRPP experiments indicate that more than half of the photoproduct population can be reexcited to a short lived state, that eventually decays to hot ground state manifold of the photoproduct PES. These transient dynamics likewise induce a short term (ca. 20 ps) $\sim$ 20 % modulation of the PA signal.

- An experimental FSRS study was carried out on chemically-induced and optically-generated molecular forms of phenyl-substituted IBs. The full vibronic spectra of the "factual" ring-opened molecules show an inherent similarity to PNPHE, whereas the UV excitation generated species exhibit a single dominant vibrational peak at ca. 1600 cm^{-1}. The latter results suggest an increased vibronic activity (i.e., excitation re-allocation) within the phenyl-indolic (and not the nitrophenolic) moiety, thus indicating that the substituents heavily alter the vibronic photodynamics of IB systems. The SRS/FSRS data likewise support the assumptions that the ring-opening competes with an auxiliary electronic process.

Part VI

APPENDIX

A

APPENDIX

A.1 SECOND HARMONIC GENERATION UNDER GVM AND GVD

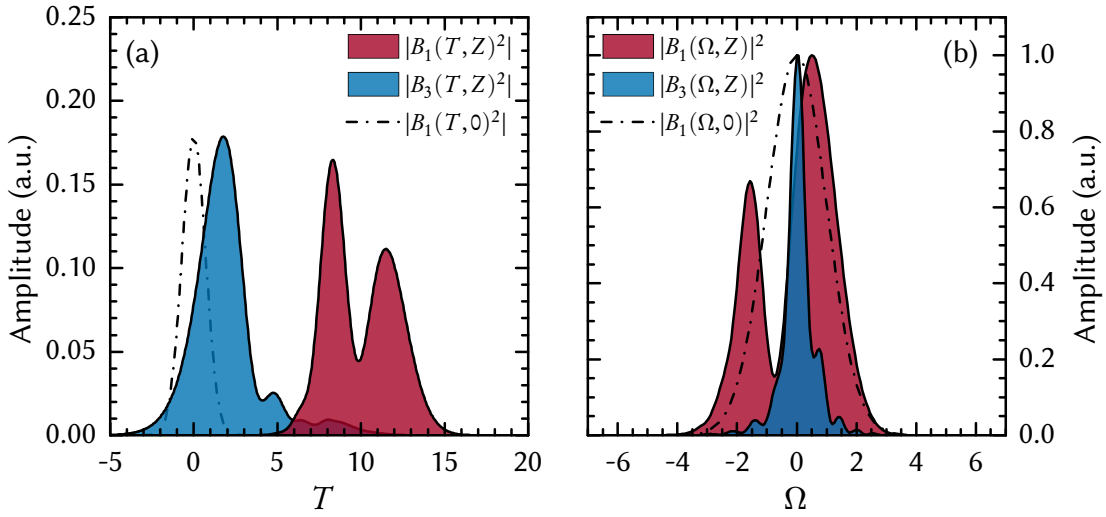

FIGURE A.1: Numeric simulation of 2nd harmonic generation in a lengthy nonlinear medium under both GVM and GVD conditions. GVD was incorporated to Equations (2.11) and (2.12) by the addition of the dispersive term $-i(L_D/L_\nu)\partial^2 B_j/\partial T^2$, where $j = 1,3$, $L_D = 2\tau_0^2/g_j$ is the dispersive propagation length, and g_j is the GVD coefficient. Assuming that $g_1 \simeq -g_2$ (which is close to the actual conditions for 1300/650 nm wave interaction in KDP), the differential equations were simulated under $L_N/L_\nu = 2.0$ and $L_N/L_D = 0.15$. With the introduction of the GVD term we begin to observe more complex spectral and temporal transformations of the interacting pulses. Second order approximation of the dispersion theory accounts for such effects as intensity-selective depletion (i.e., the biggest losses are observed at the peak of the pulse), spectral and temporal aberrations of the envelopes, regeneration of the fundamental wave, etc.

A.2 SUPPLEMENTS FOR THE FX PDP AND FSRS EXPERIMENTS

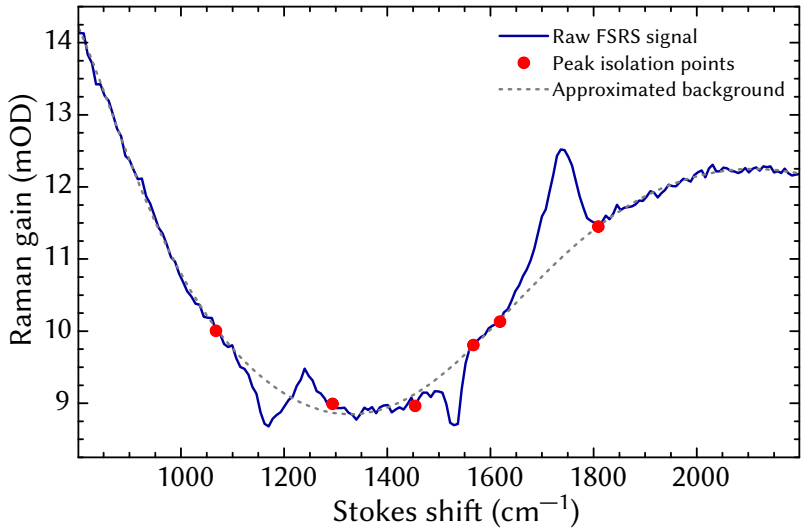

FIGURE A.2: FSRS signal recovery procedure for FX at $t_{P_R} = 200\,\text{fs}$. A set of $N = 6$ points is used to define the peak or peak cluster locations (with the odd i^{th} point signifying the "beginning" and the even $(i+1)^{\text{th}}$ point signifying the "end" of a single peak region). All of the remaining (i.e., "non-peak") points are then assumed to represent only the baseline and are approximated by a 5^{th} order polynomial curve.

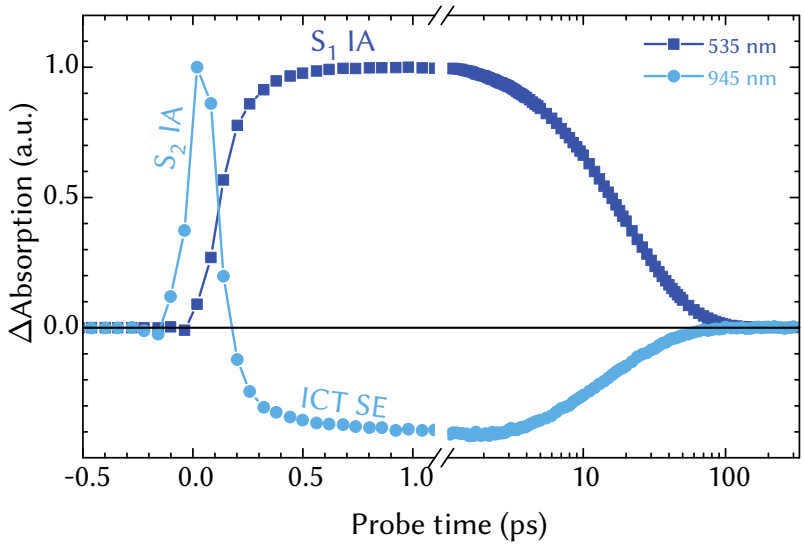

FIGURE A.3: Normalized kinetic traces of the FX PP dynamics at 535 and 945 nm. Labels indicate transient signals associated with the S_2, S_1 and the ICT states (note the "slower" sub-picosecond growth of S_1 IA at 535 nm).

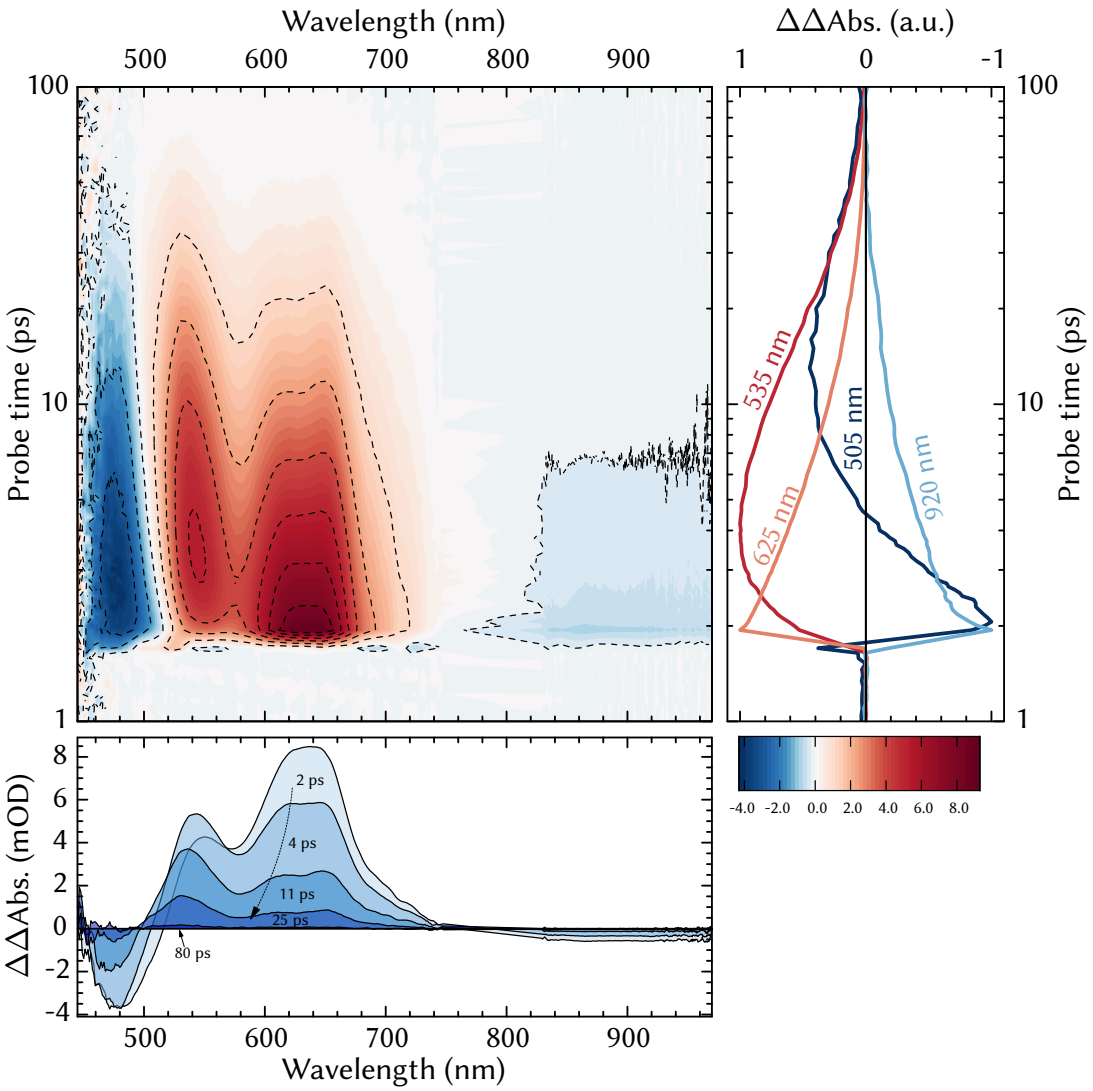

FIGURE A.4: Time- and wavelength-resolved ΔΔOD signals of FX. Central panel depicts the entire experimentally-resolved ΔΔOD spectrum, obtained as the difference of the PP, DP, and PDP signals ($\Delta\Delta OD = \Delta\Delta OD_{PP} + \Delta\Delta OD_{DP} - \Delta\Delta OD_{PDP}$). Spectral and temporal cuts of the full dataset are presented in bottom and right-hand side panels, respectively. Note that the ΔΔOD kinetic traces are normalized for better viewing.

A.3 SUPPLEMENTS FOR THE IB PP EXPERIMENTS

Steady-state absorption and time-resolved TA experiments were additionally performed on 5-phenyl-3H-indolium iodides (see Figure A.5). Structurally these compounds resemble the indolic moieties of the ring-open forms of compounds IB_{1A} and IB_{1B}, and similar prototypes were previously used for interpreting the time-resolved data of parent IB molecule IB_o in ref. [176] (particularly, the sub-picosecond photoevolution of IB_o was attributed to the formation of IND-like chromophore in an excited state [176]). Since an extended π-electron system is already present in 5-phenyl-3H-indolium iodide systems, a complete analogy cannot be drawn between the excited state behavior of these compounds and that of the individual indolic fragments of the parent molecules. Due to the intricacy of the time-resolved spectra and the obvious spectro-kinetic discrepancies from the PP data of GROUP I compounds (see Figure 4.3), these results are presented as a merely supplementary guide and are not analyzed in greater detail.

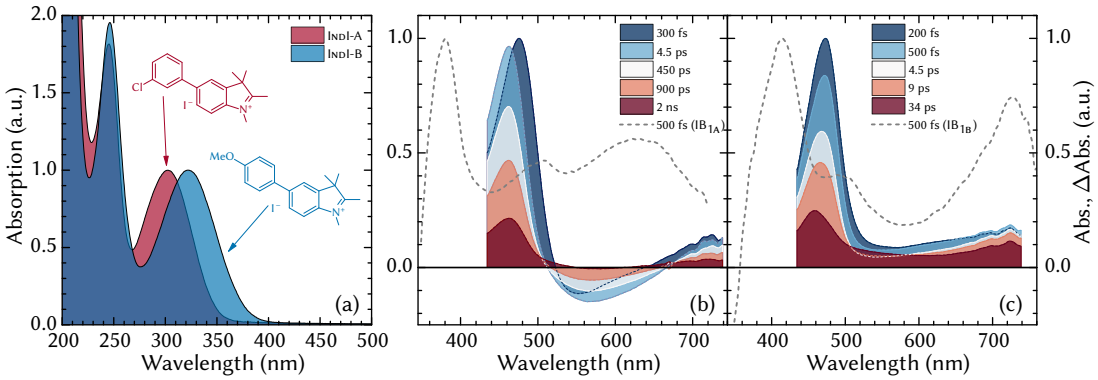

FIGURE A.5: Normalized ground state (panel (a)) and transient excited state (panels (b) and (c)) absorption spectra of 5-phenyl-3H-indolium iodides in MECN. Time resolved measurements were carried out on 1 OD samples with $\lambda_{PU} = 335\,nm$, $\tau_{PU} = 100\,fs$, $E_{PU} = 350\,nJ$ laser radiation. Early ($t_{PR} = 500\,fs$) time-resolved spectra of the counterpart photochromic compounds are presented in dashed curves in panels (b) and (c).

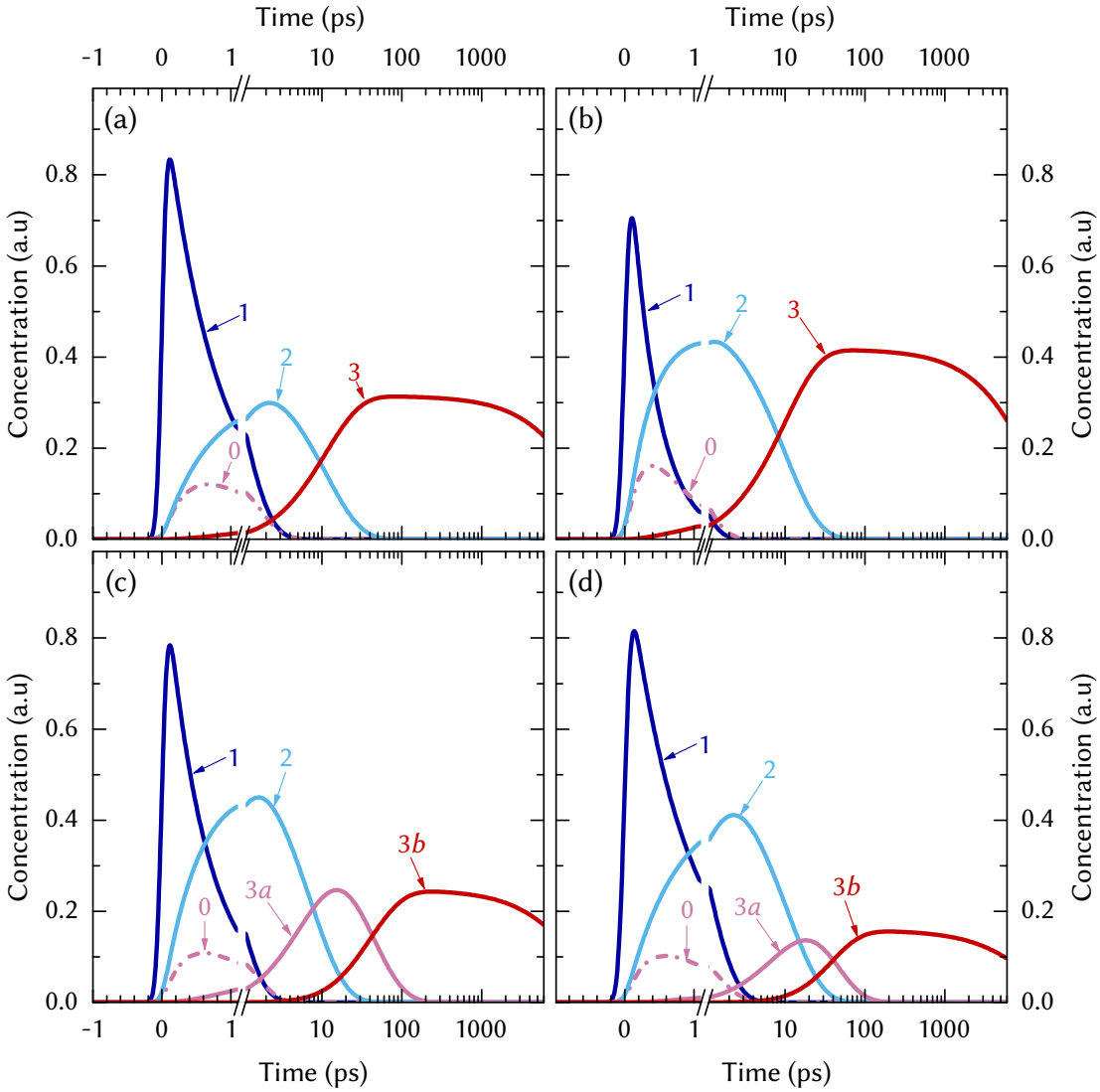

FIGURE A.6: Temporal concentrations of the SADS of compounds (a) IB_{1A}, (b) IB_{1B}, (c) IB_{2A}, and (d) IB_{2B}. Solid traces represent population dynamics along the primary photoevolutionary pathway, whereas the pink dashed-dotted traces correspond to the temporal concentration of the auxiliary photoproduct route (note the semi-logarithmic timescale in all the graphs). The connectivity scheme between the SADS is presented in Figure 4.6 of the main text.

A.4 SUPPLEMENTS FOR THE IB PRPP AND PRPAT EXPERIMENTS

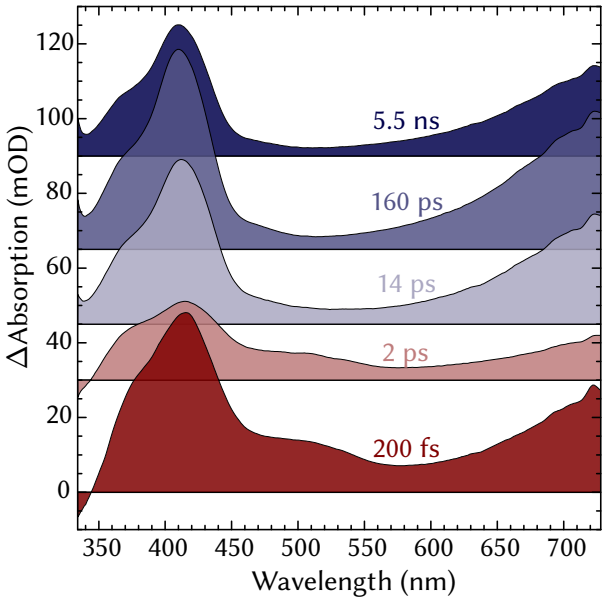

FIGURE A.7: Dispersion-corrected transient PP-only spectra of compound IB_{1B} from the joint PP/PRPP experiments. The time-gated PP spectra are offset vertically and the temporal evolution advanced from bottom to top.

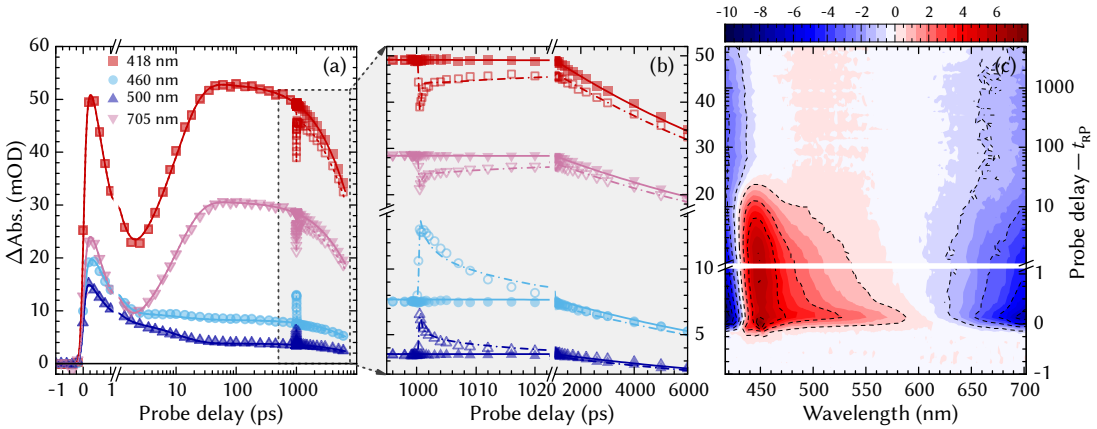

FIGURE A.8: Results of the PRPP experiment, performed with a 400 nm repump pulse. The full sub-10-nanosecond PP and PRPP spectral dynamics at selected wavelengths are presented in panel (a); post-repump ($t_{RP} = 1$ ns) evolution is highlighted in panel (b); the full ΔΔOD spectrum is given in panel (c). Solid and dashed curves in panels (a) and (b) represent the global fit of the experimental data. Spectral data below 415 nm is omitted due to intense scattering of the repump pulse.

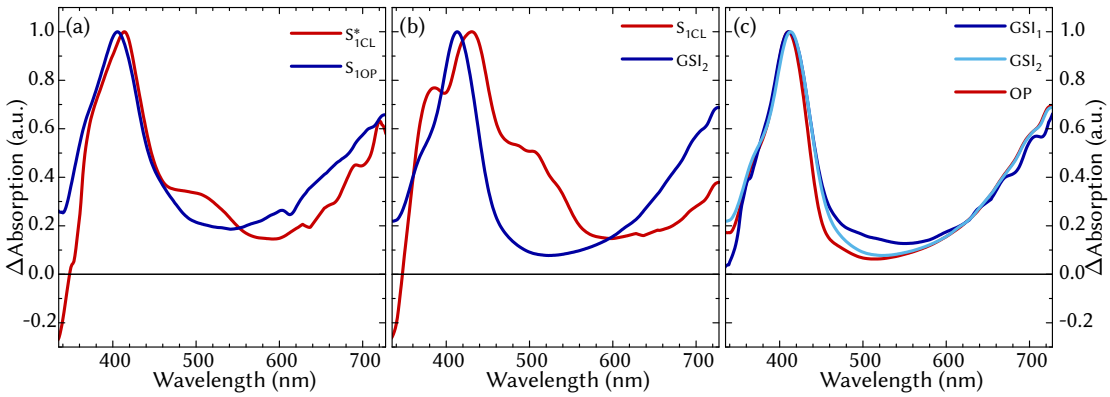

FIGURE A.9: Normalized SADS of the photoevolutionary states that exhibit either similar lifetimes (panels (a) and (b)) or spectra (panel (c)). Refer to Table 4.2 and Figure 4.12 in the main text for more information.

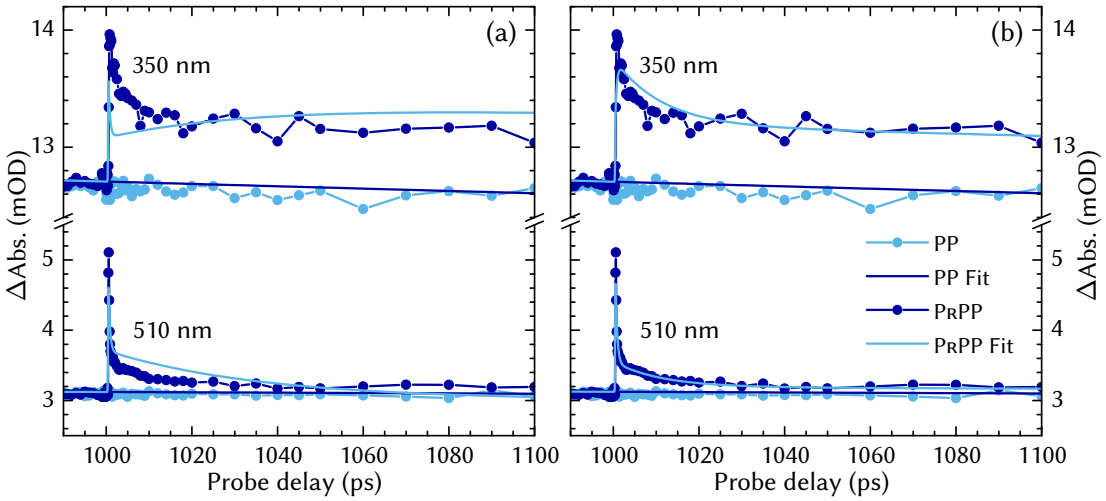

FIGURE A.10: Selected PP and PRPP kinetic traces and their global analysis estimates (a) with and (b) without the spectral constraint on SADS of GSI_1 and GSI_2 (i.e., $\sigma_{GSI_1}(\lambda) = \sigma_{GSI_2}(\lambda)$). If intermediates GSI_1 and GSI_2 are forced to have identical spectra (panel (a)) the fitted PRPP curves begin to notably deviate from the experimental values at $\lambda < 380\,\text{nm}$ and $450\,\text{nm} < \lambda < 600\,\text{nm}$ due to inherent dissimilarity of these spectral species in these particular spectral regions (see Figure A.9).

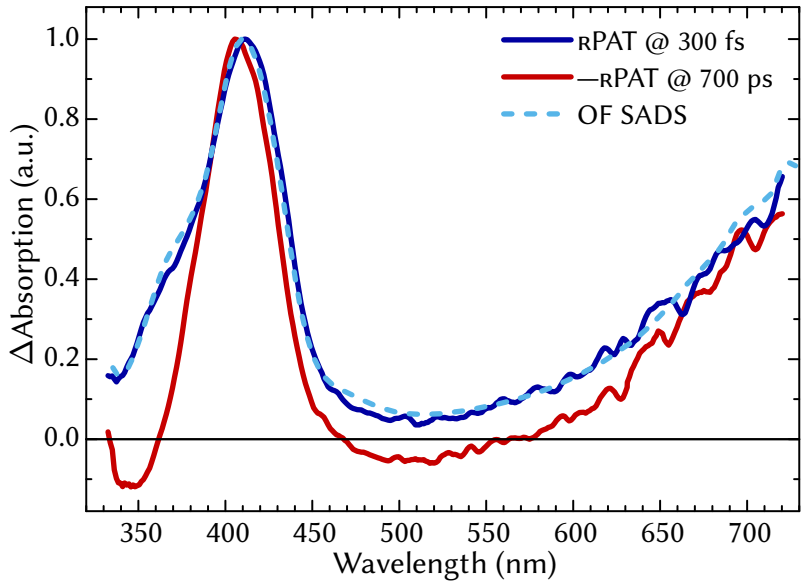

FIGURE A.11: A comparison of early (t_{RP} = 300 fs) and late (t_{RP} = 700 ps) PRPAT time-resolved spectra with the SADS of final photoproduct. Note that the normalized 700 ps spectrum is multiplied by −1 (see Figure 4.11 in main text for more details).

A.5 SUPPLEMENTS FOR THE IB FSRS EXPERIMENTS

TRANSITION	IB_{1B}	IB_{1A}
$\tau_{1\to2}$	0.75	0.95
$\tau_{2\to3}$	7	18
$\tau_{3\to3}$	25 000	13 300
$\tau_{1\to0}$	0.9	0.7
$\tau_{0\to0}$	0.4	0.4

TABLE A.1: Reciprocal transition rates (in ps) between the intermediate states of compound IB_{1B} and IB_{1A} FSRS photodynamics. The model for the global fit was for simplicity purposes adapted from previous studies on substituted IBs (refs. [134, 192] and/or Figure 4.6) and used as is. Result of the global fit are depicted as continuous curves in Figure 5.4 in the main text.

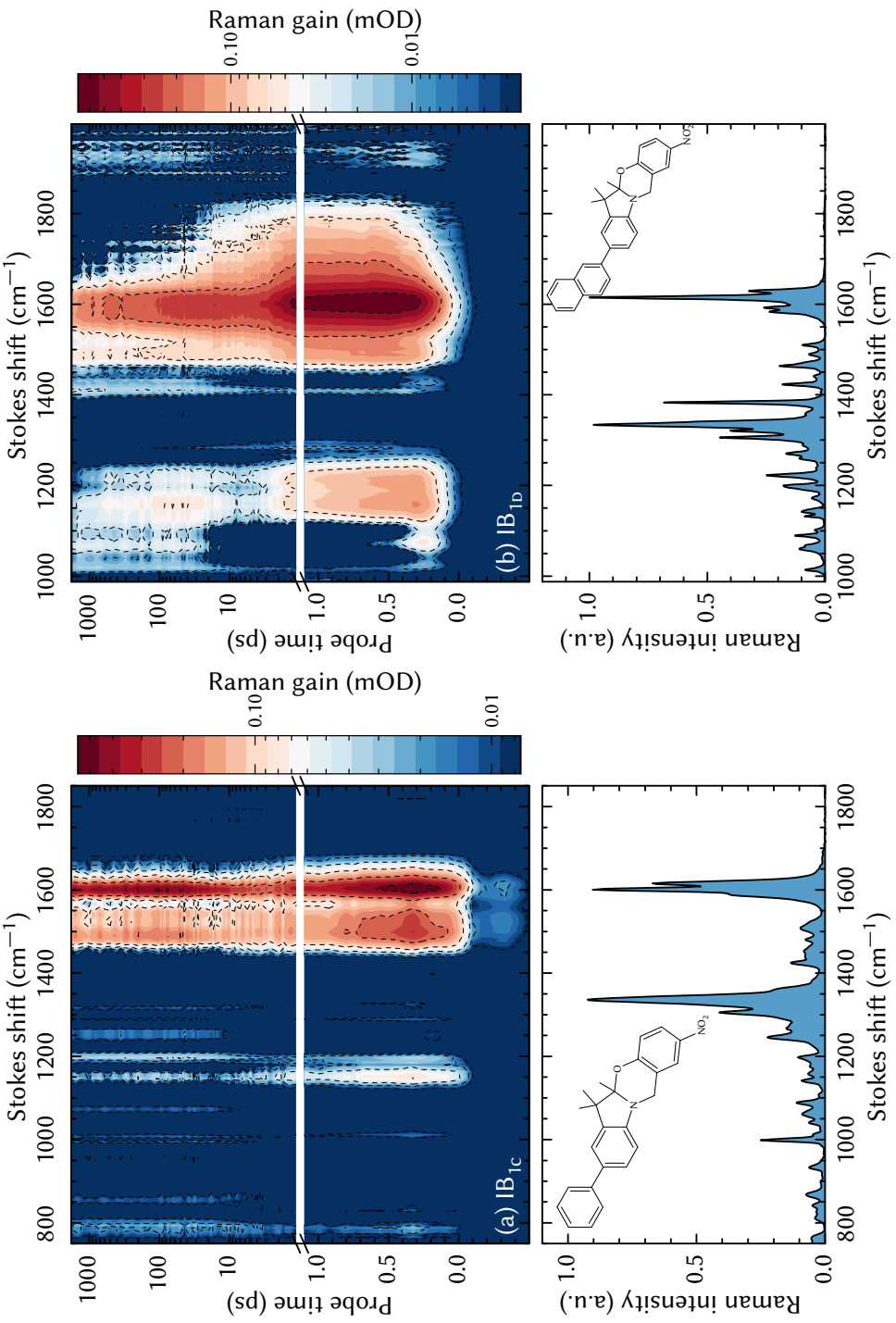

FIGURE A.12: Experimentally-resolved background-corrected FSRS datamaps (top panels) of several additional *para*-substituted IB compounds (structural formulae, along with their spontaneous Raman scattering spectra, are presented in the bottom panels). Optical excitation was performed with $\lambda_{AP} = 325\,\text{nm}$, $E_{AP} = 1\,\mu\text{J}$, $\tau_{AP} = 70\,\text{fs}$ actinic pulses; the Raman pumps, acknowledging the results of ref. [177], were set to (a) IB$_{1C}$: $\lambda_{RP} = 610\,\text{nm}$, $E_{RP} = 4\,\mu\text{J}$, $\tau_{RP} = 4\,\text{ps}$, and (b) IB$_{1D}$: $\lambda_{RP} = 795\,\text{nm}$, $E_{RP} = 5\,\mu\text{J}$, $\tau_{RP} = 3.5\,\text{ps}$.

BIBLIOGRAPHY

[1] Henry Eyring. "The Activated Complex in Chemical Reactions." In: *The Journal of Chemical Physics* 3.2 (1935), pp. 107–115. DOI: 10.1063/1.1749604.

[2] Keith J. Laidler and M.Christine King. "Development of transition-state theory." In: *The Journal of Physical Chemistry* 87.15 (1983), pp. 2657–2664. DOI: 10.1021/j100238a002.

[3] Ahmed H. Zewail. "Femtochemistry. Past, present, and future." In: *Pure and Applied Chemistry* 72.12 (2000), p. 2219. DOI: 10.1351/pac200072122219.

[4] Ahmed H. Zewail. "Femtochemistry: Atomic-Scale Dynamics of the Chemical Bond." In: *The Journal of Physical Chemistry A* 104.24 (2000), pp. 5660–5694. DOI: 10.1021/jp001460h.

[5] Britton Chance. "The accelerated flow method for rapid reactions." In: *Journal of the Franklin Institute* 229.6 (1940), pp. 737–766. DOI: 10.1016/S0016-0032(40)90963-2.

[6] Britton Chance. "The Kinetics of The Enzyme-Substrate Compound of Peroxidase." In: *Journal of Biological Chemistry* 151.2 (1943), pp. 553–577. DOI: 10.1002/9780470123195.ch1.

[7] Ronald George Wreyford Norrish and George Porter. "Chemical Reactions Produced by Very High Light Intensities." In: *Nature* 164 (1949), pp. 658–658. DOI: 10.1038/164658a0.

[8] George Porter. "Flash Photolysis and Spectroscopy. A New Method for the Study of Free Radical Reactions." In: *Proceedings of the Royal Society of London A: Mathematical, Physical and Engineering Sciences* 200.1061 (1950), pp. 284–300. DOI: 10.1098/rspa.1950.0018.

[9] Theodore H. Maiman. "Stimulated Optical Radiation in Ruby." In: *Nature* 187.4736 (1960), pp. 493–494. DOI: 10.1038/187493a0.

[10] F.J. McClung and R.W. Hellwarth. "Giant Optical Pulsations from Ruby." In: *Journal of Applied Physics* 33.3 (1962), pp. 828–829. DOI: 10.1063/1.1777174.

[11] L.E. Hargrove, R.L. Fork, and M.A. Pollack. "Locking of He-Ne Laser Modes Induced by Synchronous Intercavity Modulation." In: *Applied Physics Letters* 5.1 (1964), pp. 4–5. DOI: 10.1063/1.1754025.

[12] J.A. Giordmaine and Robert C. Miller. "Tunable Coherent Parametric Oscillation in $LiNbO_3$ at Optical Frequencies." In: *Physical Review Letters* 14.24 (1965), pp. 973–976. DOI: 10.1103/PhysRevLett.14.973.

[13] Dongping Zhong and Ahmed H. Zewail. "Femtosecond dynamics of dative bonding: Concepts of reversible and dissociative electron transfer reactions." In: *Proceedings of the National Academy of Sciences* 96.6 (1999), pp. 2602–2607. DOI: 10.1073/pnas.96.6.2602.

[14] Ahmed H. Zewail. "Laser Femtochemistry." In: *Science* 242.4886 (1988), pp. 1645–1653. DOI: 10.1126/science.242.4886.1645.

[15] Rudi Berera, Rienk Grondelle, and John T.M. Kennis. "Ultrafast transient absorption spectroscopy: principles and application to photosynthetic systems." In: *Photosynthesis Research* 101.2 (2009), pp. 105–118. DOI: 10.1007/s11120-009-9454-y.

[16] Wolfgang Zinth and Josef Wachtveitl. "The First Picoseconds in Bacterial Photosynthesis—Ultrafast Electron Transfer for the Efficient Conversion of Light Energy." In: *ChemPhysChem* 6.5 (2005), pp. 871–880. DOI: 10.1002/cphc.200400458.

[17] Thomas Elsaesser and Wolfgang Kaiser. "Vibrational and Vibronic Relaxation of Large Polyatomic Molecules in Liquids." In: *Annual Review of Physical Chemistry* 42.1 (1991), pp. 83–107. DOI: 10.1146/annurev.pc.42.100191.000503.

[18] Ralph Jimenez, Graham R. Fleming, P.V. Kumar, and M. Maroncelli. "Femtosecond solvation dynamics of water." In: *Nature* 369.6480 (1994), pp. 471–473. DOI: 10.1038/369471a0.

[19] L.A. Peteanu, R.W. Schoenlein, Q. Wang, R.A. Mathies, and C.V. Shank. "The first step in vision occurs in femtoseconds: complete blue and red spectral studies." In: *Proceedings of the National Academy of Sciences* 90.24 (1993), pp. 11762–11766. DOI: 10.1073/pnas.90.24.11762.

[20] Dario Polli et al. "Conical intersection dynamics of the primary photoisomerization event in vision." In: *Nature* 467.7314 (2010), pp. 440–443. DOI: 10.1038/nature09346.

[21] Alexandra S. Landsman and Ursula Keller. "Attosecond science and the tunnelling time problem." In: *Physics Reports* 547 (2015), pp. 1–24. DOI: 10.1016/j.physrep.2014.09.002.

[22] Harry A. Frank, Andrew J. Young, George Britton, and Richard J. Cogdell. *The Photochemistry of Carotenoids*. Vol. 8. Advances in Photosynthesis and Respiration. Dordrecht, Netherlands: Kluwer Academic Publishers, 1999, p. 420. ISBN: 978-0-7923-5942-5.

[23] Halina Abramczyk. *Introduction to Laser Spectroscopy*. 1st ed. The Netherlands: Elsevier Science, 2005, p. 384. ISBN: 9780444516626.

[24] Vytautas Butkus, Darius Abramavicius, Andrius Gelzinis, and Leonas Valkunas. "Two-Dimensional Optical Spectroscopy of Molecular Aggregates." In: *Lithuanian Journal of Physics* 50.3 (2010), pp. 267–303. DOI: 10.3952/lithjphys.50305.

[25] Shaul Mukamel. *Principles of Nonlinear Optical Spectroscopy*. Oxford Series in Optical and Imaging Sciences. New York, USA: Oxford University Press, 1999, p. 576. ISBN: 978-0195132915.

[26] Patrick Nuernberger, Stefan Ruetzel, and Tobias Brixner. "Multidimensional Electronic Spectroscopy of Photochemical Reactions." In: *Angewandte Chemie International Edition* 54.39 (2015), pp. 11368–11386. DOI: 10.1002/anie.201502974.

[27] Mikas Vengris, Delmar S. Larsen, Leonas Valkunas, Gerdenis Kodis, Christian Herrero, Devens Gust, Thomas Moore, Ana Moore, and Rienk van Grondelle. "Separating Annihilation and Excitation Energy Transfer Dynamics in Light Harvesting Systems." In: *The Journal of Physical Chemistry B* 117.38 (2013), pp. 11372–11382. DOI: 10.1021/jp403301c.

[28] K. Ekvall, P. van der Meulen, C. Dhollande, L.-E. Berg, S. Pommeret, R. Naskrecki, and J.-C. Mialocq. "Cross phase modulation artifact in liquid phase transient absorption spectroscopy." In: *Journal of Applied Physics* 87.5 (2000), pp. 2340–2352. DOI: 10.1063/1.372185.

[29] M. Lorenc, M. Ziolek, R. Naskrecki, J. Karolczak, J. Kubicki, and A. Maciejewski. "Artifacts in femtosecond transient absorption spectroscopy." In: *Applied Physics B* 74.1 (2002), pp. 19–27. DOI: 10.1007/s003400100750.

[30] M.V. Lebedev, O.V. Misochko, T. Dekorsy, and N. Georgiev. "On the nature of "coherent artifact"." In: *Journal of Experimental and Theoretical Physics* 100.2 (2005), pp. 272–282. DOI: 10.1134/1.1884668.

[31] Johannes Buback, Martin Kullmann, Florian Langhojer, Patrick Nuernberger, Ralf Schmidt, Frank Würthner, and Tobias Brixner. "Ultrafast Bidirectional Photoswitching of a Spiropyran." In: *Journal of the American Chemical Society* 132.46 (2010), pp. 16510–16519. DOI: 10.1021/ja1062746.

[32] Delmar S. Larsen, Emmanouil Papagiannakis, Ivo H.M. van Stokkum, Mikas Vengris, John T.M. Kennis, and Rienk van Grondelle. "Excited state dynamics of β-carotene explored with dispersed multipulse transient absorption." In: *Chemical Physics Letters* 381.5–6 (2003), pp. 733–742. DOI: 10.1016/j.cplett.2003.10.016.

[33] Delmar S. Larsen, Mikas Vengris, Ivo H.M. van Stokkum, Michael A. van der Horst, Frank L. de Weerd, Klaas J. Hellingwerf, and Rienk van Grondelle. "Photoisomerization and Photoionization of the Photoactive Yellow Protein Chromophore in Solution." In: *Biophysical Journal* 86.4 (2004), pp. 2538–2550. DOI: 10.1016/S0006-3495(04)74309-X.

[34] P.O. Stoutland, R.B. Dyer, and W.H. Woodruff. "Ultrafast infrared spectroscopy." In: *Science* 257.5078 (1992), pp. 1913–1917. DOI: 10.1126/science.1329200.

[35] Michael D. Fayer. *Ultrafast Infrared And Raman Spectroscopy*. 1st ed. Practical Spectroscopy. New York, USA: CRC Press, 2001, 728 p. ISBN: 978-0-8247-0451-3.

[36] Johannes Knorr, Philipp Rudolf, and Patrick Nuernberger. "A comparative study on chirped-pulse upconversion and direct multichannel MCT detection." In: *Optics Express* 21.25 (2013), pp. 30693–30706. DOI: 10.1364/OE.21.030693.

[37] Carlos R. Baiz and Kevin J. Kubarych. "Ultrabroadband detection of a mid-IR continuum by chirped-pulse upconversion." In: *Optics Letters* 36.2 (2011), pp. 187–189. DOI: 10.1364/OL.36.000187.

[38] Philipp Kukura, David W. McCamant, and Richard A. Mathies. "Femtosecond Stimulated Raman Spectroscopy." In: *Annual Review of Physical Chemistry* 58.1 (2007), pp. 461–488. DOI: 10.1146/annurev.physchem.58.032806.104456.

[39] David W. McCamant, Philipp Kukura, and Richard A. Mathies. "Femtosecond Broadband Stimulated Raman: A New Approach for High-Performance Vibrational Spectroscopy." In: *Applied Spectroscopy* 57.11 (2003), pp. 1317–1323. DOI: 10.1366/000370203322554455.

[40] David W. McCamant, Philipp Kukura, Sangwoon Yoon, and Richard A. Mathies. "Femtosecond broadband stimulated Raman spectroscopy: Apparatus and methods." In: *Review of Scientific Instruments* 75.11 (2004), pp. 4971–4980. DOI: 10.1063/1.1807566.

[41] Daniel R. Dietze and Richard A. Mathies. "Femtosecond Stimulated Raman Spectroscopy." In: *ChemPhysChem* 17.9 (2016), pp. 1224–1251. DOI: 10.1002/cphc.201600104.

[42] David P. Hoffman and Richard A. Mathies. "Femtosecond Stimulated Raman Exposes the Role of Vibrational Coherence in Condensed-Phase Photoreactivity." In: *Accounts of Chemical Research* 49.4 (2016), pp. 616–625. DOI: 10.1021/acs.accounts.5b00508.

[43] David W. McCamant, Philipp Kukura, and Richard A. Mathies. "Femtosecond Time-Resolved Stimulated Raman Spectroscopy: Application to the Ultrafast Internal Conversion in β-Carotene." In: *The Journal of Physical Chemistry A* 107.40 (2003), pp. 8208–8214. DOI: 10.1021/jp030147n.

[44] Hikaru Kuramochi, Satoshi Takeuchi, and Tahei Tahara. "Ultrafast Structural Evolution of Photoactive Yellow Protein Chromophore Revealed by Ultraviolet Resonance Femtosecond Stimulated Raman Spectroscopy." In: *The Journal of Physical Chemistry Letters* 3.15 (2012), pp. 2025–2029. DOI: 10.1021/jz300542f.

[45] Chong Fang, Renee R. Frontiera, Rosalie Tran, and Richard A. Mathies. "Mapping GFP structure evolution during proton transfer with femtosecond Raman spectroscopy." In: *Nature* 462.7270 (2009), pp. 200–204. DOI: 10.1038/nature08527.

[46] Sangdeok Shim and Richard A. Mathies. "Development of a Tunable Femtosecond Stimulated Raman Apparatus and Its Application to β-Carotene." In: *The Journal of Physical Chemistry B* 112.15 (2008), pp. 4826–4832. DOI: 10.1021/jp710518y.

[47] Philipp Kukura, David W. McCamant, and Richard A. Mathies. "Femtosecond Time-Resolved Stimulated Raman Spectroscopy of the S_2 ($1B_u^+$) Excited State of β-Carotene." In: *The Journal of Physical Chemistry A* 108.28 (2004), pp. 5921–5925. DOI: 10.1021/jp0482971.

[48] David W. McCamant, Philipp Kukura, and Richard A. Mathies. "Femtosecond Stimulated Raman Study of Excited-State Evolution in Bacteriorhodopsin." In: *The Journal of Physical Chemistry B* 109.20 (2005), pp. 10449–10457. DOI: 10.1021/jp050095x.

[49] Sascha Frobel, Laura Buschhaus, Torben Villnow, Oliver Weingart, and Peter Gilch. "The photoformation of a phthalide: a ketene intermediate traced by FSRS." In: *Physical Chemistry Chemical Physics* 17.1 (2015), pp. 376–386. DOI: 10.1039/C4CP03351E.

[50] David P. Hoffman and Richard A. Mathies. "Photoexcited structural dynamics of an azobenzene analog 4-nitro-4′-dimethylamino-azobenzene from femtosecond stimulated Raman." In: *Physical Chemistry Chemical Physics* 14.18 (2012), pp. 6298–6306. DOI: 10.1039/C2CP23468H.

[51] A.L. Dobryakov, I. Ioffe, A.A. Granovsky, N.P. Ernsting, and S.A. Kovalenko. "Femtosecond Raman spectra of *cis*-stilbene and *trans*-stilbene with isotopomers in solution." In: *The Journal of Chemical Physics* 137.24 (2012), p. 244505. DOI: 10.1063/1.4769971.

[52] Amanda L. Smeigh, Mark Creelman, Richard A. Mathies, and James K. McCusker. "Femtosecond Time-Resolved Optical and Raman Spectroscopy of Photoinduced Spin Crossover: Temporal Resolution of Low-to-High Spin Optical Switching." In: *Journal of the American Chemical Society* 130.43 (2008), pp. 14105–14107. DOI: 10.1021/ja805949s.

[53] Sangwoon Yoon, Philipp Kukura, Christina M. Stuart, and Richard A. Mathies. "Direct observation of the ultrafast intersystem crossing in tris(2,2′-bipyridine)ruthenium(II) using femtosecond stimulated Raman spectroscopy." In: *Molecular Physics* 104.8 (2006), pp. 1275–1282. DOI: 10.1080/00268970500525846.

[54] Tomotsumi Fujisawa, Mark Creelman, and Richard A. Mathies. "Structural Dynamics of a Noncovalent Charge Transfer Complex from Femtosecond Stimulated Raman Spectroscopy." In: *The Journal of Physical Chemistry B* 116.35 (2012), pp. 10453–10460. DOI: 10.1021/jp3001306.

[55] Kristen E. Brown, Brad S. Veldkamp, Dick T. Co, and Michael R. Wasielewski. "Vibrational Dynamics of a Perylene-Perylenediimide Donor-Acceptor Dyad Probed with Femtosecond Stimulated Raman Spectroscopy." In: *The Journal of Physical Chemistry Letters* 3.17 (2012), pp. 2362–2366. DOI: 10.1021/jz301107c.

[56] Ryan M. Young, Scott M. Dyar, Jonathan C. Barnes, Michal Juríček, J.Fraser Stoddart, Dick T. Co, and Michael R. Wasielewski. "Ultrafast Conformational Dynamics of Electron Transfer in $ExBox^{4+} \subset$ Perylene." In: *The Journal of Physical Chemistry A* 117.47 (2013), pp. 12438–12448. DOI: 10.1021/jp409883a.

[57] Erik M. Grumstrup, Zhuo Chen, Ryan P. Vary, Andrew M. Moran, Kirk S. Schanze, and John M. Papanikolas. "Frequency Modulated Femtosecond Stimulated Raman Spectroscopy of Ultrafast Energy Transfer in a Donor-Acceptor Copolymer." In: *The Journal of Physical Chemistry B* 117.27 (2013), pp. 8245–8255. DOI: 10.1021/jp404498u.

[58] Renee R. Frontiera and Richard A. Mathies. "Polarization dependence of vibrational coupling signals in femtosecond stimulated Raman spectroscopy." In: *The Journal of Chemical Physics* 127.12 (2007), p. 124501. DOI: 10.1063/1.2780843.

[59] Sangdeok Shim and Richard A. Mathies. "Femtosecond Raman-induced Kerr effect spectroscopy." In: *Journal of Raman Spectroscopy* 39.11 (2008), pp. 1526–1530. DOI: 10.1002/jrs.2109.

[60] Renee R. Frontiera, Anne-Isabelle Henry, Natalie L. Gruenke, and Richard P. Van Duyne. "Surface-Enhanced Femtosecond Stimulated Raman Spectroscopy." In: *The Journal of Physical Chemistry Letters* 2.10 (2011), pp. 1199–1203. DOI: 10.1021/jz200498z.

[61] David P. Hoffman, Scott R. Ellis, and Richard A. Mathies. "Characterization of a Conical Intersection in a Charge-Transfer Dimer with Two-Dimensional Time-Resolved Stimulated Raman Spectroscopy." In: *The Journal of Physical Chemistry A* 118.27 (2014), pp. 4955–4965. DOI: 10.1021/jp5041986.

[62] David T. Valley, David P. Hoffman, and Richard A. Mathies. "Reactive and unreactive pathways in a photochemical ring opening reaction from 2D femtosecond stimulated Raman." In: *Physical Chemistry Chemical Physics* 17.14 (2015), pp. 9231–9240. DOI: 10.1039/C4CP05323K.

[63] Barbara Dunlap, Peter Richter, and David W. McCamant. "Stimulated Raman spectroscopy using chirped pulses." In: *Journal of Raman Spectroscopy* 45.10 (2014), pp. 918–929. DOI: 10.1002/jrs.4578.

[64] Konstantin E. Dorfman, Frank Schlawin, and Shaul Mukamel. "Stimulated Raman Spectroscopy with Entangled Light: Enhanced Resolution and Pathway Selection." In: *The Journal of Physical Chemistry Letters* 5.16 (2014), pp. 2843–2849. DOI: 10.1021/jz501124a.

[65] Weijie Hua, Sven Oesterling, Jason D. Biggs, Yu Zhang, Hideo Ando, Regina de Vivie-Riedle, Benjamin P. Fingerhut, and Shaul Mukamel. "Monitoring conical intersections in the ring opening of furan by attosecond stimulated X-ray Raman spectroscopy." In: *Structural Dynamics* 3.2 (2016), p. 023601. DOI: 10.1063/1.4933007.

[66] Bin Zhao, Kai Niu, XiuTing Li, and Soo-Ying Lee. "Simple aspects of femtosecond stimulated Raman spectroscopy." In: *Science China Chemistry* 54.12 (2011), pp. 1989–2008. DOI: 10.1007/s11426-011-4430-8.

[67] Renee R. Frontiera, Chong Fang, Jyotishman Dasgupta, and Richard A. Mathies. "Probing structural evolution along multidimensional reaction coordinates with femtosecond stimulated Raman spectroscopy." In: *Physical Chemistry Chemical Physics* 14.2 (2012), pp. 405–414. DOI: 10.1039/C1CP22767J.

[68] Martynas Barkauskas. "Time-Resolved Spectroscopy of Nonlinear Crystals and Photochromic Swiches." Thesis. 2009.

[69] S.A. Kovalenko, A.L. Dobryakov, and N.P. Ernsting. "An efficient setup for femtosecond stimulated Raman spectroscopy." In: *Review of Scientific Instruments* 82.6 (2011), p. 063102. DOI: 10.1063/1.3596453.

[70] Liangdong Zhu, Weimin Liu, and Chong Fang. "A versatile femtosecond stimulated Raman spectroscopy setup with tunable pulses in the visible to near infrared." In: *Applied Physics Letters* 105.4 (2014), p. 041106. DOI: 10.1063/1.4891766.

[71] David P. Hoffman, Olivia P. Lee, Jill E. Millstone, Mark S. Chen, Timothy A. Su, Mark Creelman, Jean M.J. Fréchet, and Richard A. Mathies. "Electron Transfer Dynamics of Triphenylamine Dyes Bound to TiO_2 Nanoparticles from Femtosecond Stimulated Raman Spectroscopy." In: *The Journal of Physical Chemistry C* 117.14 (2013), pp. 6990–6997. DOI: 10.1021/jp400369b.

[72] William Rock, Yun-Liang Li, Philip Pagano, and Christopher M. Cheatum. "2D IR Spectroscopy using Four-Wave Mixing, Pulse Shaping, and IR Upconversion: A Quantitative Comparison." In: *The Journal of Physical Chemistry A* 117.29 (2013), pp. 6073–6083. DOI: 10.1021/jp312817t.

[73] W.Ruchira Silva, Emily L. Keller, and Renee R. Frontiera. "Determination of Resonance Raman Cross-Sections for Use in Biological SERS Sensing with Femtosecond Stimulated Raman Spectroscopy." In: *Analytical Chemistry* 86.15 (2014), pp. 7782–7787. DOI: 10.1021/ac501701h.

[74] Dominique Verreault, Volker Kurz, Caitlin Howell, and Patrick Koelsch. "Sample cells for probing solid/liquid interfaces with broadband sum-frequency-generation spectroscopy." In: *Review of Scientific Instruments* 81.6 (2010), p. 063111. DOI: 10.1063/1.3443096.

[75] Matthew J. Nee, Robert McCanne, Kevin J. Kubarych, and Manuel Joffre. "Two-dimensional infrared spectroscopy detected by chirped pulse upconversion." In: *Optics Letters* 32.6 (2007), pp. 713–715. DOI: 10.1364/OL.32.000713.

[76] Jingyi Zhu, Tilo Mathes, Andreas D. Stahl, John T.M. Kennis, and Marie Louise Groot. "Ultrafast mid-infrared spectroscopy by chirped pulse upconversion in 1800–1000 cm^{-1} region." In: *Optics Express* 20.10 (2012), pp. 10562–10571. DOI: 10.1364/OE.20.010562.

[77] Wenjian Yu, Paul J. Donohoo-Vallett, Jiawang Zhou, and Arthur E. Bragg. "Ultrafast photo-induced nuclear relaxation of a conformationally disordered conjugated polymer probed with transient absorption and femtosecond stimulated Raman spectroscopies." In: *The Journal of Chemical Physics* 141.4 (2014), p. 044201. DOI: 10.1063/1.4890326.

[78] A. Weigel and N.P. Ernsting. "Excited Stilbene: Intramolecular Vibrational Redistribution and Solvation Studied by Femtosecond Stimulated Raman Spectroscopy." In: *The Journal of Physical Chemistry B* 114.23 (2010), pp. 7879–7893. DOI: 10.1021/jp100181z.

[79] *Light Conversion TOPAS-800*. URL: www.lightcon.com/Product/TOPAS-800.html.

[80] E. Pontecorvo, C. Ferrante, C.G. Elles, and T. Scopigno. "Spectrally tailored narrowband pulses for femtosecond stimulated Raman spectroscopy in the range 330–750 nm." In: *Optics Express* 21.6 (2013), pp. 6866–6872. DOI: 10.1364/OE.21.006866.

[81] M.A. Marangoni, D. Brida, M. Quintavalle, G. Cirmi, F.M. Pigozzo, C. Manzoni, F. Baronio, A.D. Capobianco, and G. Cerullo. "Narrow-bandwidth picosecond pulses by spectral compression of femtosecond pulses in second-order nonlinear crystals." In: *Optics Express* 15.14 (2007), pp. 8884–8891. DOI: 10.1364/OE.15.008884.

[82] Bahaa E.A. Saleh and Malvin Carl Teich. *Fundamentals of Photonics*. 2nd ed. New Jersey, USA: John Wiley & Sons, 2007, p. 1200. ISBN: 978-0-471-35832-9.

[83] Jean-Claude Diels and Wolfgang Rudolph. *Ultrashort Laser Pulse Phenomena*. 2nd ed. San Diego, California, USA: Academic Press, 2006, p. 680. ISBN: 978-0-12-215493-5.

[84] Govind P. Agrawal. *Nonlinear Fiber Optics*. 3rd ed. Optics and Photonics. San Diego, CA, USA: Academic Press, 2001. ISBN: 0-12-045143-3.

[85] Valentin G. Dmitriev, Gagik G. Gurzadyan, and David N. Nikogosyan. *Handbook of Nonlinear Optical Crystals*. 3rd ed. Vol. 64. Springer Series in Optical Sciences. Berlin, Germany: Springer, 1999, 413 p. ISBN: 3-540-65394-5.

[86] E. Pontecorvo, S.M. Kapetanaki, M. Badioli, D. Brida, M. Marangoni, G. Cerullo, and T. Scopigno. "Femtosecond stimulated Raman spectrometer in the 320–520 nm range." In: *Optics Express* 19.2 (2011), pp. 1107–1112. DOI: 10.1364/OE.19.001107.

[87] Fangyuan Han, Weimin Liu, and Chong Fang. "Excited-state proton transfer of photoexcited pyranine in water observed by femtosecond stimulated Raman spectroscopy." In: *Chemical Physics* 422 (2013), pp. 204–219. DOI: 10.1016/j.chemphys.2013.03.009.

[88] Miroslav Kloz, Rienk van Grondelle, and John T.M. Kennis. "Wavelength-modulated femtosecond stimulated raman spectroscopy—approach towards automatic data processing." In: *Physical Chemistry Chemical Physics* 13.40 (2011), pp. 18123–18133. DOI: 10.1039/C1CP21650C.

[89] A. Weigel, A. Dobryakov, B. Klaumünzer, M. Sajadi, P. Saalfrank, and N.P. Ernsting. "Femtosecond Stimulated Raman Spectroscopy of Flavin after Optical Excitation." In: *The Journal of Physical Chemistry B* 115.13 (2011), pp. 3656–3680. DOI: 10.1021/jp1117129.

[90] S. Laimgruber, H. Schachenmayr, B. Schmidt, W. Zinth, and P. Gilch. "A femtosecond stimulated raman spectrograph for the near ultraviolet." In: *Applied Physics B* 85.4 (2006), pp. 557–564. DOI: 10.1007/s00340-006-2386-8.

[91] Hideo Ando, Benjamin P. Fingerhut, Konstantin E. Dorfman, Jason D. Biggs, and Shaul Mukamel. "Femtosecond Stimulated Raman Spectroscopy of the Cyclobutane Thymine Dimer Repair Mechanism: A Computational Study." In: *Journal of the American Chemical Society* 136.42 (2014), pp. 14801–14810. DOI: 10.1021/ja5063955.

[92] John R. Ferraro, Kazuo Nakamoto, and Chris W. Brown. *Introductory Raman Spectroscopy*. 2nd ed. Amsterdam, The Netherlands: Academic Press, 2003, 434 p.

[93] Jyotishman Dasgupta, Renee R. Frontiera, Keenan C. Taylor, J. Clark Lagarias, and Richard A. Mathies. "Ultrafast excited-state isomerization in phytochrome revealed by femtosecond stimulated Raman spectroscopy." In: *Proceedings of the National Academy of Sciences* 106.6 (2009), pp. 1784–1789. DOI: 10.1073/pnas.0812056106.

[94] *Qt | Cross-platform application development for desktop & embedded*. URL: www.qt.io.

[95] *Qt Plotting Widget QCustomPlot*. URL: www.qcustomplot.com.

[96] *Raman Manager | A Qt/C++ FSRS Data Management Tool*. URL: www.github.com/KiprasR/RamanManager.

[97] Ivo H.M. van Stokkum, Delmar S. Larsen, and Rienk van Grondelle. "Global and target analysis of time-resolved spectra." In: *Biochimica et Biophysica Acta (BBA) – Bioenergetics* 1657.2–3 (2004), pp. 82–104. DOI: 10.1016/j.bbabio.2004.04.011.

[98] Alfred R. Holzwarth. "Data Analysis of Time-Resolved Measurements." In: *Biophysical Techniques in Photosynthesis*. Ed. by Jan Amesz and Arnold J. Hoff. Springer Netherlands, 1996, pp. 75–92. ISBN: 978-0-306-47960-1. DOI: 10.1007/0-306-47960-5_5.

[99] Luuk J.G.W. van Wilderen, Craig N. Lincoln, and Jasper J. van Thor. "Modelling Multi-Pulse Population Dynamics from Ultrafast Spectroscopy." In: *PLoS ONE* 6.3 (2011), pp. 1–14. DOI: 10.1371/journal.pone.0017373.

[100] John T.M. Kennis, Delmar S. Larsen, Ivo H.M. van Stokkum, Mikas Vengris, Jasper J. van Thor, and Rienk van Grondelle. "Uncovering the hidden ground state of green fluorescent protein." In: *Proceedings of the National Academy of Sciences* 101.52 (2004), pp. 17988–17993. DOI: 10.1073/pnas.0404262102.

[101] Mikas Vengris, Ivo H.M. van Stokkum, Xiang He, Alasdair F. Bell, Peter J. Tonge, Rienk van Grondelle, and Delmar S. Larsen. "Ultrafast Excited and Ground-State Dynamics of the Green Fluorescent Protein Chromophore in Solution." In: *The Journal of Physical Chemistry A* 108.21 (2004), pp. 4587–4598. DOI: 10.1021/jp037902h.

[102] Harry A. Frank and Richard J. Cogdell. "Carotenoids in Photosynthesis." In: *Photochemistry and Photobiology* 63.3 (1996), pp. 257–264. DOI: 10.1111/j.1751-1097.1996.tb03022.x.

[103] Barbara Demmig-Adams and William W. Adams III. "The role of xanthophyll cycle carotenoids in the protection of photosynthesis." In: *Trends in Plant Science* 1.1 (1996), pp. 21–26. DOI: 10.1016/S1360-1385(96)80019-7.

[104] Yasushi Koyama, Michitaka Kuki, Per Ola Andersson, and Tomas Gillbro. "Singlet Excited States and the Light-Harvesting Function of Carotenoids in Bacterial Photosynthesis." In: *Photochemistry and Photobiology* 63.3 (1996), pp. 243–256. DOI: 10.1111/j.1751-1097.1996.tb03021.x.

[105] Herbert van Amerongen, Leonas Valkunas, and Rienk van Grondelle. *Photosynthetic Excitons*. Singapore: World Scientific, 2000, p. 590. ISBN: 978-981-02-3280-1.

[106] Tomáš Polívka and Villy Sundström. "Ultrafast Dynamics of Carotenoid Excited States—From Solution to Natural and Artificial Systems." In: *Chemical Reviews* 104.4 (2004), pp. 2021–2072. DOI: 10.1021/cr020674n.

[107] Andrew Young and George Britton. *Carotenoids in Photosynthesis*. 1st ed. Dordrecht, The Netherlands: Springer Science & Business Media, 1993, 498 p.

[108] Miroslav Kloz, Rienk van Grondelle, and John T.M. Kennis. "Correction for the time dependent inner filter effect caused by transient absorption in femtosecond stimulated Raman experiment." In: *Chemical Physics Letters* 544 (2012), pp. 94–101. DOI: 10.1016/j.cplett.2012.07.005.

[109] T. Noguchi, S. Kolaczkowski, C. Arbour, S. Aramaki, G.H. Atkinson, H. Hayashi, and M. Tasumi. "Resonance Raman spectrum of the excited $2^1A_g^-$ state of β-carotene." In: *Photochemistry and Photobiology* 50.5 (1989), pp. 603–609. DOI: 10.1111/j.1751-1097.1989.tb04315.x.

[110] David W. McCamant, Judy E. Kim, and Richard A. Mathies. "Vibrational Relaxation in β-Carotene Probed by Picosecond Stokes and Anti-Stokes Resonance Raman Spectroscopy." In: *The Journal of Physical Chemistry A* 106.25 (2002), pp. 6030–6038. DOI: 10.1021/jp0203595.

[111] Jian-Ping Zhang, Leif H. Skibsted, Ritsuko Fujii, and Yasushi Koyama. "Transient Absorption from the $1B_u^+$ State of All-*trans*-β-carotene Newly Identified in the Near-infrared Region." In: *Photochemistry and Photobiology* 73.3 (2001), pp. 219–222. DOI: 10.1562/0031-8655(2001)0730219TAFTUS2.0.CO2.

[112] Hideki Hashimoto, Yasushi Koyama, Yoshinori Hirata, and Noboru Mataga. "S_1 and T_1 species of β-carotene generated by direct photoexcitation from the all-trans, 9-cis, 13-cis, and 15-cis isomers as revealed by picosecond transient absorption and transient Raman spectroscopies." In: *The Journal of Physical Chemistry* 95.8 (1991), pp. 3072–3076. DOI: 10.1021/j100161a022.

[113] Renee R. Frontiera, Sangdeok Shim, and Richard A. Mathies. "Origin of negative and dispersive features in anti-Stokes and resonance femtosecond stimulated Raman spectroscopy." In: *The Journal of Chemical Physics* 129.6 (2008), p. 064507. DOI: 10.1063/1.2966361.

[114] Zhigang Sun, Zhongqi Jin, J. Lu, Dong H. Zhang, and Soo-Y. Lee. "Wave packet theory of dynamic stimulated Raman spectra in femtosecond pump-probe spectroscopy." In: *The Journal of Chemical Physics* 126.17 (2007), p. 174104. DOI: 10.1063/1.2715593.

[115] Donatas Zigmantas, Roger G. Hiller, Villy Sundström, and Tomáš Polívka. "Carotenoid to chlorophyll energy transfer in the peridinin-chlorophyll-*a*-protein complex involves an intramolecular charge transfer state." In: *Proceedings of the National Academy of Sciences* 99.26 (2002), pp. 16760–16765. DOI: 10.1073/pnas.262537599.

[116] Vytautas Butkus, Andrius Gelzinis, Ramūnas Augulis, Andrew Gall, Claudia Büchel, Bruno Robert, Donatas Zigmantas, Leonas Valkunas, and Darius Abramavicius. "Coherence and population dynamics of chlorophyll excitations in FCP complex: Two-dimensional spectroscopy study." In: *The Journal of Chemical Physics* 142.21 (2015), p. 212414. DOI: 10.1063/1.4914098.

[117] Emmanouil Papagiannakis, John T.M. Kennis, Ivo H.M. van Stokkum, Richard J. Cogdell, and Rienk van Grondelle. "An alternative carotenoid-to-bacteriochlorophyll energy transfer pathway in photosynthetic light harvesting." In: *Proceedings of the National Academy of Sciences* 99.9 (2002), pp. 6017–6022. DOI: 10.1073/pnas.092626599.

[118] Tomáš Polívka and Villy Sundström. "Dark excited states of carotenoids: Consensus and controversy." In: *Chemical Physics Letters* 477.1–3 (2009), pp. 1–11. DOI: 10.1016/j.cplett.2009.06.011.

[119] Evgeny E. Ostroumov, Marc G.Müller Michael Reus, and Alfred R. Holzwarth. "On the Nature of the "Dark S*" Excited State of β-Carotene." In: *The Journal of Physical Chemistry A* 115.16 (2011), pp. 3698–3712. DOI: 10.1021/jp105385c.

[120] Claudia Büchel. "Fucoxanthin-Chlorophyll Proteins in Diatoms: 18 and 19 kDa Subunits Assemble into Different Oligomeric States†." In: *Biochemistry* 42.44 (2003), pp. 13027–13034. DOI: 10.1021/bi0349468.

[121] Paul G. Falkowski, Richard T. Barber, and Victor Smetacek. "Biogeochemical Controls and Feedbacks on Ocean Primary Production." In: *Science* 281.5374 (1998), pp. 200–206. DOI: 10.1126/science.281.5374.200.

[122] Daisuke Kosumi et al. "One- and two-photon pump-probe optical spectroscopic measurements reveal the S_1 and intramolecular charge transfer states are distinct in fucoxanthin." In: *Chemical Physics Letters* 483.1–3 (2009), pp. 95–100. DOI: 10.1016/j.cplett.2009.10.077.

[123] James A. Bautista, Robert E. Connors, B.Bangar Raju, Roger G. Hiller, Frank P. Sharples, David Gosztola, Michael R. Wasielewski, and Harry A. Frank. "Excited State Properties of Peridinin: Observation of a Solvent Dependence of the Lowest Excited Singlet State Lifetime and Spectral Behavior Unique among Carotenoids." In: *The Journal of Physical Chemistry B* 103.41 (1999), pp. 8751–8758. DOI: 10.1021/jp9916135.

[124] Harry A. Frank, James A. Bautista, Jesusa Josue, Zeus Pendon, Roger G. Hiller, Frank P. Sharples, David Gosztola, and Michael R. Wasielewski. "Effect of the Solvent Environment on the Spectroscopic Properties and Dynamics of the Lowest Excited States of Carotenoids." In: *The Journal of Physical Chemistry B* 104.18 (2000), pp. 4569–4577. DOI: 10.1021/jp000079u.

[125] Donatas Zigmantas, Tomáš Polívka, Roger G. Hiller, Arkady Yartsev, and Villy Sundström. "Spectroscopic and Dynamic Properties of the Peridinin Lowest Singlet Excited States†." In: *The Journal of Physical Chemistry A* 105.45 (2001), pp. 10296–10306. DOI: 10.1021/jp010022n.

[126] Daisuke Kosumi et al. "Ultrafast S_1 and ICT state dynamics of a marine carotenoid probed by femtosecond one- and two-photon pump-probe spectroscopy." In: *Journal of Luminescence* 131.3 (2011), pp. 515–518. DOI: 10.1016/j.jlumin.2010.09.018.

[127] Daisuke Kosumi, Ritsuko Fujii, Mitsuru Sugisaki, Naohiro Oka, Masahiko Iha, and Hideki Hashimoto. "Characterization of the intramolecular transfer state of marine carotenoid fucoxanthin by femtosecond pump-probe spectroscopy." In: *Photosynthesis Research* 121.1 (2014), pp. 61–68. DOI: 10.1007/s11120-014-9995-6.

[128] Daisuke Kosumi et al. "Ultrafast excited state dynamics of fucoxanthin: excitation energy dependent intramolecular charge transfer dynamics." In: *Physical Chemistry Chemical Physics* 13.22 (2011), pp. 10762–10770. DOI: 10.1039/C0CP02568B.

[129] Daisuke Kosumi, Takayuki Kajikawa, Satoshi Okumura, Mitsuru Sugisaki, Kazuhiko Sakaguchi, Shigeo Katsumura, and Hideki Hashimoto. "Elucidation and Control of an Intramolecular Charge Transfer Property of Fucoxanthin by a Modification of Its Polyene Chain Length." In: *The Journal of Physical Chemistry Letters* 5.5 (2014), pp. 792–797. DOI: 10.1021/jz5000287.

[130] Donatas Zigmantas, Roger G. Hiller, Frank P. Sharples, Harry A. Frank, Villy Sundstrom, and Tomas Polivka. "Effect of a conjugated carbonyl group on the photophysical properties of carotenoids." In: *Physical Chemistry Chemical Physics* 6.11 (2004), pp. 3009–3016. DOI: 10.1039/B315786E.

[131] Emmanouil Papagiannakis, Delmar S. Larsen, Ivo H.M. van Stokkum, Mikas Vengris, Roger G. Hiller, and Rienk van Grondelle. "Resolving the Excited State Equilibrium of Peridinin in Solution†." In: *Biochemistry* 43.49 (2004), pp. 15303–15309. DOI: 10.1021/bi047977r.

[132] Emmanouil Papagiannakis, Mikas Vengris, Delmar S. Larsen, Ivo H.M. van Stokkum, Roger G. Hiller, and Rienk van Grondelle. "Use of Ultrafast Dispersed Pump-Dump-Probe and Pump-Repump-Probe Spectroscopies to Explore the Light-Induced Dynamics of Peridinin in Solution." In: *The Journal of Physical Chemistry B* 110.1 (2006), pp. 512–521. DOI: 10.1021/jp053094d.

[133] Mark Creelman, Masato Kumauchi, Wouter D. Hoff, and Richard A. Mathies. "Chromophore Dynamics in the PYP Photocycle from Femtosecond Stimulated Raman Spectroscopy." In: *The Journal of Physical Chemistry B* 118.3 (2014), pp. 659–667. DOI: 10.1021/jp408584v.

[134] Kipras Redeckas, Vladislava Voiciuk, Rasa Steponavičiūtė, Vytas Martynaitis, Algirdas Šačkus, and Mikas Vengris. "Optically Controlled Molecular Switching of an Indolobenzoxazine-Type Photochromic Compound." In: *The Journal of Physical Chemistry A* 118.30 (2014), pp. 5642–5651. DOI: 10.1021/jp505723q.

[135] Kipras Redeckas, Vladislava Voiciuk, and Mikas Vengris. "A Tunable Femtosecond Stimulated Raman Scattering System Based on Spectrally Narrowed Second Harmonic Generation." In: *Lithuanian Journal of Physics* 56 (2016), pp. 21–34. DOI: 10.3952/physics.v56i1.3273.

[136] T.M. Kardaś, B. Ratajska-Gadomska, A. Lapini, E. Ragnoni, R. Righini, M. Di Donato, P. Foggi, and W. Gadomski. "Dynamics of the time-resolved stimulated Raman scattering spectrum in presence of transient vibronic inversion of population on the example of optically excited trans-β-apo-8′-carotenal." In: *The Journal of Chemical Physics* 140.20 (2014), p. 204312. DOI: 10.1063/1.4879060.

[137] Mariangela Di Donato, Elena Ragnoni, Andrea Lapini, Tomasz M. Kardaś, Bożena Ratajska-Gadomska, Paolo Foggi, and Roberto Righini. "Identification of the Excited-State C=C and C=O Modes of *trans*-β-Apo-8′-carotenal with Transient 2D-IR-EXSY and Femtosecond Stimulated Raman Spectroscopy." In: *The Journal of Physical Chemistry Letters* 6.9 (2015), pp. 1592–1598. DOI: 10.1021/acs.jpclett.5b00528.

[138] L.J. Ballard, L.A. Glasgow, L.C. Hoskins, and T. Krohe. "The resonance Raman excitation profile of fucoxanthin." In: *Spectrochimica Acta Part A: Molecular Spectroscopy* 45.12 (1989), pp. 1235–1238. DOI: 10.1016/0584-8539(89)80235-1.

[139] Lavanya Premvardhan, Luc Bordes, Anja Beer, Claudia Büchel, and Bruno Robert. "Carotenoid Structures and Environments in Trimeric and Oligomeric Fucoxanthin Chlorophyll a/c_2 Proteins from Resonance Raman Spectroscopy." In: *The Journal of Physical Chemistry B* 113.37 (2009), pp. 12565–12574. DOI: 10.1021/jp903029g.

[140] Mariangela Di Donato, Elena Ragnoni, Andrea Lapini, Paolo Foggi, Roger G. Hiller, and Roberto Righini. "Femtosecond transient infrared and stimulated Raman spectroscopy shed light on the relaxation mechanisms of photo-excited peridinin." In: *The Journal of Chemical Physics* 142.21 (2015), p. 212409. DOI: 10.1063/1.4915072.

[141] Alisdair N. Macpherson and Tomas Gillbro. "Solvent Dependence of the Ultrafast S_2–S_1 Internal Conversion Rate of β-Carotene." In: *The Journal of Physical Chemistry A* 102.26 (1998), pp. 5049–5058. DOI: 10.1021/jp980979z.

[142] Marilena Ricci, Stephen E. Bradforth, Ralph Jimenez, and Graham R. Fleming. "Internal conversion and energy transfer dynamics of spheroidene in solution and in the LH-1 and LH-2 light-harvesting complexes." In: *Chemical Physics Letters* 259.3–4 (1996), pp. 381–390. DOI: 10.1016/0009-2614(96)00832-9.

[143] Frank L. de Weerd, Ivo H.M. van Stokkum, and Rienk van Grondelle. "Subpicosecond dynamics in the excited state absorption of all-*trans*-β-Carotene." In: *Chemical Physics Letters* 354.1–2 (2002), pp. 38–43. DOI: 10.1016/S0009-2614(02)00095-7.

[144] Helena Hörvin Billsten, Donatas Zigmantas, Villy Sundström, and Tomáš Polívka. "Dynamics of vibrational relaxation in the S_1 state of carotenoids having 11 conjugated C=C bonds." In: *Chemical Physics Letters* 355.5–6 (2002), pp. 465–470. DOI: 10.1016/S0009-2614(02)00268-3.

[145] Cosimo Bonetti, Maxime T.A. Alexandre, Ivo H.M. van Stokkum, Roger G. Hiller, Marie Louise Groot, Rienk van Grondelle, and John T.M. Kennis. "Identification of excited-state energy transfer and relaxation pathways in the peridinin-chlorophyll complex: an ultrafast mid-infrared study." In: *Physical Chemistry Chemical Physics* 12.32 (2010), pp. 9256–9266. DOI: 10.1039/B923695C.

[146] Henri Bouas-Laurent and Heinz Dürr. "Organic photochromism (IUPAC Technical Report)." In: *Pure and Applied Chemistry* 73.4 (2001), pp. 639–665. DOI: 10.1351/pac200173040639.

[147] Timothy L. Dawson. "Changing colours: now you see them, now you don't." In: *Coloration Technology* 126.4 (2010), pp. 177–188. DOI: 10.1111/j.1478-4408.2010.00247.x.

[148] Heinz Dürr and Henri Bouas-Laurent. *Photochromism: Molecules and Systems*. 1st ed. Amsterdam: Elsevier Science, 2003, p. 1218. ISBN: 978-0-444-87432-0.

[149] Naoto Tamai and Hiroshi Miyasaka. "Ultrafast Dynamics of Photochromic Systems." In: *Chemical Reviews* 100.5 (2000), pp. 1875–1890. DOI: 10.1021/cr9800816.

[150] Edm ter Meer. "Ueber Dinitroverbindungen der Fettreihe." In: *Justus Liebigs Annalen der Chemie* 181.1 (1876), pp. 1–22. DOI: 10.1002/jlac.18761810102.

[151] Garry Berkovic, Valeri Krongauz, and Victor Weiss. "Spiropyrans and Spirooxazines for Memories and Switches." In: *Chemical Reviews* 100.5 (2000), pp. 1741–1754. DOI: 10.1021/cr9800715.

[152] Tamim A. Darwish, Richard A. Evans, and Tracey L. Hanley. "Spiropyran, chromene and spirooxazine, mélange á trois: Molecular logic systems through selective and reversible deactivation of photochromism mediated by CO_2 gas." In: *Dyes and Pigments* 92.2 (2012), pp. 817–824. DOI: 10.1016/j.dyepig.2011.03.021.

[153] Masahiro Irie. "Diarylethenes for Memories and Switches." In: *Chemical Reviews* 100.5 (2000), pp. 1685–1716. DOI: 10.1021/cr980069d.

[154] Masahiro Irie, Tuyoshi Fukaminato, Takatoshi Sasaki, Naoto Tamai, and Tsuyoshi Kawai. "Organic chemistry: A digital fluorescent molecular photoswitch." In: *Nature* 420.6917 (2002), pp. 759–760. DOI: 10.1038/420759a.

[155] Satoshi Kawata and Yoshimasa Kawata. "Three-Dimensional Optical Data Storage Using Photochromic Materials." In: *Chemical Reviews* 100.5 (2000), pp. 1777–1788. DOI: 10.1021/cr980073p.

[156] Shouzhi Pu, Huohong Tang, Bing Chen, Jingkun Xu, and Wenhao Huang. "Photochromic diarylethene for two-photon 3D optical storage." In: *Materials Letters* 60.29-30 (2006), pp. 3553–3557. DOI: 10.1016/j.matlet.2006.03.050.

[157] Shouzhi Pu, Baoli Yao, Gang Liu, and Yingli Wang. "Polarization multiplexing holographic optical recording of a new photochromic diarylethene." In: *Optical Engineering* 47.3 (2008), pp. 0305021–0305021. DOI: 10.1117/1.2890426.

[158] Erhan Deniz, Massimiliano Tomasulo, Janet Cusido, Salvatore Sortino, and Françisco M. Raymo. "Fast and Stable Photochromic Oxazines for Fluorescence Switching." In: *Langmuir* 27.19 (2011), pp. 11773–11783. DOI: 10.1021/la201062h.

[159] In Sung Park, Eun-Joo Heo, and Jong-Man Kim. "A photochromic phenoxyquinone based cyanide ion sensor." In: *Tetrahedron Letters* 52.19 (2011), pp. 2454–2457. DOI: 10.1016/j.tetlet.2011.02.105.

[160] Françisco M. Raymo and Massimiliano Tomasulo. "Optical Processing with Photochromic Switches." In: *Chemistry – A European Journal* 12.12 (2006), pp. 3186–3193. DOI: 10.1002/chem.200501178.

[161] Maria-Melanie Russew and Stefan Hecht. "Photoswitches: From Molecules to Materials." In: *Advanced Materials* 22.31 (2010), pp. 3348–3360. DOI: 10.1002/adma.200904102.

[162] Massimiliano Tomasulo, Salvatore Sortino, Andrew J.P. White, and Françisco M. Raymo. "Chromogenic Oxazines for Cyanide Detection." In: *The Journal of Organic Chemistry* 71.2 (2006), pp. 744–753. DOI: 10.1021/jo052096r.

[163] Massimiliano Tomasulo, Salvatore Sortino, and Françisco M. Raymo. "A Fast and Stable Photochromic Switch Based on the Opening and Closing of an Oxazine Ring." In: *Organic Letters* 7.6 (2005), pp. 1109–1112. DOI: 10.1021/ol050045a.

[164] Massimiliano Tomasulo, Salvatore Sortino, Andrew J.P. White, and Françisco M. Raymo. "Fast and Stable Photochromic Oxazines." In: *The Journal of Organic Chemistry* 70.20 (2005), pp. 8180–8189. DOI: 10.1021/jo051417w.

[165] Massimiliano Tomasulo, Salvatore Sortino, and Françisco M. Raymo. "Bichromophoric Photochromes Based on the Opening and Closing of a Single Oxazine Ring." In: *The Journal of Organic Chemistry* 73.1 (2008), pp. 118–126. DOI: 10.1021/jo7017119.

[166] Erhan Deniz, Massimiliano Tomasulo, Salvatore Sortino, and Françisco M. Raymo. "Substituent Effects on the Photochromism of Bichromophoric Oxazines." In: *The Journal of Physical Chemistry C* 113.19 (2009), pp. 8491–8497. DOI: 10.1021/jp901494c.

[167] Massimiliano Tomasulo, Erhan Deniz, Tiziana Benelli, Salvatore Sortino, and Françisco M. Raymo. "Photochromic Polymers Based on the Photoinduced Opening and Thermal Closing of [1,3]Oxazine Rings." In: *Advanced Functional Materials* 19.24 (2009), pp. 3956–3961. DOI: 10.1002/adfm.200901364.

[168] Massimiliano Tomasulo, Salvatore Sortino, and Françisco M. Raymo. "A new family of photochromic compounds based on the photoinduced opening and thermal closing of [1,3]oxazine rings." In: *Journal of Photochemistry and Photobiology A: Chemistry* 200.1 (2008), pp. 44–49. DOI: 10.1016/j.jphotochem.2008.03.016.

[169] Michael Åxman Petersen, Erhan Deniz, Mogens Brøndsted Nielsen, Salvatore Sortino, and Françisco M. Raymo. "Photochromic Oxazines with Extended Conjugation." In: *European Journal of Organic Chemistry* 2009.25 (2009), pp. 4333–4339. DOI: 10.1002/ejoc.200900604.

[170] S.A. Antipin, A.N. Petrukhin, F.E. Gostev, V.S. Marevtsev, A.A. Titov, V.A. Barachevsky, Y.P. Strokach, and O.M. Sarkisov. "Femtosecond transient absorption spectroscopy of non-substituted photochromic spirocompounds." In: *Chemical Physics Letters* 331.5-6 (2000), pp. 378–386. DOI: 10.1016/s0009-2614(00)01213-6.

[171] Alexander K. Chibisov and Helmut Görner. "Photochromism of spirobenzopyranindolines and spironaphthopyranindolines." In: *Physical Chemistry Chemical Physics* 3.3 (2001), pp. 424–431. DOI: 10.1039/b007713p.

[172] N.P. Ernsting, B. Dick, and T. Arthenengeland. "The primary photochemical reaction step of unsubstituted indolino-spiropyrans." In: *Pure and Applied Chemistry* 62.8 (1990), pp. 1483–1488. DOI: 10.1351/pac199062081483.

[173] Jonathan Hobley, Ursula Pfeifer-Fukumura, Michael Bletz, Tsuyoshi Asahi, Hiroshi Masuhara, and Hiroshi Fukumura. "Ultrafast Photo-Dynamics of a Reversible Photochromic Spiropyran†." In: *The Journal of Physical Chemistry A* 106.10 (2002), pp. 2265–2270. DOI: 10.1021/jp012564a.

[174] Matteo Rini, Ann-Kathrin Holm, Erik T.J. Nibbering, and Henk Fidder. "Ultrafast UV-mid-IR Investigation of the Ring Opening Reaction of a Photochromic Spiropyran." In: *Journal of the American Chemical Society* 125.10 (2003), pp. 3028–3034. DOI: 10.1021/ja028262j.

[175] Jin Z. Zhang, Benjamin J. Schwartz, Jason C. King, and Charles B. Harris. "Ultrafast studies of photochromic spiropyrans in solution." In: *Journal of the American Chemical Society* 114.27 (1992), pp. 10921–10927. DOI: 10.1021/Ja00053a032.

[176] Martynas Barkauskas, Vytas Martynaitis, Algirdas Šačkus, Ričardas Rotomskis, Valdas Sirutkaitis, and Mikas Vengris. "Ultrafast dynamics of photochromic compound based on oxazine ring opening." In: *Lithuanian Journal of Physics* 48.3 (2008), pp. 231–242. DOI: 10.3952/lithjphys.48311.

[177] Vladislava Voiciuk, Kipras Redeckas, Vytas Martynaitis, Rasa Steponavičiūtė, Algirdas Šačkus, and Mikas Vengris. "Improving the photochromic properties of indolo[2,1-*b*][1,3]benzoxazines with phenylic substituents." In: *Journal of Photochemistry and Photobiology A: Chemistry* 278 (2014), pp. 60–68. DOI: 10.1016/j.jphotochem.2013.12.022.

[178] Martin Handschuh, Martin Seibold, Helmut Port, and Hans Christoph Wolf. "Dynamics of the Cyclization Reaction in Photochromic Furyl Fulgides." In: *The Journal of Physical Chemistry A* 101.4 (1997), pp. 502–506. DOI: 10.1021/jp961905v.

[179] Guy Buntinx, Sarah Foley, Christophe Lefumeux, Vladimir Lokshin, Olivier Poizat, and André Samat. "Evidence for a photophysical deactivation pathway competing with the photochromic transformation in a cyano-substituted spironaphthoxazine." In: *Chemical Physics Letters* 391.1-3 (2004), pp. 33–37. DOI: 10.1016/j.cplett.2004.04.057.

[180] Hooi Ling Kee et al. "Structural Control of the Photodynamics of Boron-Dipyrrin Complexes." In: *The Journal of Physical Chemistry B* 109.43 (2005), pp. 20433–20443. DOI: 10.1021/jp0525078.

[181] Erhan Deniz, Mutlu Battal, Janet Cusido, Salvatore Sortino, and Françisco M. Raymo. "Insights into the isomerization of photochromic oxazines from the excitation dynamics of BODIPY-oxazine dyads." In: *Physical Chemistry Chemical Physics* 14.29 (2012), pp. 10300–10307. DOI: 10.1039/c2cp41089c.

[182] Françisco M. Raymo. "Computational Insights on the Isomerization of Photochromic Oxazines." In: *The Journal of Physical Chemistry A* 116.48 (2012), pp. 11888–11895. DOI: 10.1021/jp3095787.

[183] R.Sai Santosh Kumar, Larry Lüer, Dario Polli, Michele Garbugli, and Guglielmo Lanzani. "Primary photo-events in a metastable photomerocyanine of spirooxazines." In: *Optical Materials Express* 1.2 (2011), pp. 293–304. DOI: 10.1364/OME.1.000293.

[184] Thomas Brust, Stephan Malkmus, Simone Draxler, Saleh A. Ahmed, Karola Rück-Braun, Wolfgang Zinth, and Markus Braun. "Photochemistry with thermal versus optical excess energy: Ultrafast cycloreversion of indolylfulgides and indolylfulgimides." In: *Journal of Photochemistry and Photobiology A: Chemistry* 207.2–3 (2009), pp. 209–216. DOI: 10.1016/j.jphotochem.2009.07.012.

[185] Jörg Kohl-Landgraf, Markus Braun, Cem Özçoban, Diana P.N. Gonçalves, Alexander Heckel, and Josef Wachtveitl. "Ultrafast Dynamics of a Spiropyran in Water." In: *Journal of the American Chemical Society* 134.34 (2012), pp. 14070–14077. DOI: 10.1021/ja304395k.

[186] Simone Draxler, Thomas Brust, Stephan Malkmus, Jessica A. DiGirolamo, Watson J. Lees, Wolfgang Zinth, and Markus Braun. "Ring-opening reaction of a trifluorinated indolylfulgide: mode-specific photochemistry after pre-excitation." In: *Physical Chemistry Chemical Physics* 11.25 (2009), pp. 5019–5027. DOI: 10.1039/B819585D.

[187] Emmanouil Papagiannakis, Delmar S. Larsen, Mikas Vengris, Ivo H.M. van Stokkum, and Rienk van Grondelle. "Multi-Pulse Transient Absorption and Carotenoid Excited-State Dynamics: β-Carotene." In: *Ultrafast Phenomena XIV*. Ed. by Takayoshi Kobayashi, Tadashi Okada, Keith A. Nelson, and Sandro De Silvestri. Vol. 79. Springer Series in Chemical Physics. Berlin: Springer Berlin Heidelberg, 2005, pp. 592–594. ISBN: 978-3-540-24110-2. DOI: 10.1007/3-540-27213-5_180.

[188] Stepas Toliautas, Juozas Sulskus, Leonas Valkunas, and Mikas Vengris. "Quantum chemical studies of photochromic properties of benzoxazine compound." In: *Chemical Physics* 404 (2012), pp. 64–73. DOI: 10.1016/j.chemphys.2012.03.006.

[189] John C. Crano and Robert J. Guglielmetti. *Organic Photochromic and Thermochromic Compounds*. Vol. 1: Photochromic Families. Topics in Applied Chemistry. New York: Kluwer Academic, 1999, p. 400. ISBN: 978-0-306-45882-8.

[190] F.M. Raymo. "Digital Processing and Communication with Molecular Switches." In: *Advanced Materials* 14.6 (2002), pp. 401–414. DOI: 10.1002/1521-4095(20020318)14:6<401::AID-ADMA401>3.0.CO;2-F.

[191] S. Aramaki and G.H. Atkinson. "Spironaphthopyran photochromism: picosecond time-resolved spectroscopy." In: *Journal of the American Chemical Society* 114.2 (1992), pp. 438–444. DOI: 10.1021/ja00028a007.

[192] Kipras Redeckas, Vladislava Voiciuk, Rasa Steponavičiūtė, Vytas Martynaitis, Algirdas Šačkus, and Mikas Vengris. "Ultrafast spectral dynamics of structurally modified photochromic indolo[2,1-*b*][1,3]benzoxazines." In: *Journal of Photochemistry and Photobiology A: Chemistry* 285 (2014), pp. 7–15. DOI: 10.1016/j.jphotochem.2014.04.010.

[193] A.A. Šačkus, J.A. Degutis, and A.G. Urbonavičius. "Synthesis and study of 5a,6-dihydro-12H-indolo[2,1-*b*][1,3]-benzoxazines." In: *Chemistry of Heterocyclic Compounds* 25.5 (1989), pp. 562–565. DOI: 10.1007/bf00482508.

[194] Virginė Amankavičienė, Svajus J. Asadauskas, Jolanta Girnienė, and Algirdas Šačkus. "Synthesis of Functionalized Indoline Spiropyrans by Condensation of Indolo[2,1-*b*][1,3]benzoxazines with ortho-Hydroxy-Substituted Aromatic Aldehydes." In: *Journal of Chemical Research* 2005.9 (2005), pp. 580–582. DOI: 10.3184/030823405774308817.

[195] Stephanie C. Doan and Benjamin J. Schwartz. "Ultrafast Studies of Excess Electrons in Liquid Acetonitrile: Revisiting the Solvated Electron/Solvent Dimer Anion Equilibrium." In: *The Journal of Physical Chemistry B* 117.16 (2012), pp. 4216–4221. DOI: 10.1021/jp303591h.

[196] Stephanie C. Doan and Benjamin J. Schwartz. "Nature of Excess Electrons in Polar Fluids: Anion-Solvated Electron Equilibrium and Polarized Hole-Burning in Liquid Acetonitrile." In: *The Journal of Physical Chemistry Letters* 4.9 (2013), pp. 1471–1476. DOI: 10.1021/jz400621m.

[197] Delmar S. Larsen, Ivo H.M. van Stokkum, Mikas Vengris, Michael A. van der Horst, Frank L. de Weerd, Klaas J. Hellingwerf, and Rienk van Grondelle. "Incoherent Manipulation of the Photoactive Yellow Protein Photocycle with Dispersed Pump-Dump-Probe Spectroscopy." In: *Biophysical Journal* 87.3 (2004), pp. 1858–1872. DOI: 10.1529/biophysj.104.043794.

[198] Stefan Ruetzel, Martin Kullmann, Johannes Buback, Patrick Nuernberger, and Tobias Brixner. "Tracing the Steps of Photoinduced Chemical Reactions in Organic Molecules by Coherent Two-Dimensional Electronic Spectroscopy Using Triggered Exchange." In: *Physical Review Letters* 110.14 (2013), p. 148305. DOI: 10.1103/PhysRevLett.110.148305.

[199] Vladislava Voiciuk, Kipras Redeckas, Vytas Martynaitis, Rasa Steponavičiūtė, Algirdas Šačkus, and Mikas Vengris. "Redefining the established understanding of excitation dynamics of photochromic oxazines." In: *Physical Chemistry Chemical Physics* 17.27 (2015), pp. 17828–17837. DOI: 10.1039/C5CP02143J.

[200] Vladislava Voiciuk. "Photophysical Transformations in Molecules Studied by Ultrafast Multi-Pulse Spectroscopy." Thesis. 2015.

[201] M. Tomasulo, S. Sortino, and F.M. Raymo. "Amplification of the Coloration Efficiency of Photochromic Oxazines." In: *Advanced Materials* 20.4 (2008), pp. 832–835. DOI: 10.1002/adma.200602843.

[202] Soo-Y. Lee, Donghui Zhang, David W. McCamant, Philipp Kukura, and Richard A. Mathies. "Theory of femtosecond stimulated Raman spectroscopy." In: *The Journal of Chemical Physics* 121.8 (2004), pp. 3632–3642. DOI: 10.1063/1.1777214.

[203] Kipras Redeckas, Vladislava Voiciuk, and Mikas Vengris. "Investigation of the S_1/ICT equilibrium in fucoxanthin by ultrafast pump-dump-probe and femtosecond stimulated Raman scattering spectroscopy." In: *Photosynthesis Research* 128.2 (2016), pp. 169–181. DOI: 10.1007/s11120-015-0215-9.

[204] R.G. Parr. *Density-Functional Theory of Atoms and Molecules*. Oxford University Press, USA, 1989. ISBN: 9780195357738.

[205] P.J. Stephens, F.J. Devlin, C.F. Chabalowski, and M.J. Frisch. "Ab Initio Calculation of Vibrational Absorption and Circular Dichroism Spectra Using Density Functional Force Fields." In: *The Journal of Physical Chemistry* 98.45 (1994), pp. 11623–11627. DOI: 10.1021/j100096a001.

[206] Rick A. Kendall, Thom H. Dunning, and Robert J. Harrison. "Electron affinities of the first-row atoms revisited. Systematic basis sets and wave functions." In: *The Journal of Chemical Physics* 96.9 (1992), pp. 6796–6806. DOI: 10.1063/1.462569.

[207] Vincenzo Barone. "Anharmonic vibrational properties by a fully automated second-order perturbative approach." In: *The Journal of Chemical Physics* 122.1 (2005), p. 014108. DOI: 10.1063/1.1824881.

[208] Michael J. Frisch et al. *Gaussian 09, Revision D.01*. 2013.

[209] *High Performance Computing Center "HPC Saulėtekis"*. URL: www.supercomputing.ff.vu.lt.

[210] Danuta Michalska and Rafał Wysokiński. "The prediction of Raman spectra of platinum(II) anticancer drugs by density functional theory." In: *Chemical Physics Letters* 403.1–3 (2005), pp. 211–217. DOI: 10.1016/j.cplett.2004.12.096.

[211] Kipras Redeckas, Stepas Toliautas, Rasa Steponavičiūtė, Algirdas Šačkus, Juozas Sulskus, and Mikas Vengris. "A femtosecond stimulated Raman spectroscopic study on the oxazine ring opening dynamics of structurally-modified indolobenzoxazines." In: *Chemical Physics Letters* 653 (2016), pp. 67–72. DOI: 10.1016/j.cplett.2016.04.030.

[212] Daimay Lin-Vien, Norman B. Colthup, William G. Fateley, and Jeanette G. Grasselli. *The Handbook of Infrared and Raman Characteristic Frequencies of Organic Molecules*. San Diego, USA: Academic Press, 1991, 503 p. ISBN: 0-12-451160-0.

[213] Attila Kovács, Vladiszlav Izvekov, Gábor Keresztury, and Gábor Pongor. "Vibrational analysis of 2-nitrophenol. A joint FT-IR, FT-Raman and scaled quantum mechanical study." In: *Chemical Physics* 238.2 (1998), pp. 231–243. DOI: 10.1016/S0301-0104(98)00307-3.

[214] P. Sett, S. Chattopadhyay, and P.K. Mallick. "Excited state molecular configuration of biphenyl." In: *Chemical Physics Letters* 331.2–4 (2000), pp. 215–223. DOI: 10.1016/S0009-2614(00)01173-8.

[215] Chihiro Kato, Hiro-o Hamaguchi, and Mitsuo Tasumi. "Transient absorption and Raman spectra of the S_1 state and the cation radical of biphenyl in solution." In: *Chemical Physics Letters* 120.2 (1985), pp. 183–187. DOI: 10.1016/0009-2614(85)87037-8.

[216] G. Buntinx and O. Poizat. "Triplet (T_1) state and radical cation resonance Raman investigation of biphenyl derivatives." In: *The Journal of Chemical Physics* 91.4 (1989), pp. 2153–2162. DOI: 10.1063/1.457023.

[217] Michael W. Allen, Jay R. Unruh, Brian D. Slaughter, Sarah J. Pyszczynski, Thaddaus R. Hellwig, Tim J. Kamerzell, and Carey K. Johnson. "Spectroscopy and Photophysics of Indoline and Indoline-2-Carboxylic Acid." In: *The Journal of Physical Chemistry A* 107.30 (2003), pp. 5660–5669. DOI: 10.1021/jp027813p.

[218] Luis Serrano-Andrés and Björn O. Roos. "Theoretical Study of the Absorption and Emission Spectra of Indole in the Gas Phase and in a Solvent." In: *Journal of the American Chemical Society* 118.1 (1996), pp. 185–195. DOI: 10.1021/ja952035i.

[219] Rômulo A. Ando, Antônio C. Borin, and Paulo S. Santos. "Saturation of the Electron-Withdrawing Capability of the NO_2 Group in Nitroaromatic Anions: Spectroscopic and Quantum-Chemical Evidence." In: *The Journal of Physical Chemistry A* 111.30 (2007), pp. 7194–7199. DOI: 10.1021/jp072097i.

[220] Maurizio Muniz-Miranda. "SERS monitoring of the catalytic reduction of 4-nitrophenol on Ag-doped titania nanoparticles." In: *Applied Catalysis B: Environmental* 146 (2014), pp. 147–150. DOI: 10.1016/j.apcatb.2013.03.008.

[221] Senghane D. Dieng and Johannes P.M. Schelvis. "Analysis of Measured and Calculated Raman Spectra of Indole, 3-Methylindole, and Tryptophan on the Basis of Observed and Predicted Isotope Shifts." In: *The Journal of Physical Chemistry A* 114.40 (2010), pp. 10897–10905. DOI: 10.1021/jp107295p.

[222] Ann-Kathrin Holm, Matteo Rini, Erik T.J. Nibbering, and Henk Fidder. "Femtosecond UV/mid-IR study of photochromism of the spiropyran 1′,3′-dihydro-1′,3′,3′-trimethyl-6-nitrospiro[2H-1-benzopyran-2, 2′-(2H)-indole] in solution." In: *Chemical Physics Letters* 376.1–2 (2003), pp. 214–219. DOI: 10.1016/S0009-2614(03)00949-7.

[223] Jungkweon Choi, Dae Won Cho, Sachiko Tojo, Mamoru Fujitsuka, and Tetsuro Majima. "Structural Study of Various Substituted Biphenyls and Their Radical Anions Based on Time-Resolved Resonance Raman Spectroscopy Combined with Pulse Radiolysis." In: *The Journal of Physical Chemistry A* 119.5 (2015), pp. 851–856. DOI: 10.1021/jp511229t.

[224] K. Sehested and Edwin J. Hart. "Formation and decay of the biphenyl cation radical in aqueous acidic solution." In: *The Journal of Physical Chemistry* 79.16 (1975), pp. 1639–1642. DOI: 10.1021/j100583a005.

[225] Chiharu Takahashi and Shiro Maeda. "Raman spectra of biphenyl negative ion in tetrahydrofuran solution." In: *Chemical Physics Letters* 24.4 (1974), pp. 584–588. DOI: 10.1016/0009-2614(74)80187-9.

[226] Takakazu Nakabayashi, Satoshi Kamo, Hirochika Sakuragi, and Nobuyuki Nishi. "Time-Resolved Raman Studies of Photoionization of Aromatic Compounds in Polar Solvents: Picosecond Relaxation Dynamics of Aromatic Cation Radicals." In: *The Journal of Physical Chemistry A* 105.38 (2001), pp. 8605–8614. DOI: 10.1021/jp0110105.

[227] Yutaka Sasaki and Hiro-o Hamaguchi. "Raman spectra and structure of biphenyl isoatomers (the S_0, S_1, T_1 states and the cation and anion radicals)." In: *Spectrochimica Acta Part A: Molecular Spectroscopy* 50.8 (1994), pp. 1475–1485. DOI: 10.1016/0584-8539(94)E0058-I.